UCRL-CR-123201 Vol. 3

Independent Seismic Evaluation of the 24-580-980 South Connector Ramps Response to the South Connector Ramps to a Magnitude 7.25 Hayward Fault Earthquake

David B. McCallen
Michael A. Gerhard
David J. Trummer
Robert C. Murray

November 1996

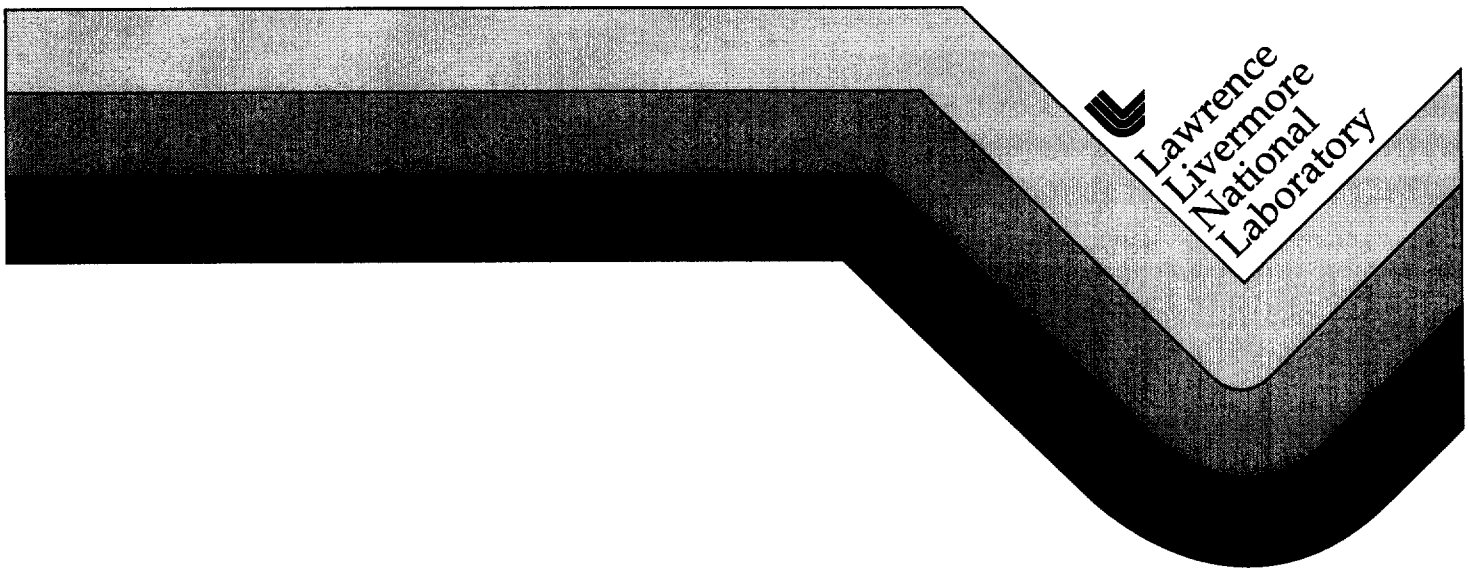

Work performed under the auspices of the U.S. Department of Energy by Lawrence Livermore National Laboratory under Contract W-7405-ENG-48.

Response of the Oakland, California 24/580/980 Interchange to a Magnitude 7.25 Hayward Fault Earthquake

Table of Contents

1.0 Background 2

2.0 Ground motion estimates for the interchange site 7

3.0 Computer model of the existing WS and ES lines 17

3.1 The as-built structure 17

3.1.1 Superstructure section properties 23

3.1.2 Nonlinear expansion joint model - restraining devices and impact model 26

3.1.3 Column-footing connectivities and representation of foundation compliance 32

3.1.4 Natural modeshapes of the structural system 37

4.0 Computer model of the retrofit WS and ES lines 45

4.1 The retrofit structure 45

4.1.1 Foundations and abutments 50

4.1.2 Nonlinear concrete model 57

4.1.3 Transient seismic response computations 70

4.1.4 Seismic demands 73

4.1.5 Capacities and demand/capacity ratios 94

5.0 Summary of results and observations 104

6.0 References 110

7.0 Acknowledgements 113

Appendix A - Bent Section Properties 114

Appendix B - Deck Section Properties 133

Appendix C - Hinge Details 163

Appendix D - Retrofit Design for WS and ES Lines 173

Response of the Oakland, California 24/580/980 Interchange to a Magnitude 7.25 Hayward Fault Earthquake

*D. McCallen**
*M. Gerhard**
*D. Trummer**
R. Murray†

Lawrence Livermore National Laboratory
New Technologies Engineering Division

**Structural Mechanics Group*
and
†*Geologic and Atmospheric Hazards Project*

1.0 Background

The 24/580/980 interchange is located near Oakland California on the Eastern perimeter of the San Francisco Bay (Fig. 1 and Fig. 2). This interchange is a major artery in the Eastern San Francisco Bay area and provides a critical link between major bay area highways. The main Concord line of the Bay Area Rapid Transit System (BART), with ridership of approximately 270,000 per day, runs underneath the interchange.

The interchange site is approximately 4 Km from the Hayward fault and 16 Km from the San Andreas fault. The reinforced concrete interchange was designed and constructed in the mid 1960's and thus the as-built structure has many of the vulnerabilities associated with typical pre-1970's concrete structures (Roberts [1], Zelinski [2], Chai et. al. [3], Priestly and Seible [4]). In 1980 some of the seismic vulnerabilities were addressed as the Interchange was retrofit with deck hinge restrainers as part of the California Department of Transportation (Caltrans) state-wide seismic retrofit of bridge expansion joints. The interchange was subjected to earthquake motion during the 1989 Loma Prieta earthquake and sustained minor damage in some of the concrete diaphragms which support the hinge restrainer forces [5]. Caltrans engineers, working together with their external consultants Imbsen and Associates, have recently completed a seismic retrofit design for portions of the interchange. The retrofit is primarily intended to fix inadequacies in many of the 1960's vintage reinforced concrete elements which constitute the bridge superstructure and foundations.

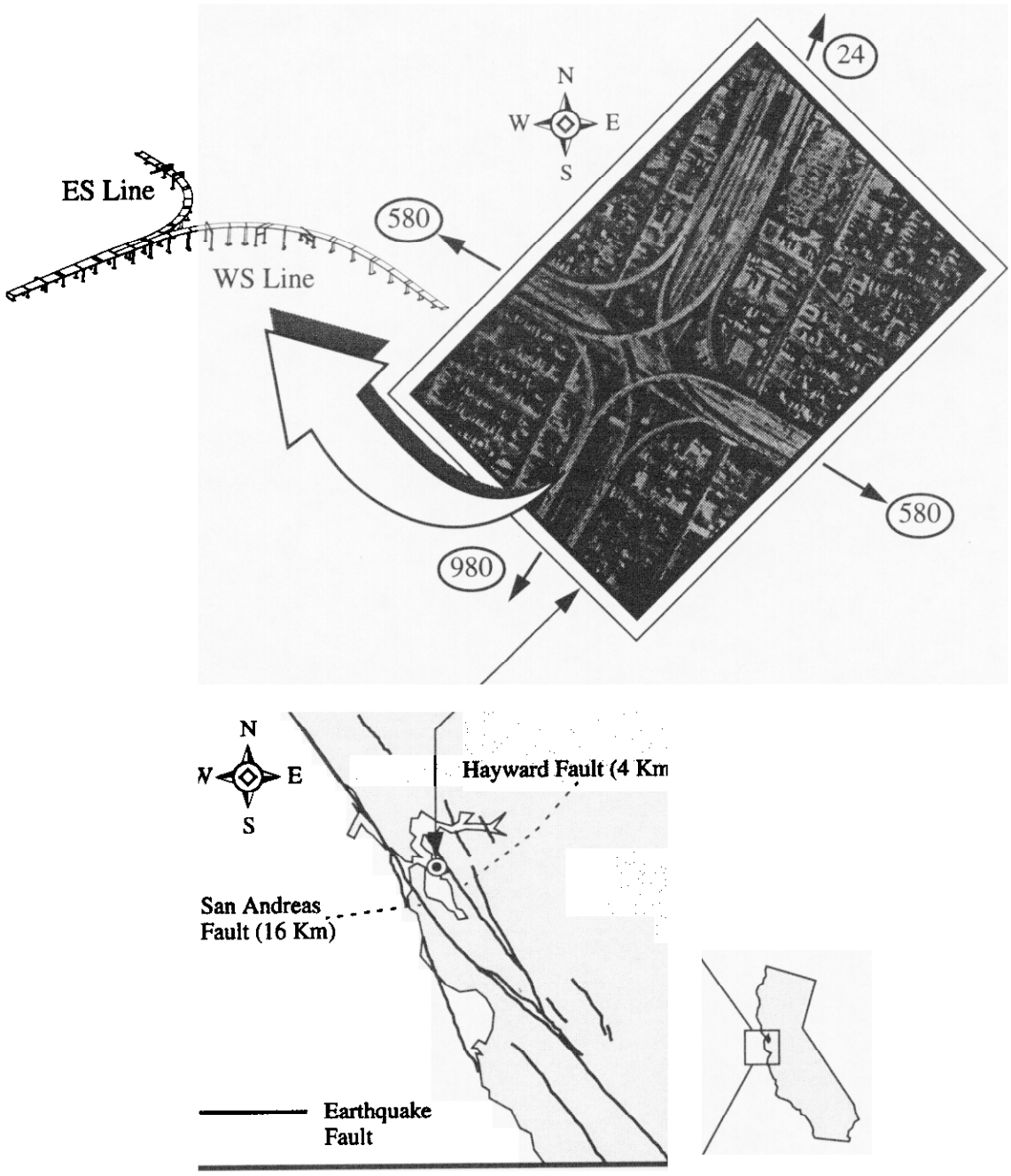

FIGURE 1. Location of the 24/580/980 interchange.

The fundamental design philosophy which governs Caltrans retrofit strategy is prevention of bridge collapse [6] during earthquakes. Thus the retrofit scheme must insure, to a high degree of reliability, that the WS and ES lines will not collapse due to earthquake ground shaking emanating from the Hayward or San Andreas Faults.

Caltrans requested that the Lawrence Livermore National Laboratory perform an independent seismic analysis evaluation of the 24/580/980 interchange retrofit concept. The scope of work consisted of three main tasks (see Fig. 3):

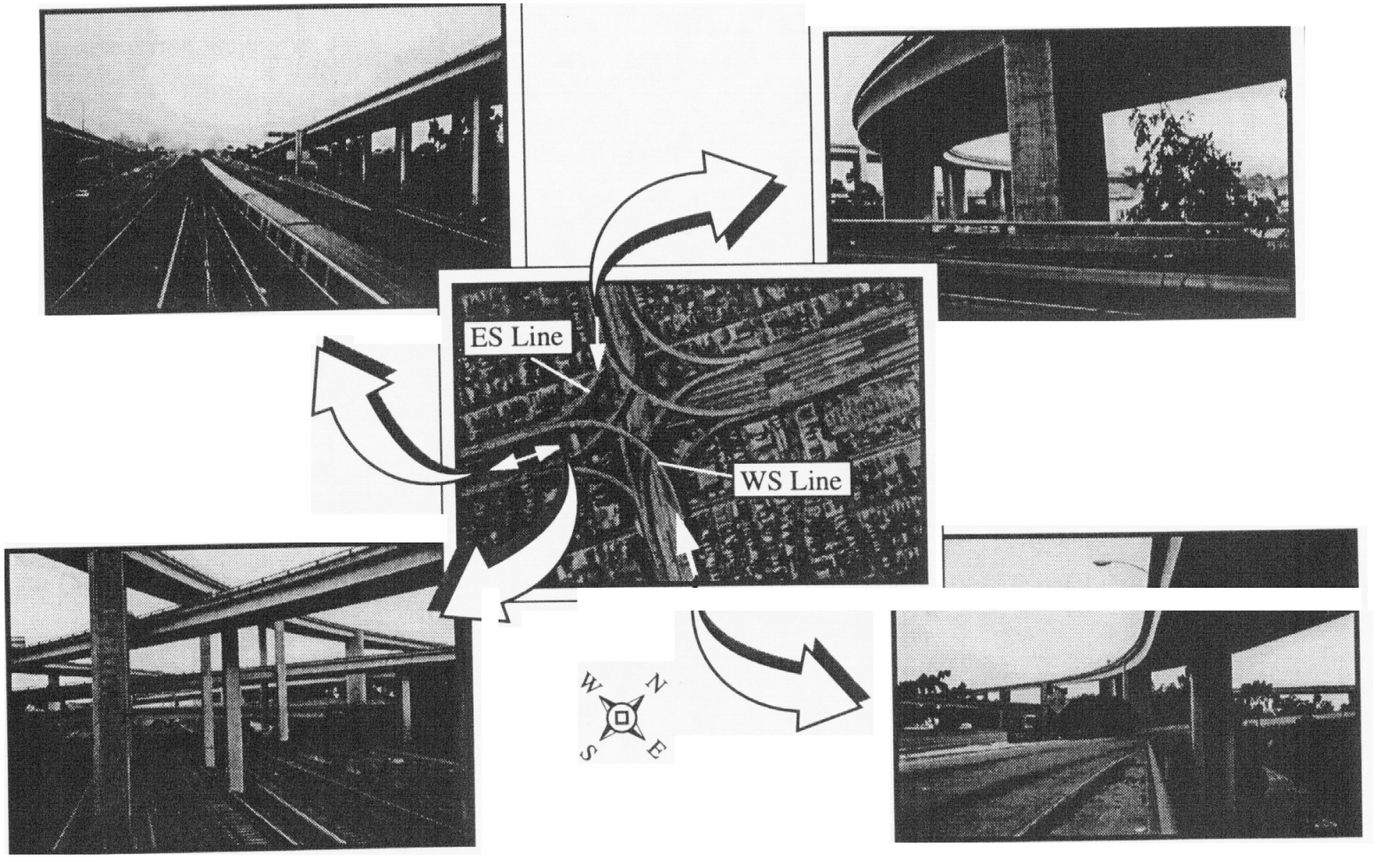

FIGURE 2. Th **(small arrows indicate viewing direction).**

① Estimation of the site seismic hazard as quantified in terms of a site rock outcrop motion

② Estimation of the bridge superstructure input motion accounting for the site soil response

③ Evaluation of the seismic demands on the structure based on computational modeling of the structure with the proposed retrofit design

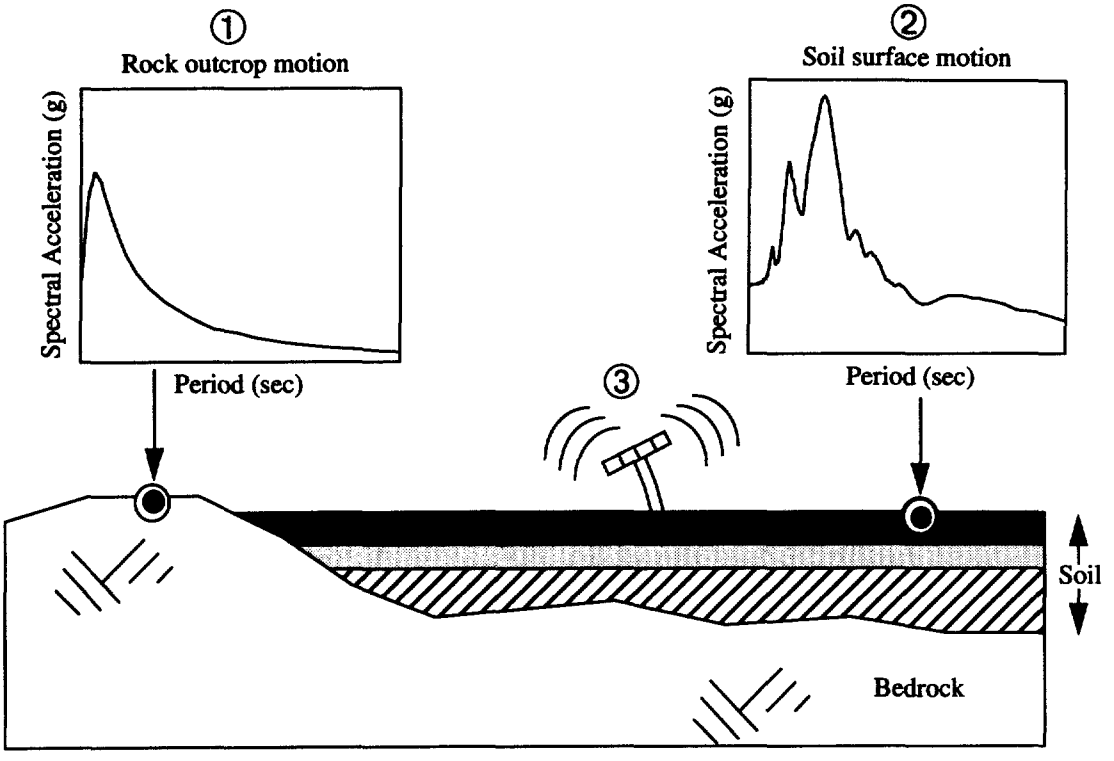

FIGURE 3. Steps in the seismic hazard evaluation.

The site hazard and soil column response evaluation are reported upon in companion documents [7,8]. The work reported on herein describes the computational modeling and assessment of seismic demands on the retrofit structure.

When subjected to extreme earthquake shaking, structures are generally expected to enter the inelastic range and exhibit some level of damage. It is economically prohibitive to design structures to remain elastic when subjected to the enormous force levels associated with strong earthquake shaking. The seismic design objective is to provide a structure with adequate ductility so that inelastic behavior can occur in a manageable way and catastrophic, brittle failure of the structure can be avoided. Unlike buildings, in which a stiff column - weak beam design philosophy results in inelastic action occurring primarily in the horizontal beam elements, bridge design philosophy attempts to ensure that inelastic action occurs in the vertical support columns. Current Caltrans design practice considers column displacement ductilities as one of the fundamental performance indicators for judging the extent of nonlinear response of concrete structures under severe seismic load-

ing. Consequently, the focus of the LLNL study was estimation of the displacements of the superstructure for extreme earthquake motions.

In order to accurately estimate the displacements of a structure responding in the nonlinear regime, nonlinear behavior must be adequately investigated. Both geometric nonlinerities and material nonlinearities may be significant contributors to structure displacements and the effect which nonlinearities have on system displacements should be addressed. In the current study, nonlinear finite element models were utilized to estimate the response of the WS and ES lines of the 24/580/980 interchange to a moment magnitude 7.25 earthquake occurring on the Hayward Fault. Displacement demands are reported for all of the WS and ES line columns, and the influence of nonlinear concrete behavior on the global structural response (i.e. system displacements) is evaluated in detail. The response of the system for two different earthquake ground motions is investigated. The first earthquake ground motion is based on the site seismic hazard definition provided to LLNL by Caltrans. This ground motion, which was based on months of analysis and Caltrans internal peer review, provided the basis for the design of the Caltrans retrofit strategy. The second earthquake motion consists of the site motion developed independently by LLNL seismologists and geotechnical engineers [7,8]. Parametric studies have been performed to assess the sensitivity of seismic displacement demands to various factors such as steel and concrete material properties, concrete nonlinearity, and the earthquake ground motion characterization. The results of the structural response parametric studies are summarized herein.

2.0 Ground motion estimates for the interchange site

The site at the 24/580/980 interchange location consists of a deep (≅ 400 ft.) soil formation as discussed in the report by Chen [8]. The site is approximately 4 Km west of the Hayward Fault. Because of the near-field proximity of the site, the existing database of measured earthquake motions provides limited insight into the level of potential ground motion which might be expected. Recent analytical and observational studies of ground motions in the near-field have indicated that unexpectedly large, longer period motions may be present in the near field which are not accounted for in classical probabilistic hazard evaluations. The 1992 Landers California earthquake [9] and the 1995 Kobe Japan earthquake [10] have provided hard evidence of both the high amplitude of shaking and the potential directionality of strong motion in the near field. In particular, large, longer period motions in the fault-normal direction have been observed [9,10]. These observations tend to validate the results of models predicting this type of radiation pattern for seismic waves in the near field.

A site seismic hazard estimate, for establishing site specific ground motions, has been performed by Geomatrix geotechnical consultants for Caltrans. The hazard definition supplied by Geomatrix consisted of a rock outcrop target spectrum for a moment magnitude 7.25 (M_w=7.25) earthquake occurring on the Hayward fault. The rock outcrop motion developed by Geomatrix is shown in Fig. 4a. This hazard definition was based on a median level of motion as a result of Caltrans internal decision making on the level of acceptable risk [11] for this particular interchange.

The rock outcrop motion was fit with existing recorded earthquake time histories, and the time histories were modified by a reduction factor to account for free surface amplification. The reduced time histories were then utilized as input motion to a 1D site soil column. The site response analysis was performed by Caltrans geotechnical staff using the nonlinear site response program *SUMDES* [12]. The surface time history for one component of motion is shown in Fig. 4a.

A number of experts, including Penzien [13], Idriss[14] and Gates[15] were consulted in developing the final surface motion that Imbsen and Associates and Caltrans ultimately used in the analysis and retrofit design for the interchange. Based on the computed Caltrans surface motions, Penzien recommended a smooth design spectra as indicated in Fig. 5. Idriss provided median and 84th percentile surface motion spectra based on empirically derived relationships for deep soil sites and he recommended a design spectra based on median ground motion per Caltrans design criteria (Fig. 5). Gates developed a spectra very similar to that proposed by Idriss as shown in Fig. 5. The final surface ground motions utilized in the Imbsen and Caltrans studies were obtained by using the Gates surface spectra as a target spectra and matching surface time histories to this spectra. The final surface time histories are shown in Fig. 6 and the corresponding spectra are shown in Fig. 7. The Caltrans surface time histories exhibit high frequency noise which one would not expect for a deep soil site. This appears to be an artifact of the fitting of the surface design spectrum.

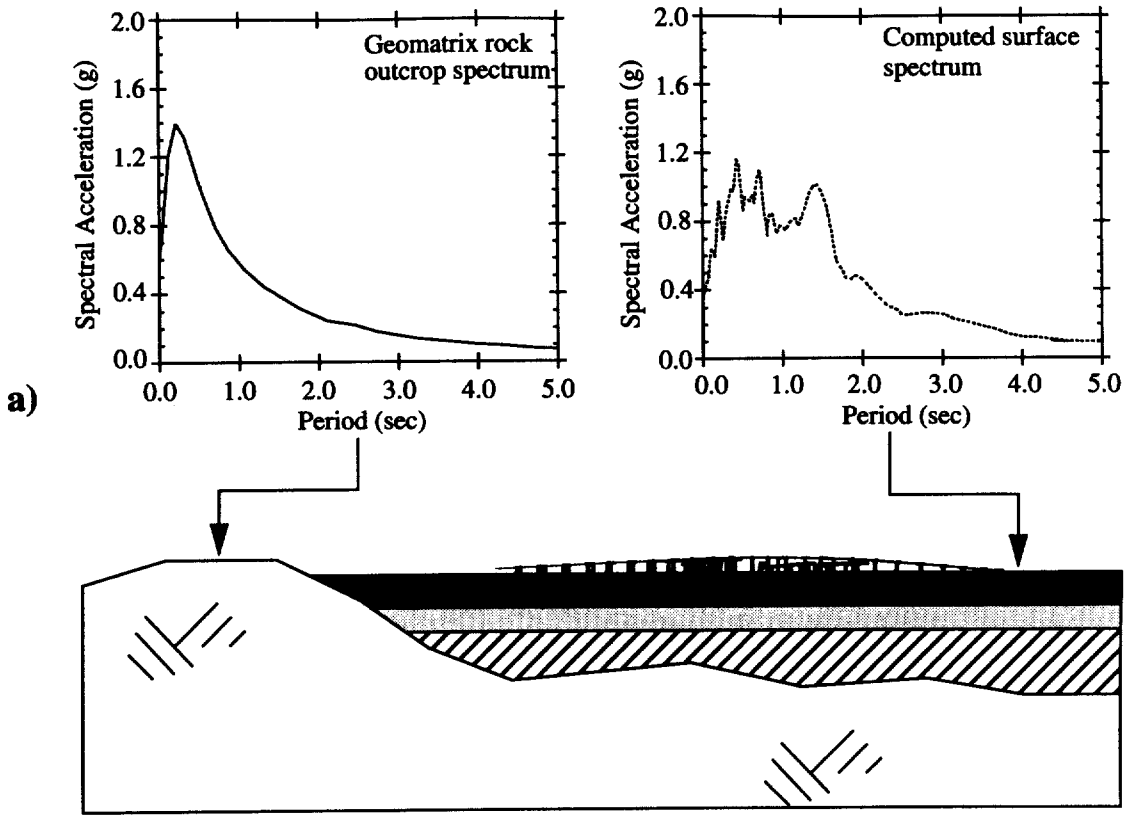

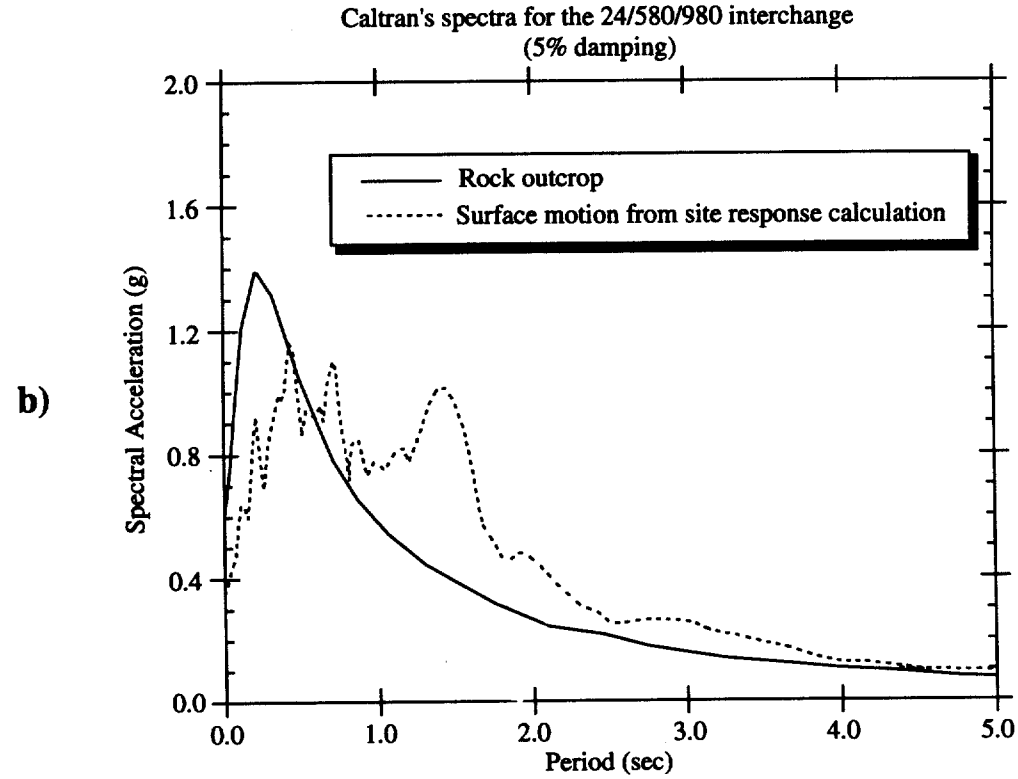

FIGURE 4. Caltrans ground motion characterization. a) Rock outcrop and computed ground surface spectra; b) rock outcrop and computed surface motion spectra.

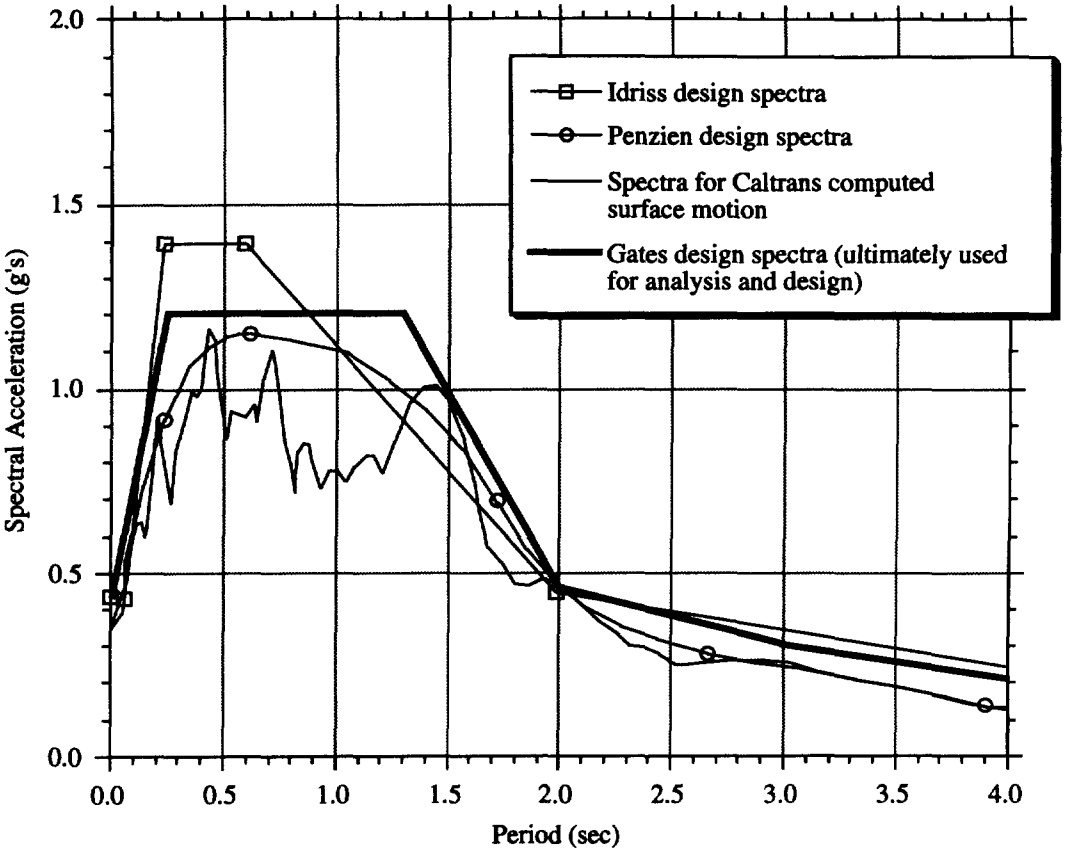

FIGURE 5. Proposed surface spectra from Penzien, Idriss and Gates.

Prior to LLNL's independent evaluation of site ground motion, LLNL did not receive a definitive policy statement from Caltrans staff on whether the analysis and retrofit design was based on median or 84th percentile motion. In light of this, ground motion estimates were initially developed for both median and 84th percentile motions. Hutchings et. al. [7] of LLNL utilized a deterministic, Empirical Green's Function (EGF) based approach to estimate ground motions at the 24/580/980 Interchange site. In their independent assessment, they reviewed the relevant geologic and seismologic data and concluded that a Hayward fault earthquake of moment magnitude 7.25 was most appropriate for definition of the hazard at this site. A probabilistic assessment of return period or yearly probability of exceedance was not within the scope of this effort. LLNL seismologists simply relied on existing geophysical data to define the Hayward fault earthquake likely to occur in the next thirty years. This independently determined magnitude matches the magnitude determined in the Caltrans hazard study.

Unlike the target spectrum approach employed in the Caltran's sponsored hazard study, the methodology employed by Hutchings and his coworkers directly generates ground motion time histories. Hutchings and his coworkers considered a suite of possible fault rupture scenarios in their ground motion estimation as detailed in reference 7. One hundred different rupture scenarios were considered and for each rupture scenario rock out-

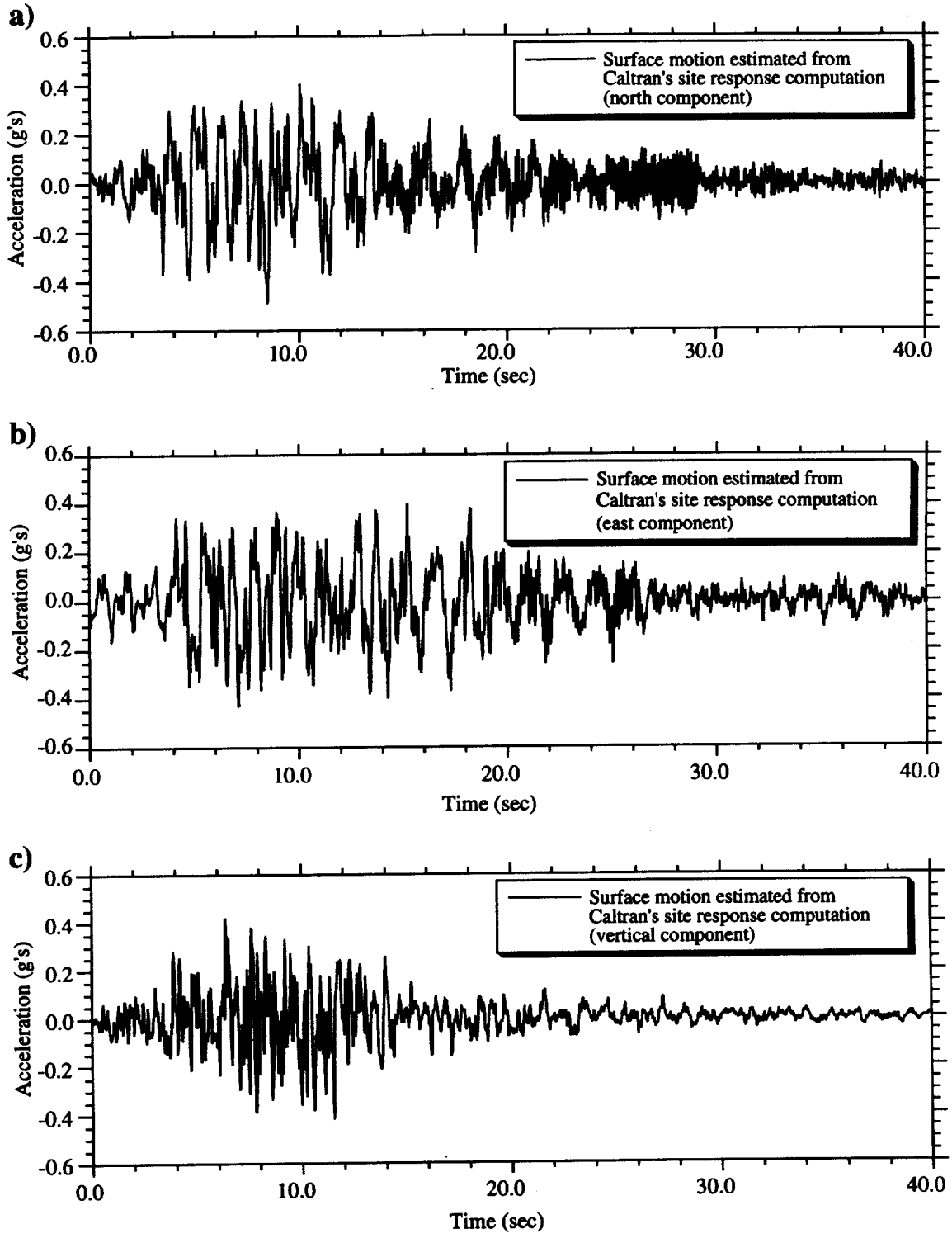

FIGURE 6. Caltrans surface motions based on SUMDES site response computation and matching of smoothed surface target spectra. a) north component of acceleration time history; b) east component acceleration time history; c) vertical component acceleration time history.

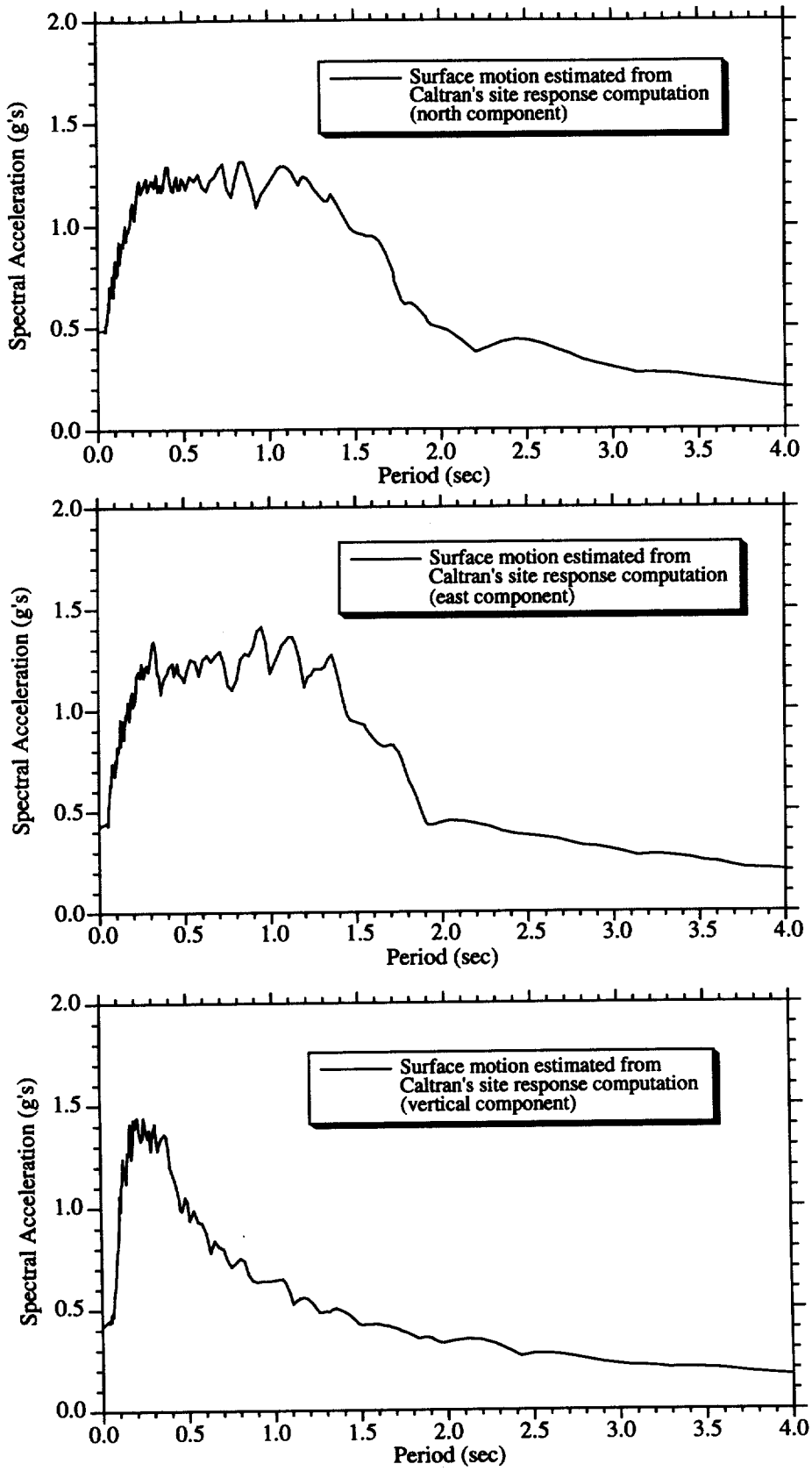

FIGURE 7. Spectra for the surface motion time histories in Fig. 6.

crop ground motion time histories were generated. The one hundred rupture scenarios provided a suite of one hundred sets of ground motion time histories, and response spectra for both the median and 84th percentile motions of this suite were generated (the average of the two horizontal components was used to develop the median and 84th percentile spectra). As the LLNL seismic study progressed, and LLNL presented ground motion results to Caltrans staff, it was determined that Caltrans policy decisions had led to their utilization of median motion. Consequently, the emphasis of the LLNL structural response evaluations were placed on consideration of the median level of earthquake motion.

In order to define ground motion time histories compatible with LLNL's estimates of the median and 84th percentile motion spectra, the rupture scenarios which provided the spectra nearest to the median and 84th percentile spectra were chosen as the rock outcrop motions defining the hazard. This approach was taken, as opposed to developing an artificial time history by matching the median or 84th percentile spectra, so that phasing information in the time history would be preserved. The outcrop motions developed by Hutchings and his coworkers were provided to Chen [8] for the soil site response calculation. Chen performed a *SHAKE* analysis to bring the motions to the surface, and the final surface time histories computed by Chen and the corresponding spectra for the median motion are shown in Fig. 8 and Fig. 9. A comparison between the Caltrans median surface motions and the LLNL median surface motions is shown in Fig. 10. It is noted that the LLNL ground motion estimates are in reasonable agreement with the Caltrans hazard definition.

The input ground motions were applied to the structural model in the appropriate global coordinate directions. The orientation of the ground motion components relative to the structure are shown in Fig. 11. Because of the manner in which the Caltrans hazard definition was developed, there is no physical basis for orienting the ground motion components in any particular direction. The directions shown in Fig. 11 for the Caltrans motions were selected solely to be consistent with the characterization used by Imbsen and Caltrans. The motions developed by LLNL, on the other hand, do have physical significance in that they truly correspond to the estimated motions in the fault normal and fault parallel directions. The directionality of the LLNL motions was accurately represented in the structural model analyses as indicated in Fig. 11.

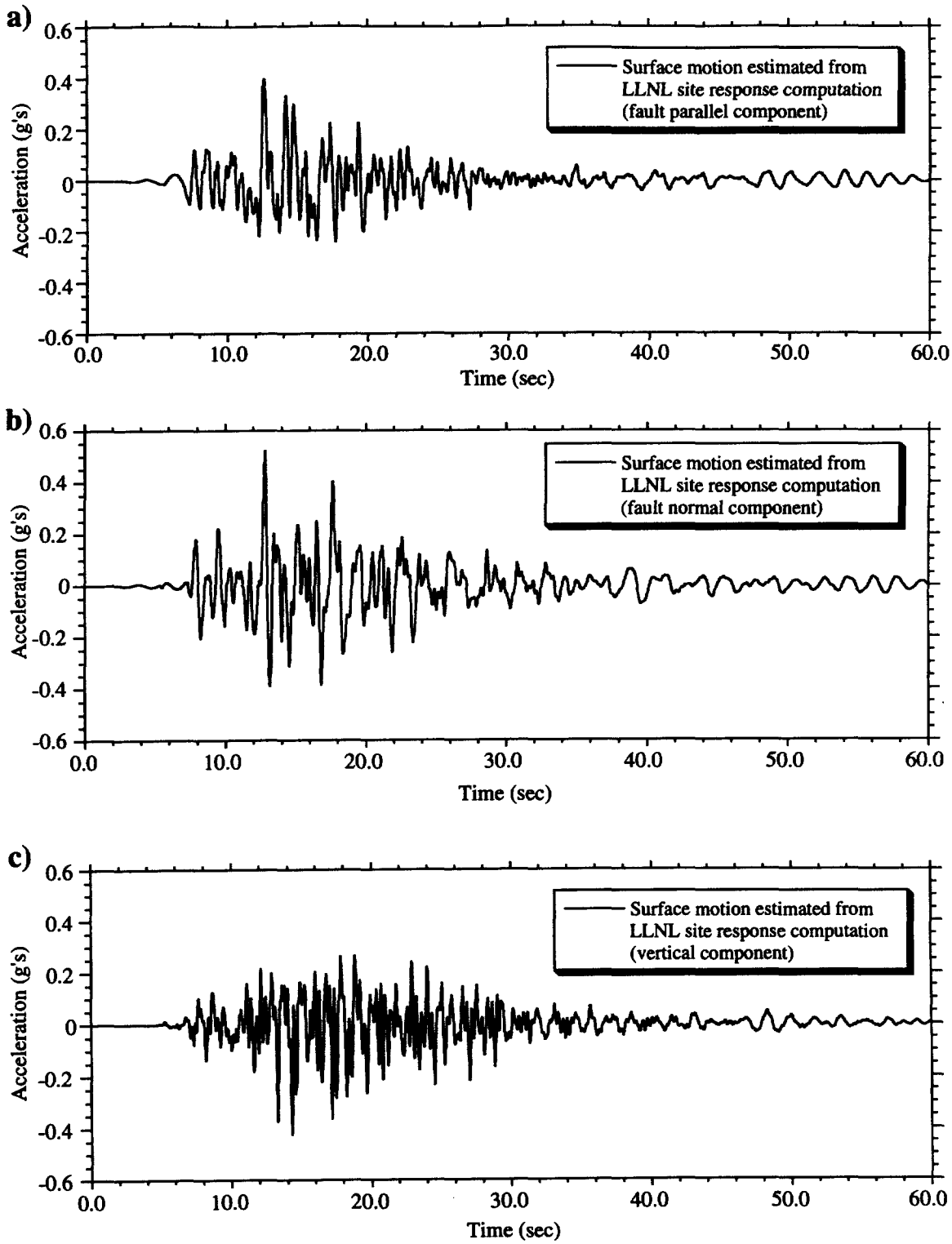

FIGURE 8. LLNL median surface motions based on SHAKE site response computation. a) fault parallel component acceleration time history; b) fault normal component acceleration time history; c) vertical component acceleration time history.

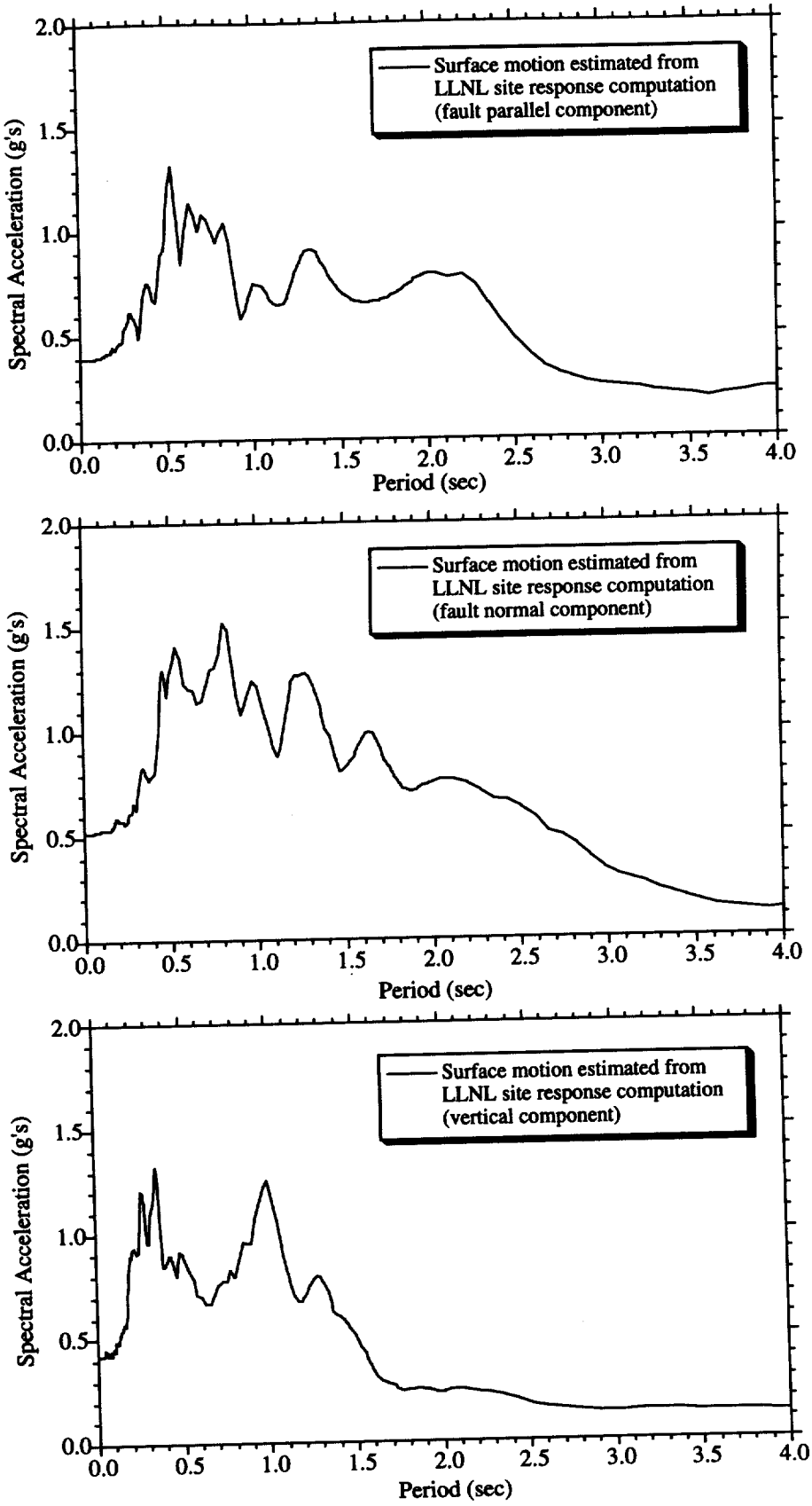

FIGURE 9. Spectra for the surface motion time histories in Fig. 8.

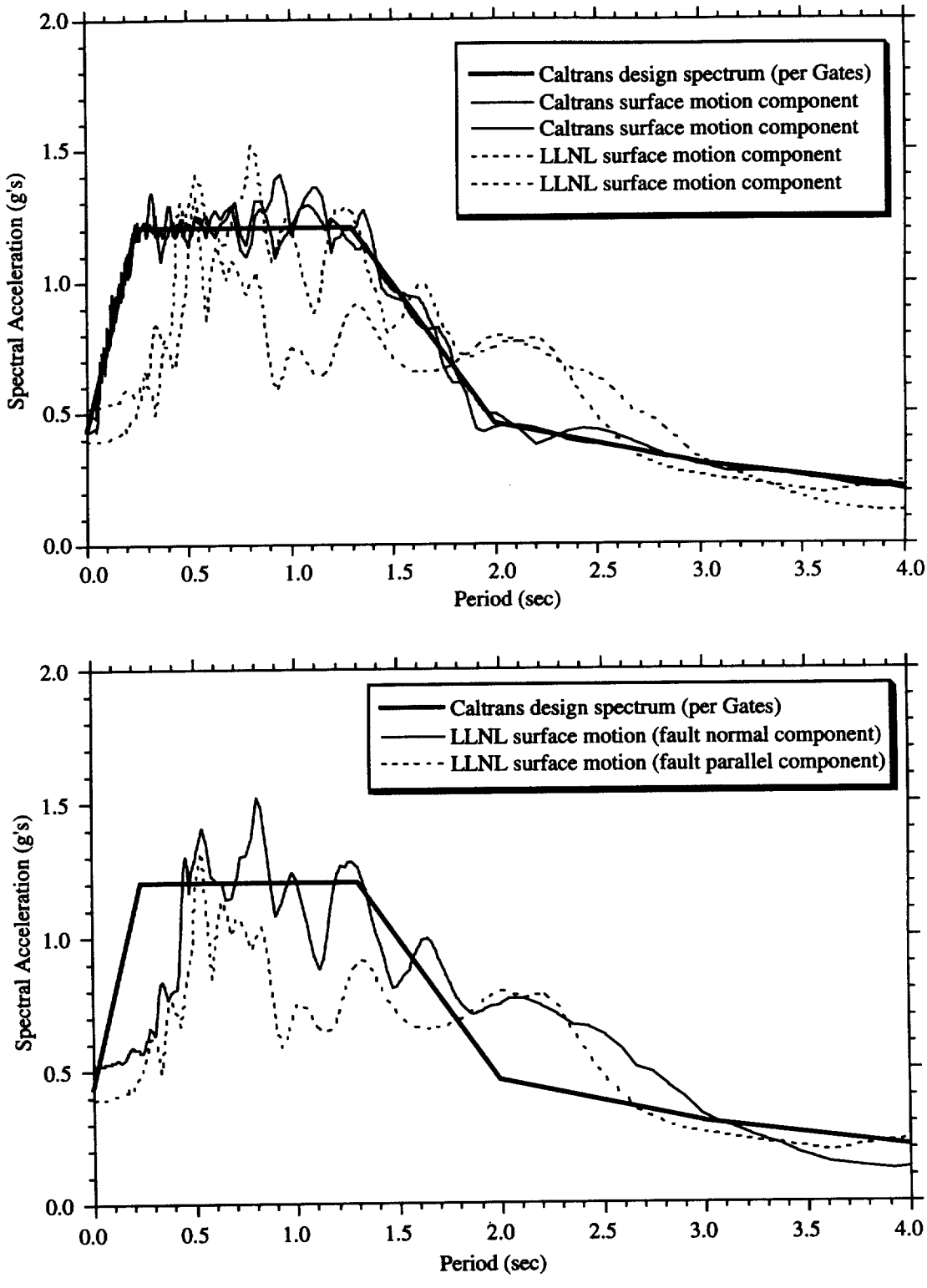

FIGURE 10. Comparison of median level motions. a) Caltrans design spectrum, Caltrans compatible time histories spectra and LLNL spectra; b) Caltrans design spectrum and LLNL spectra.

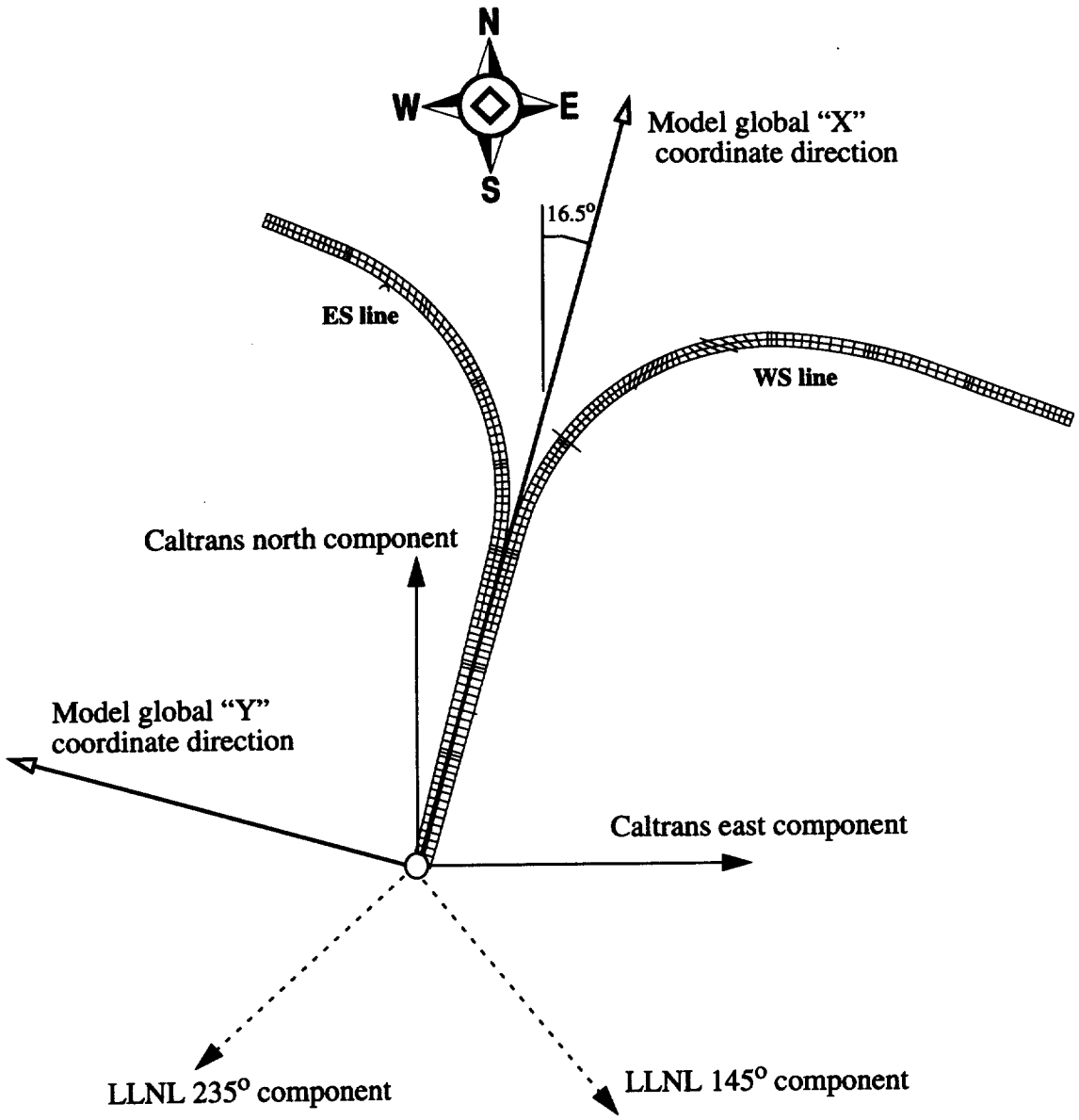

FIGURE 11. Orientation of the WS and ES lines and ground motion directions.

3.0 Computer model of the existing WS and ES lines

3.1 The as-built structure

The final scope of work for this study, as stipulated by Caltrans, was limited to investigation of the seismic demands on the retrofit WS and ES lines. However, when the project was initiated, the retrofit details and in-house check had not been completed and Caltrans staff was still actively working on the WS and ES lines. Since all of the retrofits were not immediately available, it was decided to first construct a computer model of the as-built structure, and to subsequently alter the as-built model to reflect the retrofits as they became available. This allowed significant progress to be made in the absence of the final retrofit configurations, and it also allowed for comparison of the computer predicted natural modeshapes with modeshapes of the as-built structure which were determined experimentally by Imbsen and Associates.

When constructing the as-built structural model, maximum flexibility was incorporated in the model generation process in order to facilitate model changes as the structural retrofits became available. The model generation process which was implemented is illustrated in Fig. 12. A *Pro-Engineer* [16] solid model was constructed for the ES and WS lines in order to define the three dimensional geometry of the structure. The solid model was then used to provide cartesian coordinates of selected points for the *SLIC* [17] finite element mesh generating program. The *SLIC* generation file was constructed with virtually all of the finite element model information, so that a complete finite element model input file could be generated for the *NIKE3D* [18] finite element analysis program with the push of a button. While requiring a more substantial amount of construction time in the initial stages, this approach proved to be very expedient as upgrades and structural changes became available.

The solid model and finite element model of the as-built structure are shown in Fig. 13 and Fig. 14 respectively. In the finite element model of the as-built structure, adjacent viaduct segments, which were coupled to the ES and WS lines through shared bents, were partially included so that the dynamic coupling effects could be approximately accounted for (see EN, C and SE lines in Fig. 14). The procedure which was used to approximate the adjacent lines included modeling the coupled structures an expansion joint or two away from the location of intersection of the two structures (depending on how close the nearest expansion joint was to the WS or ES line), and supplying vertical restraint to the deck segments at the expansion joints where the decks were truncated. A great deal of effort was not expended on modeling the attached lines since the structures were purposefully decoupled as part of the WS and ES line retrofits, and the coupled lines only impacted the model of the as-built structure. The model shown in Fig. 14 contained 11,578 active degrees of freedom.

The finite element model for the as-built structure utilized a linear elastic model for the concrete constitutive behavior and gross sections with concrete material moduli were used to characterize the concrete members. Since geometric nonlinearities associated with expansion joint behavior and material nonlinearities associated with potential restrainer

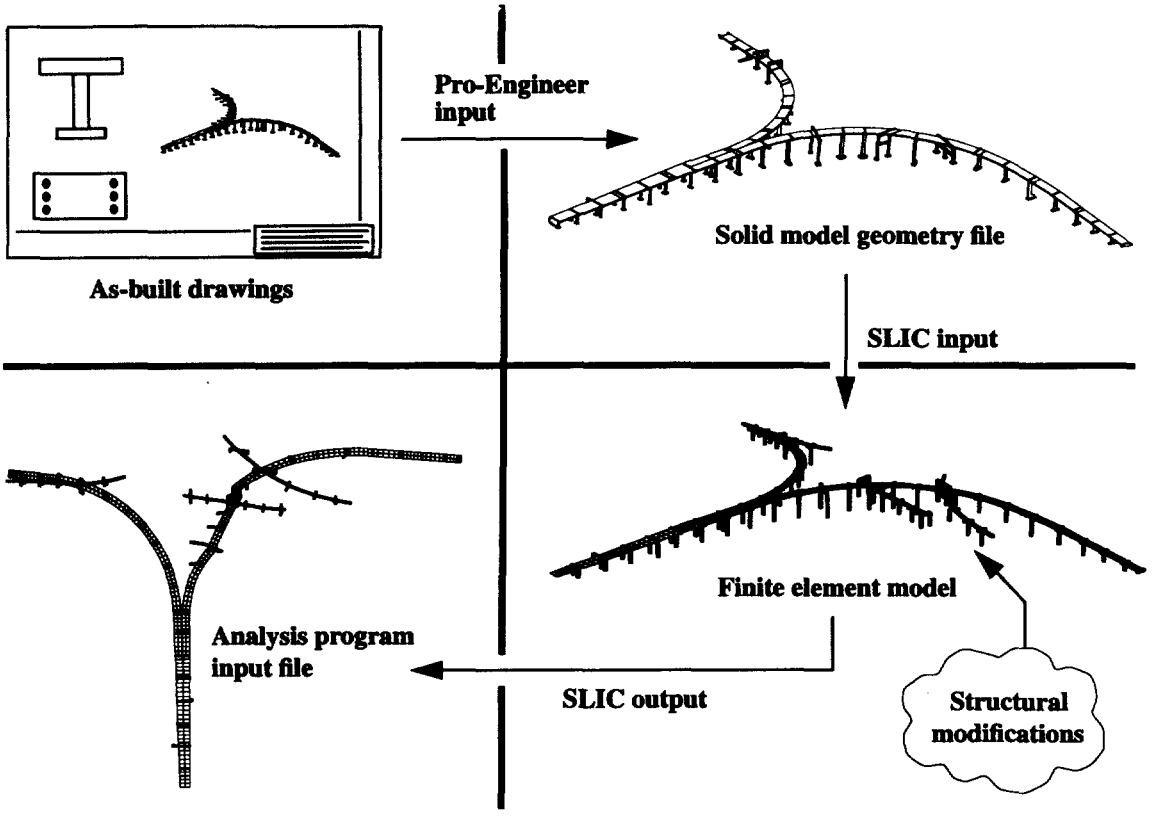

FIGURE 12. Model generation process developed to accommodate numerous structural model changes.

cable and rod yielding were to be included, the model was constructed for the nonlinear finite element program *NIKE3D*. *NIKE3D* is a general purpose program for the nonlinear analysis of solids and structures which has been developed at LLNL over approximately the past twenty years.

In order to provide a physical perspective on what the computer model is actually representing, selected segments of the as-built structure are shown in Fig. 15 and Fig. 16. Full appreciation of the massive size and height of the WS and ES line structures can only be obtained from a site visit, where the eighty foot height of the columns near the center of the WS line can be put in proper prospective. The WS line, which crosses the BART tracks is a "flyover" structure in the truest sense of the word.

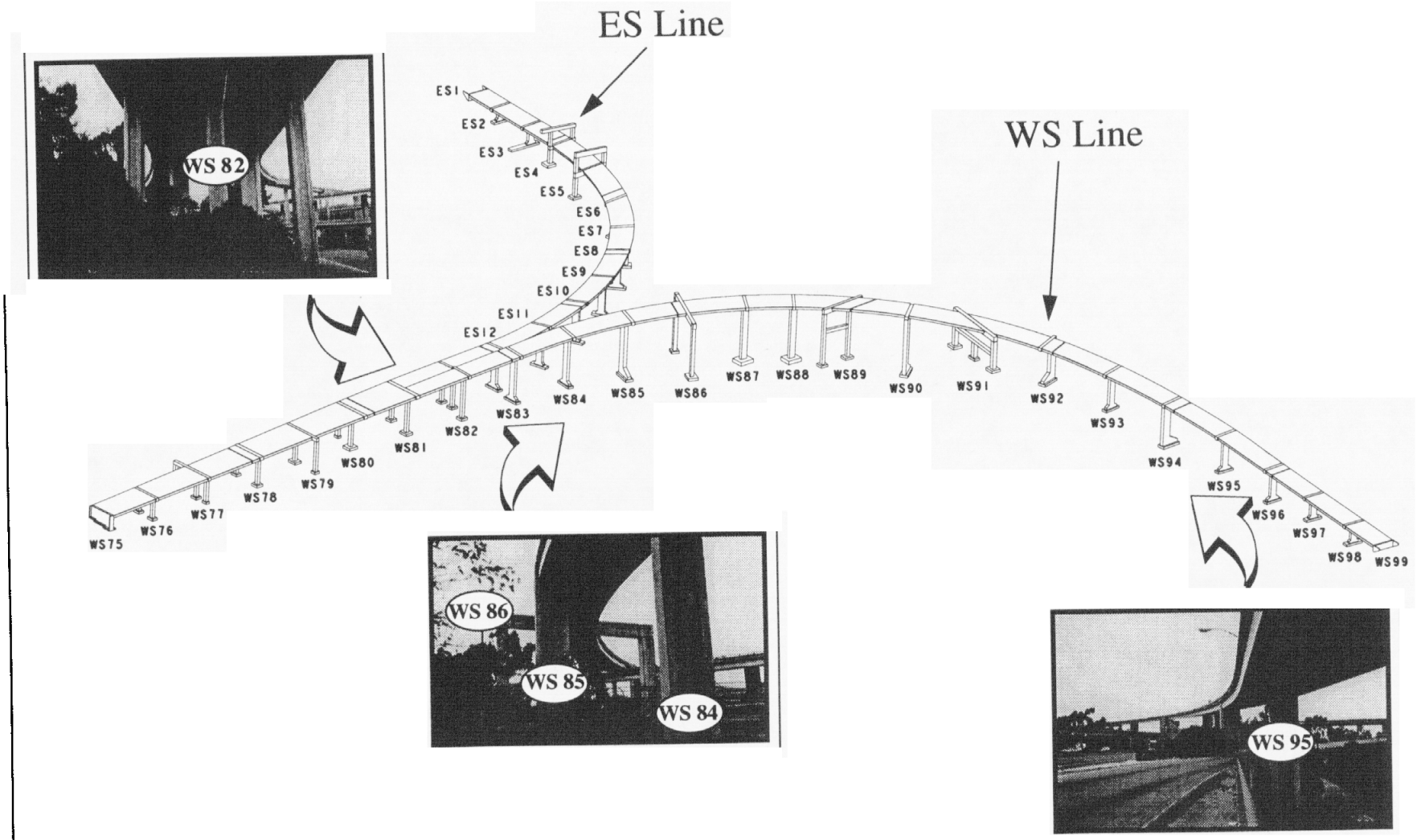

FIGURE 13. Solid model of the WS and ES lines (arrows indicate view directions).

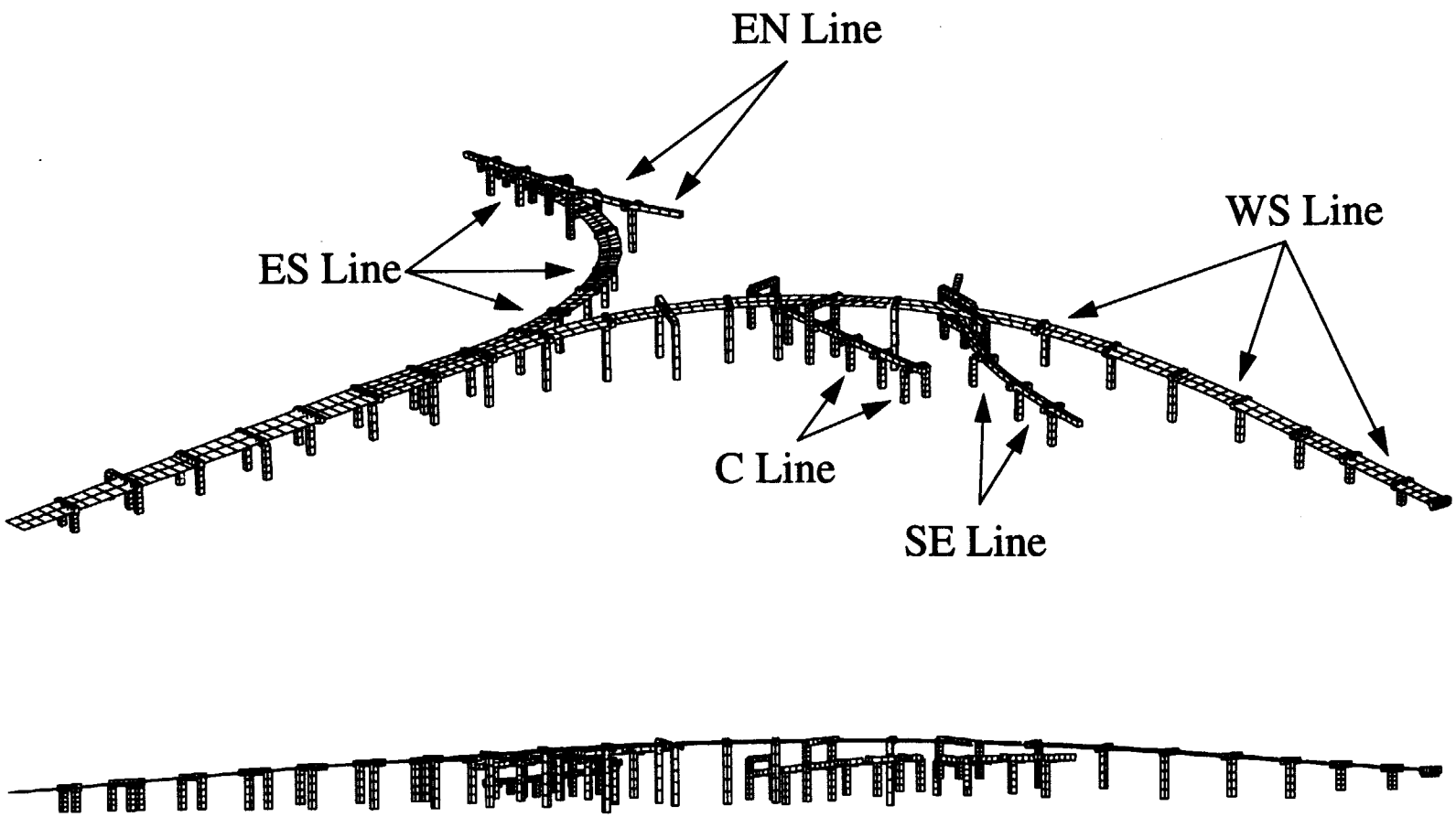

FIGURE 14. Finite element model of the WS and ES lines.

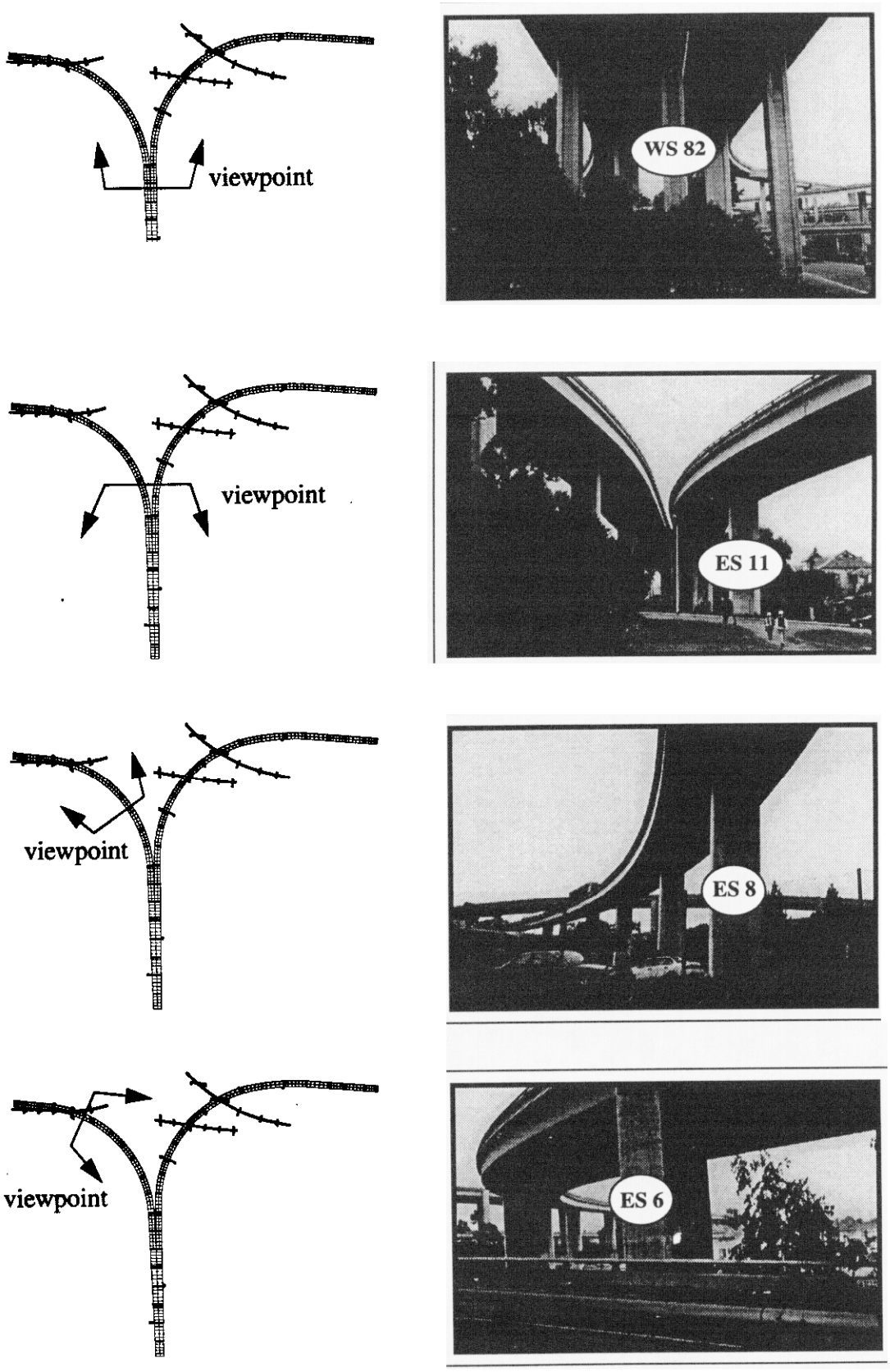

FIGURE 15. Selected views of WS and ES lines.

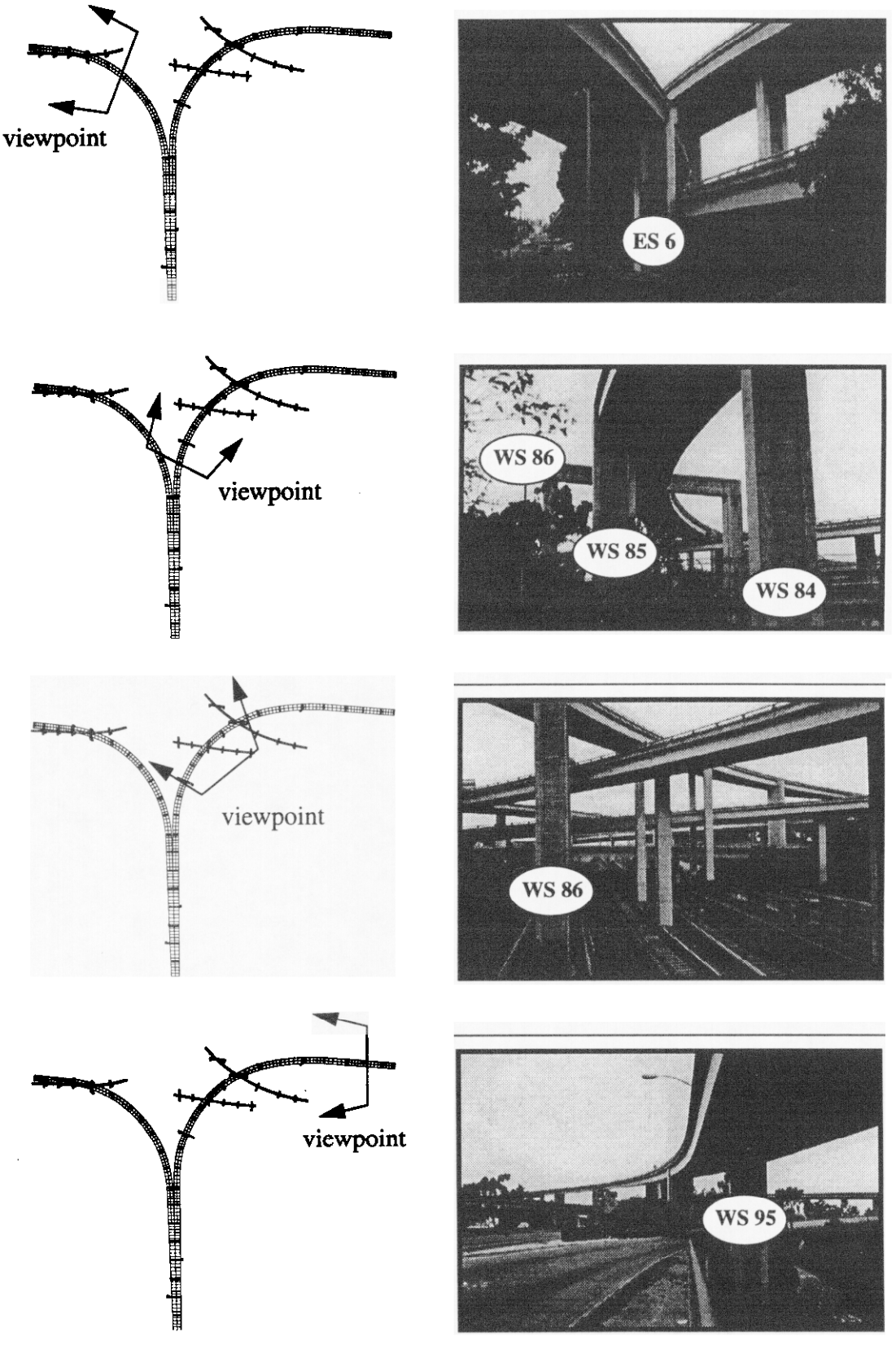

FIGURE 16. Selected views of WS and ES lines.

3.1.1 Superstructure section properties

In the computer model of the as-built structure, one dimensional beam elements were used to represent both the box girder deck structure as well as the bent columns and bent cap beams. The accuracy of beam element idealizations of the box girder deck structure has been investigated by McCallen and Romstad [19] by comparison of beam element models with detailed, three dimensional shell based models of box girder decks. Based on this previous work, it was decided that the beam element idealization was sufficiently accurate for the global analysis in this study.

The *NIKE3D* finite element program has advanced fiber type beam element capabilities which allow the user to define a generalized beam element cross section via user defined integration points (Maker, Whirley and Engelmann [20]). This element definition allows the box girder deck to be subdivided into a number of zones, with each zone defined by its location and area. The program then calculates the appropriate cross section stiffnesses based on the zone definitions and the defined material stress-strain behavior for the particular zone. As discussed in a subsequent section, this fiber element provides a powerful tool for characterizing nonlinear behavior of flexural structural elements such as beams and columns in a bridge structure.

The typical zone definitions for a section of box girder deck are shown in Fig. 17, and the deck cross section definitions for all of the WS and ES Line segments are shown in Appendix B.

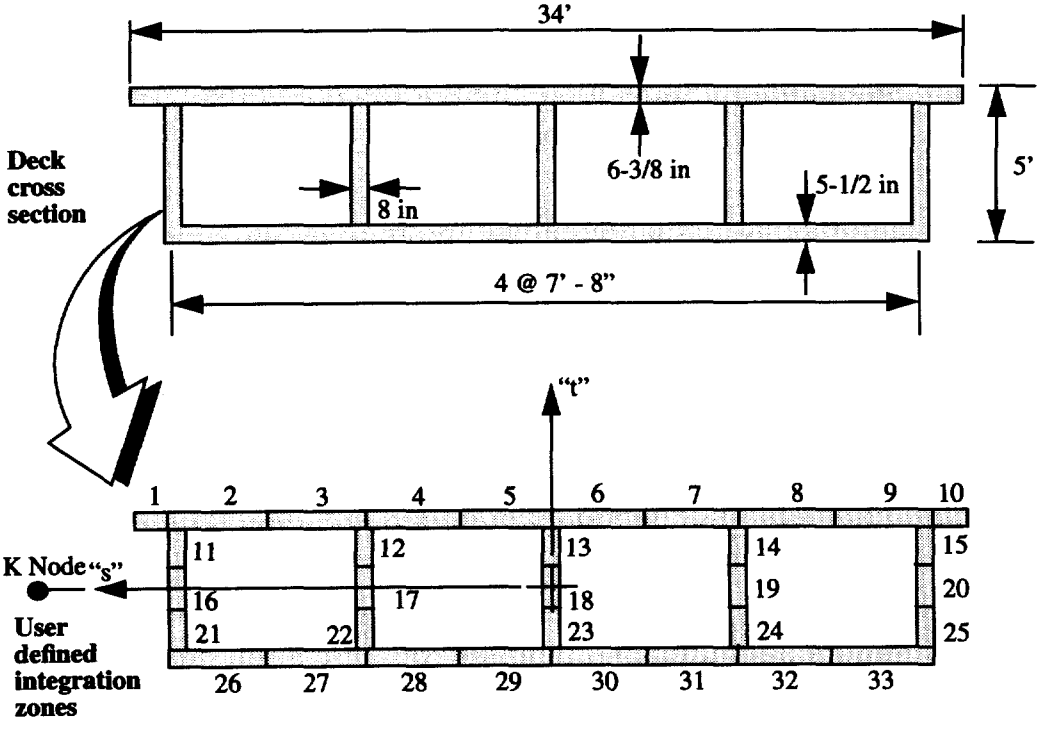

FIGURE 17. Box girder deck section and user defined cross section integration zones.

The basic user defined element was used to characterize the deck stiffness properties in the bridge finite element model. In order to assist in accurate representation of the deck torsional dynamics, and to help visually assess the bridge dynamics in computer animations, rigid and massless cross beams and massless and flexible shells were added to the basic deck beam model as indicated in Fig. 18. These added elements allowed a portion of the

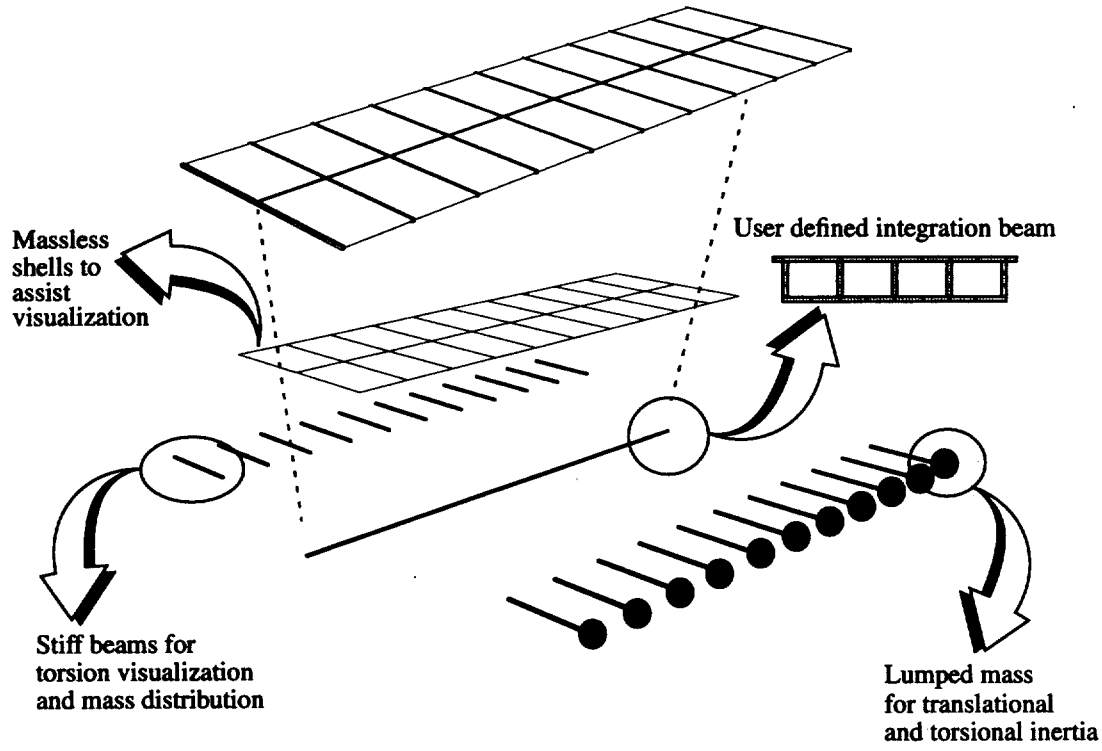

FIGURE 18. Reduced order, composite beam/shell/lumped mass model for a box girder deck section.

deck mass to be lumped at the extreme edges of the deck, which enhances the accuracy of the torsional characteristics of the beam element deck model. A comparison of the beam element based model with a three dimensional shell element based model is shown in Fig. 19, and the modal frequencies are summarized in Table 1. The reduced order composite model provides a good approximation of the deck segment dynamic properties.

TABLE 1. Modal frequencies from detailed and reduced order models

	Discrete three dimensional shell model	Composite beam/shell model	% difference
Mode #1	6.76 Hz	7.24 Hz	7%
Mode #2	12.46	14.47	16%
Mode #3	17.44	19.42	11%
Mode #4	21.45	20.24	6%

The model of the as-built structure shown in Fig. 14 (section 3.1), employs the composite deck model for all of the deck segments.

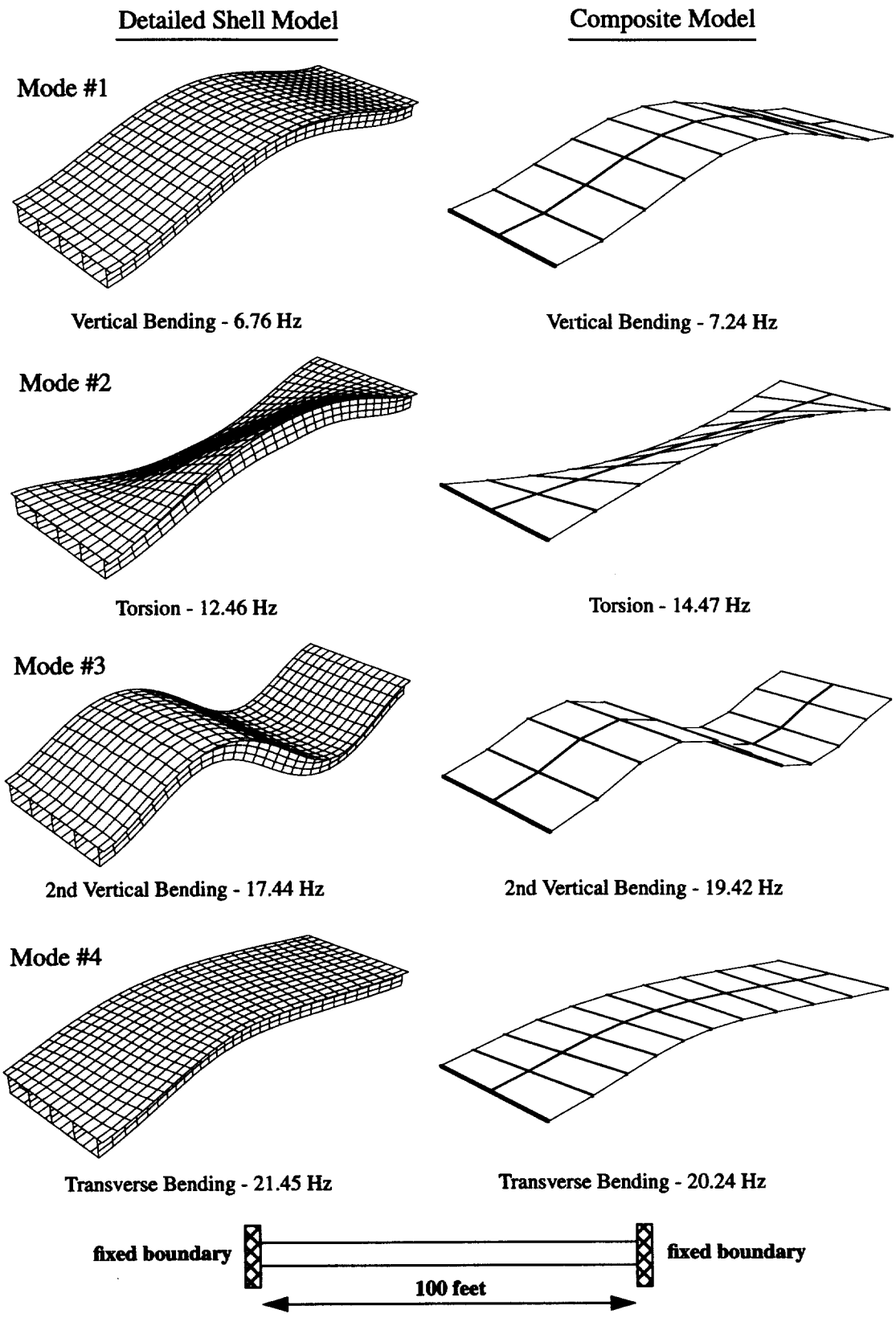

FIGURE 19. Modeshapes of a 100 foot box girder deck segment as computed from detailed discrete and reduced order composite models.

3.1.2 Nonlinear expansion joint model - restraining devices and impact model

Recent numerical simulations of seismic bridge response (Fenves [21]) and measurements of field performance of bridges in earthquakes (Shakal et. al. [22]) have indicated that during significant seismic shaking, geometric nonlinearities associated with impact and tensioning of restraining devices can have a significant influence on the global dynamic bridge response. Based on examination of bridge response records for a major Southern California concrete bridge, Malhotra et. al. [22] found that significant collisions and impact forces can occur between adjacent bridge frames even under relatively modest ground excitation levels (i.e. 0.10 pga).

As a result of deck discontinuities created by expansion hinges, many bridge structures actually behave as a system of partially coupled frames with significantly different coupling in the longitudinal and transverse directions. An accurate numerical model must address the complex, geometrically nonlinear coupling between adjacent bridge frames.

The WS and ES lines contain thirteen expansion hinges as shown in Fig. 20, and the expansion joints divide the overall structure into fourteen distinct frames. The restrainers at the expansion hinges employ both steel rod and cable restrainers as shown in Fig. 20. The length of the expansion joint seats on these particular structures range from fourteen inches to sixteen inches depending on the hinge [23].

The expansion hinge model incorporated in the structural model of the WS and ES lines consists of penalty function based contact surfaces to account for potential impact across the expansion hinge (Fig. 21). In terms of physical interpretation, the penalty contact surface essentially places a stiff, zero length spring between adjacent contacting elements in order to transfer contact forces from adjacent bridge segments across a closed joint. The forces generated by the contact surface ensure displacement compatibility is enforced across a joint, i.e. two contacting surface cannot penetrate one another. When the expansion joint is open, the penalty contact surface algorithm correctly senses that the contact surface has opened, removes the contact springs, and thus provides the appropriate stress free condition across the contact surface interface. The manner in which penalty contact forces are manifested in the global equilibrium equations is summarized in McCallen and Romstad [24].

The potential tensioning of expansion joint restrainers is modeled with discrete elements in the *NIKE3D* finite element model. *NIKE3D* discrete elements can be used to define an arbitrary, linear or nonlinear force-displacement behavior which is generated by relative displacement between two specified model node points. Caltrans load testing of restraining cables and restraining rods has shown that when tensioned, the rod and cables exhibit essentially elasto-plastic behavior once the member yield stress is obtained. Caltrans data for a steel expansion hinge restraining rod is shown in Fig. 22a. The force-deflection characteristics of a tension-only, elasto-plastic discrete member used to model the rod restrainer are shown in Fig. 22. As shown in the comparison in Fig. 22c, the simple tension-only elasto-plastic discrete element adequately represents the restrainer behavior.

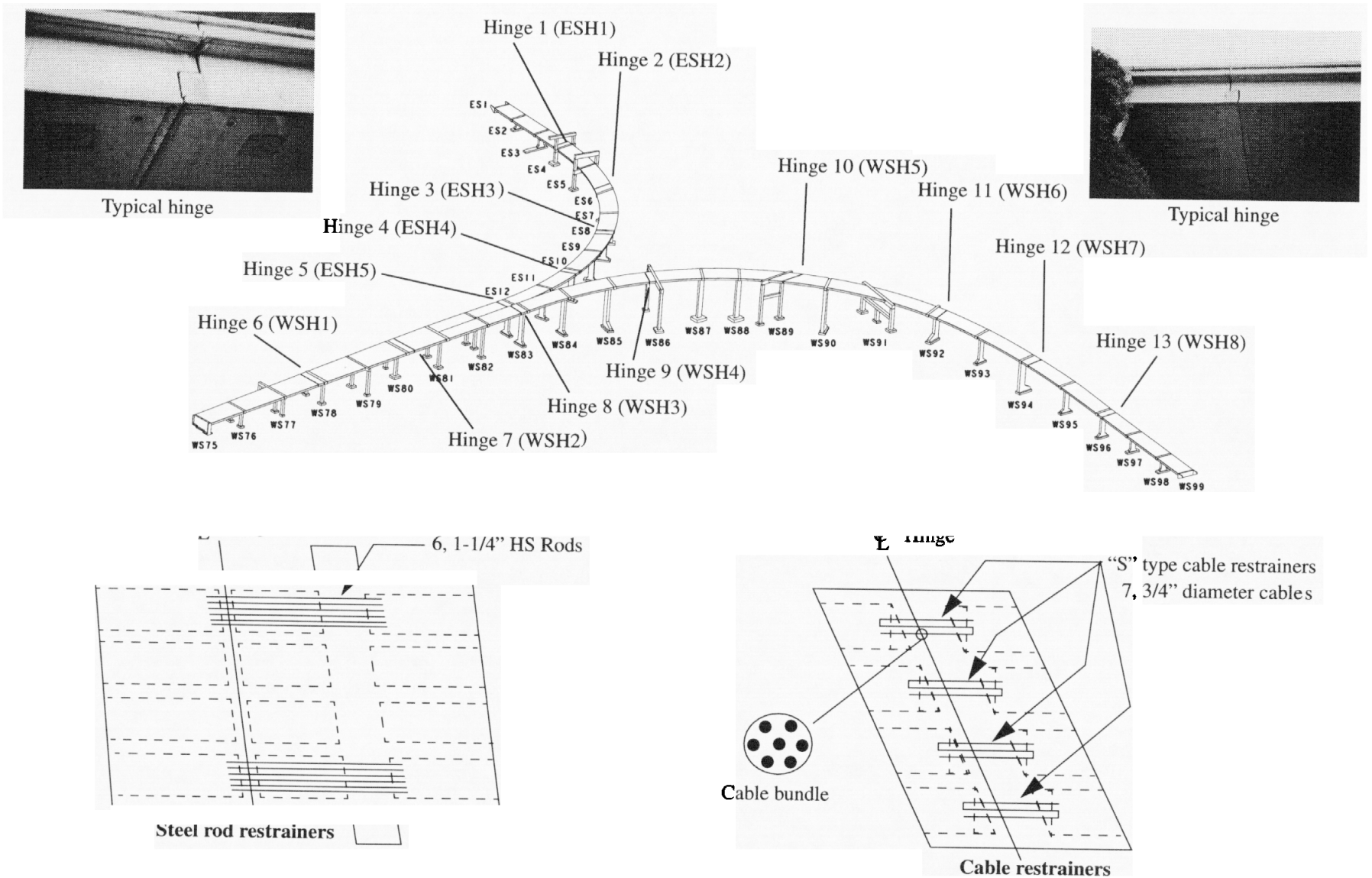

FIGURE 20. Expansion joint hinges in the WS and ES lines.

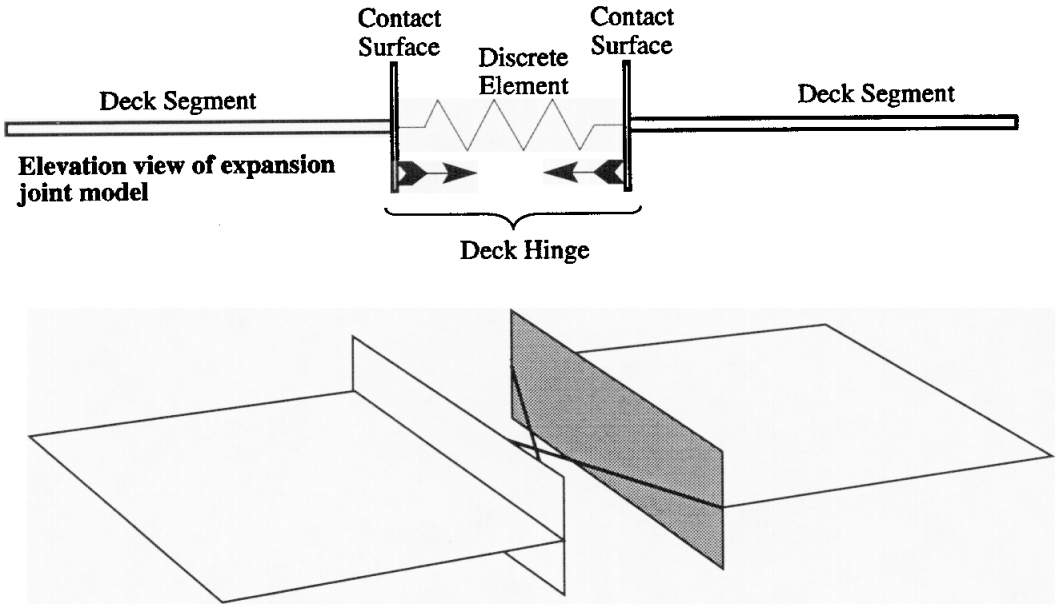

FIGURE 21. Expansion joint hinge model.

Typically, adjacent bridge frames are weakly coupled in the longitudinal direction because the expansion seats are specifically designed to accommodate relative bridge displacements. In the transverse direction, however shear keys appear to result in a strong coupling between adjacent bridge frames with minimal relative displacement of adjacent deck segments. To replicate this behavior in the finite element model, contact surfaces and discrete elements were used to model the longitudinal coupling and stiff transverse stiffness elements were used to model the coupling forces provided by transverse shear keys. In the vertical direction, large gravity forces result in continuous contact between adjacent deck segments at the expansion hinge seat and this condition was emulated by enforcing vertical displacement compatibility by master/slaving adjacent deck nodes in the vertical direction.

In the bridge joint idealization employed in this study, frictional forces at the expansion joints, which might add resistance to relative longitudinal motion between adjacent frames, were neglected. The rational for this idealization was the fact that field observations indicate that the frictional forces tend to be small relative to the shear forces in the frame members. Discussions with Fenves [25] indicated that his work tends to confirm the fact that the longitudinal friction forces have little if any influence on the dynamics of the individual frames. In addition, the observations of Shakal et. al. indicate that the friction forces were incapable of preventing significant relative bridge frame motions at 0.1g ground accelerations, and the ground motions in the current study are significantly larger than this.

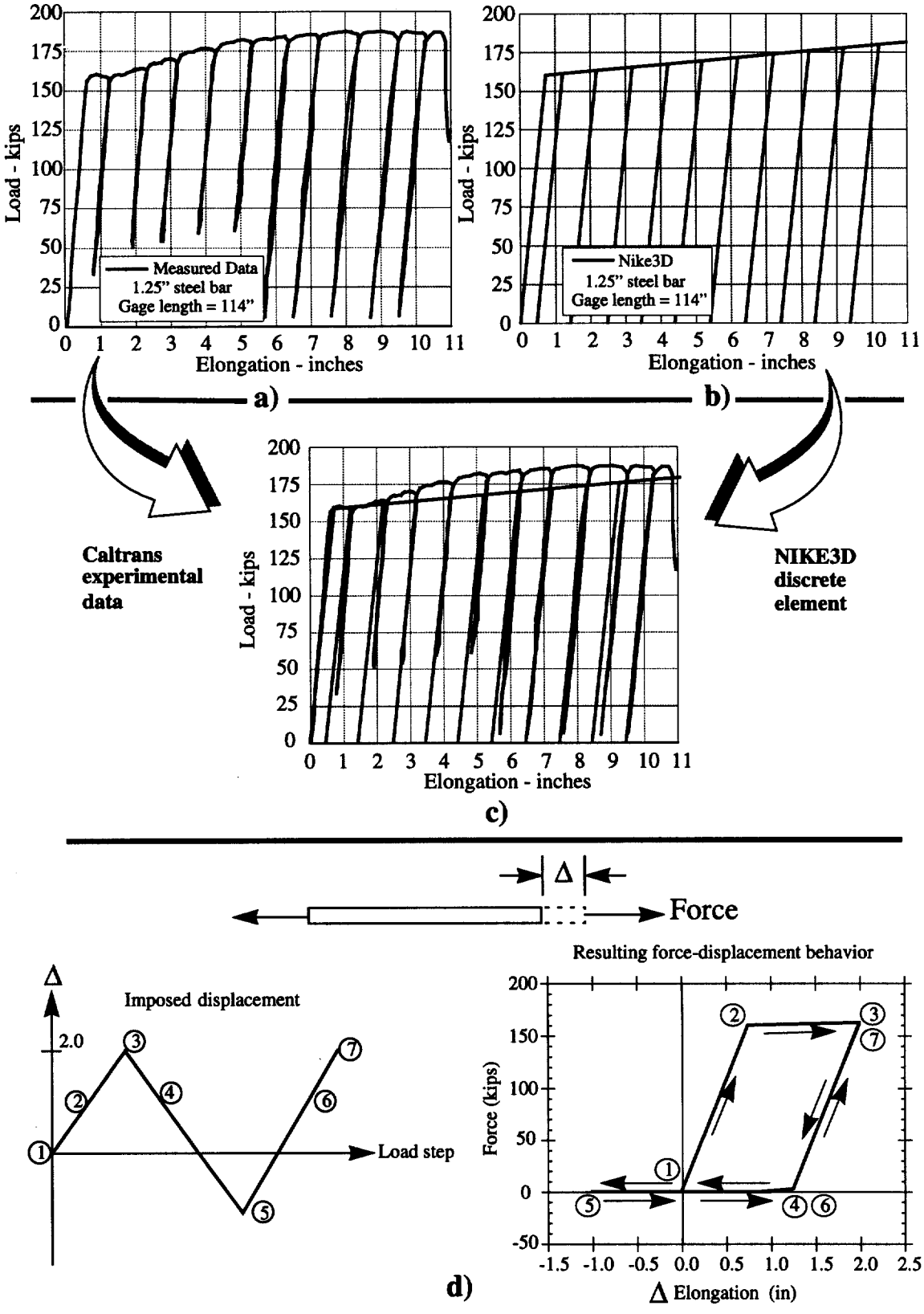

FIGURE 22. Discrete element model of rod and cable behavior. a) Measured bar force-deflection; b) discrete element force-deflection; c) comparison of measured and computed behavior; d) tension-compression characteristics of discrete element.

Based on the expansion joint idealizations used in this study, the linearized, small displacement model of two adjacent bridge frames results in the natural modeshapes shown in Fig. 23. The joint model provides the desired coupling between the adjacent bridge segments. Longitudinally, the bridge segments are essentially decoupled with each segment of the linearized model able to vibrate longitudinally independent of the adjacent bridge segment. Transversely and torsionally the bridge segments are closely coupled, and the vertical displacements of the adjacent bridge segments at the hinge location are identical, this type of vertical connectivity is desirable in light of the fact that under gravity deadload, contact should be maintained at the expansion joint seat.

The fourteen distinct frames of the WS and ES line are shown in plan view in Fig. 24. Each frame is bounded by expansion joints or abutments at either end. The retrofit strategy employed by Caltrans is intended to ensure the integrity of all fourteen individual frames against collapse.

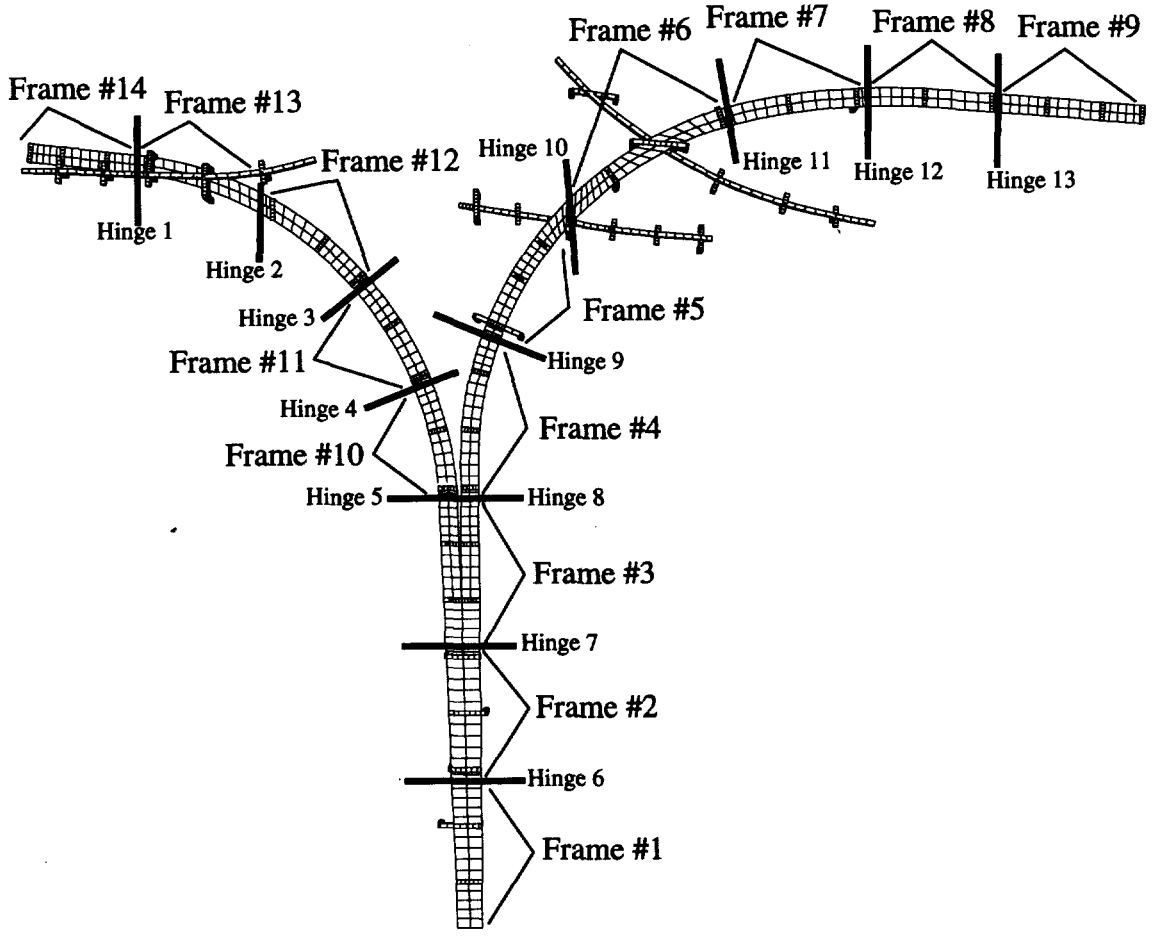

FIGURE 24. Subdivision of the overall structure: individual frames delineated by expansion joints and abutments.

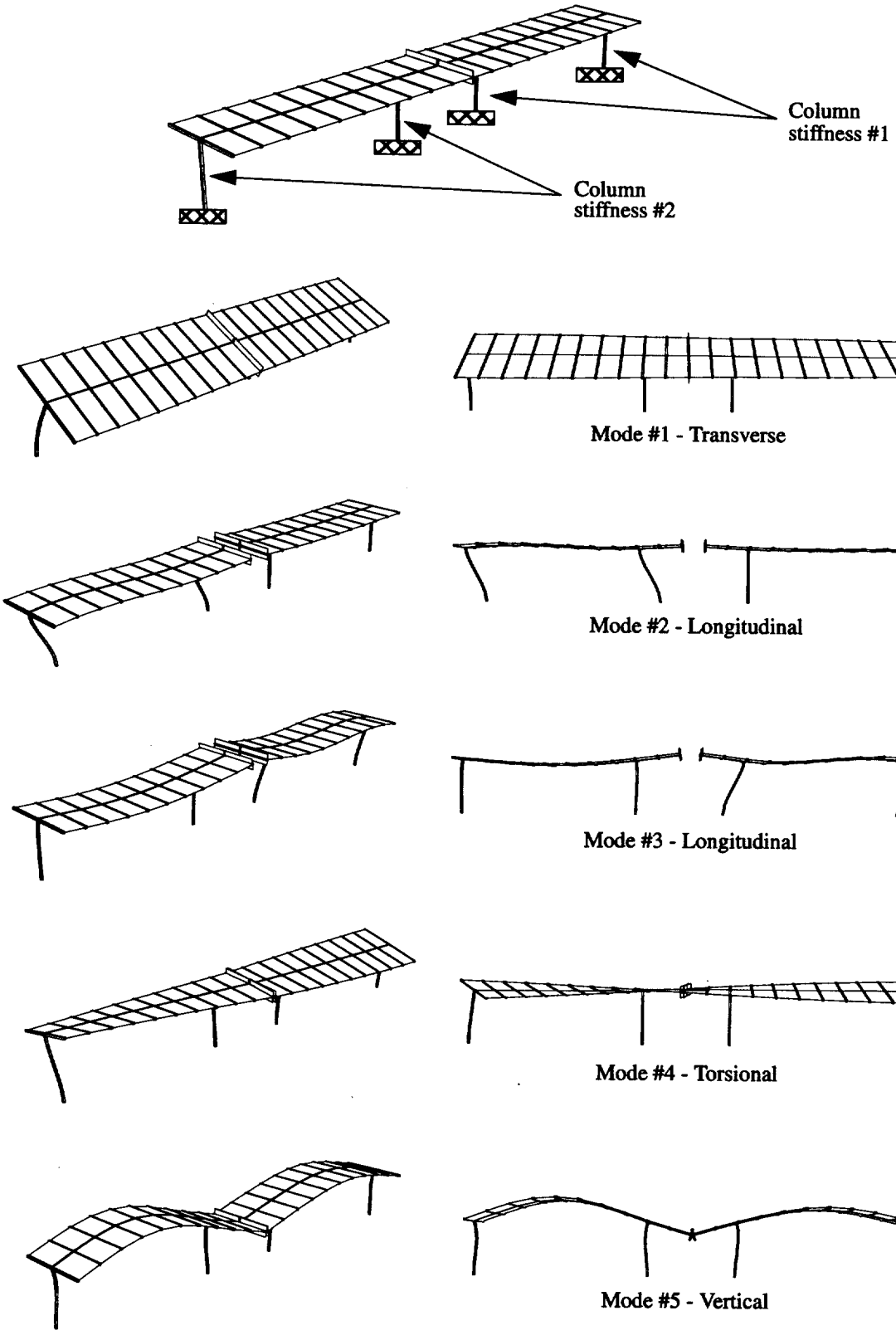

FIGURE 23. Natural modeshapes of two frames linearized about the infinitesimal deformation configuration: interaction between adjacent frames.

3.1.3 Column-footing connectivities and representation of foundation compliance

For the analyses of the as-built structure, a rigid foundation assumption was applied for all of the column footings. Thus the flexibility of the column footing/pile/soil system was neglected. Since the primary objective of the study was to investigate the retrofit structure, it was decided that construction of foundation compliance matrices for the as-built structure would not be an effective expenditure of project time. Whereas the as-built superstructure model could be expediently modified to account for the seismic retrofits, the generation of foundation compliances would essentially have to be entirely redone for the retrofit model. Consequently all analysis results for the as-built structure in the following sections are predicated on rigid foundation mat assumptions.

As designated in the as-built construction drawings, the construction details of typical column/footing connections are shown in Fig. 25 and Fig. 26. Based on the construction details, it appears that the small aspect ratio columns from the multiple column bents are intended to be pinned about both axes (i.e. about both "X" and "Y" axes in Fig. 25). The connectivity of the large aspect ratio columns, on the other hand, provides significant moment resisting capability about the longitudinal axis (i.e. the "Y" axis in Fig. 26).

The column-to-footing connectivity actually achieved in the field will likely be dependent on the amplitude of the dynamic response of the structure. For many of the bents the actual footing location is significantly below grade as indicated in Fig. 27. Under low amplitude, ambient type vibration, the actual achieved connectivity between the columns and footings will likely be closer to a fixed connection as the soil overburden helps restrain rotations at the base of the embedded columns. Under strong earthquake excitation however, when the soil surrounding the soil undergoes significantly larger strains and is pushed back from the column, the connections should more closely approximate the intended pinned connections.

As indicated in Fig. 28, the vast majority of the connections between the columns and footings were designed as pinned connections in the original as-built structure. Figure 29 shows the footing connectivity of the columns correlated with the location of each of the major structural frames.

The column - footing connectivites were one of the structural features which received the most attention in the retrofit design. As discussed in a subsequent section, the retrofit design included increasing the column - footing connectivity to a full moment connection for a large number of the columns.

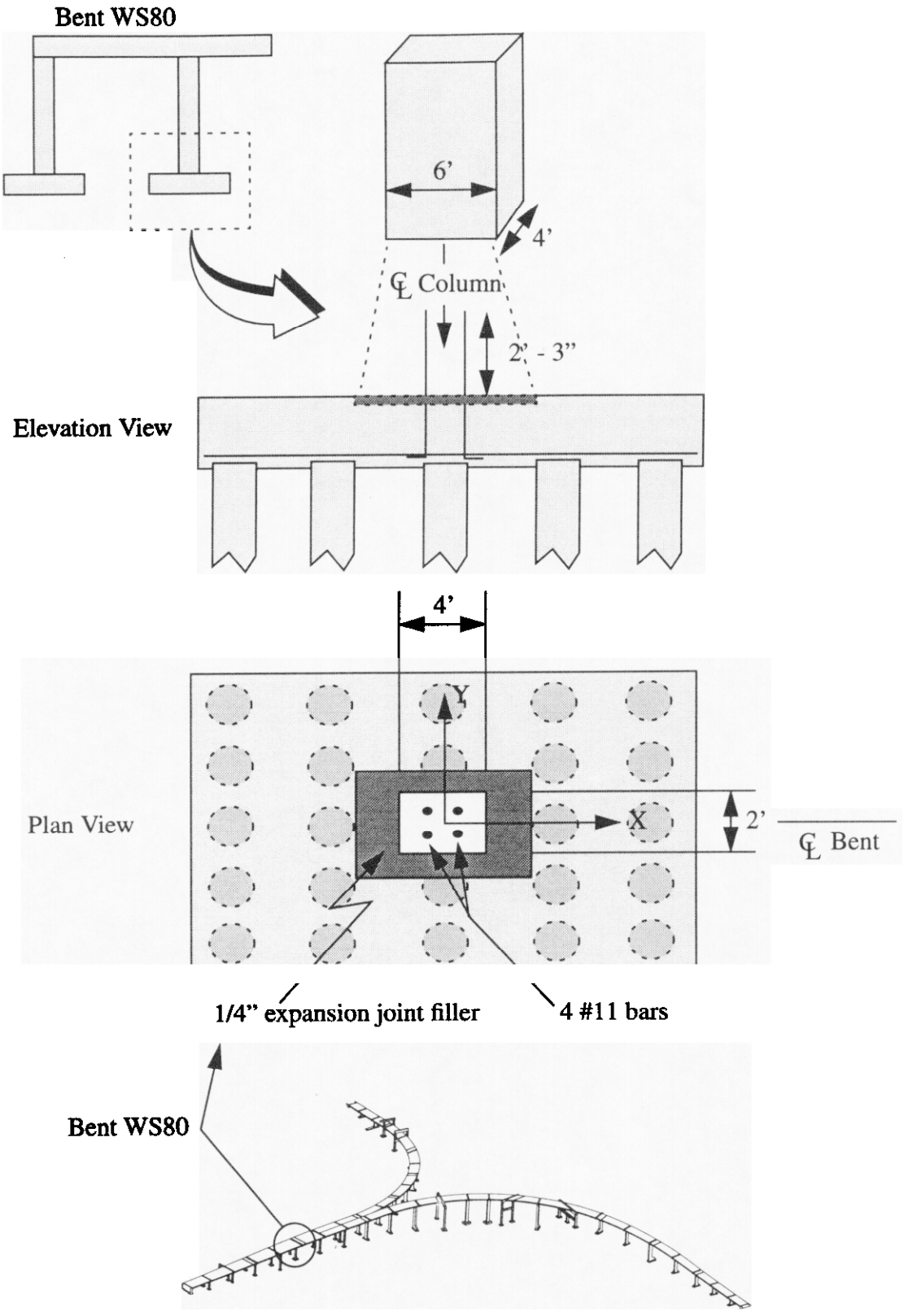

FIGURE 25. As-built construction details for pinned columns (multiple column bent).

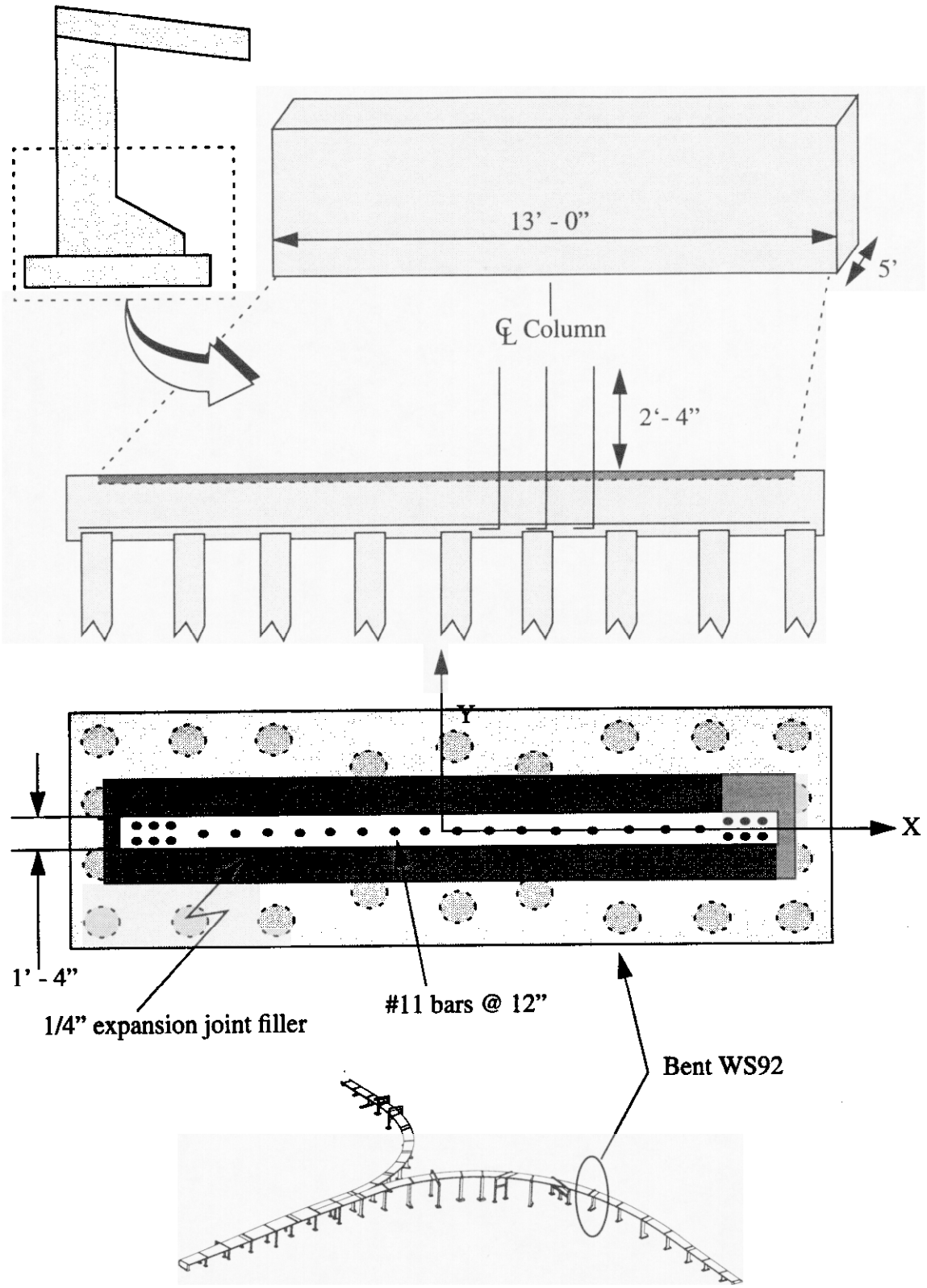

FIGURE 26. As-built construction details for pinned columns (single column bent).

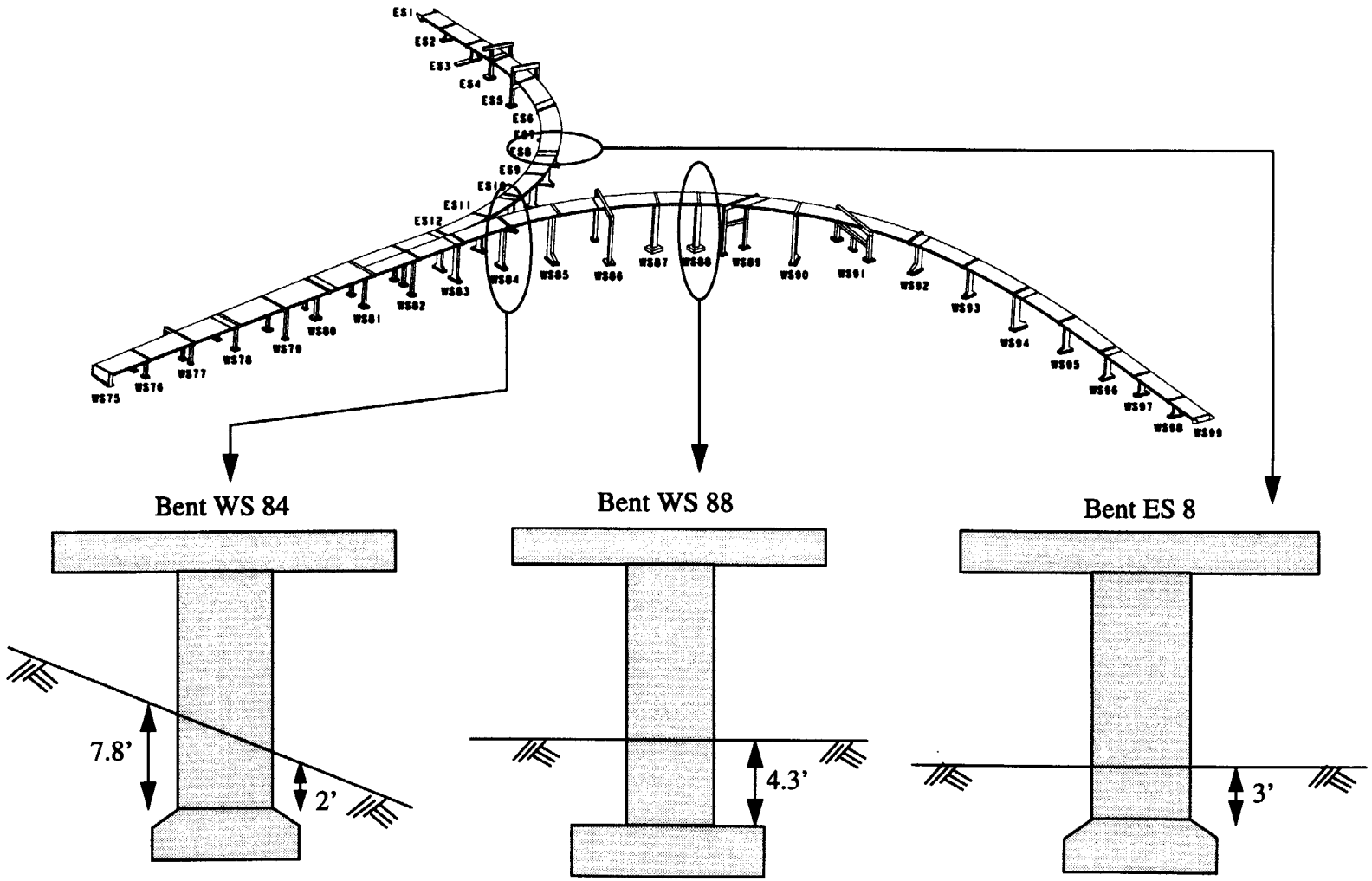

FIGURE 27. Examples of embedment depth of selected column footings.

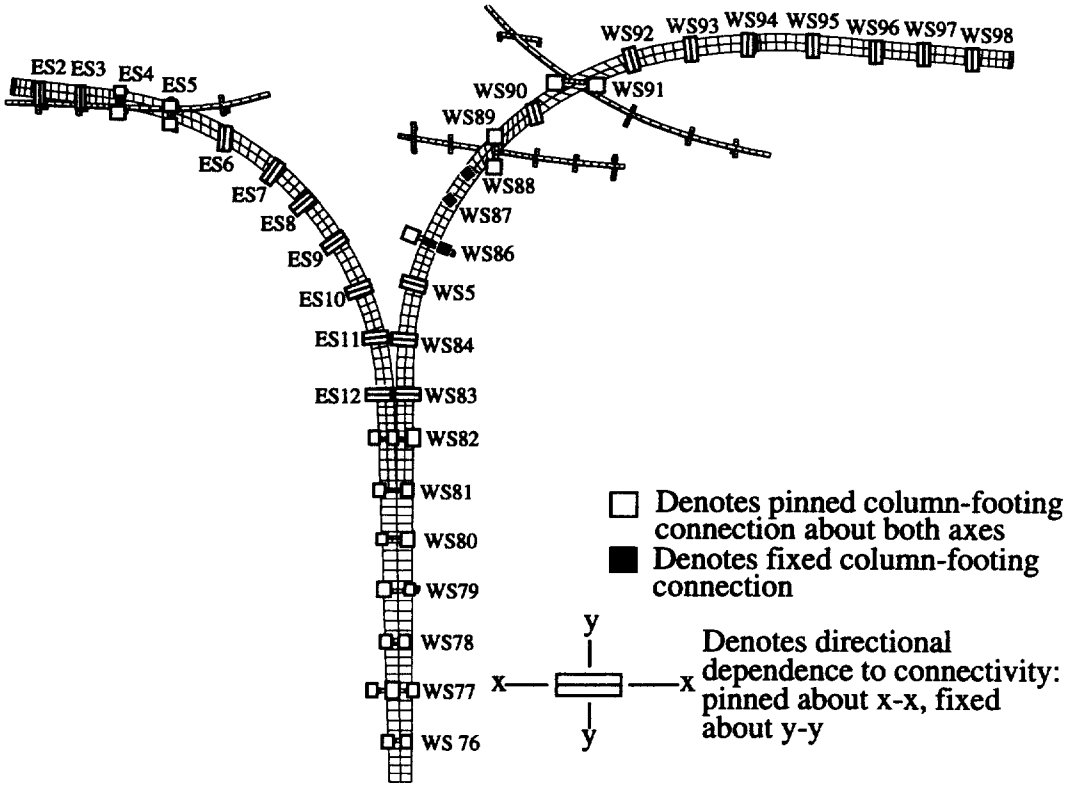

FIGURE 28. Column - footing connectivity based on the as-built construction details.

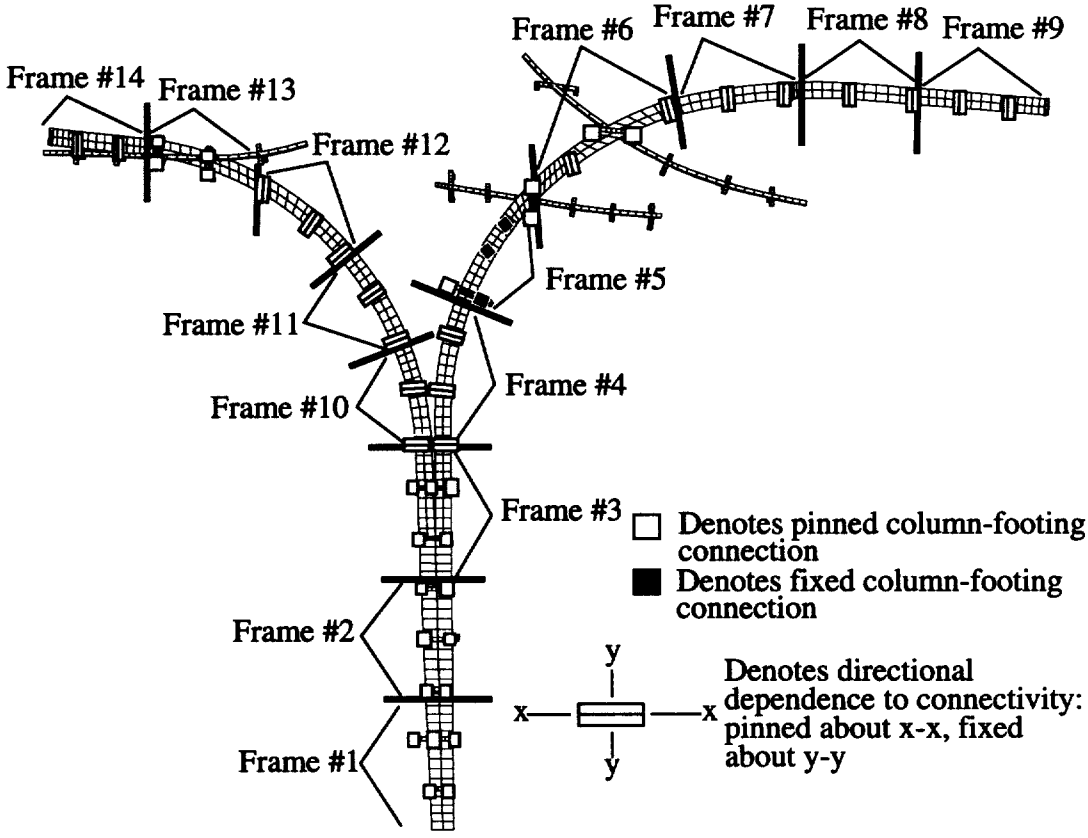

FIGURE 29. Column connectivity for each frame.

3.1.4 Natural modeshapes of the structural system

The ultimate aim of the LLNL modeling work was to develop a nonlinear model of the WS and ES line structures. However, a significant amount of information about the dynamic response characteristics of the structures can be obtained from inspection of linear analyses results. Linear, transient analyses can be performed as an economical precursor to fully nonlinear analyses in order to gain insight into the transient response of a complex dynamic system. The degree of correlation between the natural frequencies of the structural system and the dominant frequencies of the dynamic forcing function provides fundamental information on the expected level of dynamic amplification in the structural system. Solution of the eigenproblem for a linearized structural model can also provide a significant measure of model validation by inspection of the reasonableness of the computed modeshapes and by comparison to measured modeshapes if the engineer is fortunate enough to have measured modal quantities.

In the current work, modal analyses were performed to determine the relationship between the structural frequencies and the dominant ground motion frequencies and to compare with measured modeshapes and frequencies obtained by Imbsen and Associates. The natural vibration characteristics of the WS and ES line structures were investigated for two different sets of column boundary conditions. The first set of boundary conditions considered all columns as having complete moment transferring capability between the column and the footing. The second set considered the as-built specification for the column base fixity which consisted primarily of pin fixity between the columns and the footings. The first twelve natural modeshapes computed with the global computer model of the WS and ES lines are shown in Figs 30 and 31 for the fixed base case and the modal frequencies for the first seventy modes are summarized in Table 2.

TABLE 2. Computed frequencies for the first seventy modes of the ES and WS lines.

	Moment connections between column and foundation	**Pinned connections between column and foundation (i.e. as-built design details)**
Mode Number	**Modal Frequency (Hz)**	**Modal Frequency (HZ)**
1	0.776	0.392
2	0.875	0.445
3	1.038	0.514
4	1.043	0.529
5	**1.108 (1)***	0.566
6	1.121	0.631
7	1.247	0.707
8	1.304	0.715
9	1.332	0.950
10	1.345	1.004

TABLE 2. Computed frequencies for the first seventy modes of the ES and WS lines.

	Moment connections between column and foundation	Pinned connections between column and foundation (i.e. as-built design details)
Mode Number	Modal Frequency (Hz)	Modal Frequency (HZ)
11	1.365	**1.067 (1)***
12	1.409	1.224
13	1.462	1.285
14	**1.572 (2)***	1.332
15	1.684	1.361
16	1.713	1.386
17	1.849	1.593
18	1.860	**1.622 (2)***
19	1.931	1.713
20	1.943	1.778
21	2.013	1.796
22	2.131	1.848
23	2.137	1.863
24	2.147	1.932
25	2.197	1.949
26	2.295	2.009
27	2.349	2.085
28	2.463	2.143
29	2.526	2.257
30	2.550	2.311
31	2.574	2.385
32	2.815	2.422
33	2.868	2.441
34	2.874	2.459
35	2.944	2.599
36	2.999	2.613
37	3.080	2.622
38	3.105	2.623
39	3.186	2.758
40	3.191	2.809
41	3.217	2.841
42	3.270	**2.866 (3)***
43	3.304	2.883

TABLE 2. Computed frequencies for the first seventy modes of the ES and WS lines.

	Moment connections between column and foundation	Pinned connections between column and foundation (i.e. as-built design details)
Mode Number	Modal Frequency (Hz)	Modal Frequency (HZ)
44	3.368	2.886
45	**3.594 (3)***	2.922
46	3.600	3.025
47	**3.611 (4)***	3.059
48	3.704	3.076
49	3.735	3.136
50	3.858	3.252
51	3.883	3.258
52	3.924	3.301
53	3.967	3.303
54	4.016	3.374
55	4.017	3.449
56	**4.074 (5)***	**3.474 (4)***
57	4.115	3.482
58	4.180	3.511
59	4.236	3.526
60	4.327	3.539
61	4.391	3.560
62	4.402	**3.586 (5)***
63	4.478	3.615
64	4.503	3.634
65	4.542	3.656
66	4.571	3.687
67	4.615	3.691
68	4.657	3.724
69	4.700	3.836
70	4.754	3.889

*. Denotes model mode corresponding to experimentally measured mode (experimental mode number shown parenthetically)

As part of their evaluation of the WS and ES lines, Imbsen and Associates instrumented a short segment of the WS line (see inset in Fig. 32) , and measured ambient vibrations of

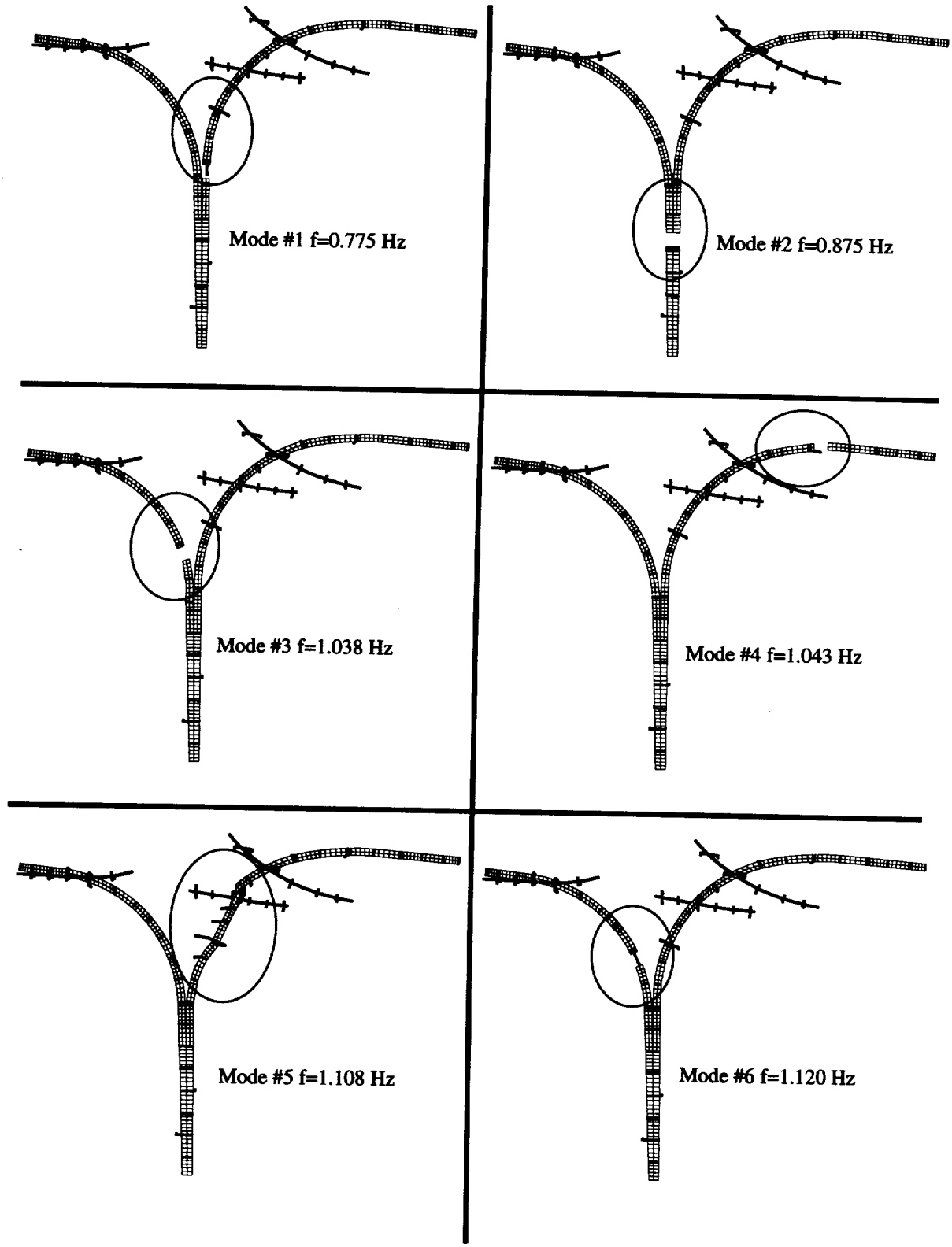

FIGURE 30. Modeshapes 1-6 of the structural model (plan view).

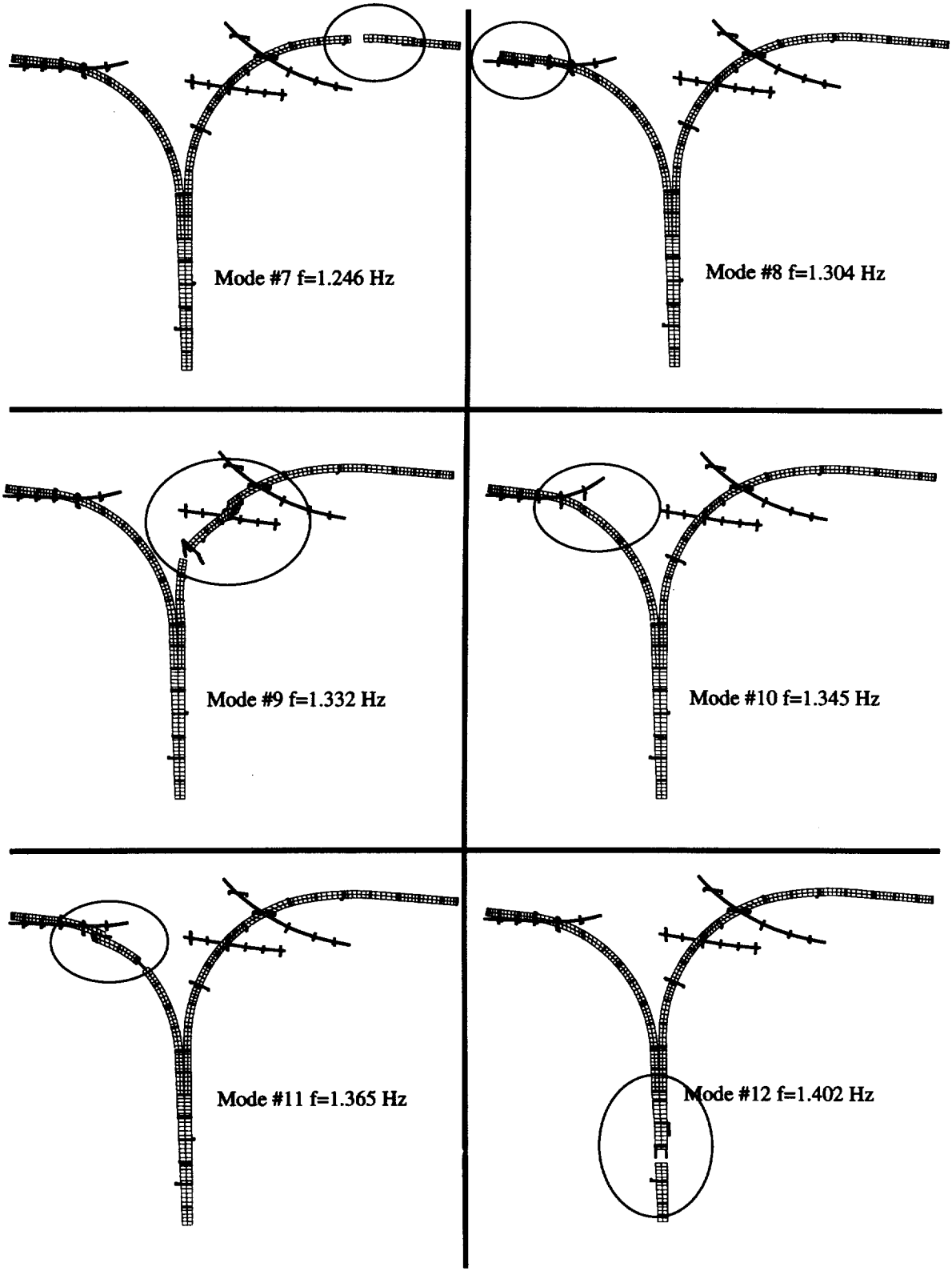

FIGURE 31. Modeshapes 7-12 of the structural model (plan view).

the structure. Imbsen and Associates processed the ambient vibration data in the frequency domain to obtain estimates of the natural frequencies and modeshapes for this portion of the structure. Based on the limited information which was provided to LLNL by Caltrans, it appears that a detailed system identification modal analysis was not performed. Rather, modeshapes were determined by identification of peaks in the Fourier amplitude spectra of measured acceleration time histories.

The modeshapes determined experimentally by Imbsen and Associates are shown in Fig. 32. Figure 32 also shows the modeshapes from the test section portion of the structural model which most closely correspond to the experimentally determined modeshapes. The modeshapes from the moment-transferring base column model are shown in Fig. 32, and the frequencies corresponding to the pinned base column model are shown parenthetically.

The modeshapes corresponding to the first two measured modes were easily identified in the computational model results. The higher modeshapes, on the other hand, required more detailed inspection and interpretation because of a higher modal density in the high frequency range. It is noted that the fifth measured mode corresponds quite well to a strong mode which consists of predominately vertical motion, with second order horizontal motion. Imbsen and Associates appear to have associated the fifth measured mode with a transverse mode obtained from their modeling results. However, for the LLNL computational results the vertical mode shown in Fig. 32 appears to provide a better correlation.

The computational model results generally agreed well with the experimentally determined modeshapes, particularly in light of the fact that a very simple approach has been employed to extract modal information from the experimental data and there is a degree of uncertainty associated with both the computational model and the measured modeshapes. Based on inspection of the modeshapes and frequencies obtained from both the fixed base column model and the pinned base column model, the fixed base column model appeared to provide a somewhat better correlation with the measured data. The experimental modeshapes were determined from structural excitation which consisted of ambient vibration and vehicular traffic. At these low levels of excitation it would not be unexpected that the column to footing connection would appear more fixed than pinned.

The relationship between computed structural frequencies and the frequency content of the surface motion employed in the Caltrans design effort is shown in Fig. 33a. The structural frequencies plotted in Fig. 33 correspond to the model with moment connections between the columns and footings. The retrofit structure was of primary concern and foundation retrofits on a large number of columns were intended to emulate this connectivity. Figure 33a shows that the lower structural modes fall into the peak region on the spectra and thus the surface ground motion would tend to strongly excite the WS and ES line structures. Figure 33b shows the structure periods relative to the LLNL developed surface motion and the correlation between the lower modes of the structure and the dominant frequency of the ground motion is also evident for the LLNL motion.

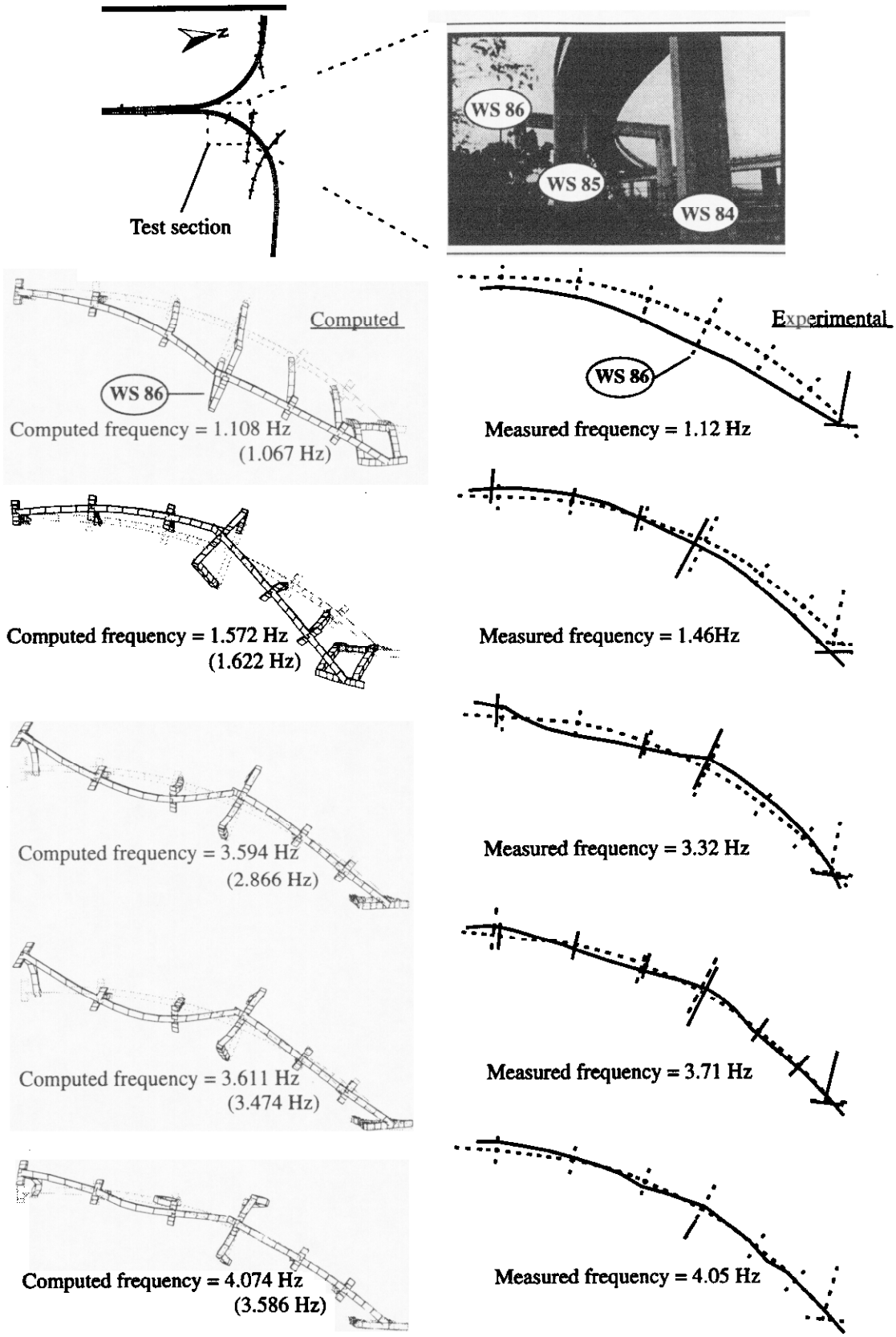

FIGURE 32. Comparison of computed and measured modeshapes for the bridge frames spanning bents WS83 to WS89 (fixed base modes are plotted, pinned base model frequencies are shown parenthetically).

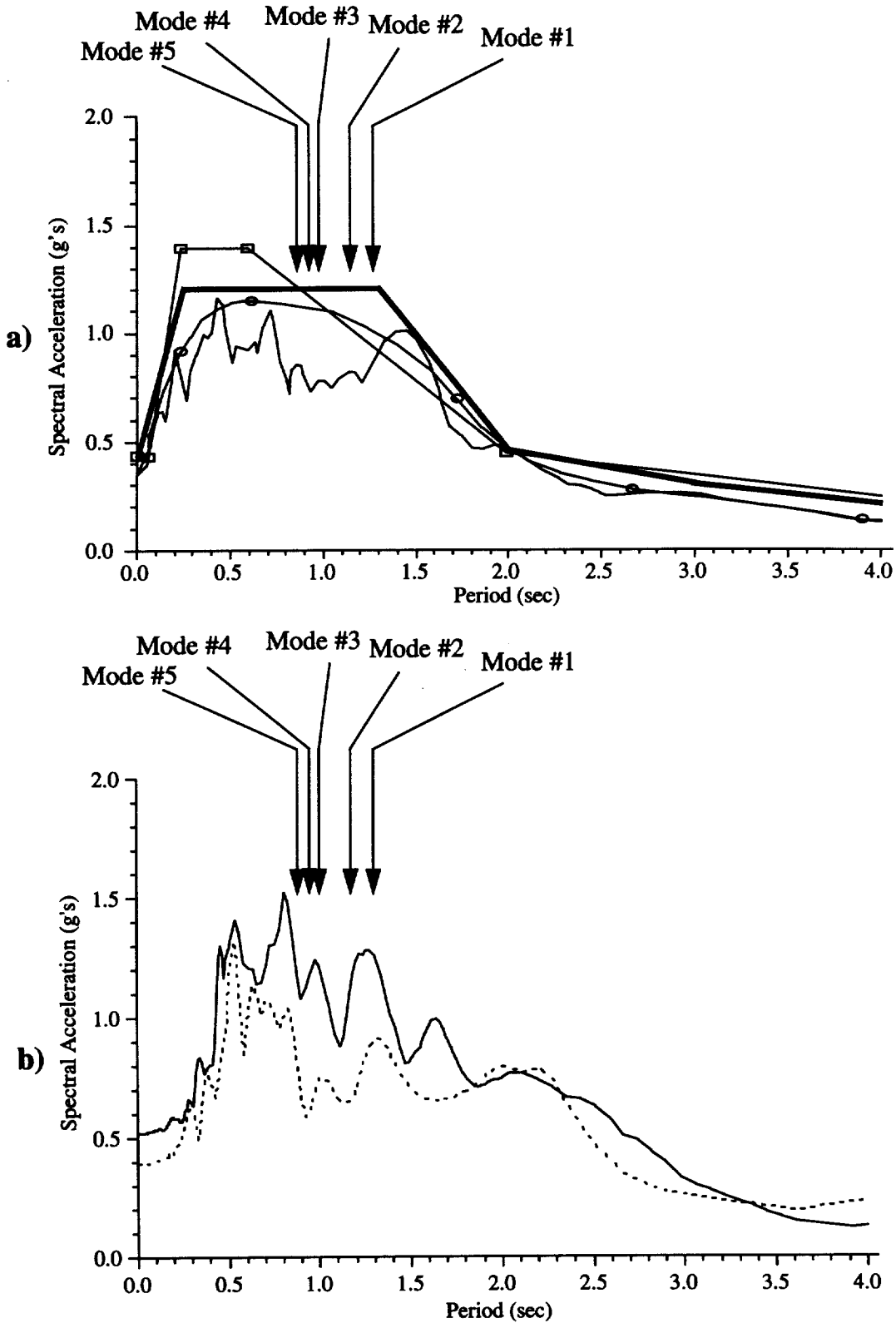

FIGURE 33. Relationship between structural frequencies and ground motion frequencies. a) Caltrans surface design motions; b) LLNL surface motions.

4.0 Computer model of the retrofit WS and ES lines

4.1 The retrofit structure

The 24/580/980 Interchange was designed and constructed in the mid 1960's and therefore has many of the problematic concrete construction details of structures with 1960's vintage. As a result of these design problems, pre-1971 concrete bridge structures in California typically have low ductility capacity and are thus vulnerable to brittle catastrophic failure under strong earthquake excitation. Some of the major problem areas which have been identified for pre-1971 bridges through observed earthquake performance and research studies include (see Chai et. al. [3], Priestly and Seible [4]);

1. inadequate expansion joint seat dimensions to prevent separation of adjacent deck segments and loss of deck support
2. lack of top bending reinforcement and shear reinforcement in column footing mats leading to potential footing failures
3. inadequate shear strength of reinforced concrete columns (typically shear reinforcement utilized #4 bars at 12 inches regardless of column dimensions), poor shear reinforcement also limits flexural strength as outer concrete spalls and longitudinal bars buckle
4. poor connectivity between columns and footings as a result of utilization of weak lap splices between footing reinforcement and column longitudinal bars, leading to a potential for pulling out of the longitudinal column reinforcement from the footing and the inability to form a plastic hinge at the base of the columns
5. inadequate strength and stiffness of bent cap beams to ensure plastic hinge formation in columns
6. inadequate flexural strength of reinforced concrete columns as a result of low lateral force design coefficients
7. abutment failures as a result of pounding between the superstructure and abutment.

The as-built 24/580/980 interchange suffers from most of these inadequacies. In 1992 the expansion joints of the ES and WS lines were retrofit with cable or steel rod restrainers as discussed in section 3.1.2. This retrofit was part of Caltrans' state-wide Phase I seismic retrofit of bridges.

The other shortcomings have been addressed in the seismic retrofit design which was recently completed by Caltrans. The proposed retrofits include the strengthening of the columns with oval steel jackets as shown in Fig. 34. Based on research studies at UC San Diego [26], the steel jackets confine the concrete core of the column in a manner similar to modern spiral reinforcement, and greatly enhance the column ductilities. Based on scale-model experimental studies, the jackets also appear to solve the problem associated with pull-out of the lap splices in the column-to-footing connections.

The retrofit strategy also calls for extensive stiffening of bent cap beams. with the addition

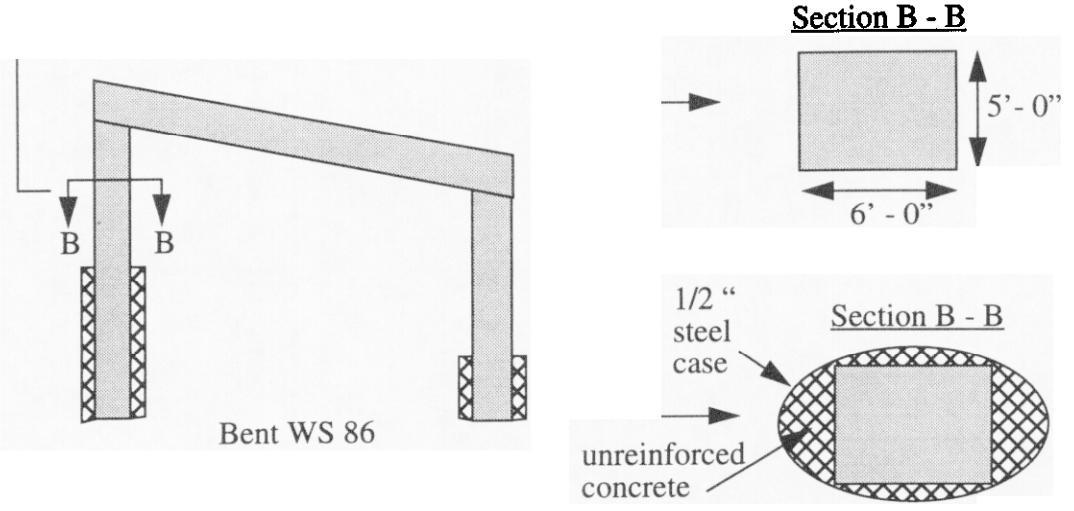

FIGURE 34. Retrofit of columns with filled, oval steel jackets

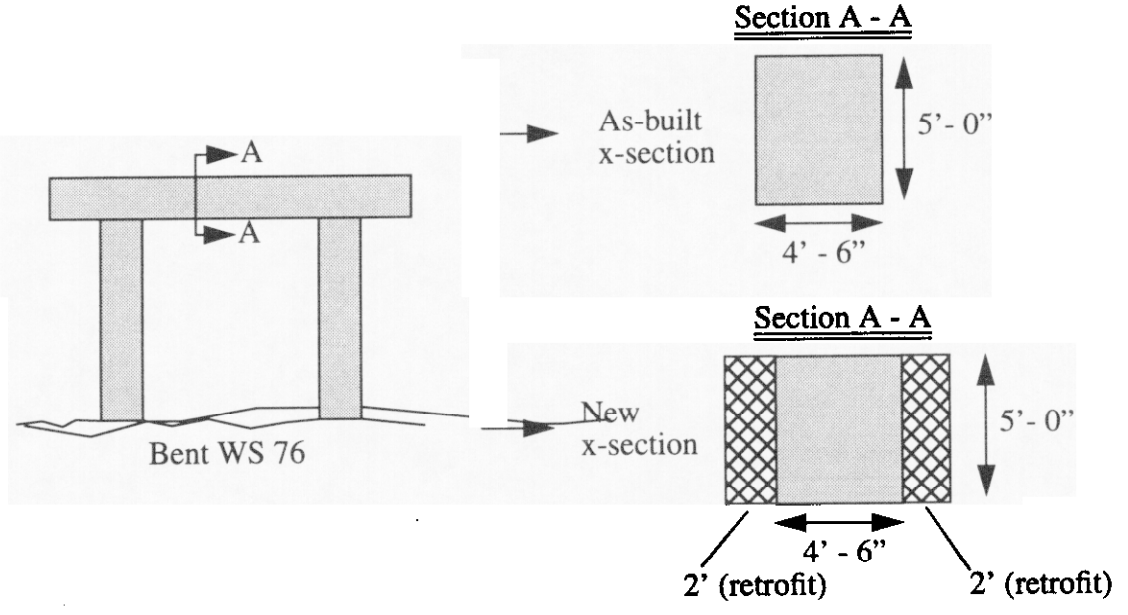

FIGURE 35. Retrofit of bent cap beams with the addition of bolsters

of bolsters to the bent cap beams as indicated in Fig. 35. This will force plastic hinging into the columns as opposed to the bent caps, as required by Caltrans design methodology.

The retrofit design calls for retrofit of many of the column footings with the addition of concrete to confine the poorly reinforced existing footings, with micro piles to tie the footings to the ground (Fig. 36).

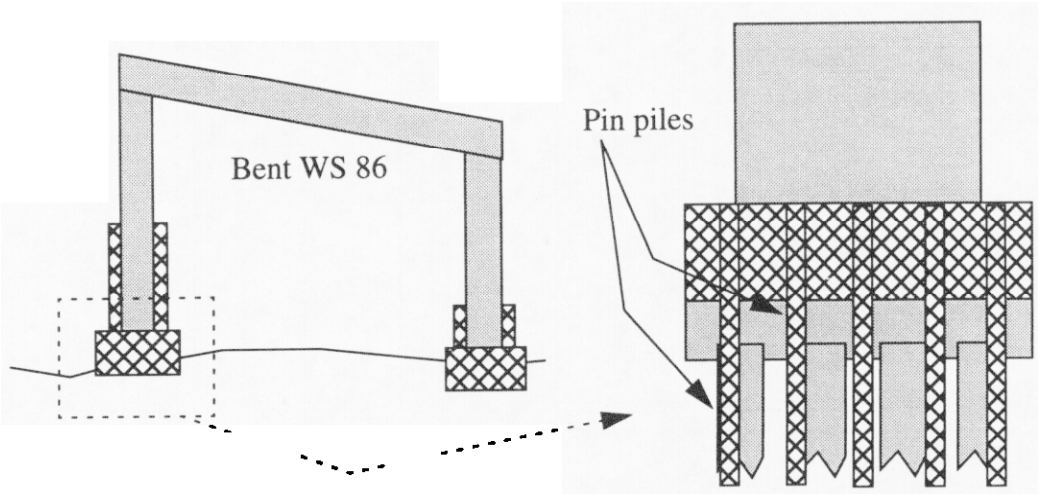

FIGURE 36. Retrofit of column footings.

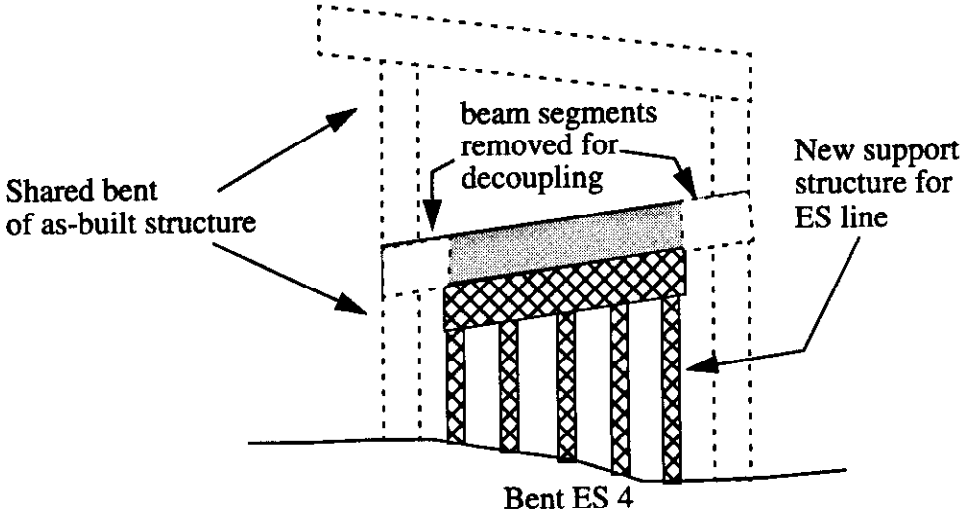

FIGURE 37. Decoupling of ES and WS lines from the EN, C and SE lines.

The Caltrans retrofit design provides for complete physical decoupling of the WS and ES lines from the EN, C and SE lines (see Fig. 14 and Fig. 37). This results in a cleaner system from the structural dynamics standpoint, and eliminates the possibility of complex, three dimensional interactions between the WS and ES lines and the other segments of the interchange.

The other major feature of the retrofit design includes the enhancement of strength and stiffness of the three abutments of the WS and ES lines. At bent WS 75 two large, six foot

diameter drilled shaft concrete members were added as a retrofit (Fig. 38) and at abutment

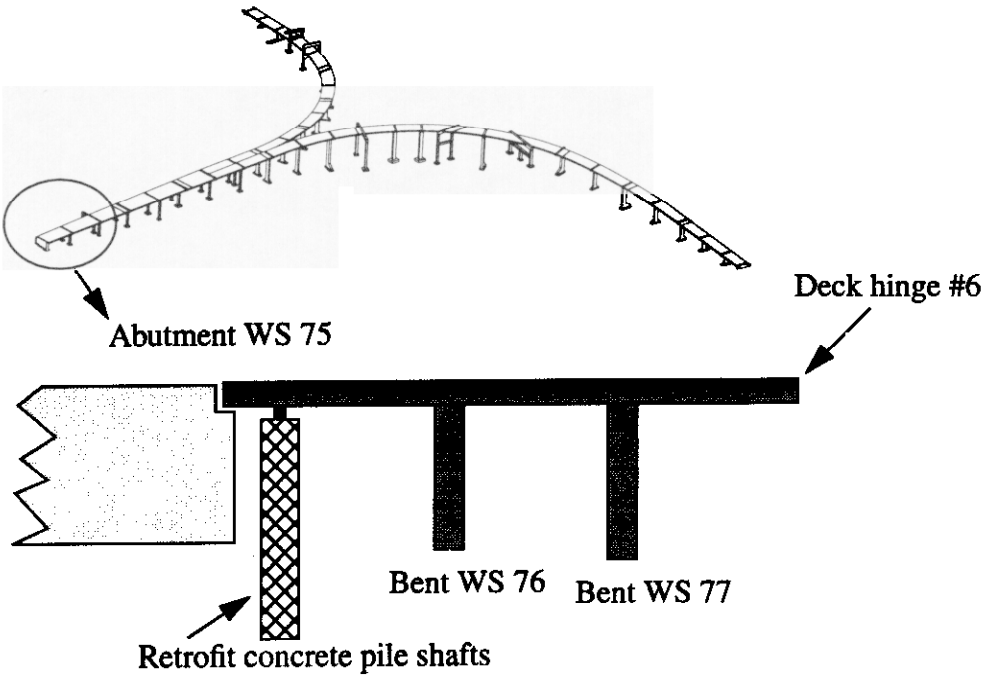

FIGURE 38. Strengthening by addition of two stiff concrete members at WS 75.

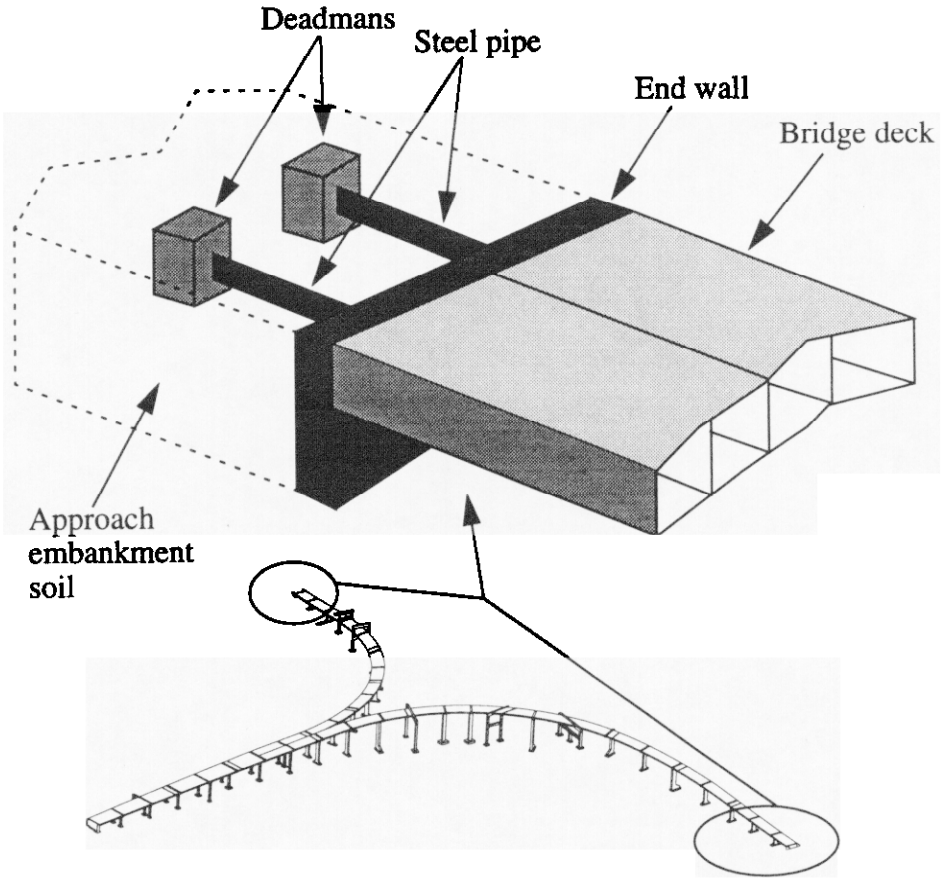

FIGURE 39. Abutment strengthening at WS99 and ES1.

ES1 and WS99 concrete "deadmans" were added with steel pipe attaching the deadmans to the end diaphragms of the bridges (see Fig. 39) The entire retrofit design for all of the superstructure elements and foundations is summarized in Appendix D.

The final computer model of the WS and ES lines of the structure, which includes all of the retrofit features, is shown in Fig. 40.

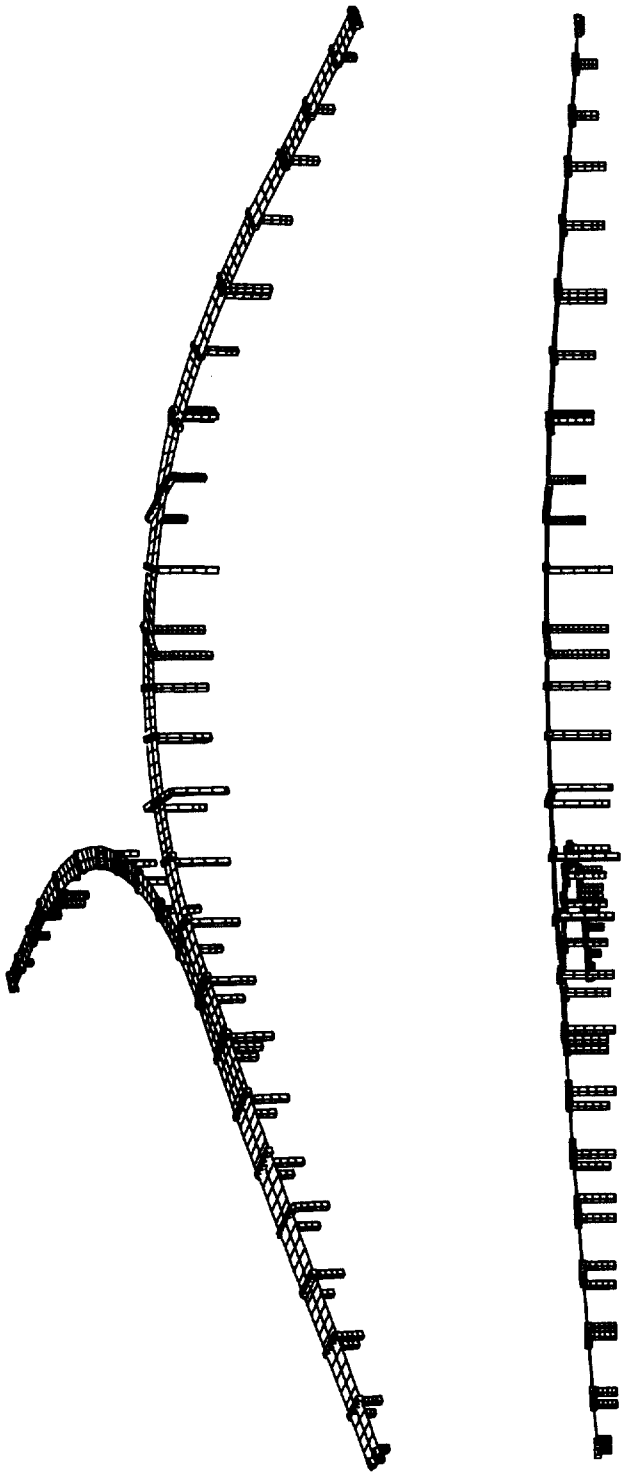

FIGURE 40. Finite element model of the retrofit structure.

4.1.1 Foundations and abutments

For the seismic analysis of the retrofit structure, the flexibility of the foundation system for each column, and the flexibility of the three abutments of the WS and ES lines, were accounted for in the structural model. In order to estimate the stiffnesses of the foundations and abutments, substructure models were constructed for ten selected foundations and for two abutment types. The ten foundation substructures were selected so as to be representative of all of the actual foundations throughout the two lines. The ten foundation types, designated A through J, are summarized in Table 3 and the correlation of the foundation type with each bent is summarized in Figure 41.

TABLE 3. Selected foundations used in determination of foundation compliances

Foundation type	Characteristic bent	Description of characteristic footing
A	ES1, WS99	abutment retrofit
B	WS76	P12 asbuilt
C	ES2	P23 retrofit
D	WS81	P20 retrofit
E	WS77	P16 retrofit
F	WS89	P20 retrofit
G	WS85	P36 retrofit
H	ES3	P41 retrofit
I	WS75	60" column
J	WS90	80" column

For each foundation type, a three dimensional substructure model was constructed and unit forces and moments were applied to the foundation mat in order to generate a six by six coupled flexibility matrix for the foundation system. The generated foundation flexibility matrix was then inverted to give a six by six stiffness matrix representation of the foundation stiffness (see Fig. 42). For the foundation substructure analyses, soil material properties were obtained from the *SHAKE* analysis results of Chen [8], thus the foundation stiffness characterizations can be considered an equivalent linear estimate of the strain level dependent foundation properties.

In the structural model of the WS and ES lines, the foundation stiffness matrix was attached to a foundation node, and the base of the corresponding columns were connected to the foundation node with the appropriate column-foundation mat connectivity (see Fig. 43). The column-foundation connectivity reflects the retrofit design in which many of the original pinned connections were upgraded to moment connections by jacketing, addition of concrete to the foundation mat and addition of pin piles at the footings. The idealized column-footing connectivities for all of the foundations of the retrofit structure are shown in Fig. 44.

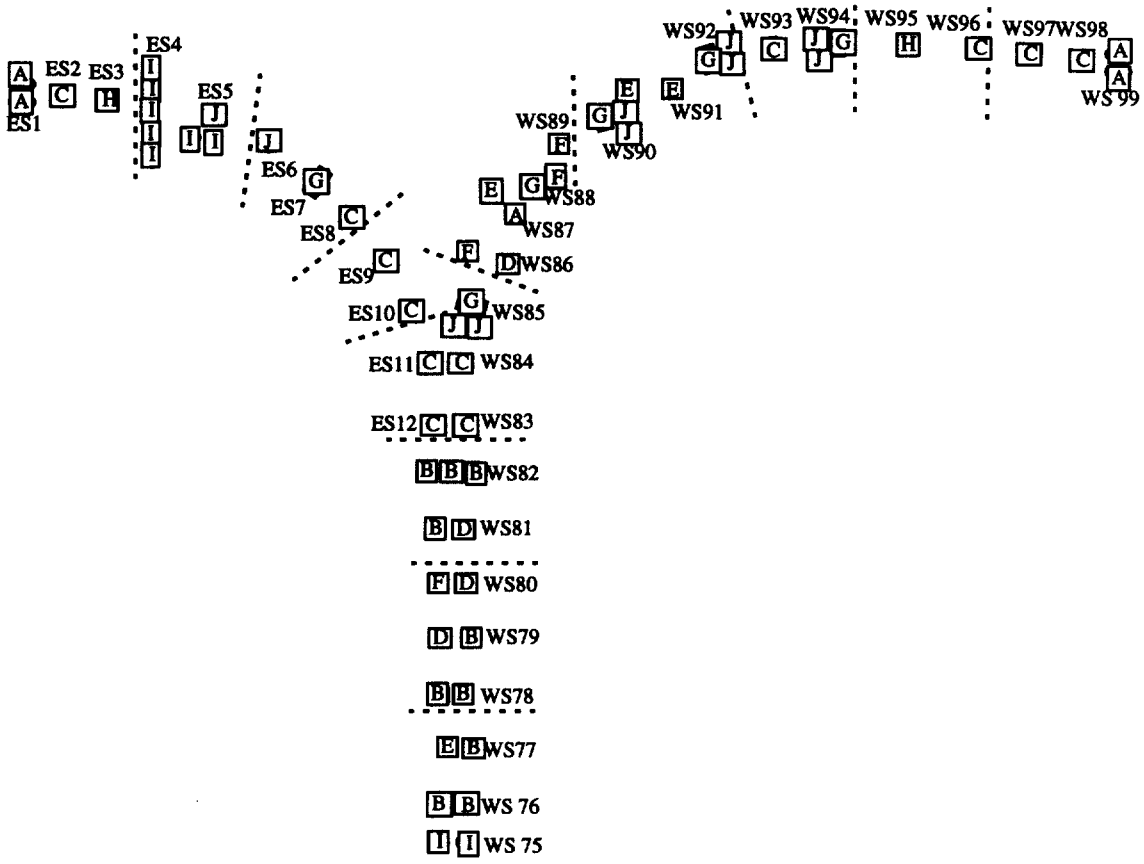

FIGURE 41. Foundation stiffness characterizations.

Two substructure models were generated for the abutments of the WS and ES lines. One model was developed to represent the retrofit abutments at WS99 and ES1. At these abutments, concrete deadmans were designed with steel pipes connecting the deadmans to the existing bridge segments at the abutment diaphragms. The detailed abutment model is shown in Fig. 45b. This model was used in a load-displacement test to estimate representative spring constants for the abutment system.

The second abutment model, shown in Fig. 45a, was constructed for the existing WS75 abutment configuration. This abutment consisted of an end wall and wing walls. The WS 75 abutment was significantly different than the ES1 and WS99 abutments in that it is a seat type abutment, in which the bridgedeck can slide longitudinally relative to the abutment wall. This was represented in the structural model by inclusion of a contact surface between the end of the bridge and the abutment wall. The details of the finite element model representation of the abutments is illustrated in Fig. 46, and the abutment stiffness values are summarized in Table 4.

As a basis for comparison, Table 4 also shows the abutment stiffness values which are obtained from the simplified hand calculation procedures provided in the Caltrans Design Guide. The stiffnesses determined from the model calculations are in reasonable agreement with the Caltrans Design Guide stiffnesses. At WS75, two very large concrete drilled

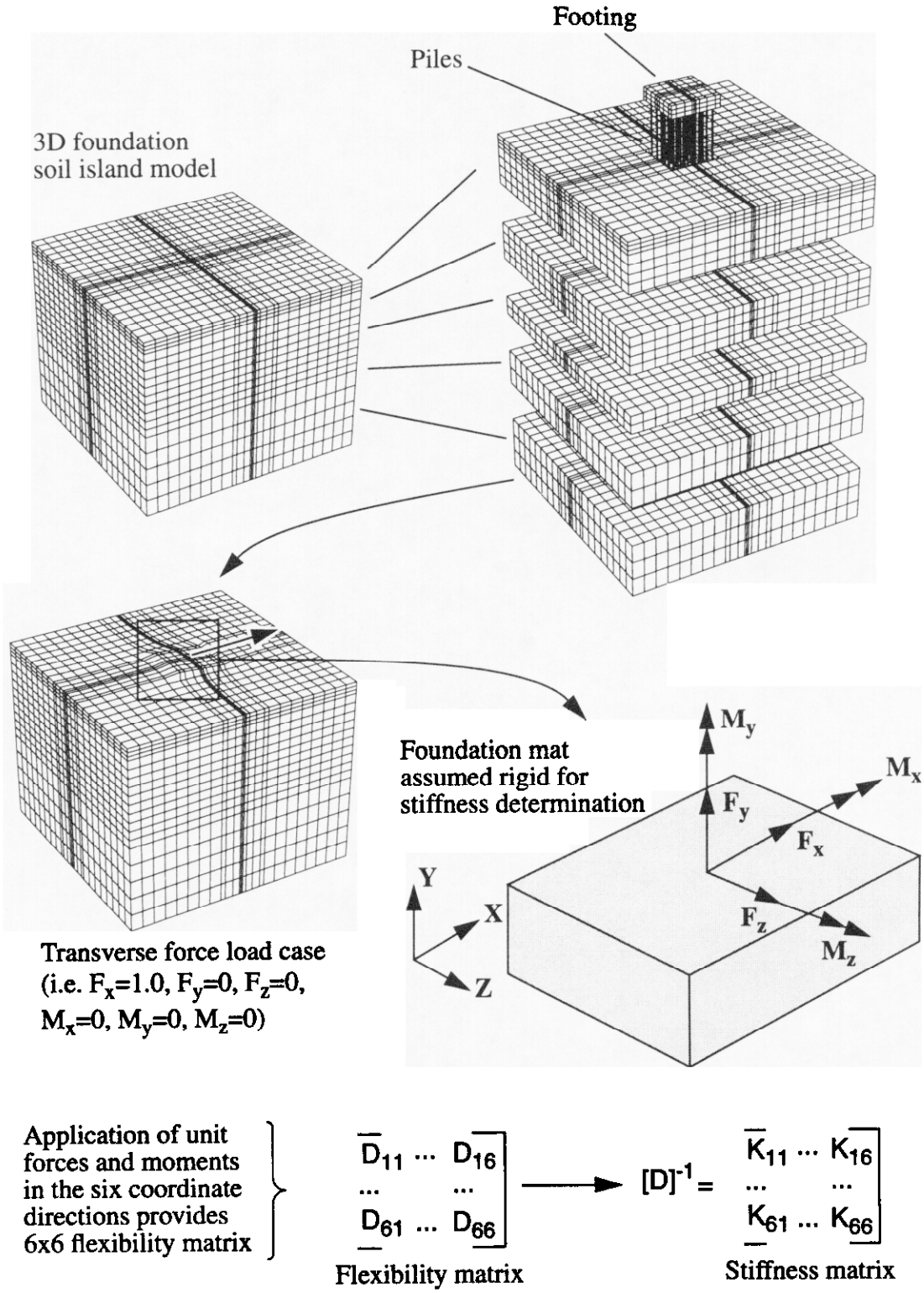

FIGURE 42. Generation of foundation stiffness matrix from analysis of a three dimensional soil island.

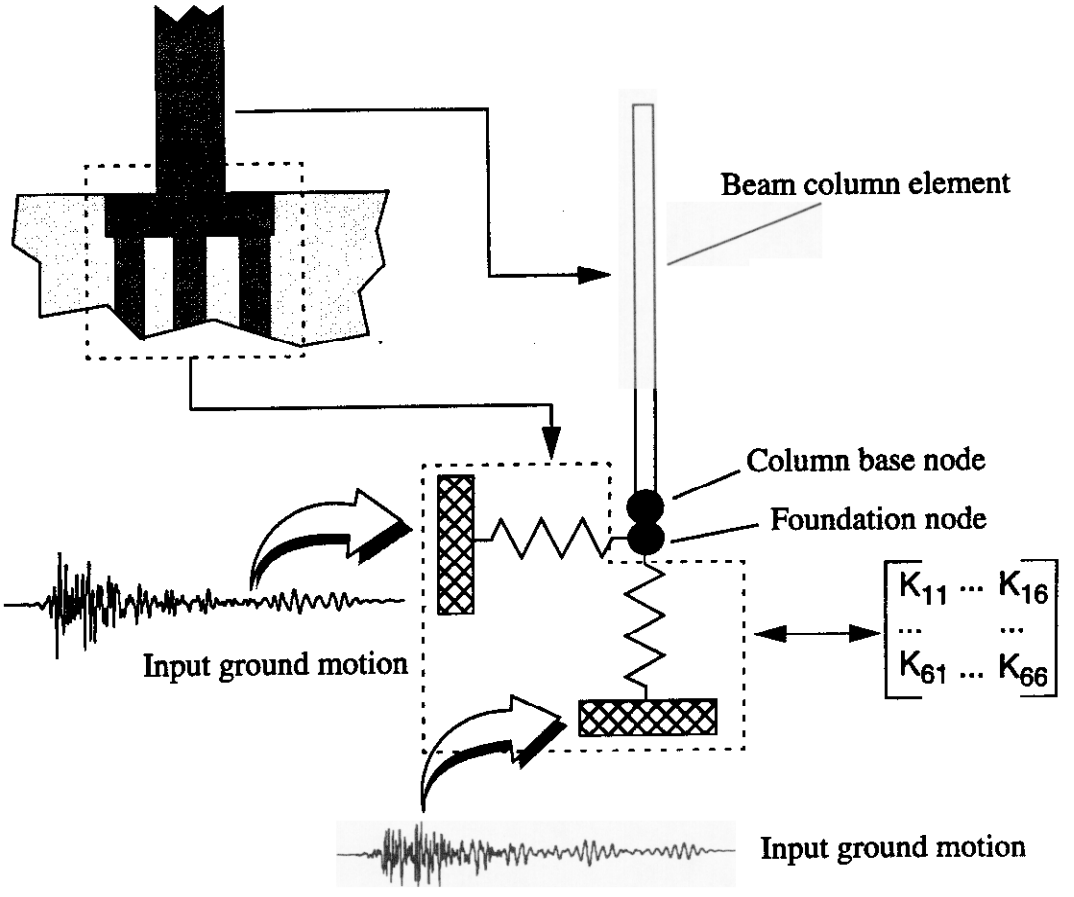

FIGURE 43. Representation of foundation compliance in the superstructure model.

shafts were added to enhance the stiffness and capacity of the first frame which is adjacent to the abutment (see Fig. 38). The added shafts are so stiff that the actual load transferred to the abutment will be much smaller than would be the case for the as-built structure. In light of this, and the fact that the construction detail of the seat type abutment at WS75 would not support transfer of large transverse forces between the bridge superstructure and the abutment, the transverse stiffness provided by the abutment at WS75 was conservatively neglected and the concrete shafts were assumed to provide all of the transverse stiffness at the end of the bridge.

TABLE 4. Abutment stiffnesses for WS 75, WS99 and ES1

Abutment	Longitudinal stiffness		Transverse stiffness	
	LLNL substructure model	Caltrans Design Guide procedure	LLNL substructure model	Caltrans Design Guide procedure
WS75	8.7e6 lb/in	9.7e6 lb/in	(see note)*	(see note)
WS99/ES1	6.4e6 compression 2.3e6 tension	6.6e6 compression 1.5e6 tension	3.8e6	1.8e6

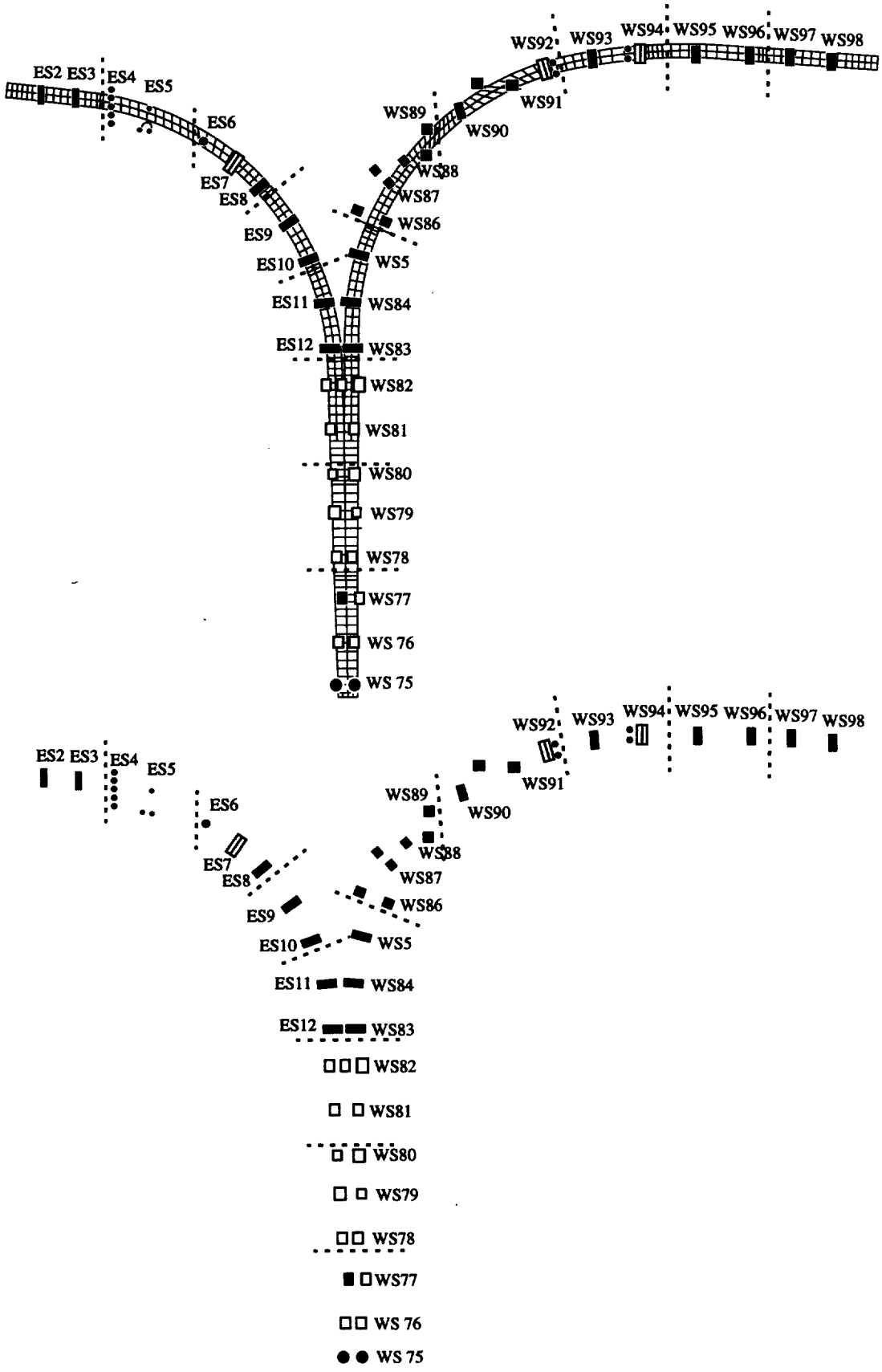

FIGURE 44. Column-footing connectivities for the retrofit structure.

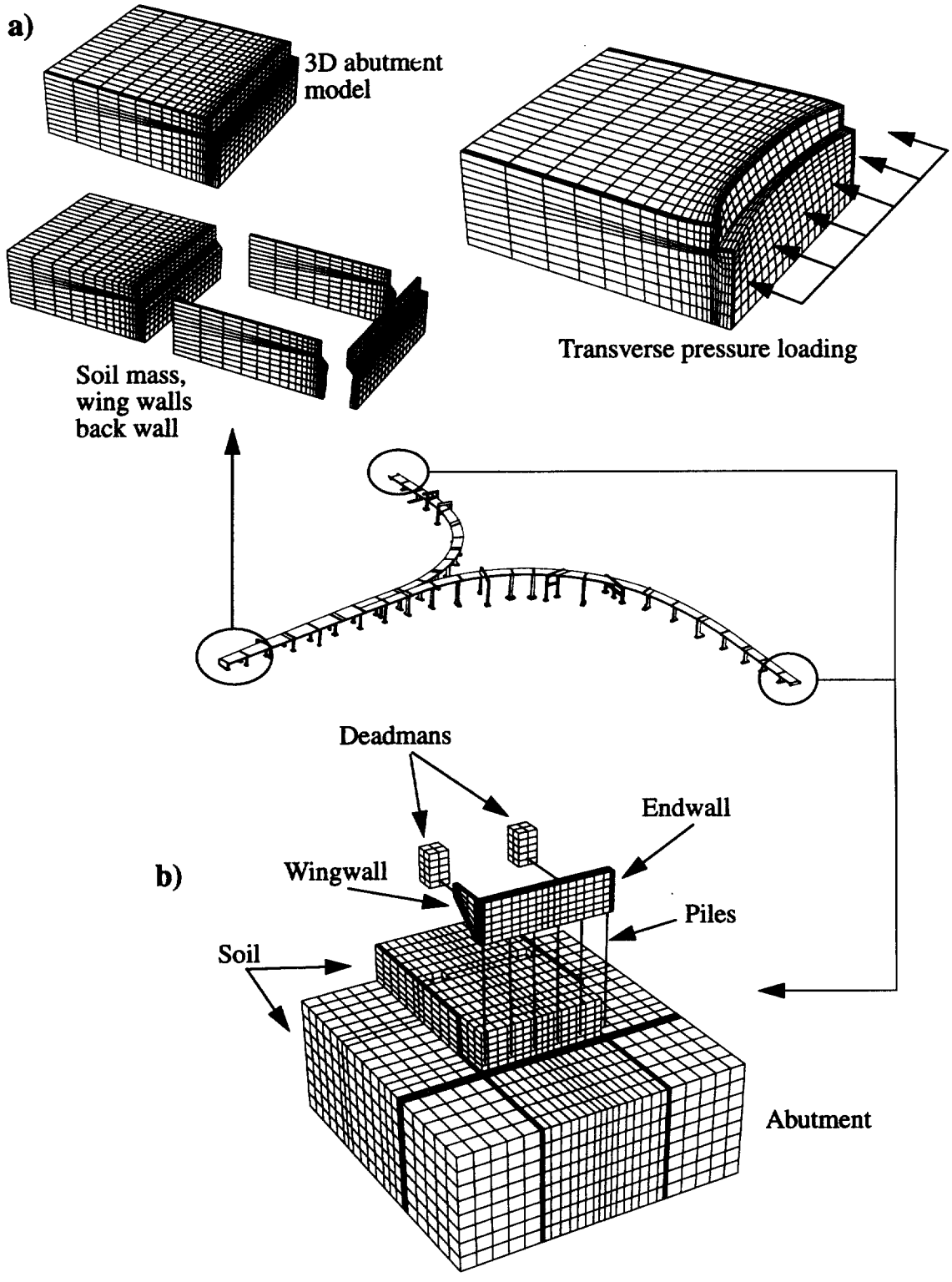

FIGURE 45. Determination of abutment and foundation stiffness from loading of substructure models. a) Abutment model (WS75), b) abutment model (ES1 and WS99).

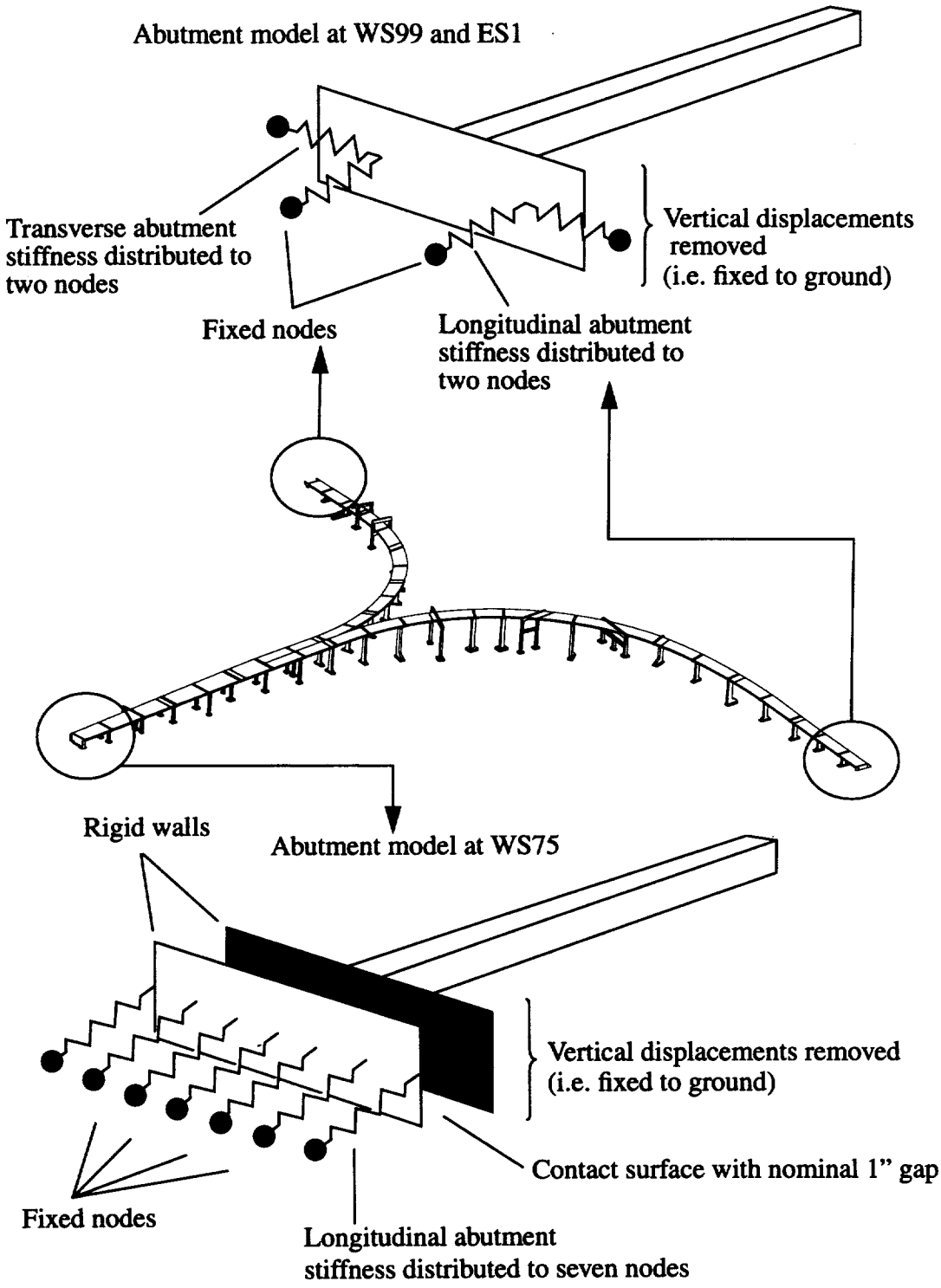

FIGURE 46. Abutment representation in the global finite element model.

*. In our judgement, the detail of the as-built connection between the abutment wall and the deck at WS75 would not provide sufficient strength to develop large transverse shear forces between the deck and the abutment at WS75. In the retrofit design, the massive drilled shafts at WS75 should attract nearly all of the transverse load at the abutment

4.1.2 Nonlinear concrete model

Under strong earthquake excitation, it is expected that many structures will undergo inelastic action. As long as the inelasticity is controlled and the behavior is ductile, the seismic performance of the inelastic structure can be quite good. Inelastic action can be a significant contributor to energy dissipation and can thus help mitigate the maximum force levels in the structure. Adequate structural ductility will also guard against sudden, brittle, explosive type failure associated with nonductile structures. On the other hand, the softening associated with inelastic action may also have less desirable effects which should be addressed. Inelastic action may result in increased structural displacements with a proportionate increase in secondary forces resulting from change of geometry of the structure (i.e. enhanced P-Δ effect from gravity dead load). Accurate computer simulation of the seismic response of a structure undergoing inelastic seismic deformations necessitates a nonlinear structural model which can adequately represent important nonlinear response features.

In concrete bridge structures, Caltrans' design methodology requires that inelastic action take place in the support columns rather than in the bent caps or deck structure. It is noted that this design philosophy is diametrically opposite to building design philosophy in which a weak-beam, strong-column philosophy prevails. Under extreme seismic events, concrete bridge columns such as those on the 24/580/980 interchange are expected to behave nonlinearly. In the current as-built configuration of the ES and WS lines, the columns lack significant ductility and would most likely fail at a relatively low loading as a result of pull-out of the column longitudinal steel from the footing, brittle fracture in high moment regions of the column because of poor confinement of the concrete core, or shear failure of the shorter columns near the abutments.

As evidenced by experimental tests at UC San Diego [26], steel jacketing of 1960's vintage concrete columns significantly improves the cyclic behavior of the columns and results in columns with enhanced ductility capacity. The extensive jacketing prescribed in the 24/580/980 retrofit design should significantly enhance the seismic performance of the concrete columns in the bridge system.

As ductile concrete columns deform laterally, the compressive gravity stresses in the column are overcome on the tension side of the column and a transverse cracked surface forms across a portion of the column cross section. As lateral displacements continue to increase, the cracked section will continue to propagate across the column, the longitudinal reinforcing steel will yield, and ultimately a plastic hinge will form in the highest moment region of the column. Formation of a plastic hinge in a column results in a drastic reduction in column stiffness with the potential for significant increase in structural displacements and redistribution of load within the structural system.

For the seismic analysis of the 25/580/980 interchange, a nonlinear reinforced concrete material model has been implemented in the *NIKE3D* finite element program. Following the work of Fillipou et. al. [27, 28, 29] the model employs the modified Kent-Park model [30] for the concrete compressive stress-strain behavior and the plasticity model of Menegotto and Pinto [31], for the characterization of the reinforcing steel.

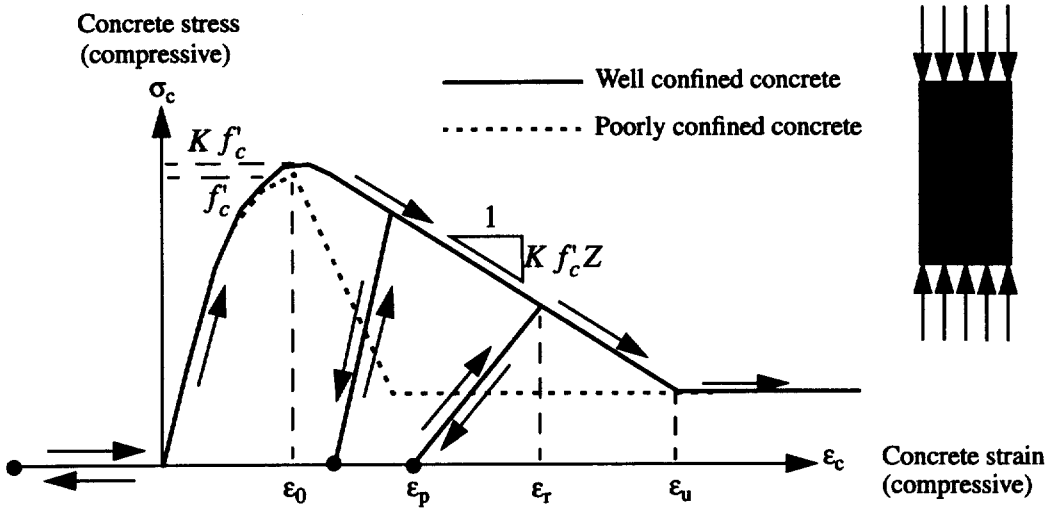

FIGURE 47. Modified Kent - Park concrete compression model.

The concrete compressive model (see Fig. 47) accounts for softening in the concrete and the ultimate compressive strength and the softening slope are a function of the degree of concrete confinement. Poorly confined concrete is represented by a steep softening slope, well confined concrete is represented by a shallower softening slope (Fig. 47).

The concrete constitutive law for compression is governed by three regions of behavior,

for $\varepsilon_c \leq \varepsilon_0$

$$\sigma_c = K f_c' \left[2\left(\frac{\varepsilon_c}{\varepsilon_0}\right) - \left(\frac{\varepsilon_c}{\varepsilon_0}\right)^2\right] \quad \text{(EQ 1)}$$

for $\varepsilon_0 \leq \varepsilon_c \leq \varepsilon_u$

$$\sigma_c = K f_c' [1 - Z(\varepsilon_c - \varepsilon_0)] \geq 0.2 K f_c' \quad \text{(EQ 2)}$$

for $\varepsilon_c \geq \varepsilon_u$

$$\sigma_c = 0.2 K f_c' \quad \text{(EQ 3)}$$

where

$$\varepsilon_0 = 0.002K \quad \text{(EQ 4)}$$

$$K = 1 + \frac{\rho_s f_{yh}}{f_c'} \quad \text{(EQ 5)}$$

For simple rectangular columns with horizontal ties shear reinforcement, an empirical relationship has been developed for the Z term. The expression is given by,

$$Z = \frac{0.5}{\frac{3 + 0.29 f'_c}{145 f'_c - 1000} + 0.75 \rho_s \sqrt{\frac{h'}{s_h}} - 0.002K} \quad \text{(EQ 6)}$$

Unloading from the compression curve follows a straight line from the point at which unloading starts (e.g. at strain ε_r in Fig. 47) to a point on the axis denoted by ε_p where ε_p is given by the equations,

$$\frac{\varepsilon_p}{\varepsilon_0} = 0.145\left(\frac{\varepsilon_r}{\varepsilon_0}\right)^2 + 0.13\left(\frac{\varepsilon_r}{\varepsilon_0}\right) \quad \text{(EQ 7)}$$

when $\left(\frac{\varepsilon_r}{\varepsilon_0}\right) < 2$ and

$$\frac{\varepsilon_p}{\varepsilon_0} = 0.707\left(\frac{\varepsilon_r}{\varepsilon_0} - 2\right) + 0.834 \quad \text{(EQ 8)}$$

when $\left(\frac{\varepsilon_r}{\varepsilon_0}\right) \geq 2$

The existing material properties of the stack interchange are not well quantified. Caltrans did not perform coring samples, thus the existing concrete compressive strength is not precisely known. Significant concrete strengthening has certainly occurred since the 1960's when the structures were first built. In order to develop a representative set of material properties for the 1960's vintage 24/580/980 structure, the effect of continued concrete curing was taken into account. In addition, properties utilized in concrete jacketing tests at UC San Diego were considered (UC San Diego apparently chose properties which would be representative of existing vintage columns which are retrofit candidates), and concrete compressive strengths observed in coring samples from other bridges were considered (Maroney et. al. [32]). The influence of confinement on the effective ultimate compressive strength was also based on information gleaned from representative columns in the UC San Diego tests. The Z factors defining the slope of the concrete softening (Fig. 47) were estimated based on existing Z factors in the literature, and from existing formulas (EQ. 6) for the unjacketed portions of columns. The Z factors for well confined concrete in the jacketed portion of the existing columns and in the spirally reinforced new columns, were deduced by numerical experimentation where computational results were compared to actual tests of well confined, jacketed columns.

Because of uncertainties in the actual properties, two sets of analyses were performed, each with a different set of concrete properties. The properties used in the analyses are summarized in Table 5.

The reinforcing steel material model, which provides a reasonable representation of the Bauschinger effect, takes the form (see Taucher, Spacone and Filippou [29]),

$$\sigma^n = b \cdot \varepsilon^n + \frac{(1-b) \cdot \varepsilon^n}{(1+\varepsilon^{nR})^{\frac{1}{R}}} \quad \text{(EQ 9)}$$

$$\varepsilon^n = \frac{\varepsilon - \varepsilon_r}{\varepsilon_o - \varepsilon_r} \quad \text{(EQ 10)}$$

$$\sigma^n = \frac{\sigma - \sigma_r}{\sigma_o - \sigma_r} \quad \text{(EQ 11)}$$

This model provides the initial yield plateau typical of ductile steels upon first yield, and subsequently provides smoothed hysteresis loops for the saturated elasto-plastic behavior as shown in Fig. 48. This model provides good agreement with cyclic tests for reinforcing bars.

TABLE 5. Material property sets assumed for the seismic analyses

	Material description	Effective concrete compressive strength	Reinforcing steel yield strength
Material Property Set #1	Original concrete, unretrofit, poorly confined (column core)	6000 psi	45.7 ksi
	Original concrete, retrofit, well confined (column core)	7500 psi	45.7 ksi
	New retrofit concrete, well confined (column core)	7000 psi	68.0 ksi
Material Property Set #2	Original concrete, unretrofit, poorly confined (column core)	5000 psi	40.0 ksi
	Original concrete, retrofit, well confined (column core)	6500 psi	40.0 ksi
	New retrofit concrete, well confined (column core)	6000 psi	60.0 ksi

The nonlinear concrete and steel models were implemented in the *NIKE3D* finite element program fiber beam element. This element discretizes the column cross section into a number of user defined zones, with the uniaxial stress-strain behavior of each zone assigned the appropriate concrete or steel stress-strain law (see Fig. 49). An evaluation of the nonlinear concrete model was performed by comparison with a jacketed concrete col-

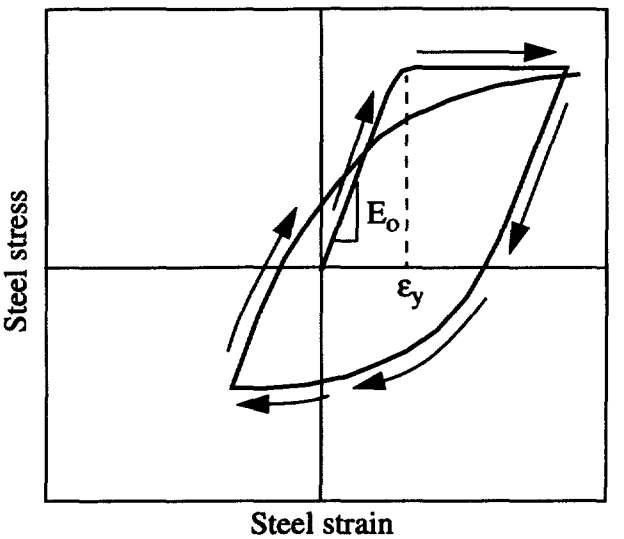

FIGURE 48. Menegotto-Pinto elastoplastic model for reinforcing bars.

umn test performed by Seible [26]. In a UC San Diego experiment, a partially jacketed scale model column was loaded cyclically up to displacement ductilities of 8. The test apparatus for the column test and the resulting force-displacement behavior is shown in Fig. 50. Based on the material properties supplied in the Seible study, a model of the concrete column was constructed with multiple beam elements representing both the confined and unconfined concrete regions. A comparison of the computed force-displacement relationship with the measured force-displacement relationship is shown in Fig. 51.

The correlation between computed and measured response is acceptable given the uncertainties in actual material properties. The computational model has appropriate pinching of the hysteresis loops and the energy loss per cycle, as defined by the area under the hysteresis loops, appears quite reasonable. The primary shortcoming of the nonlinear model is that the continued degradation of the loading stiffness with loading cycle is not very accurately reflected. Attempts to improve this aspect of the model by increasing the concrete softening behavior resulted in numerical difficulties. Future developments and improvements in the model will address this issue. In light of the reasonable comparison with experiment, the nonlinear concrete model was judged sufficiently accurate for the engineering evaluation of the 24/580/980 interchange.

The nonlinear fiber model requires definition of the column cross section for each column element which the model will be used for. In the global finite element model of WS and ES lines, a selected number of representative column cross sections were identified. The column cross sections are shown in Fig. 52 through Fig. 55 and the column section which applies to each bent is indicated in Table 6.

For each of the column cross section definitions, the column user defined integration points must be generated as input to the *NIKE3D* program. The global finite element model must update the stress at each user defined column cross section integration point at

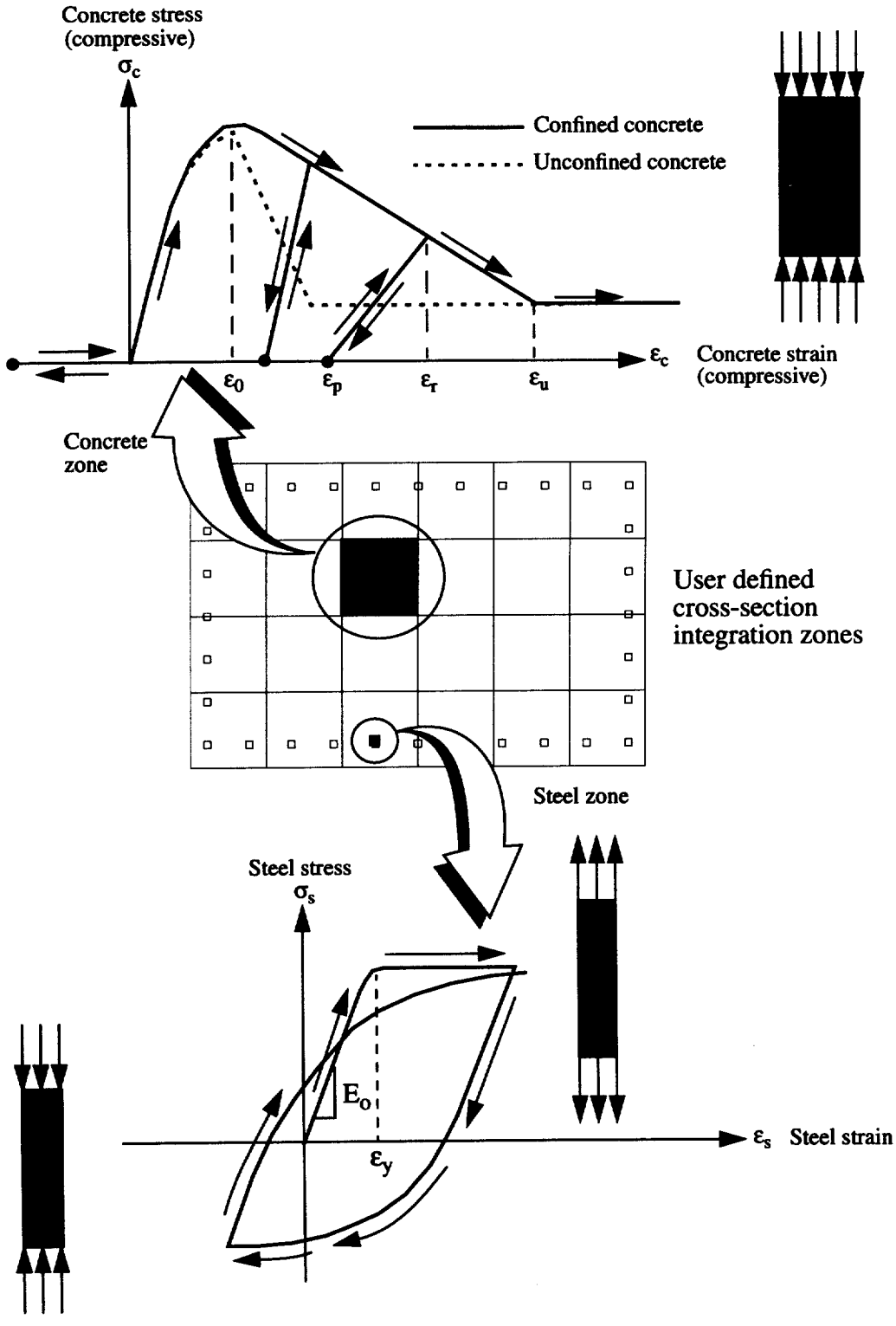

FIGURE 49. Characterization of concrete and steel in the fiber beam element.

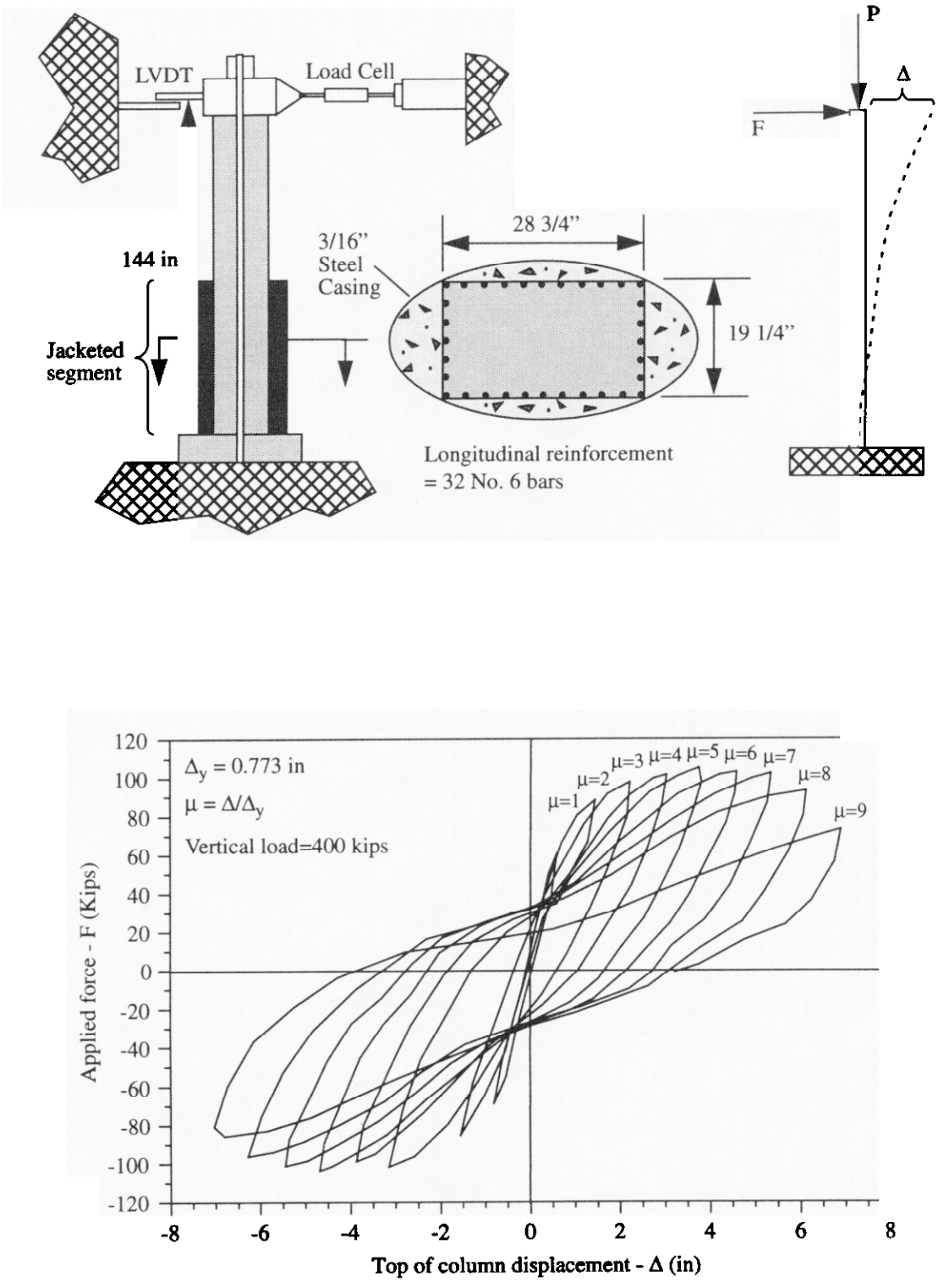

FIGURE 50. Measured force - displacement behavior of a jacketed column from a UC San Diego experiment (Ref. 26).

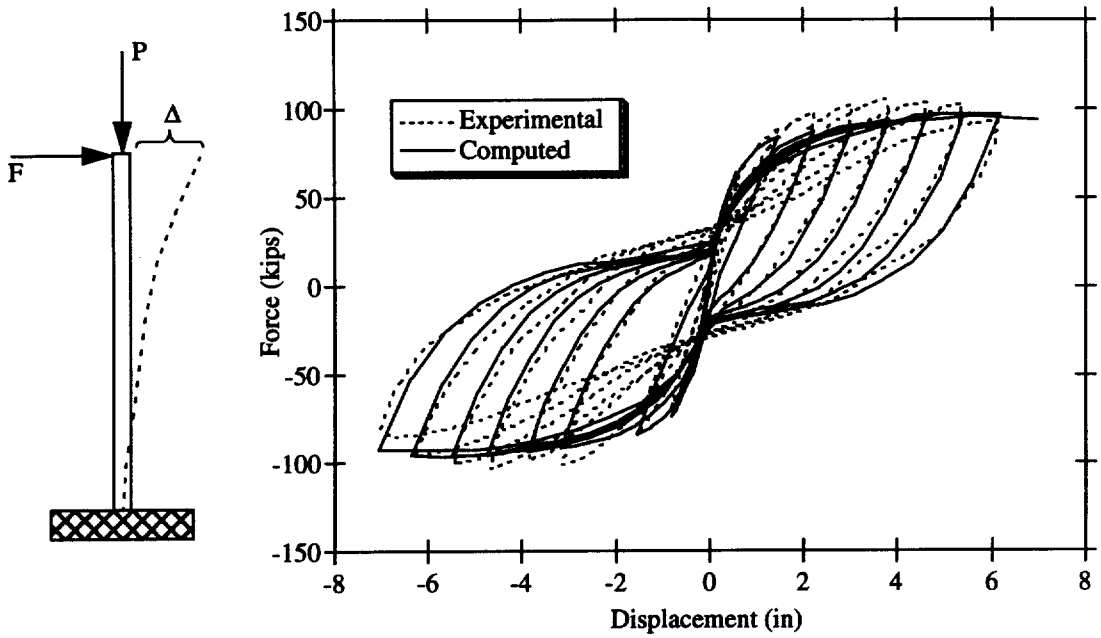

FIGURE 51. Comparison of *NIKE3D* nonlinear concrete fiber element with experimental test of UC San Diego (column in Fig. 49).

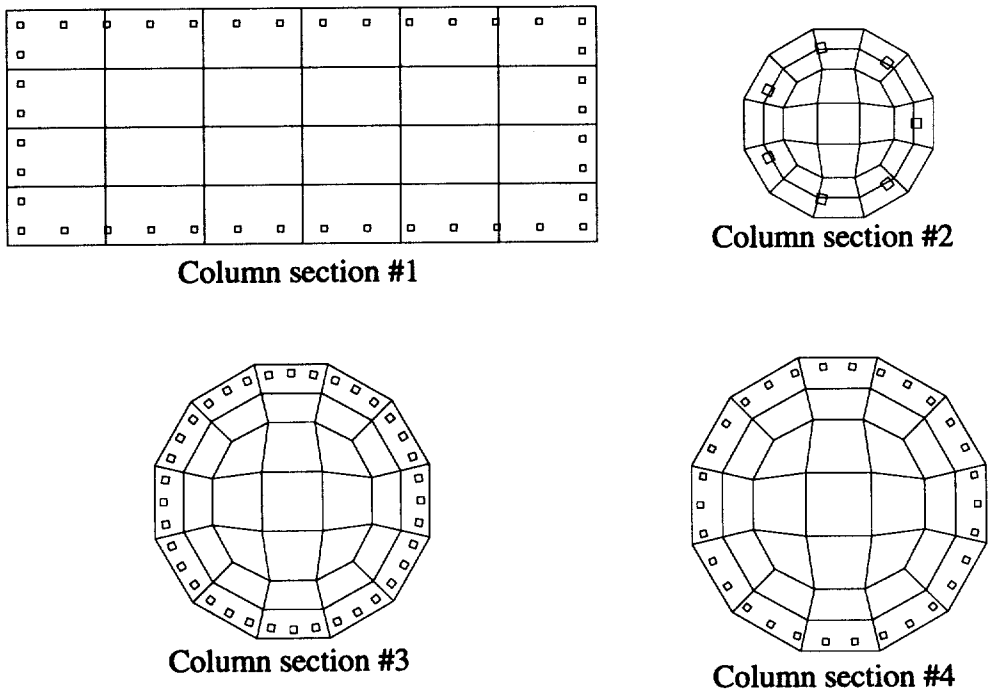

FIGURE 52. Representative column cross sections (sections 1-4).

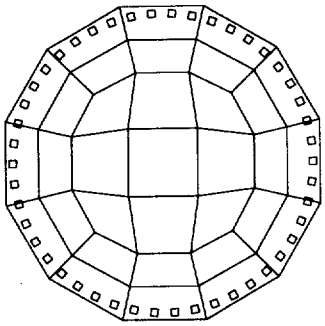

Column section #5

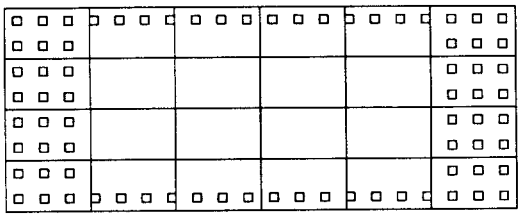

Column section #6

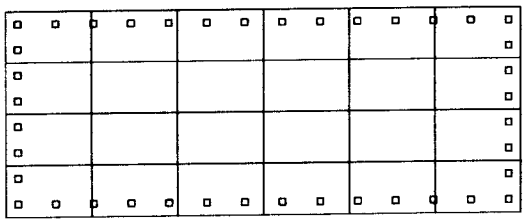

Column section #7

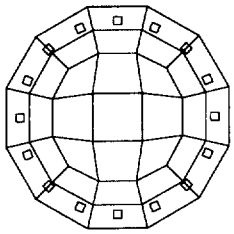

Column section #8

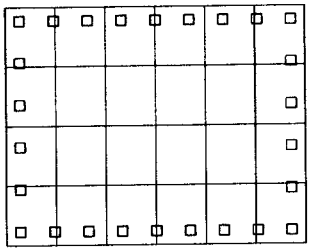

Column section #9

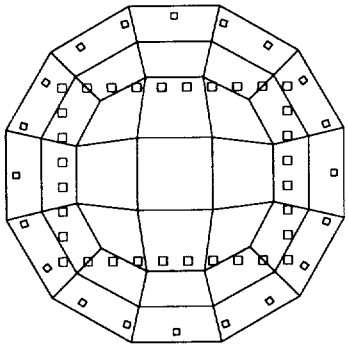

Column section #10

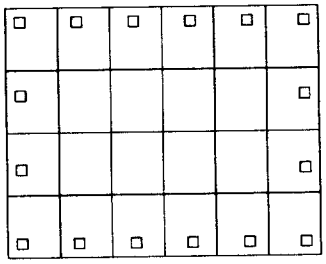

Column section #11

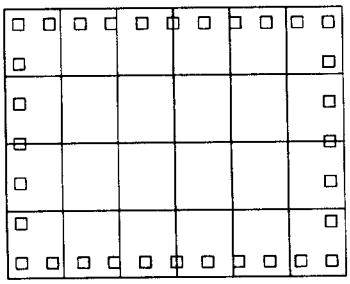

Column section #12

FIGURE 53. Representative column cross sections (sections 5-12).

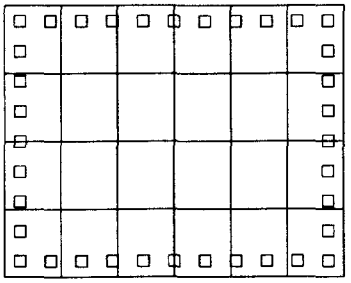

Column section #13

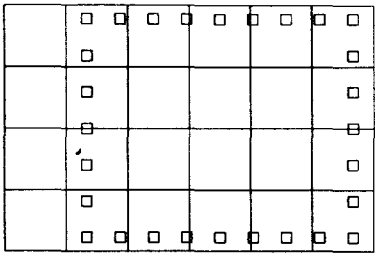

Column section #14

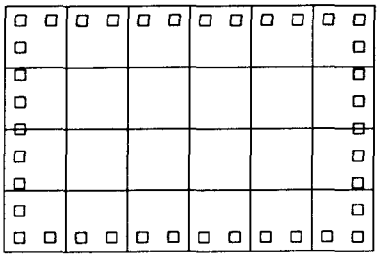

Column section #15

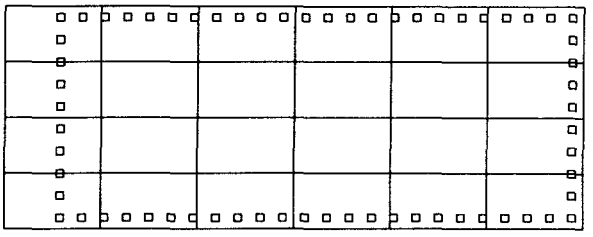

Column section #16

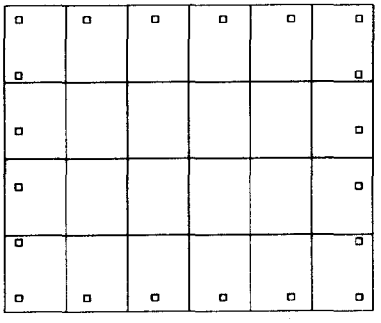

Column section #17

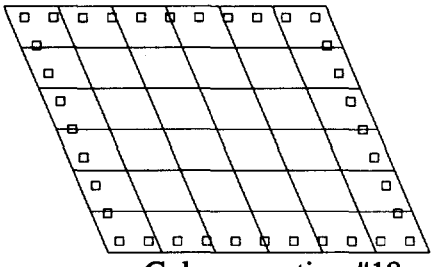

Column section #18

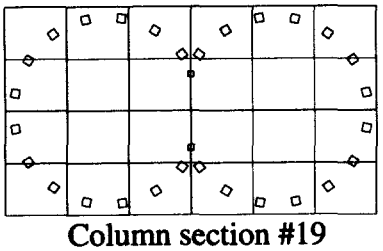

Column section #19

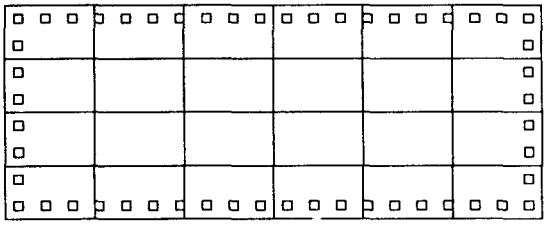

Column section #20

FIGURE 54. Representative column cross sections (sections 13-20).

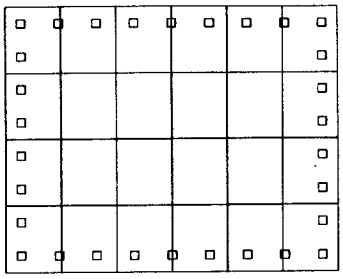

Column section #21

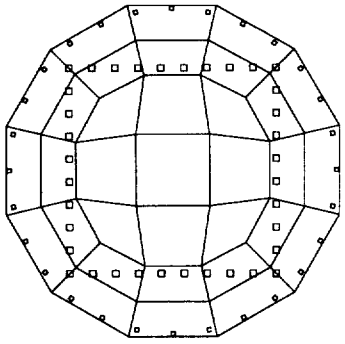

Column section #22

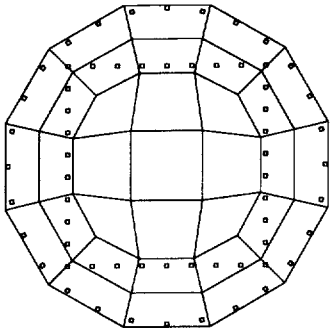

Column section #23

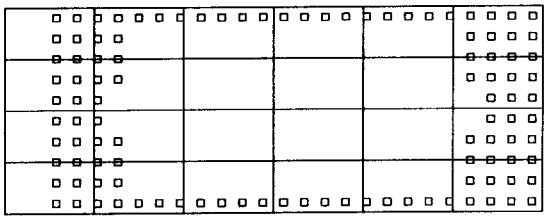

Column section #24

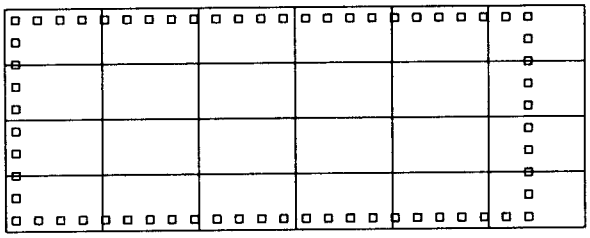

Column section #25

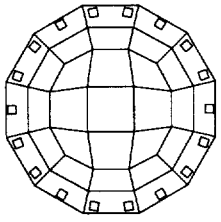

Column section #26

FIGURE 55. Representative column cross sections (sections 21-26).

each of the three thousand or so time steps of the earthquake response computation. In addition, for post-processing, the strains at each user defined integration point were dumped into an output file so that the potential for concrete crushing could be evaluated for each column at each instant in time. This results in a very large database which must be dealt with. For the 24/580/980 interchange project, special software features were developed and implemented which allowed expedient generation of the column cross sections and automated evaluation of the voluminous output files. This automation of the generation and post processing made the actual time effort of the engineering analyst minimal.

TABLE 6. User defined cross section integration (UDI) sets for representative columns.

Column section #	UDI set #	Associated bents
1	56	WS97 WS98 ES2 ES3 ES9 ES10 ES11
2	57	ES4
3	58	ES5 Right
4	59	ES5 Left (2)
5	60	ES6
6	61	ES7
7	62	WS83 WS84 WS93 WS95 WS96 ES8 ES12
8	63	WS75
9	64	WS76
10	65	WS77 middle
11	66	WS77 right
12	67	WS78
13	68	WS79 WS81
14	69	WS80 left
15	70	WS80 right
16	71	WS85 WS90
17	72	WS86 left
18	52	WS86 right (skewed)
19	73	WS87 left (new)
20	74	WS87 center WS88
21	75	WS89
22	76	WS91 lower
23	77	WS91 upper
24	78	WS92

TABLE 6. User defined cross section integration (UDI) sets for representative columns.

Column section #	UDI set #	Associated bents
25	79	WS94
26	80	WS92 companion WS94 companion

4.1.3 Transient seismic response computations

The response of the ES and WS lines has been estimated for a moment magnitude 7.25 Hayward fault earthquake. The computations performed for the response estimates consisted of transient, nonlinear, time history solutions for thirty seconds of strong motion.

Two nonlinear finite element models were utilized in the response computations. The first computer model incorporated geometric nonlinearites including finite deformation effects, which allows for accurate representation of P-Δ influence on stresses and displacements, contact and impact at expansion hinges and one-way cable tensioning at the expansion hinges. The second nonlinear model included geometric nonlinearities, and material nonlinearities were also included with the nonlinear beam fiber model for concrete columns. The sources of nonlinearity in the fully nonlinear model are summarized in Fig. 56.

For all of the computational analyses, Rayleigh mass and stiffness proportional damping was used to represent energy dissipation in the structure/foundation system. The damping representation is thus,

$$[C] = \alpha[K] + \lambda[M] \qquad \text{(EQ 12)}$$

The damping was set to 5% critical at periods of one second and three-tenths of a second respectively as indicated in Fig. 57. The same damping was assigned for cases of linear and nonlinear concrete models. For the nonlinear concrete model, the hysteresis will augment the energy dissipation developed from the Rayleigh damping. Consideration was given to lowering the Rayleigh damping in the nonlinear concrete model, however for a structure undergoing strong shaking, it was felt that the effective damping will in all likelihood be quite high, and enhanced damping is not any less defensible than a lower damping value. Existing information on strong motion structural response is simply inadequate to evaluate effective damping in structures undergoing extreme nonlinear response.

All of the analyses which were performed utilized three components of input ground motion. A *Silicon Graphics* 8000 work station was the compute platform used for the seismic calculations and the nonlinear analyses for thirty seconds of earthquake motion required on the order of twenty five hours per run. A double precision version of the *NIKE3D* program was developed for the *Silicon Graphics* work station so that all computations could be performed in 64 bit arithmetic. Early attempts at running the highly nonlinear model in standard 32 bit arithmetic proved problematic in achieving convergence of the solution. The *NIKE3D* program utilizes a quasi-Newton solution scheme in which the tangent stiffness is updated economically without the full reformation of the stiffness associated with a classical full Newton solution algorithm. Time stepping was achieved with standard Newmark-Beta time integration. The transient analyses were performed at .02 second time steps which allowed resolution of frequencies of approximately 5 Hertz.

For all of the transient analyses, a complete database of response information (i.e. structural displacements, member force resultants, concrete and steel stresses at each user defined integration point) was generated which contained the response information for each time step. This resulted in an extremely large database of earthquake response information and special features were implemented in the *TAURUS* [33] post processing rou-

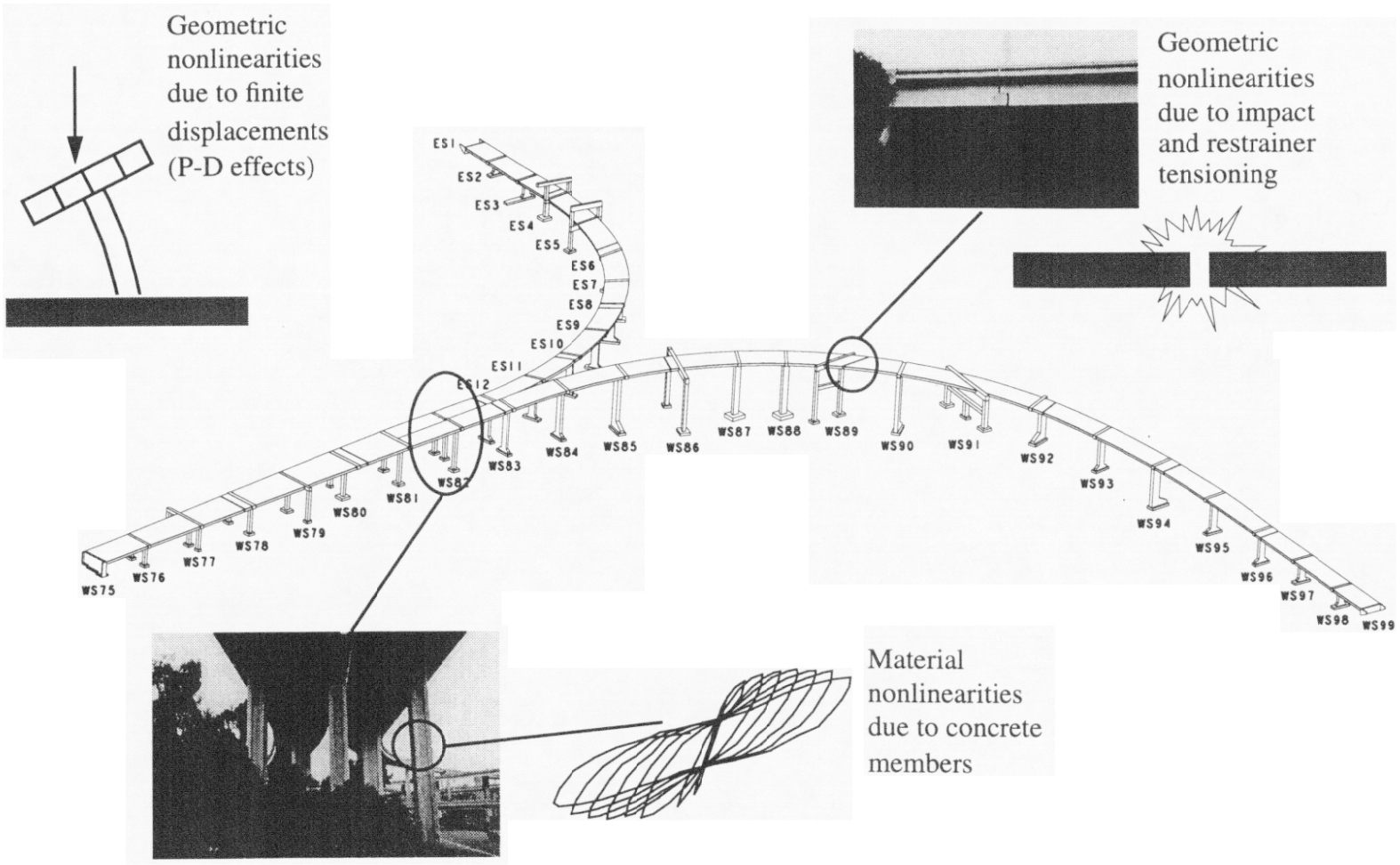
Geometric nonlinearities due to finite displacements (P-D effects)
Geometric nonlinearities due to impact and restrainer tensioning
Material nonlinearities due to concrete members
ES1
ES2
ES3
ES4
ES5
ES6
ES7
ES8
ES9
ES10
ES11
ES12
WS75
WS76
WS77
WS78
WS79
WS80
WS81
WS83
WS84
WS85
WS86
WS87
WS88
WS89
WS90
WS91
WS92
WS93
WS94
WS95
WS96
WS97
WS98
WS99

in the fully

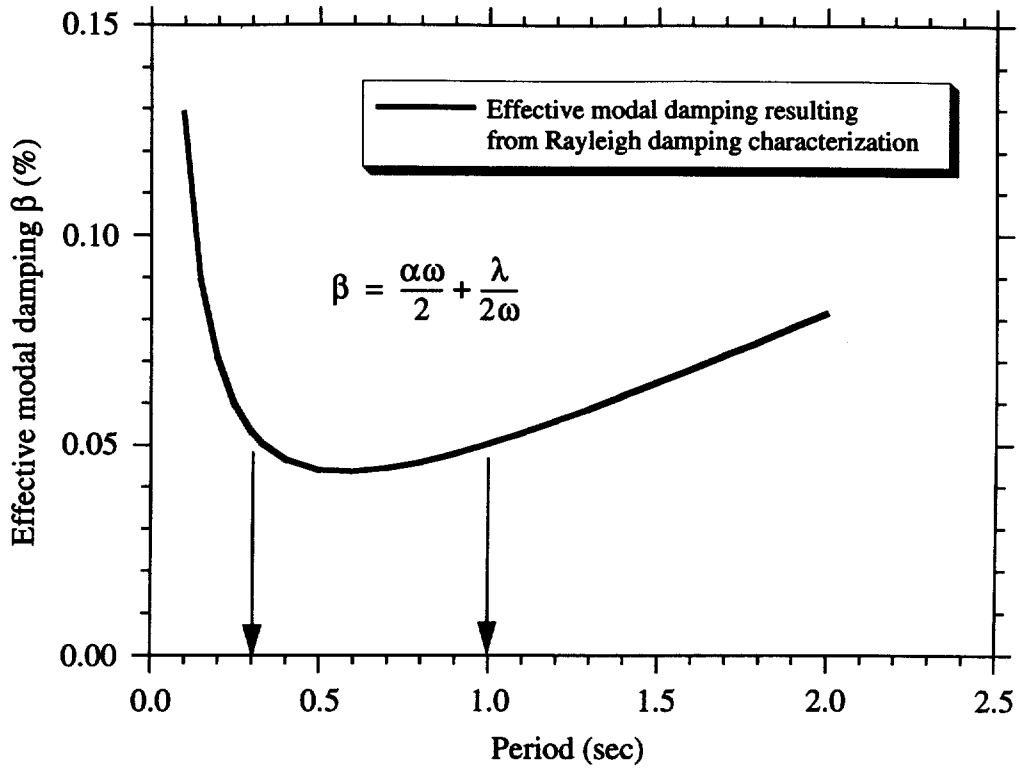

FIGURE 57. Assignment of modal damping in the structural model with a mass and stiffness proportional damping matrix

tine in order to handle management of the large volume of information. In addition, special purpose software was developed to browse the *TAURUS* database and identify members in which concrete crushing was a possibility.

4.1.4 Seismic demands

The principal objective of the LLNL study was to provide Caltrans with an independent assessment of the seismic demands that a Hayward fault earthquake would place on the ES and WS lines of the 24/580/980 interchange. Caltrans has completed their own assessment of the member capacities and an independent evaluation of demands, obtained from the LLNL detailed nonlinear global model of the structure, provides Caltrans additional data for assessing demand to capacity ratios.

Caltrans engineers requested that the seismic demands on the structural columns be reported in terms of maximum seismic displacement at the top of the individual columns. The columns of the bridge model are supported on foundation matrices which allow for translation and rotation at the base of the column, and the displacements of a given column include rigid body components due to translation and rotation of the column base as shown in Fig. 58. Caltrans developed their displacement capacity information including the displacement due to the foundation and thus Caltrans requested that the displacement demands be reported with the bottom of column translation and rotation components included. The LLNL reporting of displacements would thus be based on total nodal dis-

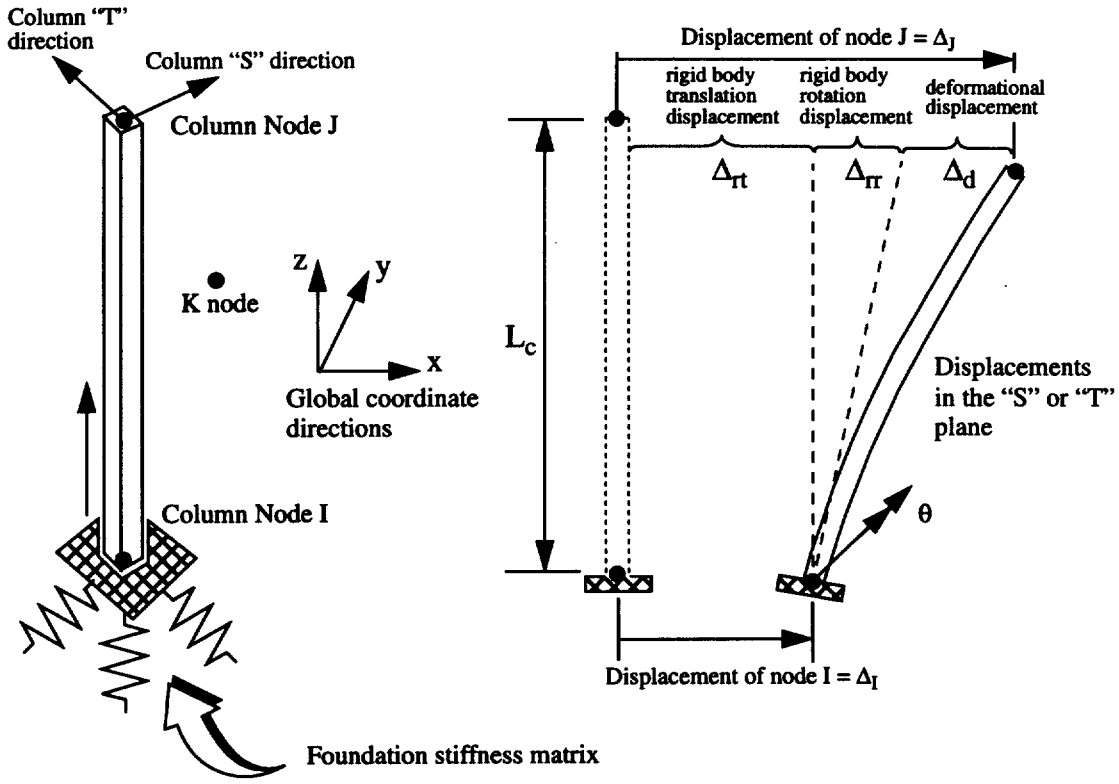

FIGURE 58. Determination of deformational displacement demands for individual columns (single column bent, moment connection between column and footing).

placement relative to the input ground motion (i.e. displacement Δ_J in Fig. 58) rather than the true column deformational displacement (Δ_d in Fig. 58). Inspection of the LLNL finite element results indicates that displacements due to rigid body translation (Δ_{rt} in Fig. 58)

are generally small to the point of being negligible, but the rigid body rotational displacements (Δ_{rt} in Fig. 58) are capable of significant contribution to the total displacement.

The nodal displacements in the finite element model are given in terms of global coordinate directions and thus it is necessary to resolve displacements into the local column directions. A post-processing feature was added to the *TAURUS* program to vectorially resolve global displacements into the column local coordinate systems. This required input defining the orientation of each column relative to the global coordinate system (i.e. an α for each column as indicated in Fig. 59). The top of column displacements were reported in the principal column coordinate directions, which for the most part are the transverse and longitudinal directions of the bridge.

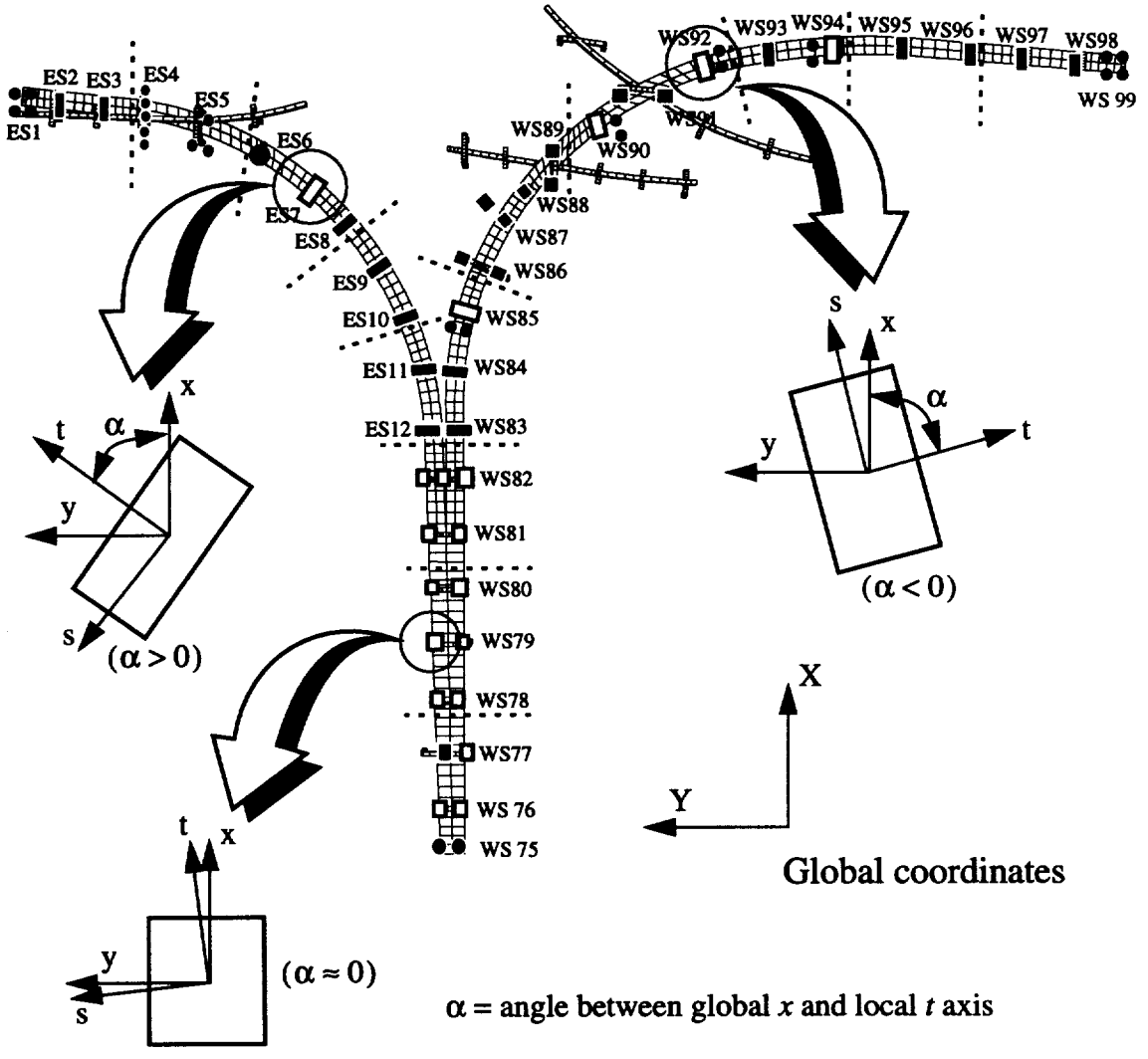

FIGURE 59. Rotation from global axes to column local principal axes.

Multiple seismic response computations were carried out in order to determine the sensitivity of system response to a number of parameters. For each analysis, the maximum displacement which occurred at the top of each column was determined and written to a database. The first analysis set considered the nonlinear response of the structure in which

geometric nonlinearities were included and material nonlinearity in the concrete was neglected. The analyses were based on Caltrans' definition of the surface earthquake ground motion. For this particular model idealization, two different modeling approaches were investigated for the concrete. In the first approach, the user defined integration beam element was employed in which linear material properties were assigned to the various concrete and steel integration points. The second approach treated the concrete as a linear material, but the column stiffnesses were based on a homogenous, uncracked rectangular cross section with an elastic modulus corresponding to the linear concrete modulus. A comparison of the two modeling approaches was developed in order to verify the accuracy of the sophisticated user defined fiber model for the simple case of linear concrete. The top of column displacements for these two modeling approaches are shown in Fig. 60 and Fig. 61[1]. From the figures, it is observed that the fiber model is in good agreement with the gross section model. The maximum displacements occur between bents WS 81 and WS 89 where the column displacements approach 15 inches.

The second set of analyses considered the nonlinear response of the structure when the fully nonlinear concrete model was employed, and the ground motion was defined by the Caltrans motion. The top of column displacements from the computational model are summarized in Fig. 62 through Fig. 65. In these figures the nonlinear concrete results are compared to the linear concrete model in order to clearly show the effect of nonlinearity in the concrete. In addition, two different material property sets were considered (see section 4.1.2) so that the sensitivity of response to material properties could be judged. The fully nonlinear model results show that the concrete nonlinearity has a pronounced influence on the displacements of the structure. The column displacements in the trunk portion of the structure, between bents WS 75 and WS 82, show a significant increase in the longitudinal direction (which corresponds to the column "t" direction). In the transverse direction, the columns exhibit significant increases in displacements but the increases are spread throughout the structure and are not as limited to the trunk region. Top of column displacements for the nonlinear analysis with the Caltrans ground motions are tabularized in Table 7 and member stress resultants are tabularized in Table 8. The element stress resultants are reported for the top and bottom of each column as indicated in Fig. 70. The *NIKE3D* program provides stress resultants at the element center for the beam elements, and short beam elements were defined in the finite element model at the ends of the columns so that resultants would be obtained in the maximum moment regions.Top of column displacements for the nonlinear analysis with the LLNL ground motions are tabularized in Table 9.

A similar set of nonlinear analyses has been performed for the LLNL median earthquake motion and the results of these analyses are summarized in Fig. 66 through Fig. 69. Comparison of the nonlinear results with Caltrans and LLNL motions shows that the two hazard estimates are in reasonable agreement in terms of structural demands.

1. For these two early linear runs, the connectivity at the top of the columns at multiple column bents WS 86, WS 89 and WS 91 assumed a moment connection between the columns and the bent cap. Subsequent runs utilized a pinned connection at the top of these columns to more accurately reflect the as-built detail.

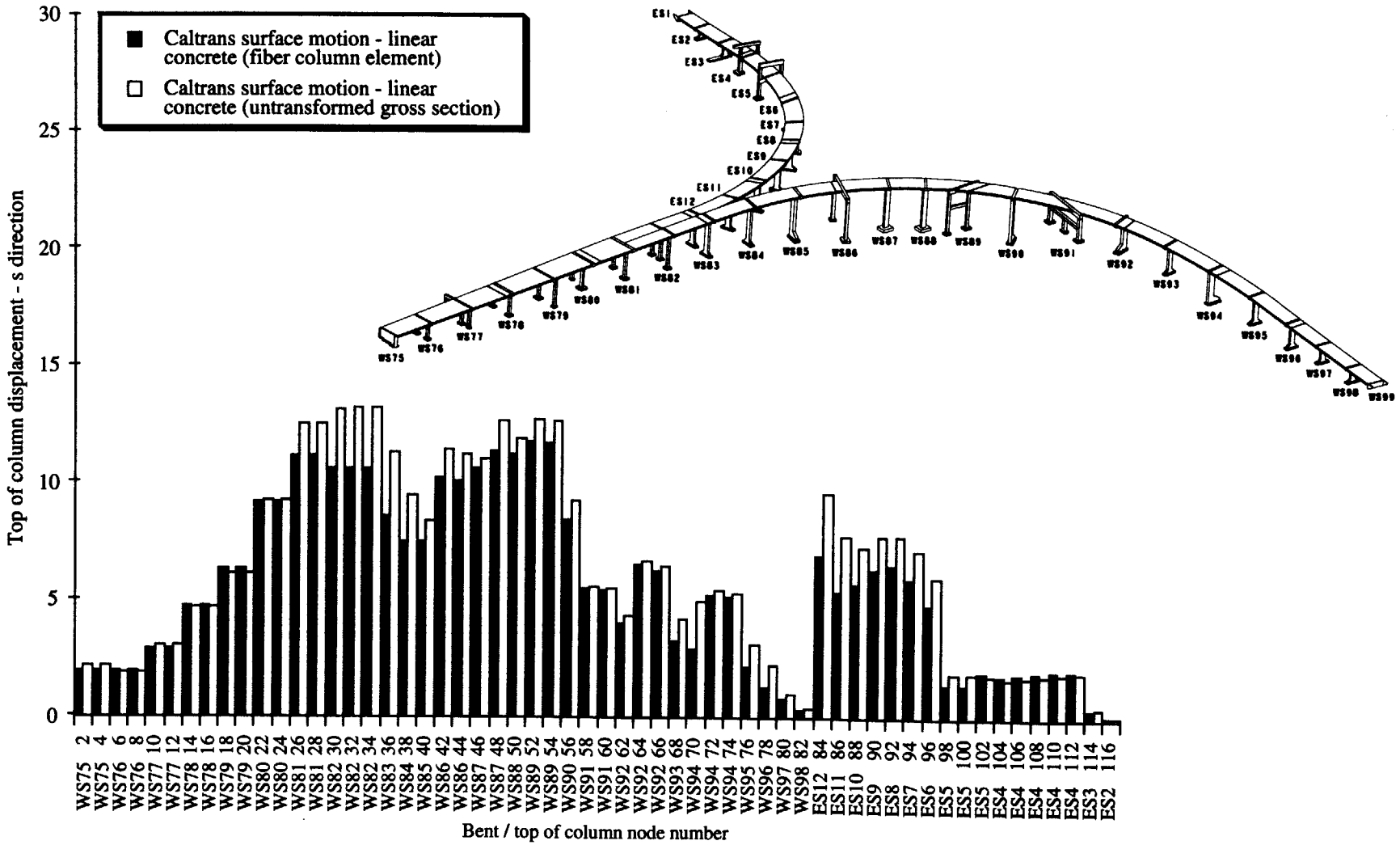

FIGURE 60. Top of column s displacements for the WS and ES lines.

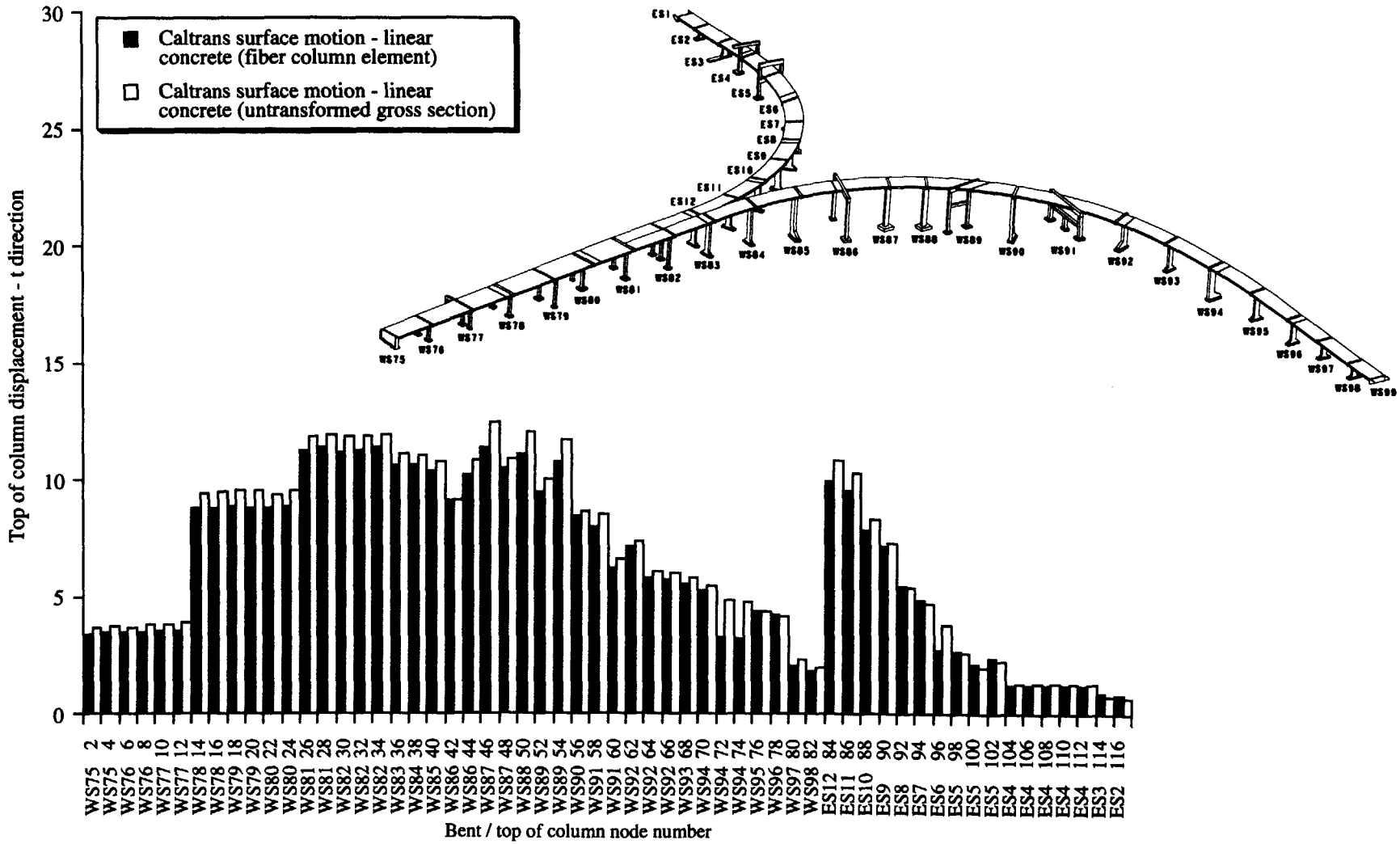

FIGURE 61. Top of column t displacements for the WS and ES lines.

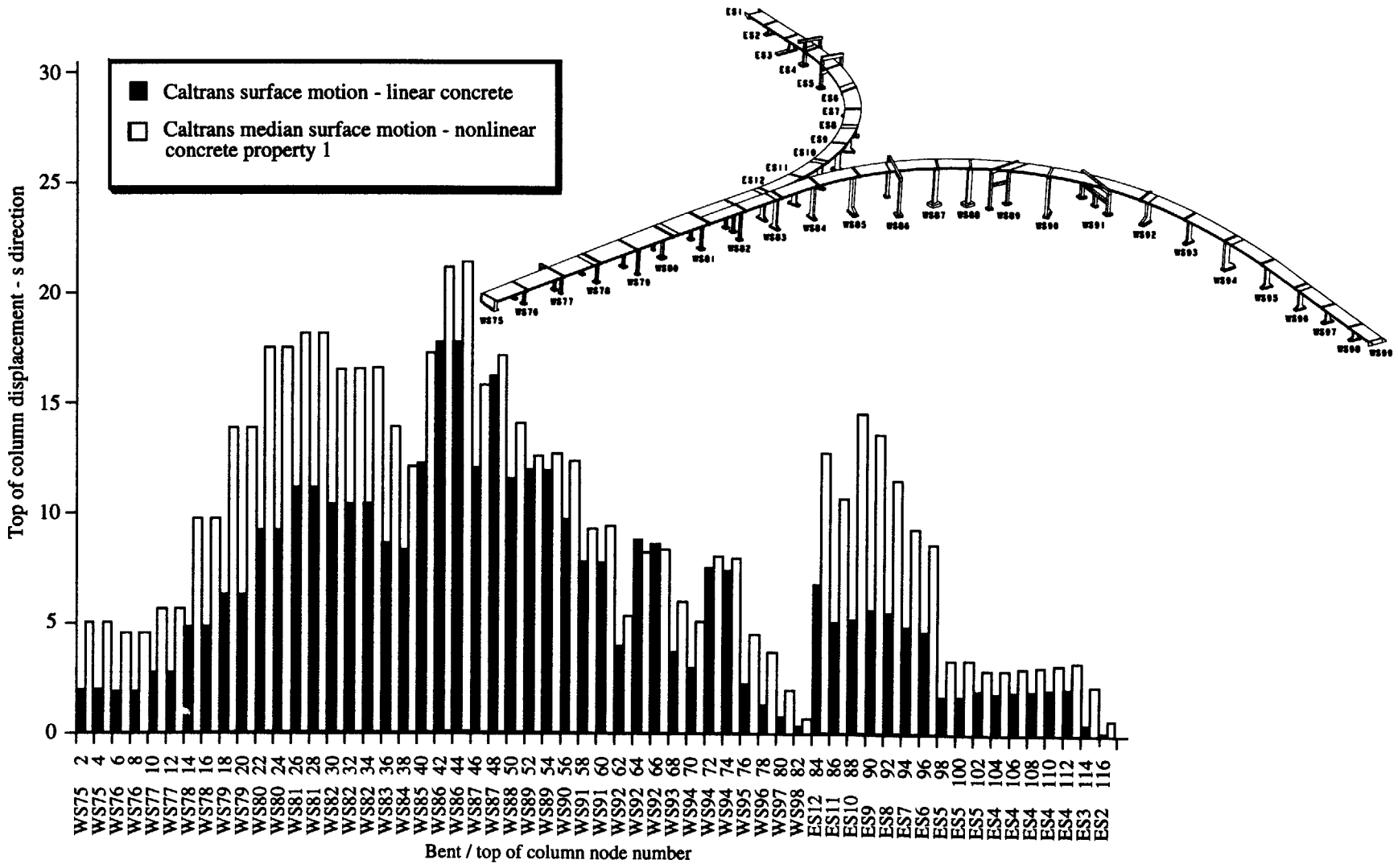

FIGURE 62. Top of column s displacements for the WS and ES lines.

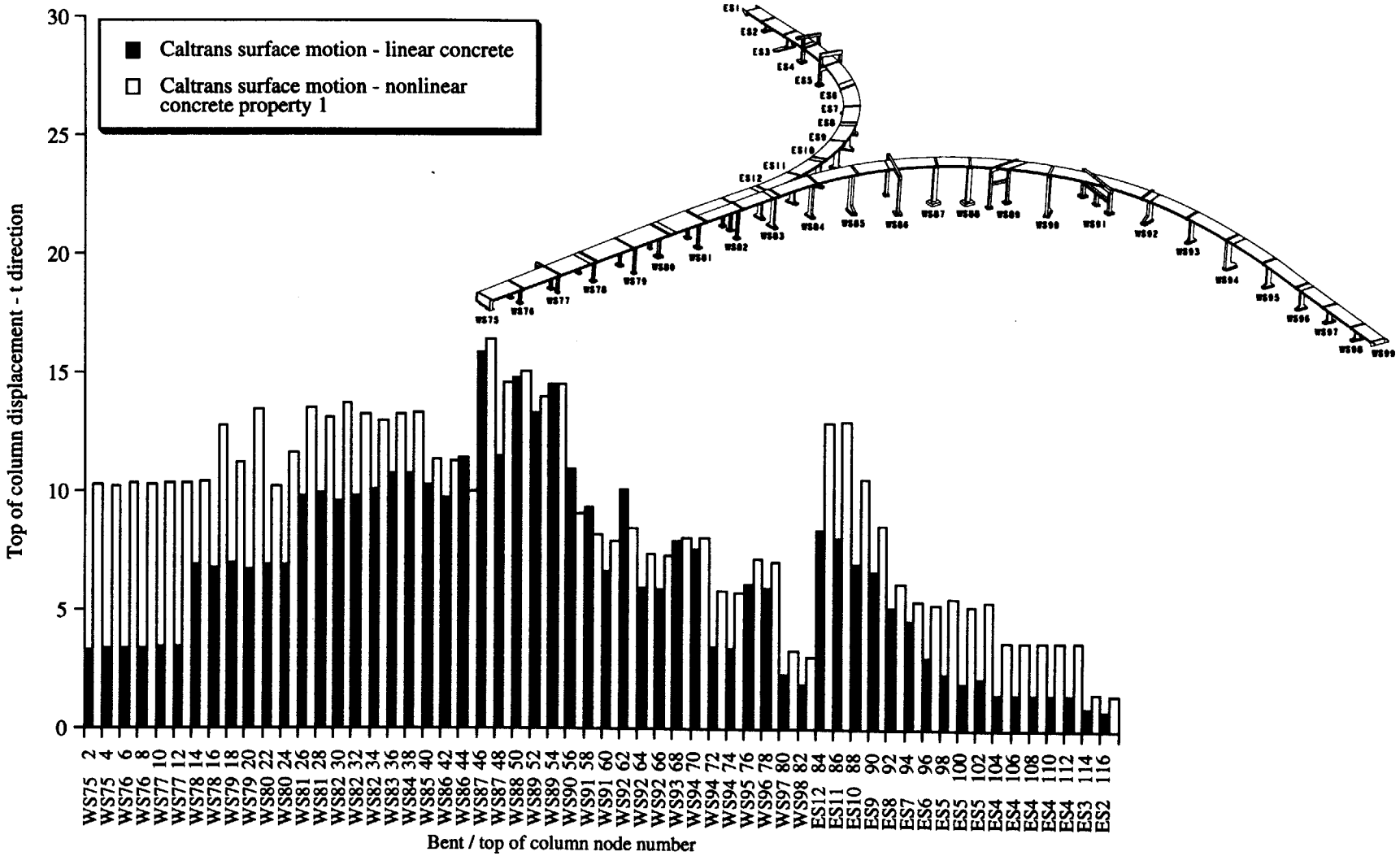

FIGURE 63. Top of column t displacements for the WS and ES lines.

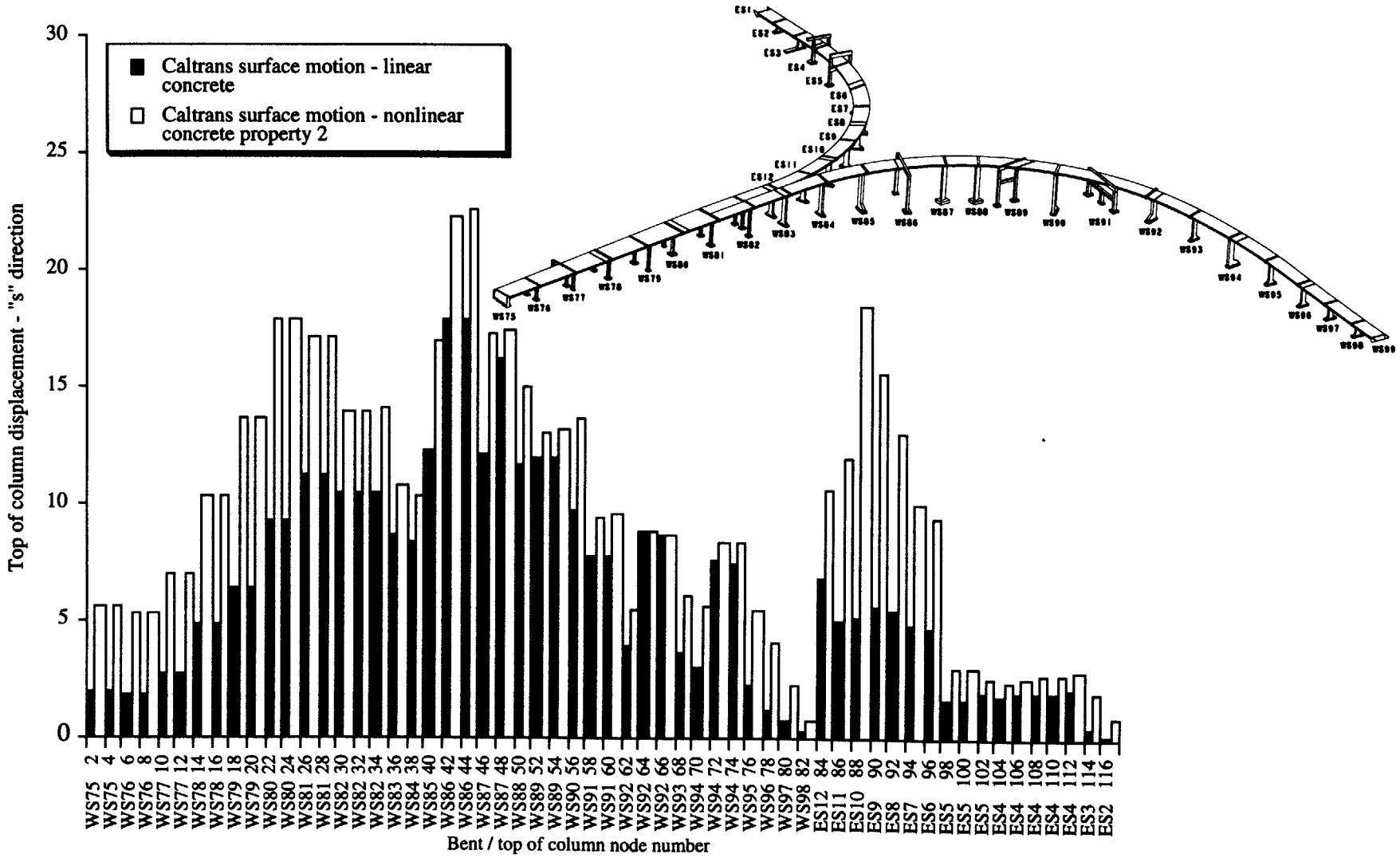

FIGURE 64. Top of column s displacements for the WS and ES lines.

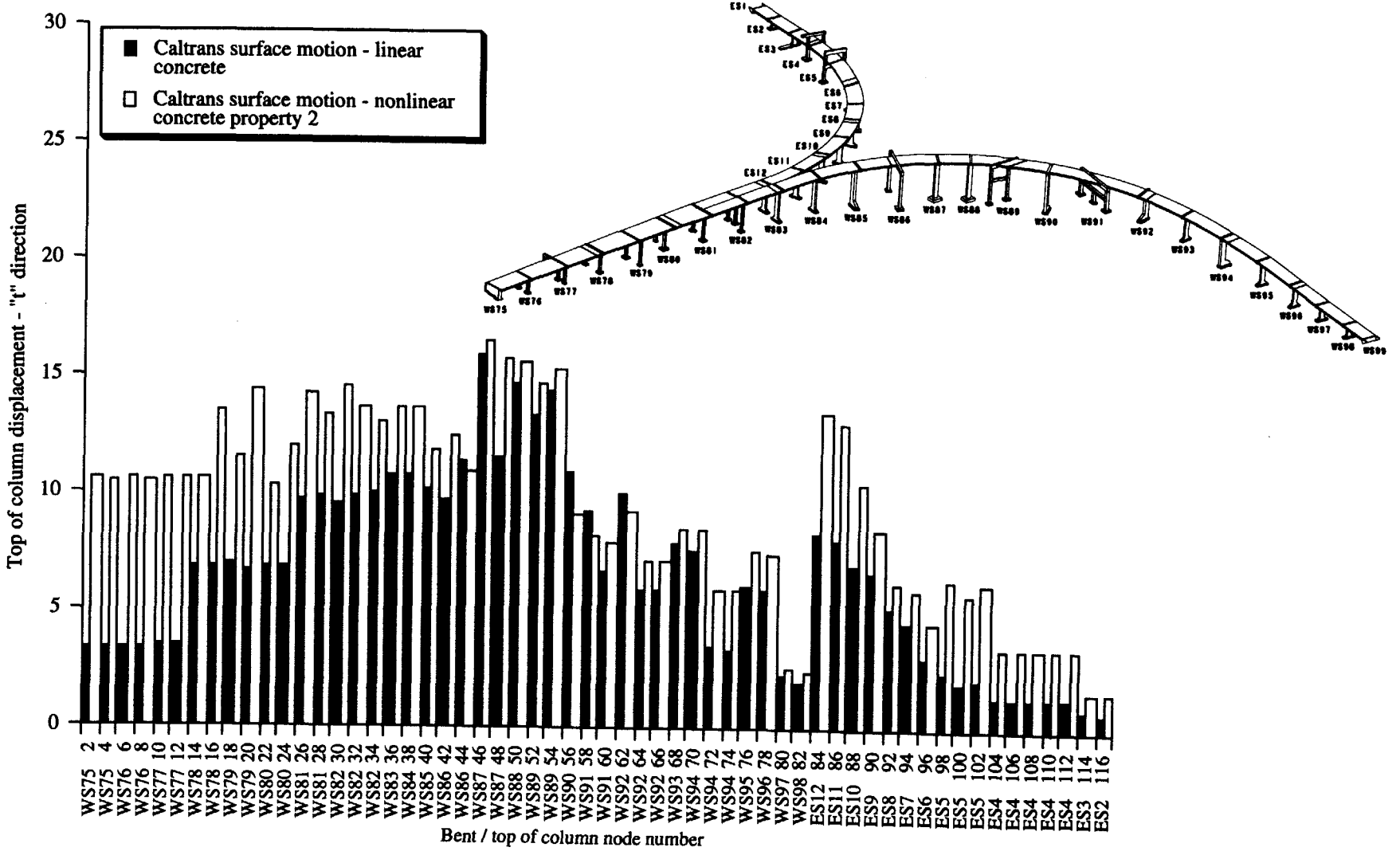

FIGURE 65. Top of column t displacements for the WS and ES lines.

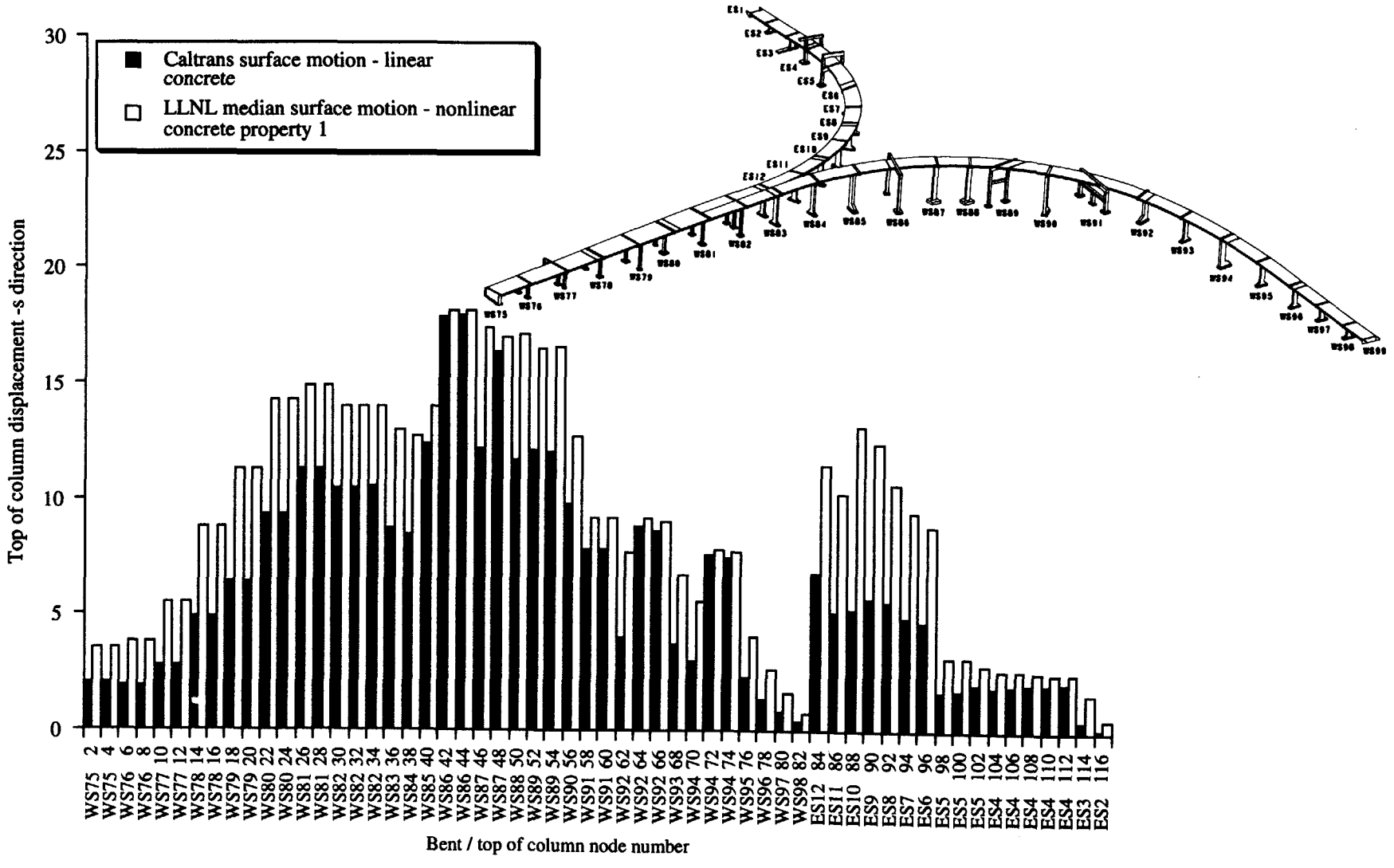

FIGURE 66. Top of column s displacements for the WS and ES lines.

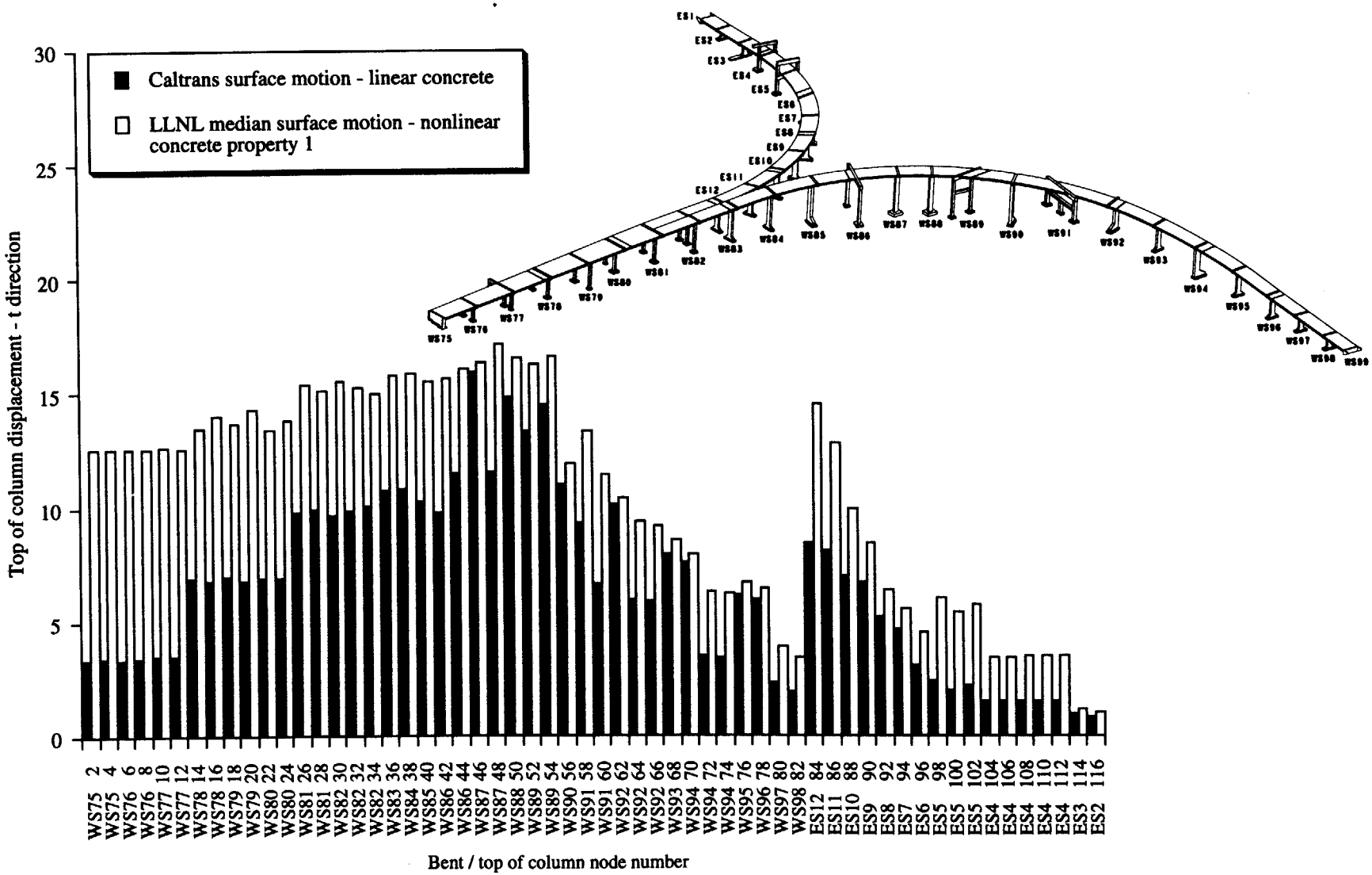

FIGURE 67. Top of column t displacements for the WS and ES lines.

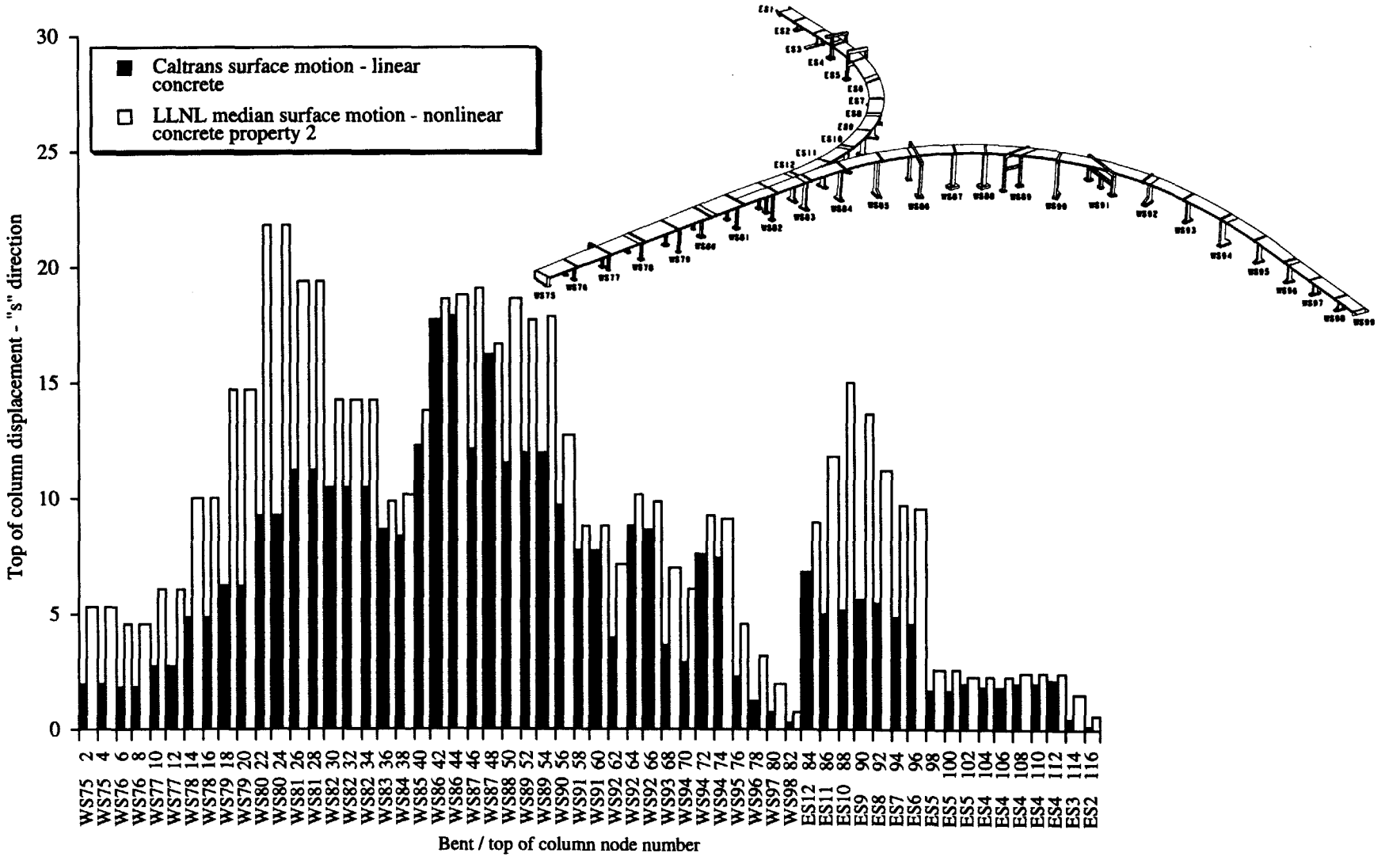

FIGURE 68. Top of column s displacements for the WS and ES lines.

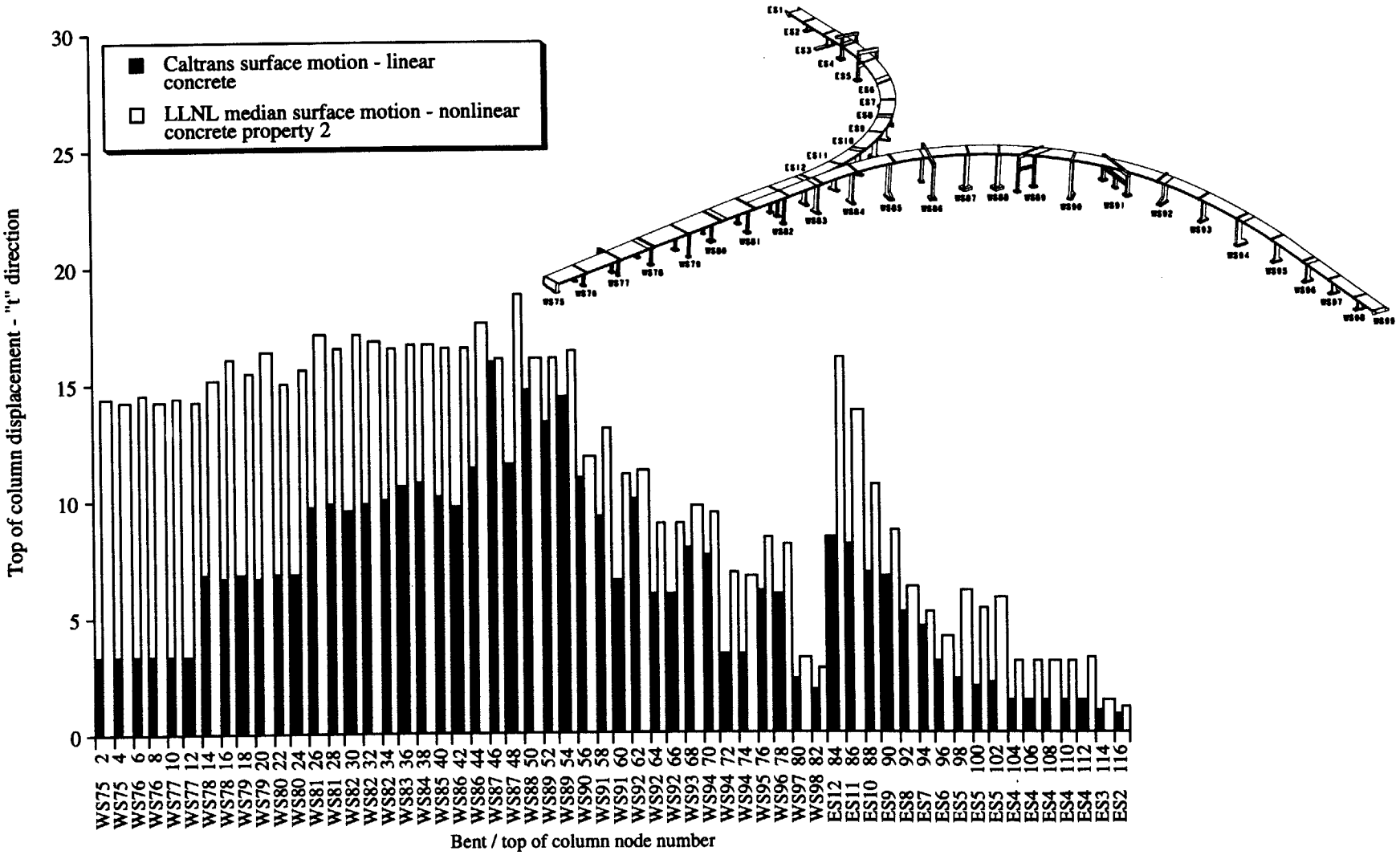

FIGURE 69. Top of column s displacements for the WS and ES lines.

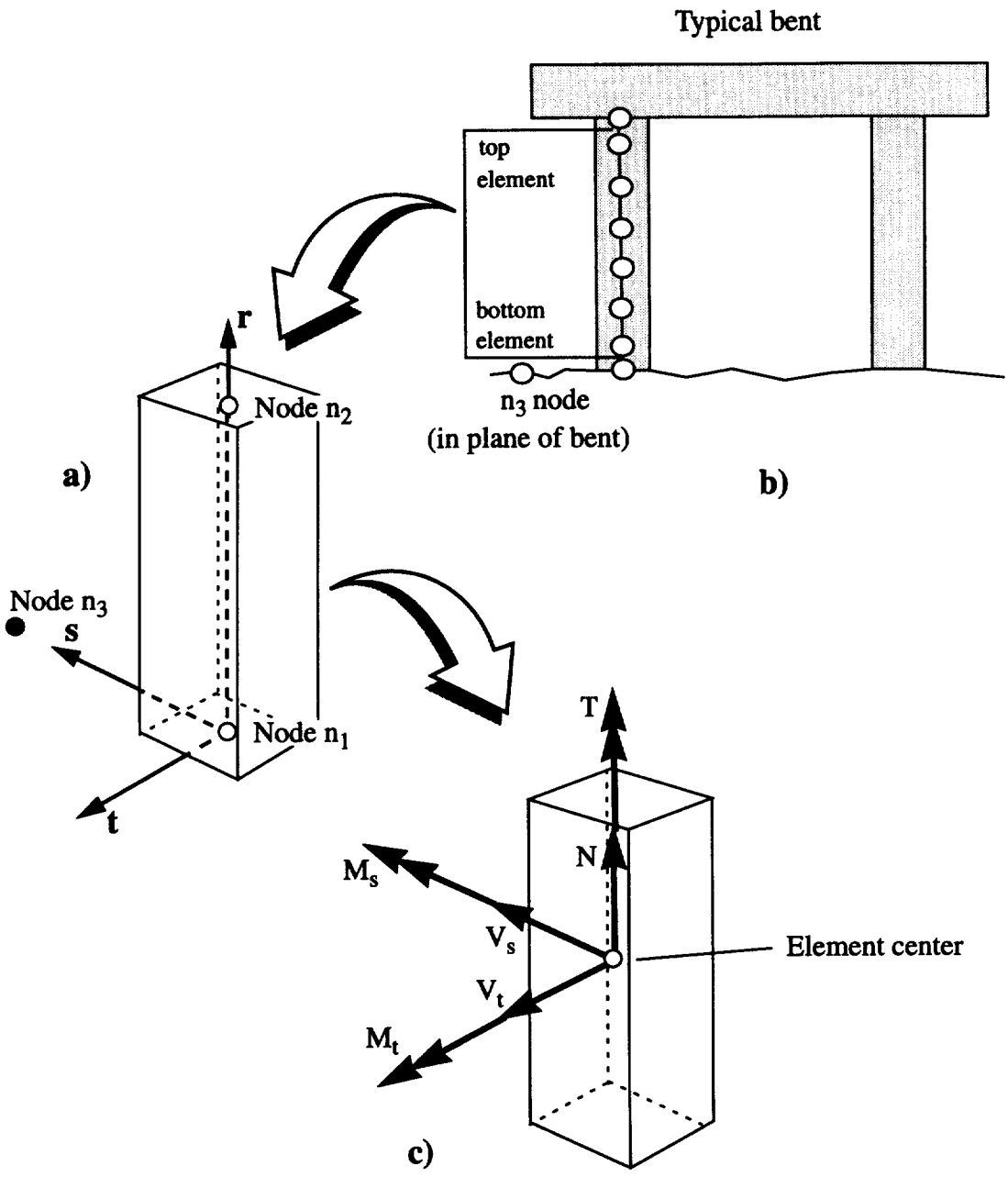

FIGURE 70. Column element orientation and local coordinate system. a) Element local coordinate system; b) orientation of elements in each bent model; c) Nike3d stress resultants at the element centroid.

TABLE 7. Top of column displacements (relative to free-field ground motion) for the M_w=7.25 Hayward fault earthquake: Caltrans surface motion, *NIKE3D* model with geometric nonlinearities and the nonlinear concrete model (property set #2).

Model node number	Bent number	Displacement demands		
		Column "t" direction (in)	Column "s" direction(in)	Vector resultant (in)
2	WS 75	1.0636E+01	5.6968E+00	1.0636E+01
4	WS 75	1.0531E+01	5.6984E+00	1.0532E+01
6	WS 76	1.0699E+01	5.4088E+00	1.0705E+01
8	WS 76	1.0569E+01	5.4112E+00	1.0579E+01
10	WS 77	1.0647E+01	7.0261E+00	1.0675E+01
12	WS 77	1.0599E+01	7.0292E+00	1.0630E+01
14	WS 78	1.0631E+01	1.0422E+01	1.0634E+01
16	WS 78	1.3540E+01	1.0425E+01	1.3542E+01
18	WS 79	1.1588E+01	1.3664E+01	1.4453E+01
20	WS 79	1.4419E+01	1.3662E+01	1.5806E+01
22	WS 80	1.0391E+01	1.7994E+01	1.8527E+01
24	WS 80	1.2093E+01	1.7999E+01	1.8802E+01
26	WS 81	1.4300E+01	1.7231E+01	1.8678E+01
28	WS 81	1.3370E+01	1.7237E+01	1.8378E+01
30	WS 82	1.4524E+01	1.4024E+01	1.6459E+01
32	WS 82	1.3749E+01	1.4043E+01	1.5781E+01
34	WS 82	1.3104E+01	1.4069E+01	1.5399E+01
36	WS 83	1.3619E+01	1.0822E+01	1.4810E+01
38	WS 84	1.3736E+01	1.0399E+01	1.5740E+01
40	WS 85	1.1860E+01	1.6966E+01	1.7818E+01
42	WS 86	1.2488E+01	2.2397E+01	2.2722E+01
44	WS 86	1.0990E+01	2.2682E+01	2.2683E+01
46	WS 87	1.6528E+01	1.7268E+01	2.1279E+01
48	WS 87	1.5806E+01	1.7553E+01	2.1098E+01
50	WS 88	1.5610E+01	1.5057E+01	1.9720E+01
52	WS 89	1.4715E+01	1.3157E+01	1.9124E+01
54	WS 89	1.5300E+01	1.3286E+01	1.9413E+01
56	WS 90	9.0882E+00	1.3653E+01	1.4257E+01
58	WS 91	8.1807E+00	9.3796E+00	9.8191E+00
60	WS 91	7.8799E+00	9.6367E+00	9.6750E+00
62	WS 92	9.2312E+00	5.5413E+00	9.2359E+00
64	WS 92c	7.2324E+00	8.8779E+00	9.2316E+00

TABLE 7. Top of column displacements (relative to free-field ground motion) for the M_w=7.25 Hayward fault earthquake: Caltrans surface motion, *NIKE3D* model with geometric nonlinearities and the nonlinear concrete model (property set #2).

Model node number	Bent number	Displacement demands		
		Column "t" direction (in)	Column "s" direction(in)	Vector resultant (in)
66	WS 92c	7.2246E+00	8.6440E+00	8.9855E+00
68	WS 93	8.5483E+00	6.1226E+00	8.5689E+00
70	WS 94	8.4632E+00	5.5853E+00	8.4661E+00
72	WS 94c	5.9824E+00	8.4438E+00	8.4834E+00
74	WS 94c	5.9141E+00	8.3833E+00	8.4083E+00
76	WS 95	7.5971E+00	5.4901E+00	7.6097E+00
78	WS 96	7.4032E+00	4.1263E+00	7.4108E+00
80	WS 97	2.6758E+00	2.2685E+00	2.6826E+00
82	WS 98	2.4160E+00	8.3789E-01	2.4297E+00
84	ES 12	1.3568E+01	1.0587E+01	1.3952E+01
86	ES 11	1.3093E+01	1.1951E+01	1.4901E+01
88	ES 10	1.0472E+01	1.8543E+01	1.9680E+01
90	ES 9	8.5595E+00	1.5648E+01	1.7048E+01
92	ES 8	6.1991E+00	1.3101E+01	1.4121E+01
94	ES 7	5.9048E+00	1.0124E+01	1.1209E+01
96	ES 6	4.6588E+00	9.3842E+00	9.6458E+00
98	ES 5	6.4746E+00	3.0552E+00	6.5013E+00
100	ES 5	5.8711E+00	3.0566E+00	5.9020E+00
102	ES 5	6.1885E+00	2.5688E+00	6.2834E+00
104	ES 4	3.5391E+00	2.4702E+00	4.1319E+00
106	ES 4	3.5498E+00	2.5908E+00	4.2273E+00
108	ES 4	3.5605E+00	2.7065E+00	4.3219E+00
110	ES 4	3.5713E+00	2.8242E+00	4.4209E+00
112	ES 4	3.5830E+00	2.9658E+00	4.5231E+00
114	ES 3	1.6688E+00	1.9725E+00	2.3548E+00
116	ES 2	1.6638E+00	8.9142E-01	1.7892E+00

TABLE 8. Column maximum stress resultants for the M_w = 7.25 Hayward fault earthquake: Caltrans surface motion, *NIKE3D* model with geometric nonlinearities and the nonlinear concrete model (property set #2).

	Element numbers	Maximum stress resultants					
Column description	bottom/ top	N (lb)	V_s (lb)	V_t (lb)	M_s (in-lb)	M_t (in-lb)	T (in-lb)
WS75 Companion Column 1	3	8.9629E+05	3.7589E+05	5.8497E+05	7.2755E+07	1.1586E+08	9.1744E+05
	9	8.2481E+05	3.4280E+05	5.7697E+05	2.0568E+06	3.4581E+06	1.8890E+02
WS75 Companion Column 2	10	9.3441E+05	3.6757E+05	5.7890E+05	7.4755E+07	1.1702E+08	9.0216E+05
	16	8.5423E+05	3.4876E+05	5.7624E+05	2.0886E+06	3.4545E+06	8.7339E+01
WS76 Column 1	37	1.2919E+06	2.3533E+05	2.6651E+05	1.4126E+06	1.5990E+06	9.7839E+01
	43	1.2495E+06	1.9436E+05	2.4211E+05	7.7003E+07	9.0726E+07	7.7595E+05
WS76 Column2	44	1.4920E+06	2.9368E+05	2.9149E+05	1.7528E+06	1.7445E+06	6.7648E+01
	50	1.3783E+06	2.3728E+05	2.4481E+05	9.9241E+07	9.7777E+07	8.5004E+05
WS77 Column 2	59	3.0330E+06	1.2205E+06	1.3614E+06	2.5861E+08	2.9368E+08	1.3495E+07
	65	3.0380E+06	1.1201E+06	1.3055E+06	2.5710E+08	2.9107E+08	1.3373E+07
WS77 Column 3	66	9.4184E+05	1.4119E+05	1.7981E+05	8.4717E+05	1.0816E+06	8.1735E+01
	72	8.8476E+05	9.9948E+04	1.8520E+05	5.0197E+07	4.0233E+07	2.6883E+05
WS78 Column 1	81	1.4578E+06	2.5899E+05	2.1010E+05	1.5584E+06	1.2606E+06	4.1626E+01
	87	1.3521E+06	2.2145E+05	3.3402E+05	1.1100E+08	8.8780E+07	6.4737E+05
WS78 Column 2	88	2.1938E+06	3.1790E+05	2.5750E+05	1.9074E+06	1.5447E+06	1.2211E+01
	94	2.0985E+06	2.4391E+05	2.6988E+05	1.3742E+08	1.0690E+08	7.5300E+05
WS79 Column 1	103	2.4774E+06	2.9282E+05	2.7819E+05	1.7568E+06	1.6688E+06	1.5541E+02
	109	2.3377E+06	2.3352E+05	2.4942E+05	1.5117E+08	1.0320E+08	1.1244E+06
WS79 Column 2	110	1.6429E+06	2.8706E+05	2.3342E+05	1.7222E+06	1.4006E+06	3.8402E+01
	116	1.4836E+06	2.2827E+05	2.4661E+05	1.4498E+08	8.4404E+07	9.9469E+05
WS80 Column 1	126	1.4176E+06	2.8576E+05	1.9492E+05	1.7151E+06	1.1692E+06	7.4993E+02
	132	1.2560E+06	2.2862E+05	2.4549E+05	1.3911E+08	5.9814E+07	8.1712E+05
WS80 Column 2	133	2.8054E+06	3.9005E+05	1.8793E+05	2.3468E+06	1.1278E+06	1.5688E+02
	139	2.5103E+06	3.6574E+05	2.9400E+05	2.1212E+08	7.7726E+07	1.7275E+06
WS81 Column 1	148	1.5717E+06	2.6323E+05	2.1619E+05	1.5762E+06	1.2968E+06	1.4770E+02
	154	1.4730E+06	2.1618E+05	2.3508E+05	1.4934E+08	8.7394E+07	1.3055E+06
WS81 Column 2	155	3.0184E+06	2.5318E+05	1.8908E+05	1.5186E+06	1.1347E+06	6.5185E+01
	161	2.7289E+06	2.3730E+05	2.5306E+05	1.4473E+08	8.5412E+07	8.6845E+05
WS82 Column 1	176	1.9008E+06	1.7060E+05	1.7680E+05	1.0238E+06	1.0608E+06	1.3364E+02
	182	1.6796E+06	1.9446E+05	2.3603E+05	8.2544E+07	5.9068E+07	4.8643E+05
WS82 Column 2	183	1.4084E+06	1.6001E+05	1.7785E+05	9.6010E+05	1.0638E+06	4.8258E+01
	189	1.1958E+06	1.6646E+05	1.8039E+05	7.4051E+07	5.8388E+07	4.2750E+05
WS82 Column 3	190	2.6961E+06	1.7822E+05	1.9236E+05	1.0528E+06	1.1385E+06	3.0091E+02
	196	2.4544E+06	1.5084E+05	2.2575E+05	9.6193E+07	5.1162E+07	2.8454E+05
WS83 Column 1	213	2.3145E+06	6.4468E+05	3.8763E+05	2.5435E+08	9.2540E+07	1.0347E+07
	219	1.5655E+06	5.5904E+05	3.9616E+05	2.2360E+08	7.6998E+07	9.7749E+06
WS84 Column 1	227	2.6160E+06	5.4877E+05	3.8459E+05	2.3432E+08	9.3360E+07	9.6477E+06
	233	1.6054E+06	4.2583E+05	3.0579E+05	1.7448E+08	8.1244E+07	8.6548E+06
WS85 Column 1	241	2.8983E+06	1.4629E+06	7.7961E+05	7.8949E+08	2.1787E+08	5.0353E+07
	247	1.4511E+06	1.2343E+06	4.9384E+05	6.0778E+08	1.8970E+08	4.8272E+07

TABLE 8. Column maximum stress resultants for the M_w = 7.25 Hayward fault earthquake: Caltrans surface motion, *NIKE3D* model with geometric nonlinearities and the nonlinear concrete model (property set #2).

	Element numbers	Maximum stress resultants					
Column description	bottom/ top	N (lb)	V_s (lb)	V_t (lb)	M_s (in-lb)	M_t (in-lb)	T (in-lb)
WS86 Column 1	255	1.0124E+07	7.8895E+05	6.0189E+05	1.4863E+08	9.1949E+07	2.0651E+05
	261	4.7418E+06	2.2184E+06	1.8655E+06	2.6762E+07	1.9536E+07	1.2950E+05
WS86 Column 2	262	2.0924E+06	4.1046E+05	3.4865E+05	2.1587E+08	1.0667E+08	1.1674E+06
	268	3.5133E+06	6.4954E+05	3.3778E+05	4.5121E+06	5.0957E+06	2.2516E+03
WS87 Column 1(new to left)	280	2.1074E+06	4.4995E+05	4.7383E+05	1.3515E+08	1.7799E+08	8.1230E+06
	286	1.8396E+06	3.8594E+05	2.7006E+05	1.7413E+08	1.3994E+08	8.3960E+06
WS87 Column 2	287	3.4047E+06	9.5161E+05	4.2995E+05	4.1184E+08	1.7041E+08	2.1826E+07
	293	2.7848E+06	7.1242E+05	2.6400E+05	3.6209E+08	1.5090E+08	2.2374E+07
WS88 Column 1	302	2.3738E+06	9.0786E+05	4.7538E+05	4.7242E+08	1.4685E+08	2.2214E+07
	308	1.6910E+06	6.8982E+05	3.2861E+05	4.0381E+08	1.3960E+08	2.2683E+07
WS89 Column 1	316	2.4427E+06	2.2800E+05	1.8769E+05	8.0836E+07	5.9492E+07	2.5340E+05
	328	1.9638E+06	1.3715E+05	1.2755E+05	8.2284E+05	7.6527E+05	9.0518E+01
WS89 Column 2	329	1.0412E+06	1.6067E+05	3.0934E+05	6.0276E+07	5.0680E+07	1.8991E+05
	341	7.5361E+05	1.1103E+05	1.6899E+05	2.4673E+06	3.7366E+06	6.2305E+02
WS90 Column 1	351	2.7453E+06	1.4329E+06	5.8448E+05	7.4455E+08	1.8864E+08	3.6842E+07
	357	1.4781E+06	9.7442E+05	4.5895E+05	5.1473E+08	1.6680E+08	3.5031E+07
WS91 Column 1	365	1.9856E+06	5.9548E+05	4.6649E+05	2.7325E+08	2.6645E+08	4.1044E+05
	377	1.3252E+06	3.6273E+05	3.9426E+05	2.1763E+06	2.3655E+06	1.3172E+02
WS91 Column 2	378	1.8596E+06	6.6297E+05	5.1323E+05	2.9464E+08	2.4875E+08	6.4594E+05
	390	1.1198E+06	5.0085E+05	3.7405E+05	3.0052E+06	5.2480E+06	2.9810E+02
WS92 Column 1	401	2.7321E+06	1.6040E+06	5.4327E+05	6.8770E+08	2.0553E+07	6.4069E+07
	407	1.9764E+06	1.3652E+06	5.0866E+05	4.5400E+08	1.9974E+08	6.3967E+07
WS92 Companion Column 1	415	2.2332E+06	4.1539E+05	2.9903E+05	1.4222E+08	1.1685E+08	1.0191E+07
	421	1.9406E+06	3.3876E+05	2.7818E+05	1.3672E+08	1.3956E+07	1.0110E+07
WS92 Companion Column 2	422	3.2667E+06	4.6807E+05	2.6378E+05	1.5097E+08	1.3560E+08	1.0332E+07
	428	2.9965E+06	3.3105E+05	2.7187E+05	1.3542E+08	1.5211E+07	1.0341E+07
WS93 Column 1	435	2.1940E+06	6.8982E+05	4.5845E+05	2.4733E+08	8.6552E+07	4.6315E+06
	441	1.8178E+06	5.1401E+05	3.5472E+05	1.7301E+08	8.9111E+07	4.7058E+06
WS94 Column 1	449	2.6790E+06	1.2278E+06	5.4415E+05	5.2776E+08	2.0736E+07	1.5656E+07
	455	1.8374E+06	9.2714E+05	5.0472E+05	3.1302E+08	1.5408E+08	1.5521E+07
WS94 Companion Column 1	463	4.4002E+06	4.2366E+05	2.8265E+05	1.5026E+08	1.2409E+08	3.6652E+06
	469	3.9526E+06	3.0163E+05	3.3940E+05	1.1011E+08	1.5962E+07	3.6891E+06
WS94 Companion Column 2	470	1.7942E+06	3.7854E+05	3.4778E+05	1.3419E+08	1.2973E+08	3.7461E+06
	476	1.8525E+06	3.0138E+05	2.7532E+05	1.1538E+08	1.4607E+07	3.7656E+06
WS95 Column 1	484	2.7328E+06	6.7563E+05	5.0059E+05	2.3425E+08	9..625E+07	3.8231E+06
	490	1.7888E+06	5.3525E+05	6.2876E+05	1.6577E+08	9.3687E+07	3.3428E+06
WS96 Column 1	498	4.8312E+06	7.1389E+05	7.1014E+05	2.1355E+08	9.3045E+07	4.9784E+06
	504	3.9286E+06	5.4115E+05	8.2587E+05	1.5269E+08	8.9423E+07	4.9663E+06
WS97 Column 1	512	7.0329E+06	6.0336E+05	5.6408E+05	1.6213E+08	6.4877E+07	4.4426E+06
	518	1.6379E+07	5.7131E+05	6.1634E+05	2.1317E+08	8.2460E+07	4.2607E+06

TABLE 8. Column maximum stress resultants for the M_w = 7.25 Hayward fault earthquake: Caltrans surface motion, *NIKE3D* model with geometric nonlinearities and the nonlinear concrete model (property set #2).

	Element numbers	Maximum stress resultants					
Column description	bottom/ top	N (lb)	V_s (lb)	V_t (lb)	M_s (in-lb)	M_t (in-lb)	T (in-lb)
WS98 Column 1	526	1.3729E+07	3.5120E+05	8.0774E+05	1.7260E+08	1.7147E+08	3.5949E+06
	532	1.9391E+07	5.7772E+05	1.1379E+06	1.3430E+08	1.0062E+08	3.5843E+06
ES12 Column 1	1030	2.0205E+06	7.2669E+05	3.8155E+05	2.6656E+08	8.9795E+07	2.1193E+07
	1036	1.4860E+06	6.3440E+05	4.2517E+05	2.2631E+08	8.1797E+07	2.1136E+07
ES11 Column 1	1044	2.7158E+06	7.0462E+05	4.7189E+05	2.1752E+08	7.7422E+07	1.3701E+07
	1050	1.7952E+06	5.4528E+05	3.5940E+05	1.7997E+08	7.4451E+07	1.4161E+07
ES10 Column 1	1058	4.3743E+06	8.8104E+05	5.9587E+05	2.3401E+08	7.0143E+07	8.5051E+06
	1064	3.9872E+06	6.5676E+05	4.5596E+05	2.7767E+08	6.5205E+07	9.1897E+06
ES9 Column 1	1072	2.5066E+06	9.0479E+05	3.8156E+05	2.2357E+08	8.0013E+07	1.0416E+07
	1078	1.9812E+06	5.9546E+05	5.8073E+05	1.8288E+08	6.7903E+07	1.0771E+07
ES8 Column 1	1086	1.8840E+06	8.2949E+05	4.0405E+05	2.6389E+08	7.6296E+07	1.2488E+07
	1092	1.4560E+06	6.4568E+05	4.4058E+05	2.1696E+08	7.4548E+07	1.3382E+07
ES7 Column 1	1100	2.0948E+06	1.6210E+06	4.2360E+05	5.9260E+08	8.2413E+06	3.7160E+07
	1106	1.4841E+06	1.4124E+06	2.9687E+05	4.5333E+08	1.2130E+08	3.7167E+07
ES6 Column 1	1114	2.9330E+06	1.4082E+06	8.1499E+05	4.1332E+08	1.9639E+08	2.1707E+07
	1120	2.1529E+06	1.2352E+06	5.6442E+05	4.4104E+08	1.5924E+08	2.1654E+07
ES5 Column 1a (Yoke)	1128	8.9889E+05	3.6903E+05	2.8359E+05	6.7792E+07	5.1127E+07	2.7988E+06
	1134	7.6960E+05	3.2535E+05	2.2029E+05	6.8268E+07	5.0267E+07	2.7634E+06
ES5 Column 1b (Yoke)	1135	1.0939E+06	4.0750E+05	3.9020E+05	7.4845E+07	5.9791E+07	2.7954E+06
	1141	9.8315E+05	3.4320E+05	3.2632E+05	8.0718E+07	5.2451E+07	2.7867E+06
ES5 Column 2	1142	2.2447E+06	1.1127E+06	5.6517E+05	2.1636E+08	9.4647E+07	9.5313E+06
	1148	2.0544E+06	1.0430E+06	4.7010E+05	2.2437E+08	1.0221E+08	9.5219E+06
ES4 Column 1	1167	5.3027E+05	1.1430E+05	9.9125E+04	1.6354E+07	1.2462E+07	4.4378E+05
	1173	4.9739E+05	1.0647E+05	9.8966E+04	1.6285E+07	1.1617E+07	4.3892E+05
ES4 Column 2	1174	3.9480E+05	1.0441E+05	9.0911E+04	1.4570E+07	1.1724E+07	4.3696E+05
	1180	3.5279E+05	9.5325E+04	8.2873E+04	1.4610E+07	1.1550E+07	4.2759E+05
ES4 Column 3	1181	3.0550E+05	1.0506E+05	9.9766E+04	1.4849E+07	1.2886E+07	4.3203E+05
	1187	2.6588E+05	9.5633E+04	7.7130E+04	1.4292E+07	1.3057E+07	4.2035E+05
ES4 Column 4	1188	4.4294E+05	1.1363E+05	1.0479E+05	1.5545E+07	1.4221E+07	4.2662E+05
	1194	4.0696E+05	9.9253E+04	8.4748E+04	1.5446E+07	1.4281E+07	4.1532E+05
ES4 Column 5	1195	5.8751E+05	1.1793E+05	1.1744E+05	1.6546E+07	1.5826E+07	4.2168E+05
	1201	5.4576E+05	1.0477E+05	9.5123E+04	1.6869E+07	1.6198E+07	4.0593E+05
ES3 Column 1	1213	1.6292E+06	1.0185E+06	3.5344E+05	1.6738E+08	5.5285E+07	6.9291E+06
	1219	1.3514E+06	9.4638E+05	2.9298E+05	1.4099E+08	5.1471E+07	6.8586E+06
ES2 Column 1	1227	9.9198E+06	6.7809E+05	4.9053E+05	1.1401E+08	6.0417E+07	5.5970E+06
	1233	1.0111E+07	5.8097E+05	4.3491E+05	8.2048E+07	5.2304E+07	5.6149E+06

TABLE 9. Top of column displacements (relative to free-field ground motion) for the M_w=7.25 Hayward fault earthquake: LLNL surface motion, *NIKE3D* model with geometric nonlinearities and the nonlinear concrete model (property set #2).

Model node number	Bent number	Displacement demands	
		Column "t" direction (in)	Column "s" direction(in)
2	WS 75	14.465	5.3755
4	WS 75	14.266	5.3727
6	WS 76	14.561	4.6151
8	WS 76	14.299	4.6170
10	WS 77	14.451	6.1850
12	WS 77	14.268	6.1884
14	WS 78	15.168	10.072
16	WS 78	16.060	10.079
18	WS 79	15.482	14.701
20	WS 79	16.402	14.708
22	WS 80	15.050	21.819
24	WS 80	15.674	21.820
26	WS 81	17.132	19.431
28	WS 81	16.625	19.435
30	WS 82	17.175	14.324
32	WS 82	16.828	14.341
34	WS 82	16.517	14.367
36	WS 83	16.738	9.9515
38	WS 84	16.804	10.161
40	WS 85	16.591	13.887
42	WS 86	16.646	18.729
44	WS 86	17.575	18.889
46	WS 87	16.134	19.146
48	WS 87	18.816	16.743
50	WS 88	16.207	18.721
52	WS 89	16.170	17.865
54	WS 89	16.370	17.921
56	WS 90	11.906	12.864
58	WS 91	13.156	8.8872
60	WS 91	11.114	8.8999
62	WS 92	11.307	7.2438
64	WS 92c	9.0215	10.260
66	WS 92c	8.9785	9.9731

TABLE 9. Top of column displacements (relative to free-field ground motion) for the M_w=7.25 Hayward fault earthquake: LLNL surface motion, *NIKE3D* model with geometric nonlinearities and the nonlinear concrete model (property set #2).

Model node number	Bent number	Displacement demands	
		Column "t" direction (in)	Column "s" direction(in)
68	WS 93	9.7319	6.9775
70	WS 94	9.4456	6.1278
72	WS 94c	6.8145	9.3418
74	WS 94c	6.7441	9.1943
76	WS 95	8.4618	4.5918
78	WS 96	8.1674	3.1824
80	WS 97	3.2997	2.0074
82	WS 98	2.8525	0.87305
84	ES 12	16.102	8.9774
86	ES 11	13.810	11.900
88	ES 10	10.722	15.092
90	ES 9	8.6418	13.650
92	ES 8	6.2175	11.269
94	ES 7	5.2702	9.8404
96	ES 6	4.2175	9.5408
98	ES 5	6.0957	2.6235
100	ES 5	5.4375	2.6274
102	ES 5	5.7959	2.3945
104	ES 4	3.1445	2.3833
106	ES 4	3.1563	2.4146
108	ES 4	3.1670	2.4448
110	ES 4	3.1777	2.4761
112	ES 4	3.1885	2.5083
114	ES 3	1.3582	1.5343
116	ES 2	1.1829	0.63207

4.1.5 Capacities and demand/capacity ratios

In order to provide a basis for comparison of their own capacity determinations, Caltrans requested that LLNL perform capacity calculations for three selected bents of the structure. The bents which Caltrans requested capacity information on included ES 4, the WS 94 companion bent and WS 96 (see Fig. 71). A simple monotonic push-over analysis was performed in order to determine the nonlinear response of each bent in the longitudinal and transverse directions. Per Caltrans' request, the push over computations included the displacements due to foundation flexibility.

The transverse and longitudinal responses of the three bents are shown in Fig. 72 through Fig. 74. For each bent, displacements were imposed at the top of the bent as indicated in Fig. 71, and the shear force at the top of a selected column was plotted as a function of transverse displacement. On each plot, displacement ductilities are labeled and, where applicable, the displacement at first concrete crush is noted. Concrete crush is identified when the concrete compressive strain reaches .005 at any point in the column for poorly confined concrete and at a strain of .015 for well confined concrete [35].

Using jacketed column tests performed at UC San Diego as general guidance, significant deterioration of stiffness might be expected when displacement ductilities reach the level of six or seven. Thus a displacement ductility of six was assumed as an upper bound capacity for well confined columns, unless of course concrete crushing sets in prior to achieving this level of displacement ductility.

The allowable ductilities for the columns in each bent are indicated with bold numbers in Fig. 72 to Fig. 74. For the new columns in the ES 4 bent and the WS 94 companion bent, the allowable displacements are controlled by concrete crushing. The grade 60 reinforcing steel in the newer columns leads to greater compression demands in the concrete and concrete compression failure becomes more critical. The retrofit WS 96 column does not experience concrete crushing prior to achieving a displacement ductility of six.

It must be noted that assessing concrete column capacities with a simple push over test has some serious limitations. First, the columns undergo significant biaxial behavior when the structure is subjected to earthquake ground motions. The interaction between directional responses, which will tend to superpose in an additive fashion in some quadrant of the column, is not addressed with uniaxial capacity information. Second, the boundary conditions which exist at the bottom and top of an actual bridge column are a function of the displacements and deformations of the entire frame to which the given column is attached and the curvature of the columns obtained in a simple push over test may not be representative of the curvature distribution in the actual bridge column. This would be particularly true for the single column bents and multiple column bents in the longitudinal direction because the rest of the frame will provide rotation restraint at the top of these columns, and this is not accounted for in the simple push over computations.

With these caveats in mind, a rough, first order check of demand to capacity can be made for these selected columns. Figure 75 and Fig. 76 show the column capacities estimated

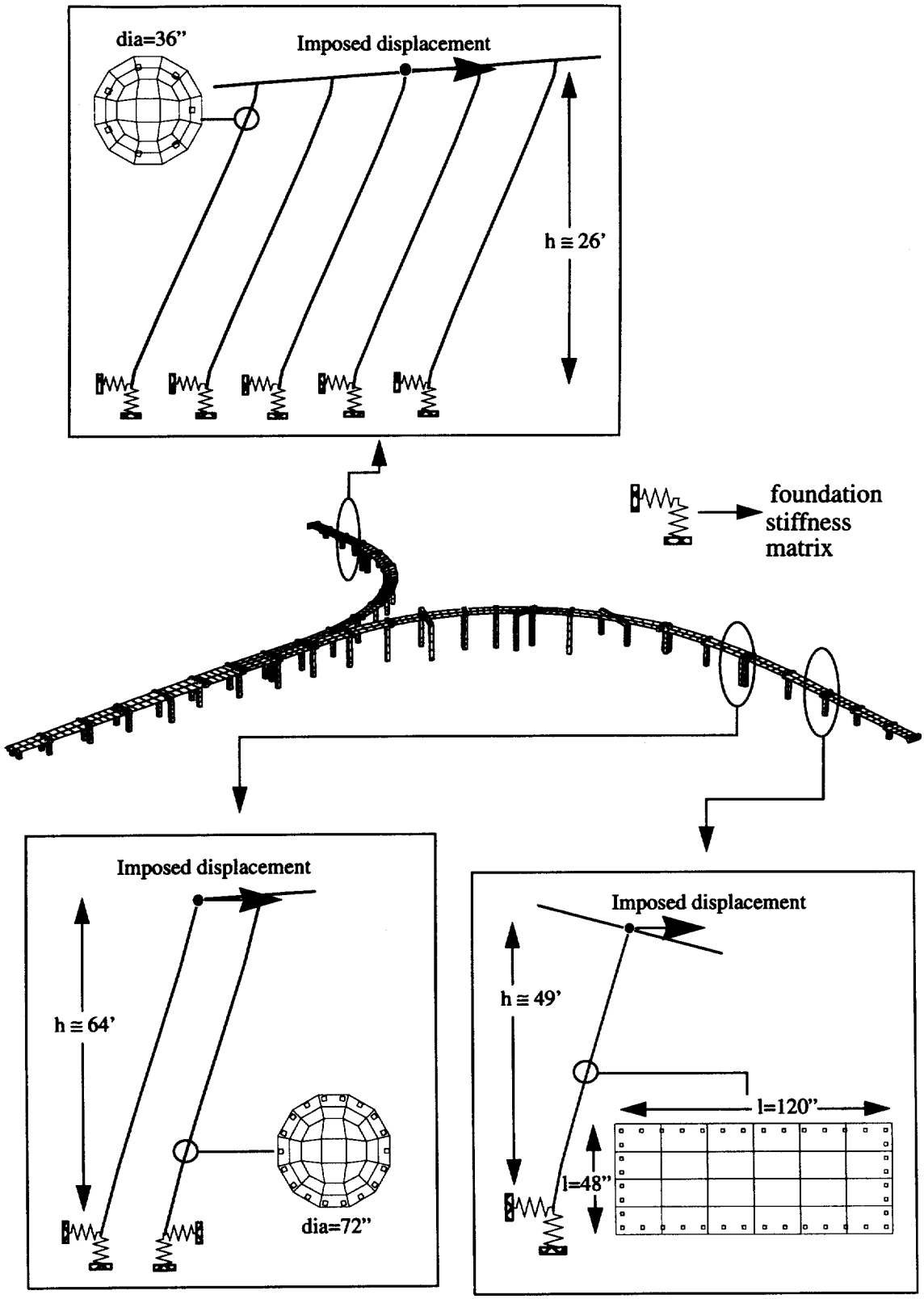

FIGURE 71. Capacity evaluation models for bents ES4, WS94 (companion) and WS96.

from the simple push over calculations compared to the column demands. For the selected columns the capacities exceed demands by a good margin.

In an attempt to provide a more rational evaluation of concrete capacity and demand estimates, a post processing procedure was developed to scan all of the concrete compressive strains in each column of the WS and ES lines at each instant of time throughout the earthquake response. The search was made to determine if concrete crushing was occurring in any of the columns. In the well confined portion of the retrofit columns, the allowable concrete compressive strain was taken as .015, in the poorly confined unretrofit columns the allowable compressive strain was taken as .005 and in the new concrete columns and drilled shafts the compressive strain was taken as .015. It is noted that inspection of the actual column strains from the global model response computations fully accounts for biaxial effects on concrete strains and the appropriate column boundary conditions are represented at each instant of time.

A plot of the ratio of maximum concrete compressive strain to the allowable concrete compressive strain is shown in Fig. 77 for the Caltrans ground motion hazard and in Fig. 78 for the LLNL ground motion response. The columns for which demand exceeds capacity are highlighted with the striped bar. Both ground motions indicated problems in the ES line near the ES line to WS line juncture. In particular, the single columns bents ES 9, ES 10 and ES 12 exhibit potential failure in the top portion of the columns. Both ground motion sets also indicated problems in Frame #1 at the very trunk of the structure.

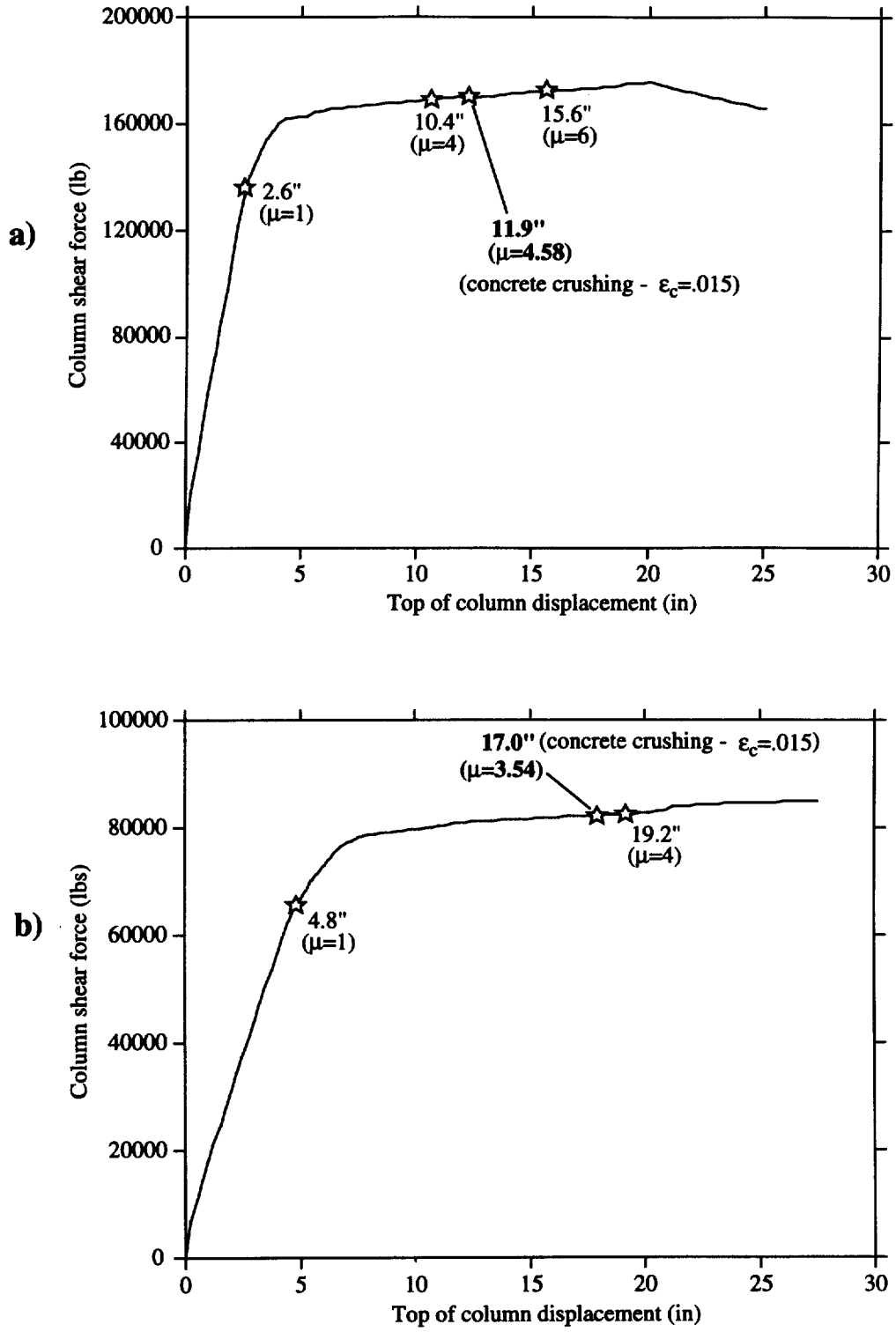

FIGURE 72. Bent ES4 column shear-displacement. a) Transverse direction; b) longitudinal direction.

a)

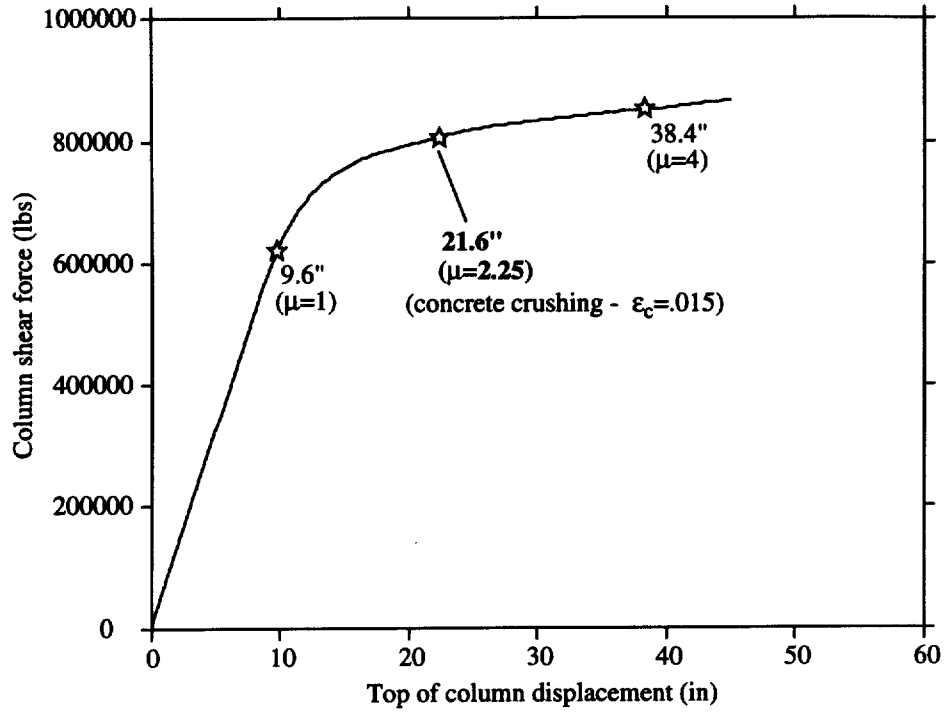

b)

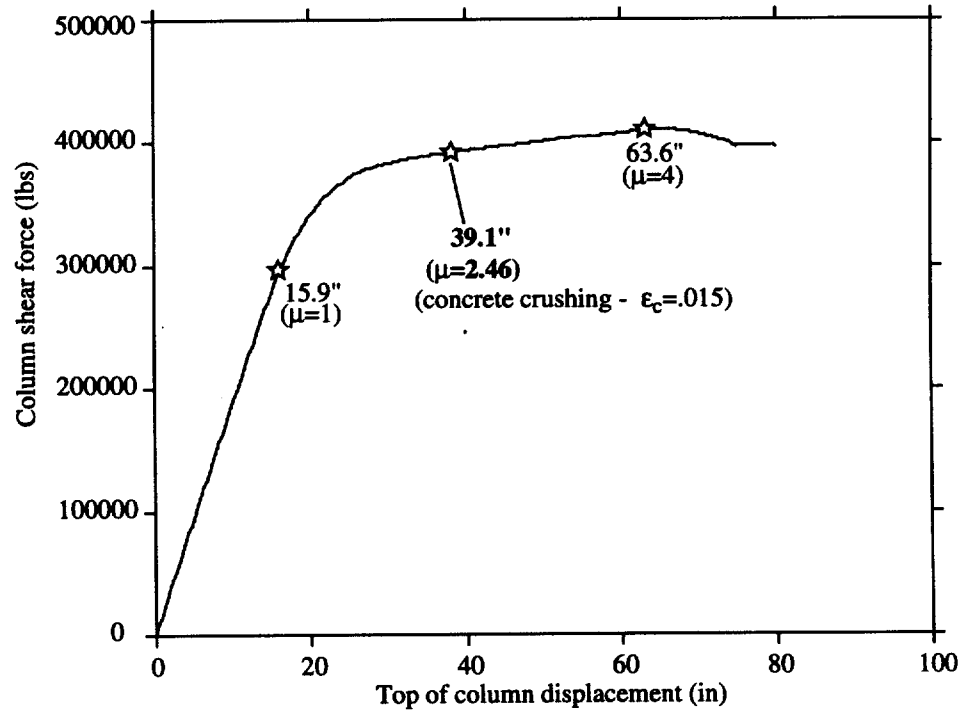

FIGURE 73. Bent WS94 (companion) column shear-displacement. a) Transverse direction; b) longitudinal direction.

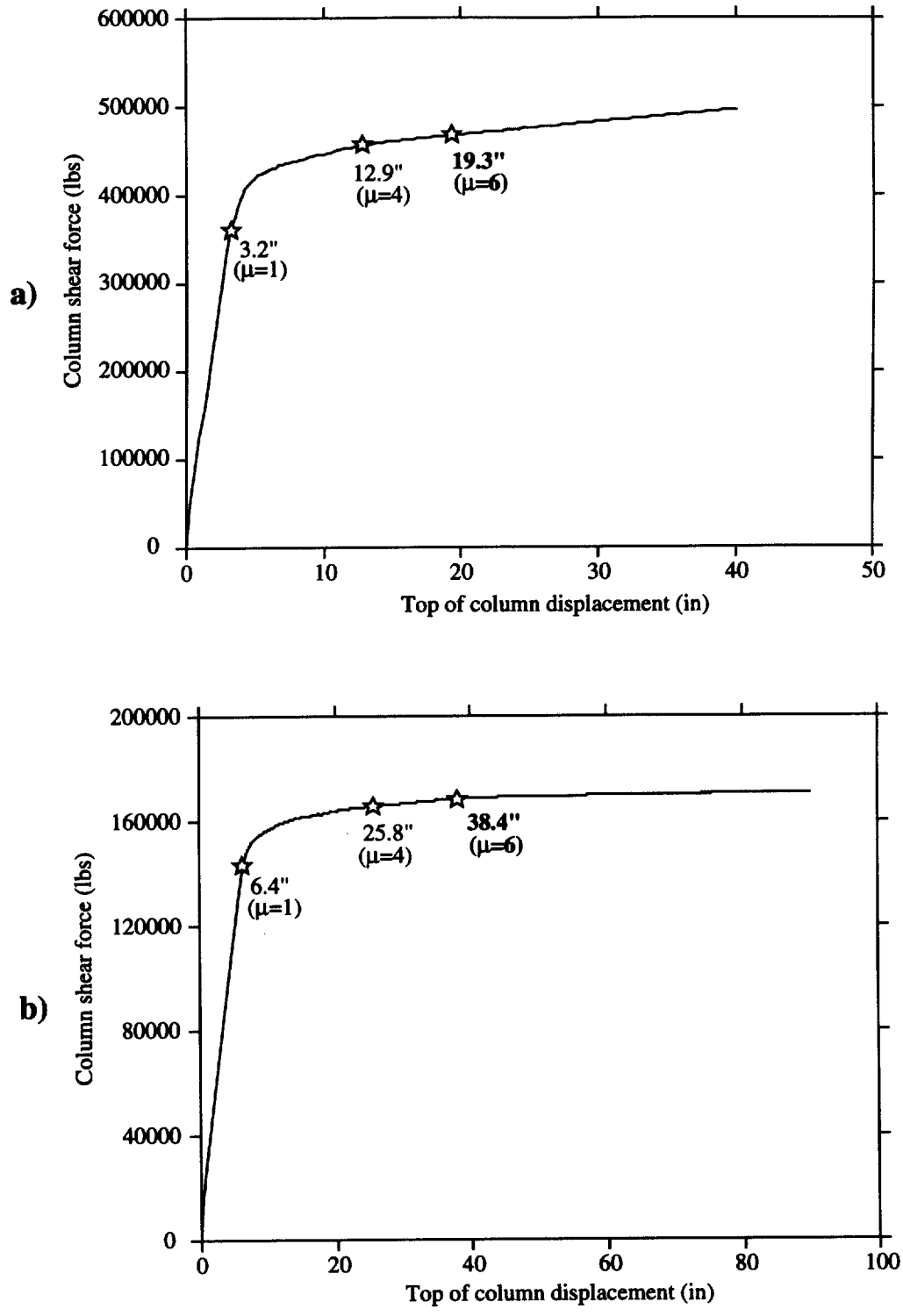

FIGURE 74. Bent WS96 (companion) column shear-displacement. a) Transverse direction; b) longitudinal direction.

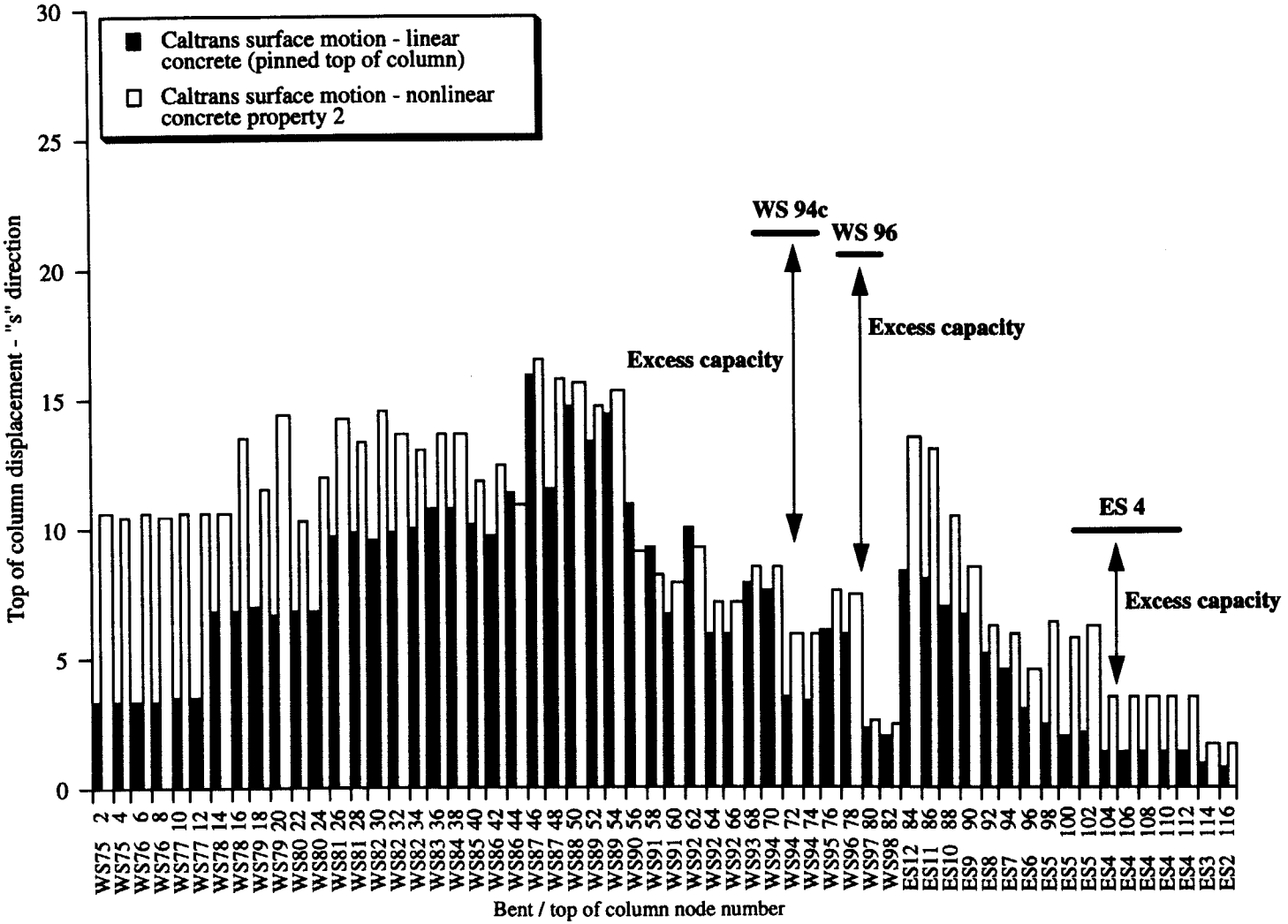

FIGURE 75. Displacement demands and capacities for selected bents (transverse direction).

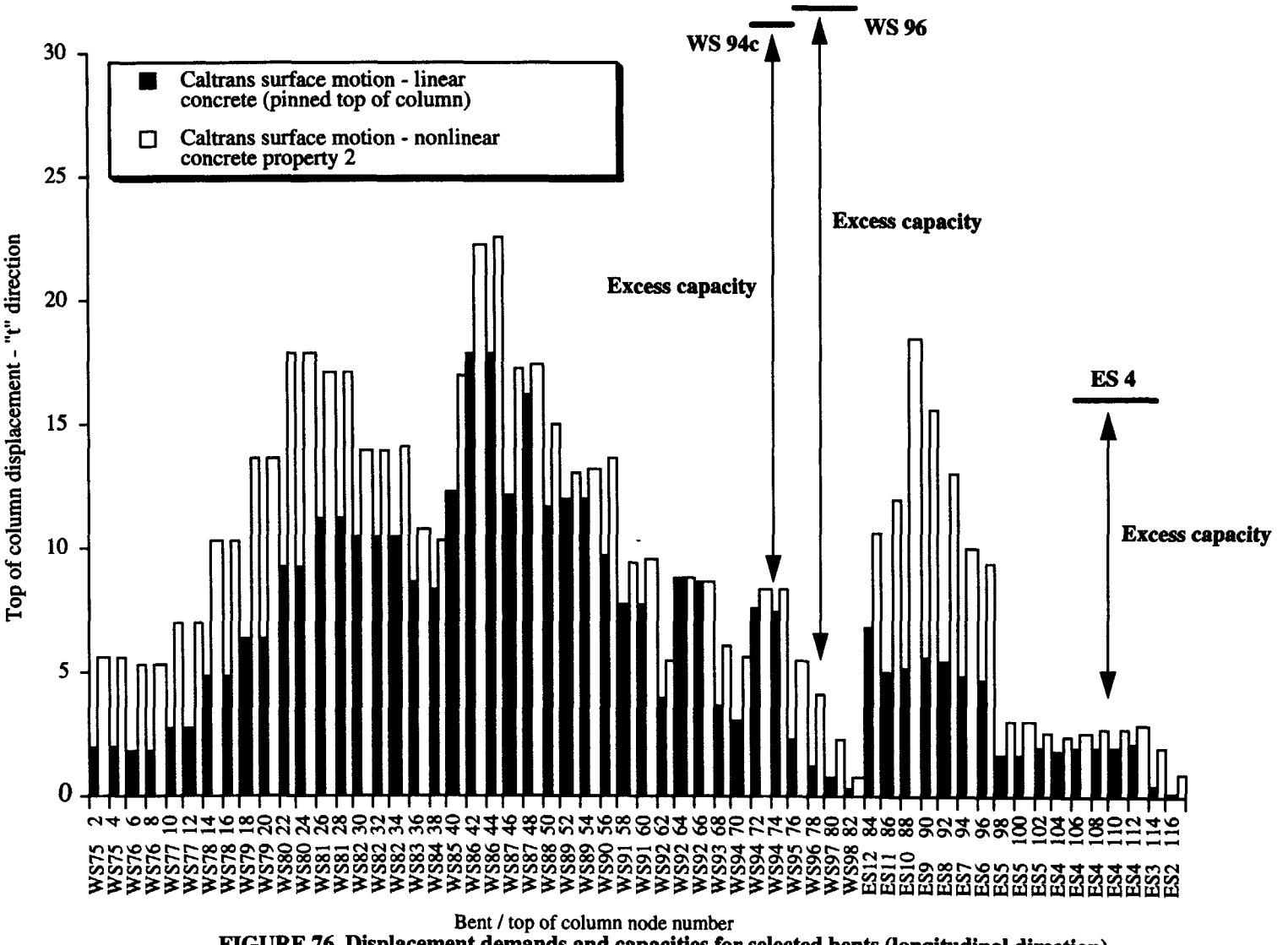

FIGURE 76. Displacement demands and capacities for selected bents (longitudinal direction).

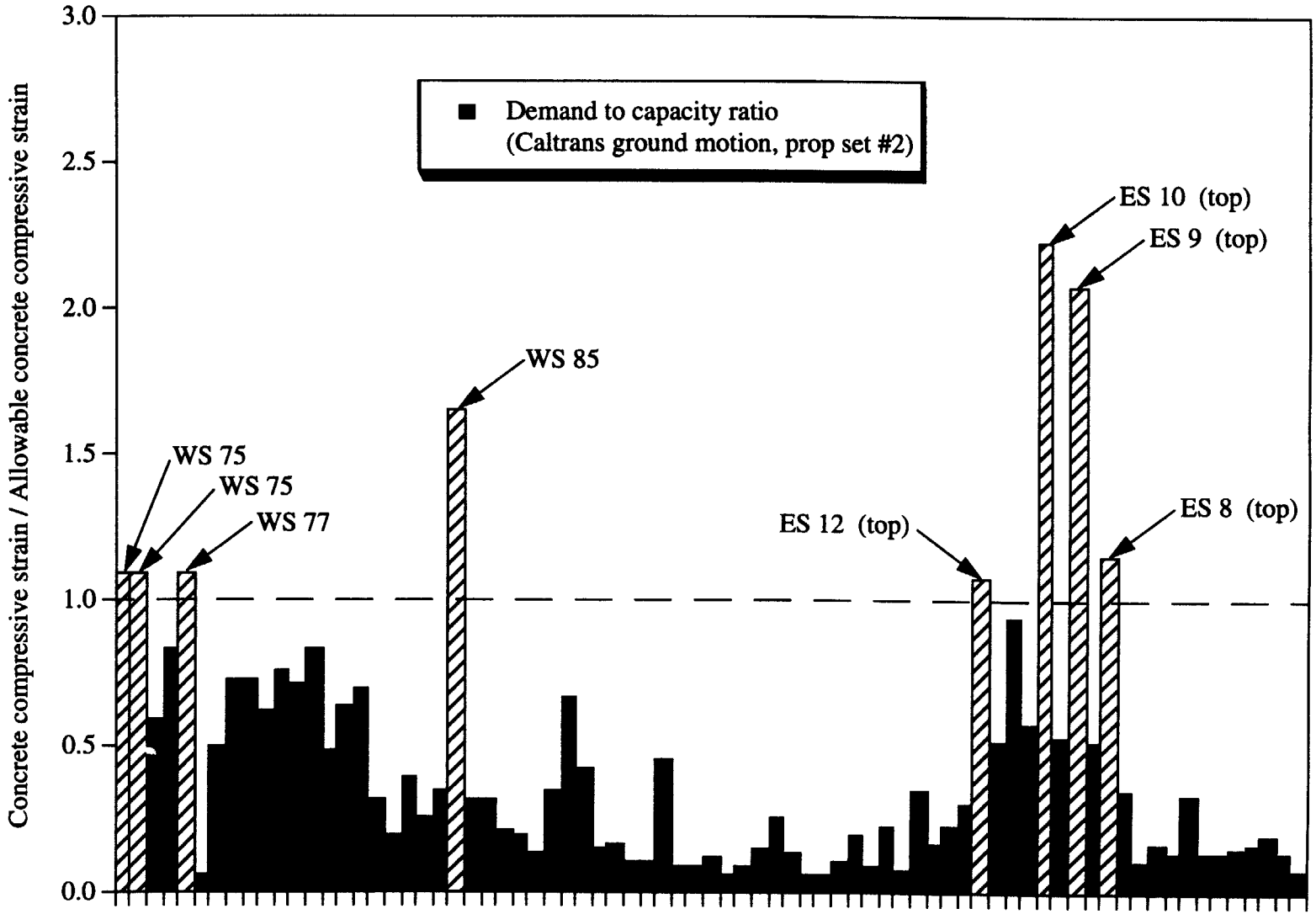

FIGURE 77. Demand to capacity ratio for concrete compressive strains (Caltrans ground motion)

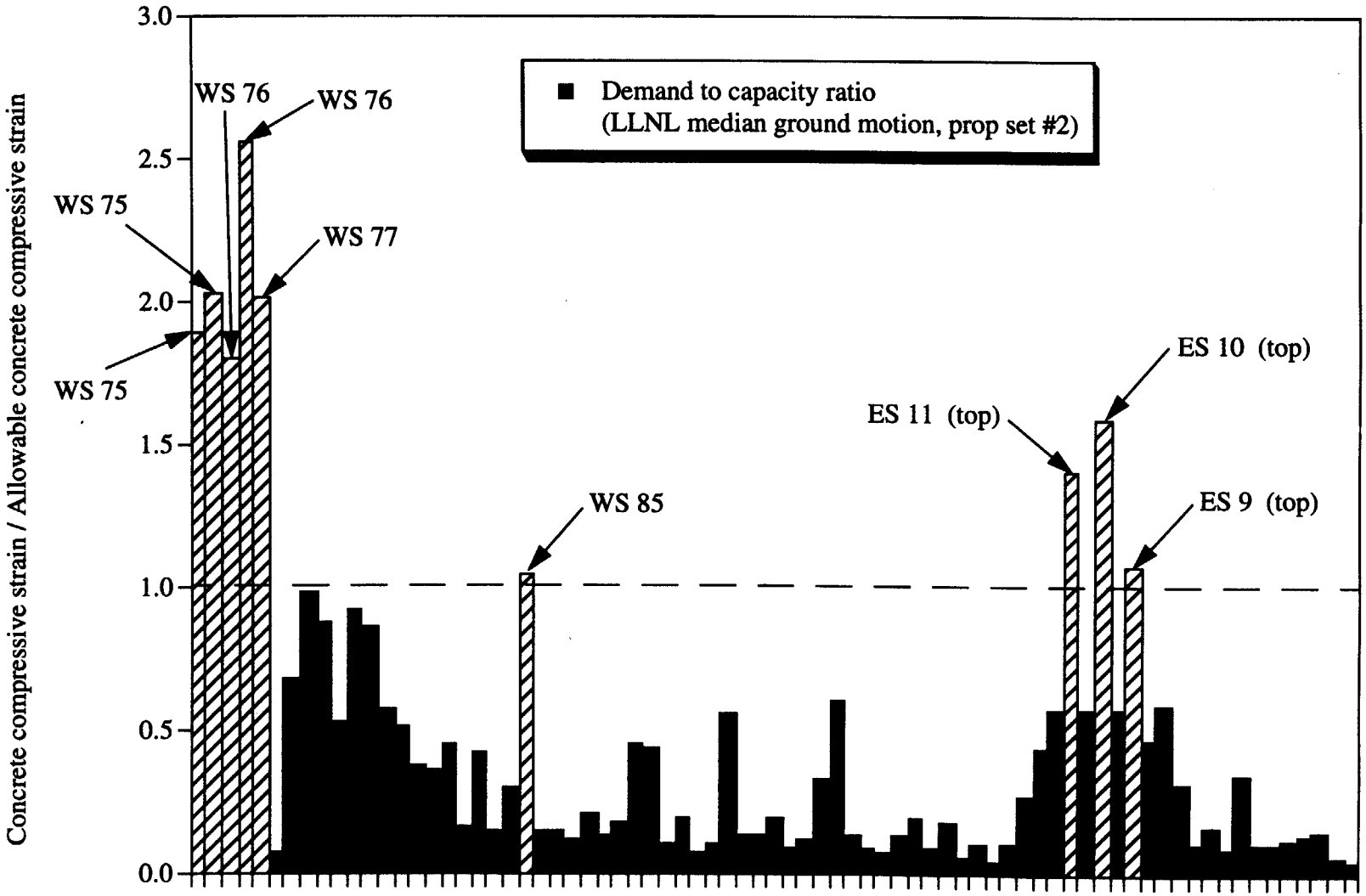

FIGURE 78. Demand to capacity ratio for concrete compressive strains (LLNL ground motion)

5.0 Summary of results and observations

A seismic response study has been completed for the ES and WS lines of the 24/580/980 interchange in Oakland California. As stipulated by Caltrans, the LLNL work focused on the estimation of the structural demands which would be placed on this structure as a result of a Hayward Fault earthquake. As requested by Caltrans, the fundamental measure of structural demands was expressed in terms of maximum displacements at the top of each column of the structure. The displacement demands computed using both Caltrans and LLNL median surface ground motions are summarized in Fig. 79.

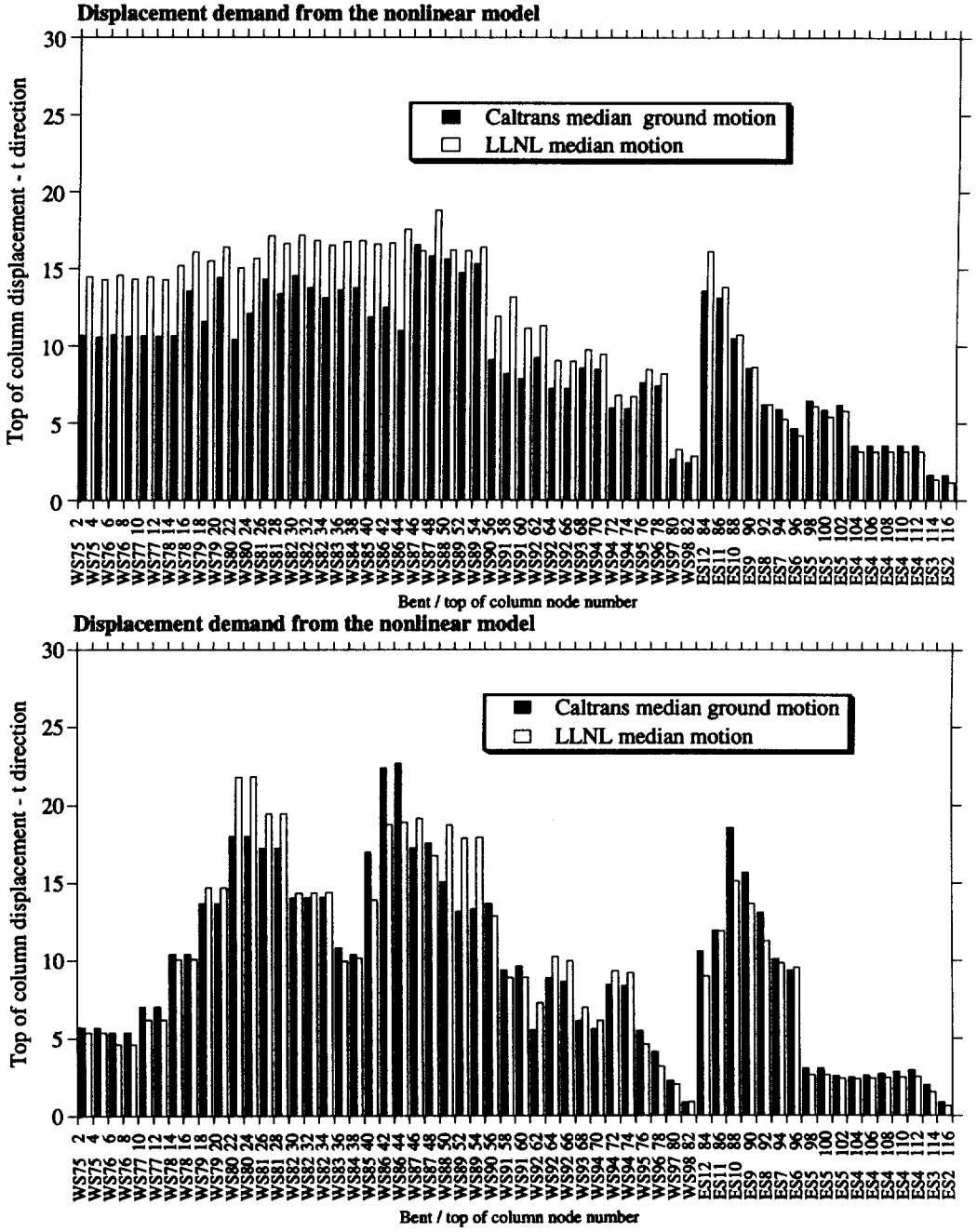

FIGURE 79. Column displacement demands based on Caltrans and LLNL median motions.

LLNL seismologists and geotechnical engineers developed an independent estimation of the ground motion at this site which would result from a M_w =7.5 Hayward Fault earthquake. Based on the Caltrans policy decision to use median level motion for this structure, the LLNL ground motion was based on the median level obtained from a suite of 100 possible Hayward Fault earthquakes. The LLNL median motion was in reasonable concurrence with the Caltrans ground motion definition.

Nonlinear, transient, earthquake response computations have been completed using a three dimensional nonlinear finite element model of the WS and ES lines. The nonlinear model accounted for potential impact and restrainer tensioning at expansion joints, finite deformation with accurate representation of associated P-Δ effects, and nonlinear hysteretic behavior of the concrete columns with softening of the concrete and plastic yielding of the reinforcing bars. Response computations have been completed for both Caltrans and LLNL ground motions.

The computed displacement demands for the columns were estimated to be on the order of two feet for the tallest columns in the structure. The concrete nonlinearity was found to have a pronounced effect on the global displacements of the structure, particularly near the trunk of the bridge system and in the ES line near the structure junction as indicated in Fig. 80. In the trunk region, the longitudinal displacements increased by more than a factor

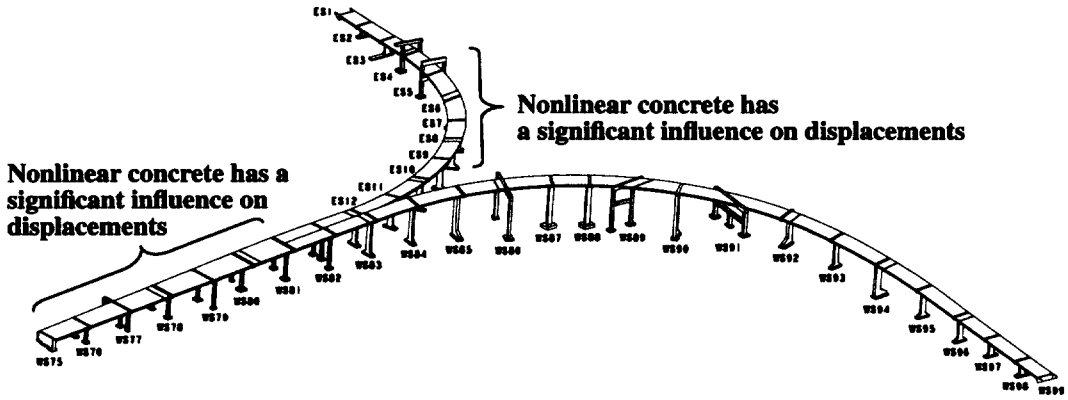

FIGURE 80. Regions in which concrete nonlinearity has a pronounced influence on structural displacements.

of two when the nonlinearity of the concrete was included.

As requested by Caltrans, simple nonlinear, static push over analyses were performed for three selected bents (ES 4, WS 94 companion bent and WS 96). The displacement capacities estimated from the push over analyses were found to exceed the displacement demands on these bents by a comfortable margin. However, a more rigorous and thorough investigation of column demands pointed to some potential problem locations for the retrofit structure. By extensive post processing of the response history database, the concrete strains in all of the bridge columns were assessed at each instant of the earthquake response and compared to appropriate allowables for poor or well confined concrete. This check illustrated that significant overstressing problems exist in the top of some of the tall single column bents on the ES lines (ES 9, ES 10 and ES 12). Marginal overstressing

problems are also evident in the very end of the trunk at WS 75, and WS 77 with the ground Caltrans ground motion characterization, and significant overstressing of the WS 75 WS 76 and WS 77 columns was observed with the LLNL median motion. Both ground motion characterizations indicated overstressing in the column of bent WS 85.

Many of the overstressing problems could be addressed with additional column jacketing. For example, if column WS 85 was jacketed at the base, and Columns ES8, ES9, ES10 and ES12 were jacketed through full height, the problems in these columns would be mitigated. Figure 81 and Fig. 82 show an approximation to the compressive strain demand to capacity ratios for the existing retrofit and for a retrofit which includes the additional jacketing. The plots of Fig. 81b and Fig. 82b are approximate in that a complete reanalysis of the structure was not performed, the plots were simply obtained by utilizing the same demand and increasing the strain capacity by a factor of three to reflect the effect of steel jacket confinement. There would be additional strength of the columns as a result of the jacketing, however the change in displacement demands as a result of the jacketing should be small and the plots of Fig. 81b and Fig. 82b are felt to provide a good estimation of the strain demand to capacity when additional jackets are added. Figures 81b and 82b indicate that the specified jacketing potentially solves of number of the indicated problems.

The problems associated with WS 75 and WS 77 are more fundamental and cannot be fixed with additional jacketing. Based on the results presented here, the drilled shafts at bent WS 75 and the columns of bent WS 77 appear to be susceptible to crushing failure of the concrete. Since the concrete of these members is already well confined, these members would require a different mitigation technique. One potential option consists of increasing the member dimensions of the drilled shafts in order to lower the member stresses.

The current retrofit design does not provide for any column retrofit for the multiple column bents of Frame #2 and Frame #3 (see Fig. 83). For these two frames, it is our opinion that careful consideration should be given to the overall frame shear capacity. Although an evaluation of shear capacity to demand was beyond the scope of the LLNL effort, and Caltrans has apparently assessed the adequate of the shear capacity of the columns [34], the shear capacity of the column-to-footing pinned connections on Frame #2 and Frame #3 does not appear to be well quantifiable. There is some research available on the shear strength of pinned connections for circular columns [36], however there seems to be a lack of information for larger rectangular columns. Based on the information available to LLNL there appears to be a significant degree of uncertainty about potential failure modes and strength capacity of these connections. Caltrans may want to consider additional retrofit schemes for the connections in light of the relative uncertainty in the capacity of these connections

Finally, based on the work of Hutchings et. al. [7], it must be noted that the possibility exists that this interchange could be subjected to motion significantly larger than the median level design basis earthquake. Caltrans may want to consider the implications of a beyond design basis event for this structure. Particularly in light of the fact that this site is situated within 4 Km of the fault and the probability of a major earthquake on the Hayward fault is continually being revised upward. .

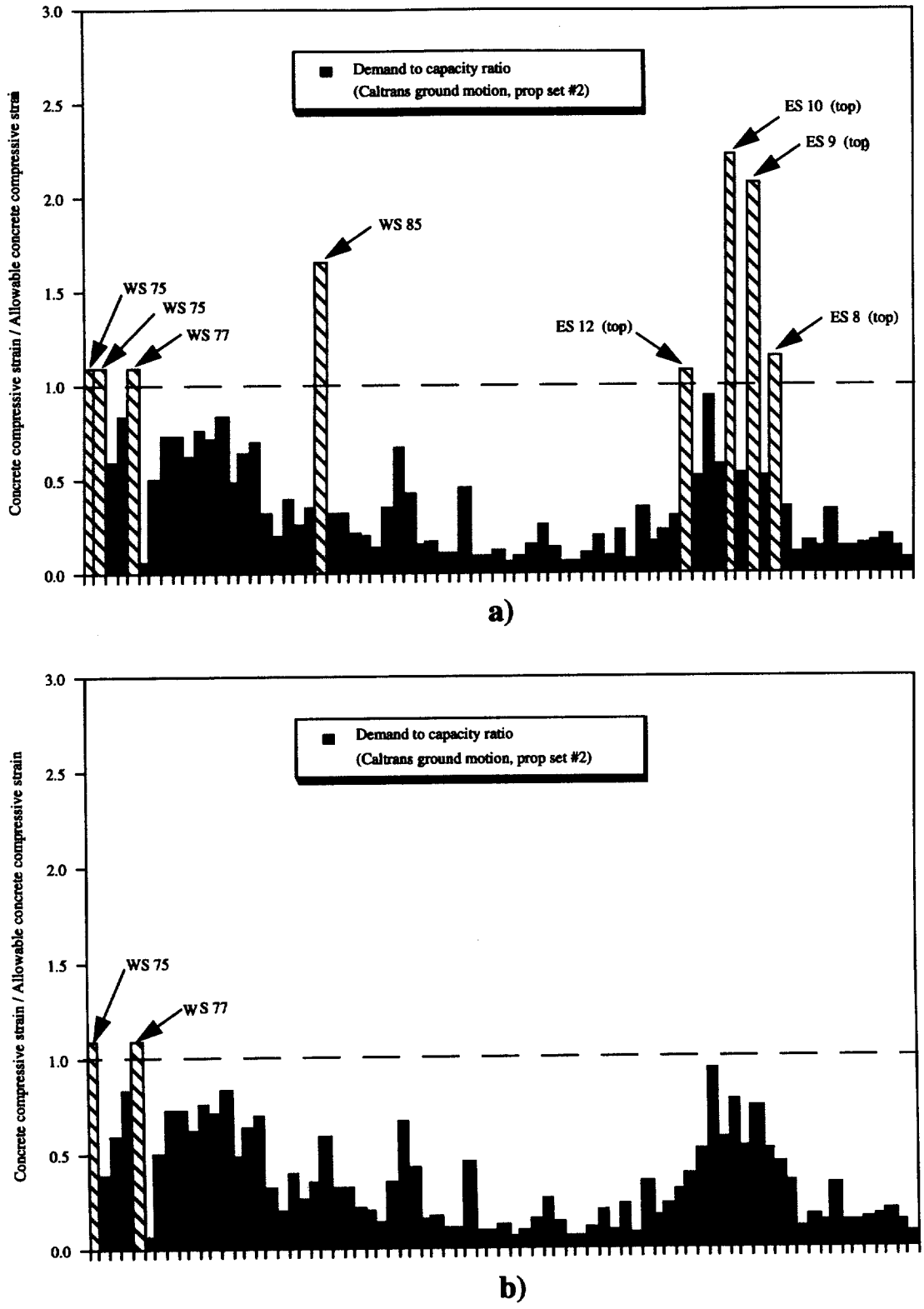

FIGURE 81. Column compressive strain demand to capacity ratios. a) existing retrofit design; b) estimation for modified retrofit design.

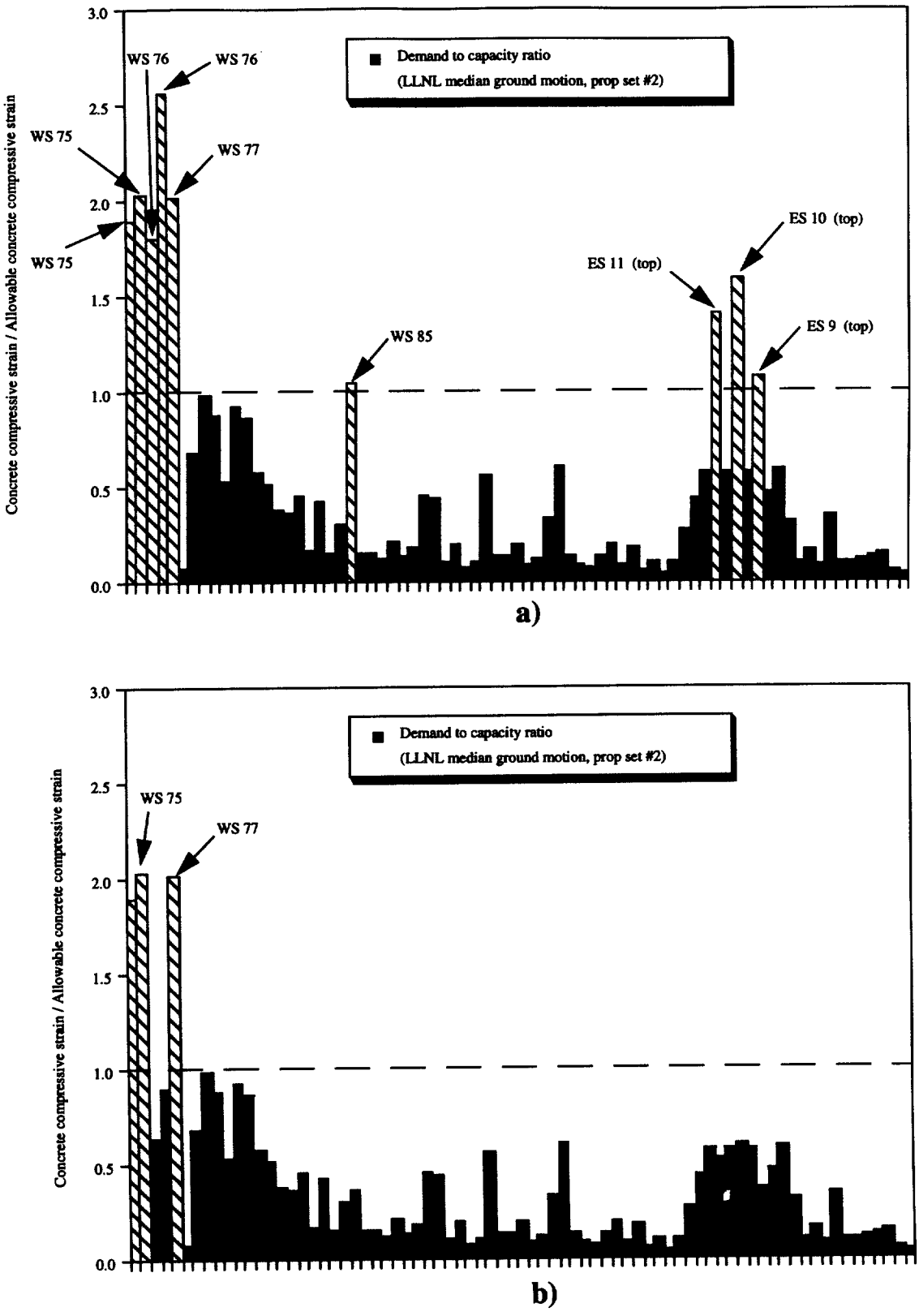

FIGURE 82. Column compressive strain demand to capacity ratios. a) existing retrofit design; b) estimation for modified retrofit design.

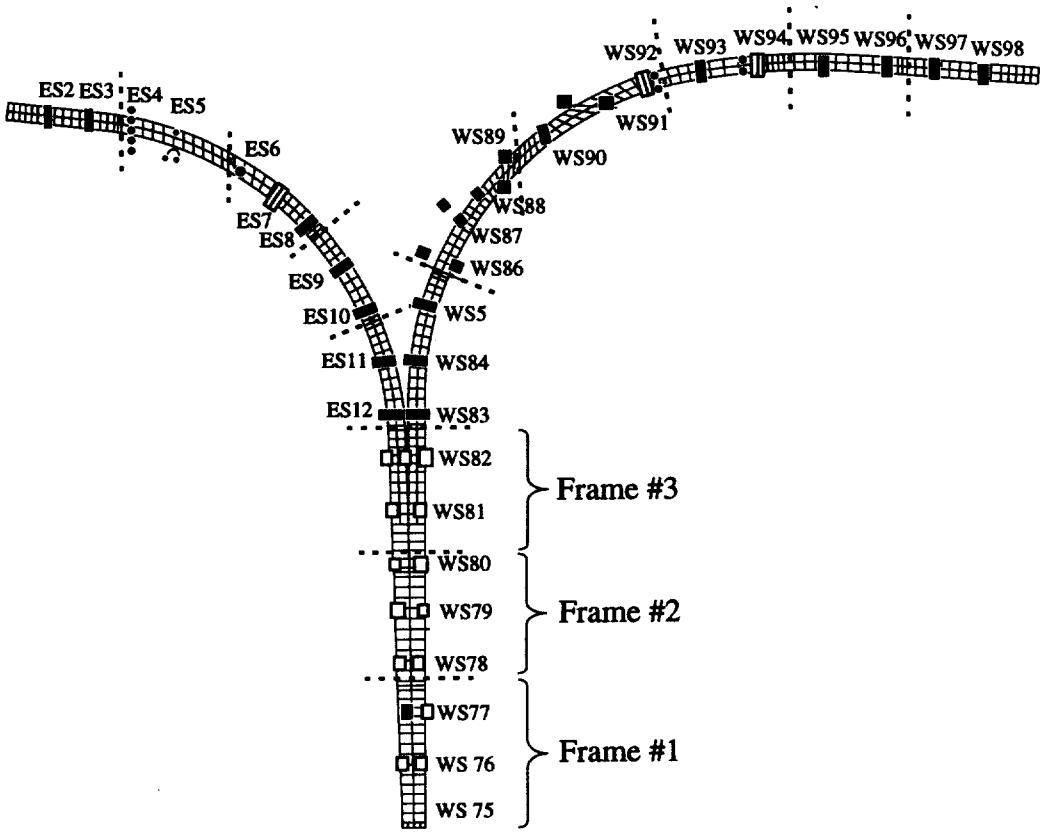

FIGURE 83. Location of Frames 1, 2 &3.

6.0 References

1. Roberts, J.E. (1995), *Improved Seismic Details for Highway Bridges*, California Department of Transportation, Draft report.

2. Zelinski, R. (1991), *Assessment of Existing Bridges Current Caltrans Practice*, Seismic Assessment and Retrofit of Bridges (M.J.N. Priestly editor), University of California, San Diego, Report No. SSRP - 91/03.

3. Chai, Y.H., M.J.N. Priestly and F. Seible (1991), *Retrofit of Bridge Columns for Enhanced Seismic Performance*, Seismic Assessment and Retrofit of Bridges (M.J.N. Priestly editor), University of California, San Diego, Report No. SSRP - 91/03.

4. M.J.N. Priestly and F. Seible (1991), *Design of Seismic Retrofit Measures for Concrete Bridges*, Seismic Assessment and Retrofit of Bridges (M.J.N. Priestly editor), University of California, San Diego, Report No. SSRP - 91/03.

5) Banks, V.A. (1989), Supplementary Bridge Report for the 24/580980 Interchange: 10-31-89, California Department of Transportation.

6) Mellon, F.L. and S.H. Post (1995), Memo to Designers 20-4, California Department of Transportation.

7) Hutchings, L., S. Jarpe, P. Kasameyer and W. Foxall (1995), Synthetic Strong Ground Motions at the Highways 24/580/980 Interchange (Stack) from Design Earthquakes on the Hayward Fault, Lawrence Livermore National Laboratory, Draft report.

8) Chen, J.C. (1995), Ground-Response Studies at the 24/580/980 Freeway Interchange Oakland Alameda County California, Lawrence Livermore National Laboratory Report (in press).

9) Sommerville, P.G., N.F. Smith, R.W. Graves and N.A. Abrahamson (1995), Representation of Near-Fault Rupture Directivity Effects in Design Ground Motions and Application to Caltrans Bridges, Proceedings of the National Seismic Conference on Bridges and Highways, San Diego CA.

10) Sommerville, P.G. (1995), Strong-Motion Records from the Kobe, Japan Earthquake of January 17, 1995 and Implications for Seismic Hazards in California, Proceedings of the SMIP95 Seminar on Seismological and Engineering Implications of Recent Strong-Motion Data, San Francisco CA.

11) Caltrans Division of Structures Memo from J. Gates to M. Barbour, April 1, 1993.

12) Department of Transportation Memo from A. Abghari and K. Jackura to T. Pollock, September 1992, File No. 04-13316K.

13) Document materials describing J. Penzien recommended spectra, Provided to LLNL by A. Abghari, date unknown.

14) Letter of transmittal from I.M. Idriss to M. Barbour, April, 1993.

15) Informal document and spectra plots of Gates, Provided to LLNL by A. Abghari, date unknown.

16) Pro/ENGINEER: Mechanical Design System Software by Parametric Technology, Waltham Mass.

17) M.A. Gerhard (1991), SLIC - The Interactive, Graphic Mesh Generator for Finite-Element and Finite-Difference Application Programs, Lawrence Livermore National Laboratory Report, UCRL-MA-108429.

18) Maker, B.N., J.O. Hallquist and R.M. Ferencz (1995), NIKE3D - A Nonlinear, Implicit, Three-Dimensional Finite Element Code for Solid and Structural Mechanics, Lawrence Livermore National Laboratory Report, UCRL-MA-105268 Rev. 1.

19) McCallen. D.B. and K.M. Romstad (1994), Dynamic Analyses of a Skewed Short-Span Box-Girder Overpass, Spectra, Earthquake Engineering Research Institute, Vol. 10, No. 4.

20) Maker, B.N., R.G. Whirley and B.E. Englemann (1992), Numerical Integration of Structural Elements in NIKE3D and DYNA3D, Lawrence Livermore National Laboratory Report, UCRL-ID-11476.

21) Fenves, G.L. and R. Desroches (1994), Response of the Northwest Connector in the Landers and Big Bear Earthquakes, University of California Berkeley Report, UCB/EERC-94/12.

22) Malhotra, P.K., M.J. Huang and A.F. Shakal (1995), Seismic Interaction at Separation Joints of an Instrumented Concrete Bridge, Earthquake Engineering and Structural Dynamics, Vol. 24.

23) Personal communication between D. McCallen and R. Bromenschenkel, 1995.

24) McCallen, D.B. and K.M. Romstad (1994), Nonlinear Model for Building-Soil Systems, ASCE Journal of Engineering Mechanics, Vol. 120, No. 5.

25) Personal communication between D. McCallen and G. Fenves, 1995.

26) Sun, Z., F. Seible and M.J.N. Priestley, Diagnostic and Retrofit of Rectangular Bridge Columns for Seismic Loads, University of California San Diego Report, SSRP-93/07.

27) Spacone, E. and F.C. Filippou (1994), RC Beam-Column Element for Nonlinear Frame, Analysis and Computation, Proceedings of the 11th ASCE Conference, Atlanta, GA.

28) Filippou, F. and A. Issa (1988), Nonlinear Analysis of Reinforced Concrete Frames under Cyclic Load Reversals, University of California Berkeley Report, UCB/EERC 88-12.

29) Taucer, F., E. Spacone and F. Filippou (1991), A Fiber Beam-Column Element for Seismic Analysis of Reinforced Concrete Structures, University of California Berkeley Report, UCB/EERC-91-17.

30) Scott, B.D., R. Park and M.J.N. Priestley (1982), Stress-Strain Behavior of Concrete Confined by Overlapping Hoops at Low and High Strain Rates, ACI Journal, January-February 1982.

31) Menegotto, M. and P.E. Pinto (1977), Slender RC Compressed Members in Biaxial Bending, Journal of Structural Engineering, ASCE, Vol. 103, No. 3.

32) Maroney, B., K. Romstad and M. Chajes (1990), Interpretation of Rio Dell Freeway Response During Six Recorded Earthquake Events, Proceedings of the Fourth U.S. National Conference on Earthquake Engineering, Palm Springs, CA.

33) Spelce, T. and J.O. Hallquist (1991), TAURUS: An Interactive Post-Processor for the Analysis Codes NIKE3D, DYNA3D and TOPAZ3D, Lawrence Livermore National Laboratory Report, UCRL-MA-105401.

34) Haroun, M.A., G.C. Pardoen and R. Shephard (1994), Shear Capacity of Bridge Pinned Columns, Department of Civil and Environmental Engineering, University of California Irvine, Final Report to the California Department of Transportation.

35) Caltrans critiera for allowable concrete compressive strains, Personal communication between D. McCallen and R. Bromenschenkel, 1995.

7.0 Acknowledgements

The authors would like to thank Mike Barbour and Ron Bromenschenkel of Caltrans for their support and input to this project. Thanks also to Larry Hutchings, Paul Kasameyer, and J.C. Chen of LLNL for their input and discussions on the nature of ground motions and to Tom Nelson for his insights into the structural details for the interchange. Professor Greg Fenves of UC Berkeley provided information on the details of his research work into the dynamic response of bridge structures and numerical modeling issues and his assistance is appreciated. A final thanks to Mike Puso of the Methods Development Group at LLNL for his critical assistance in real-time implementation of the nonlinear concrete model in the *NIKE3D* finite element program.

This work was performed at the Lawrence Livermore National Laboratory under the auspices of the United States Department of Energy, contract W-7405-Eng-48.

Appendix A - Bent Section Properties

24-580-980 Interchange - Bent Properties (asbuilt structure,

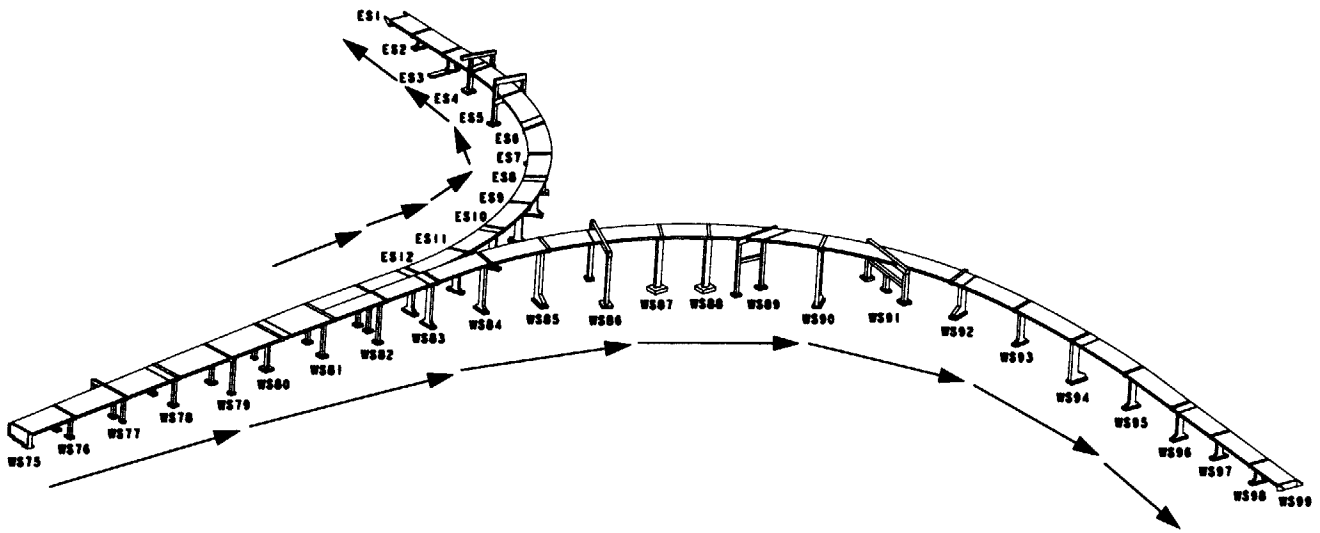

Arrows indicate direction in which bent is viewed

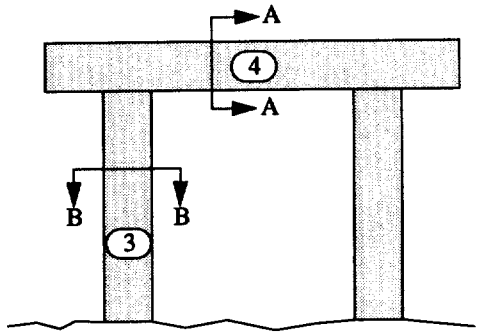

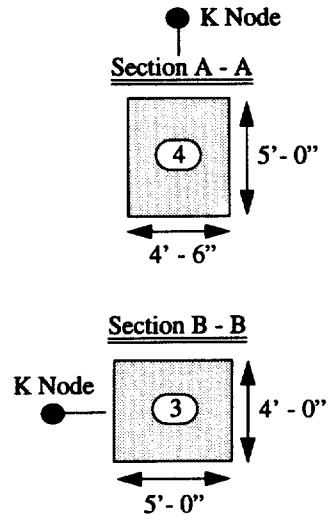

Bent WS 76 (as-built)

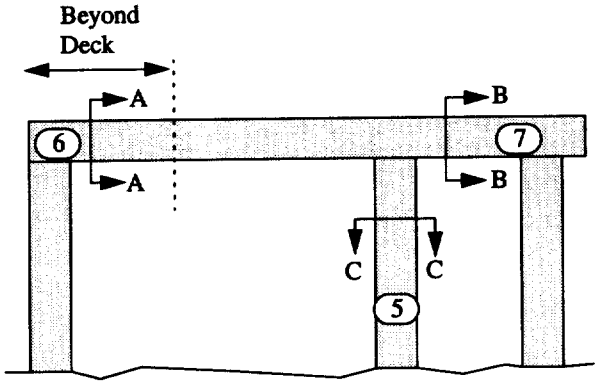

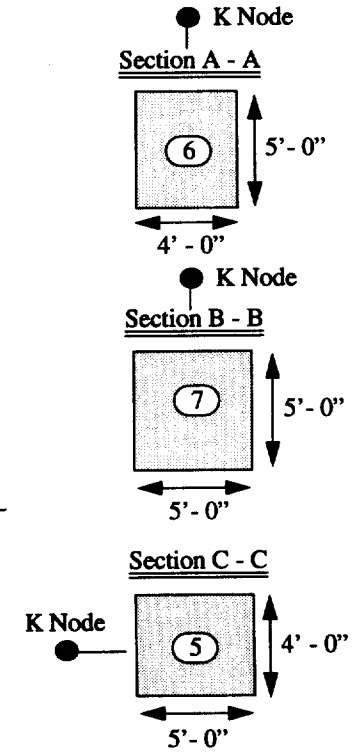

Bent WS 77 (as-built)

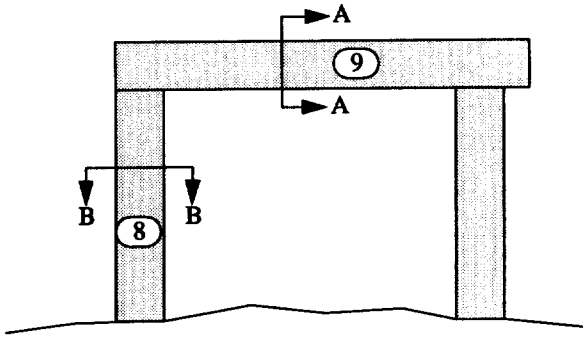

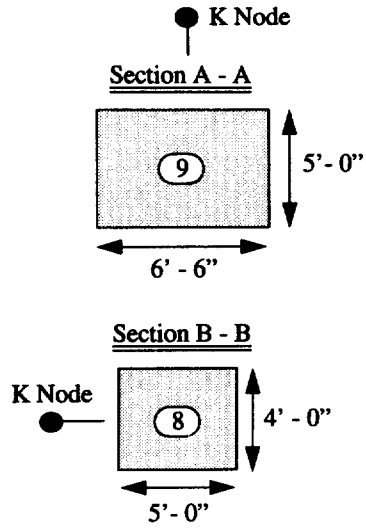

Bent WS 78 (as-built)

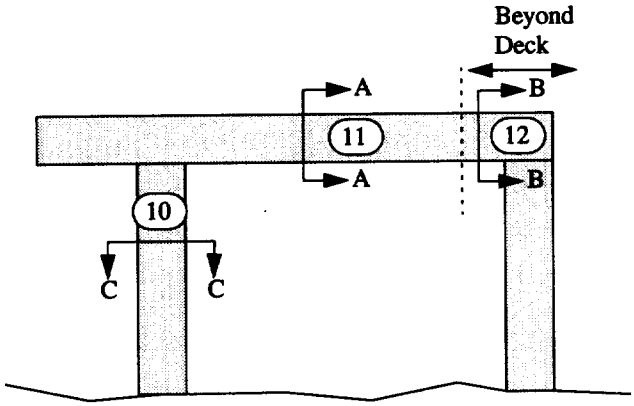

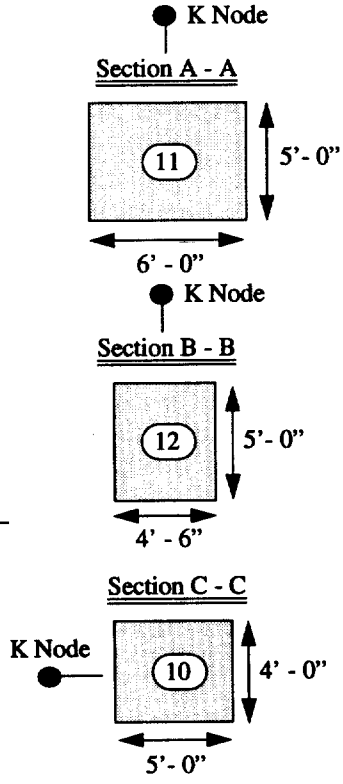

Bent WS 79 (as-built)

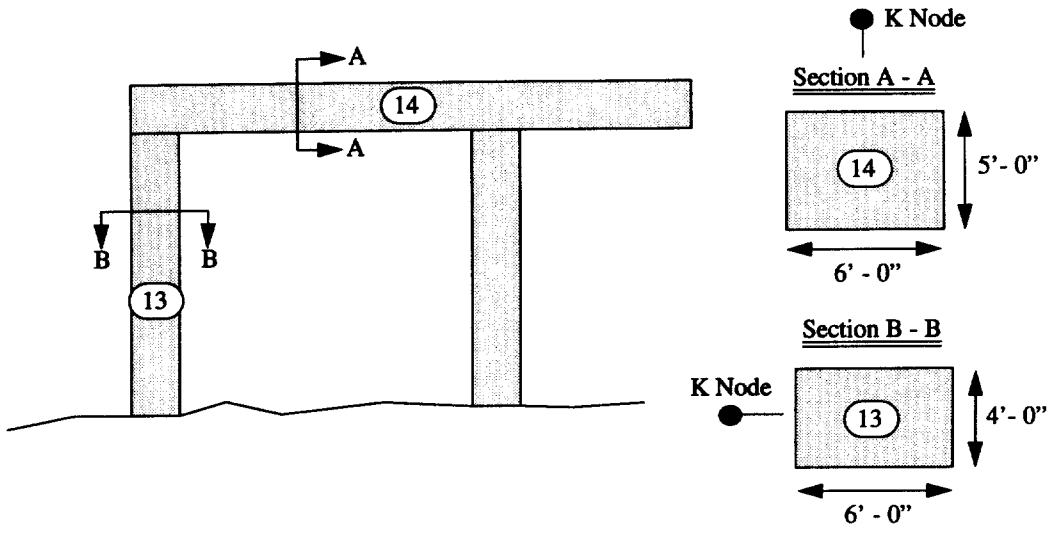

Bent WS 80 (as-built)

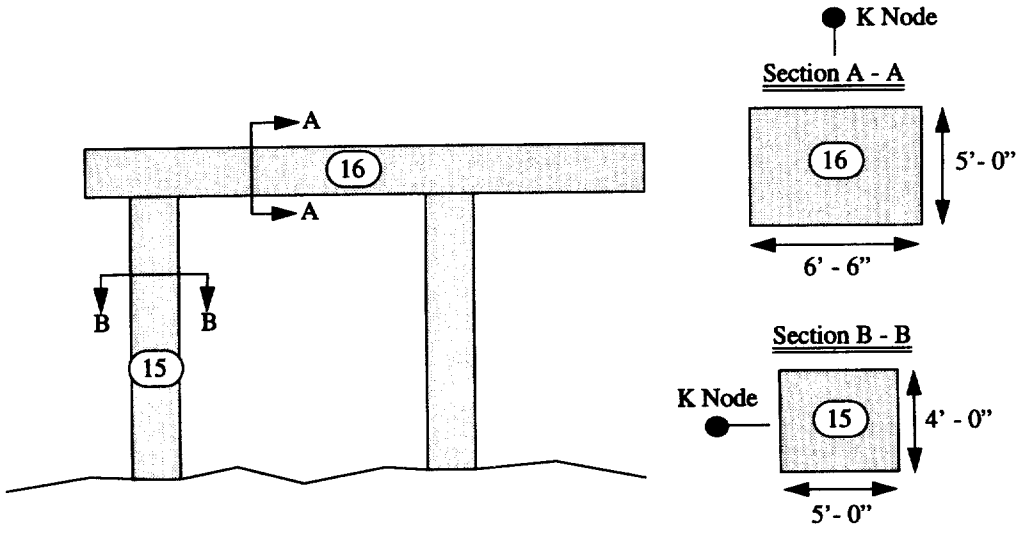

Bent WS 81 (as-built)

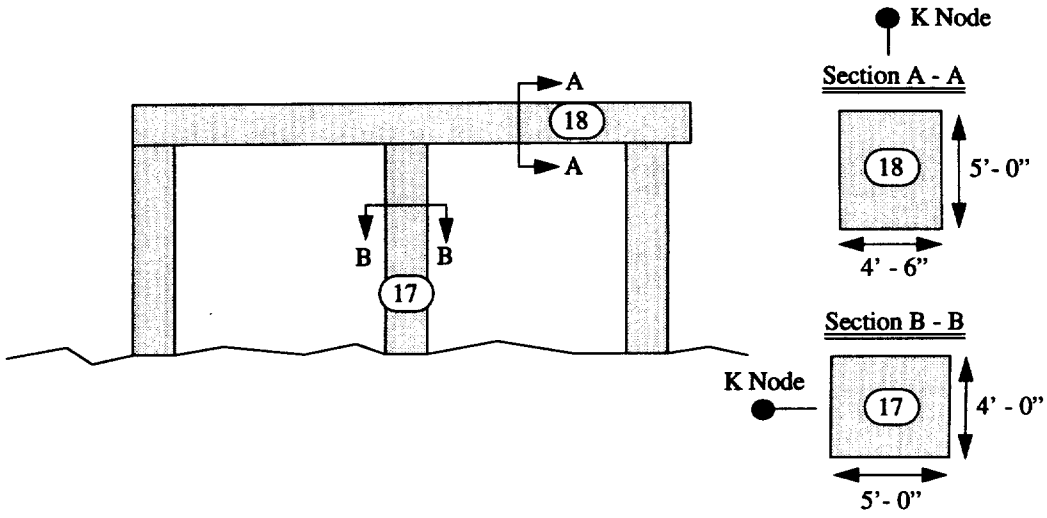

Bent WS 82 (as-built)

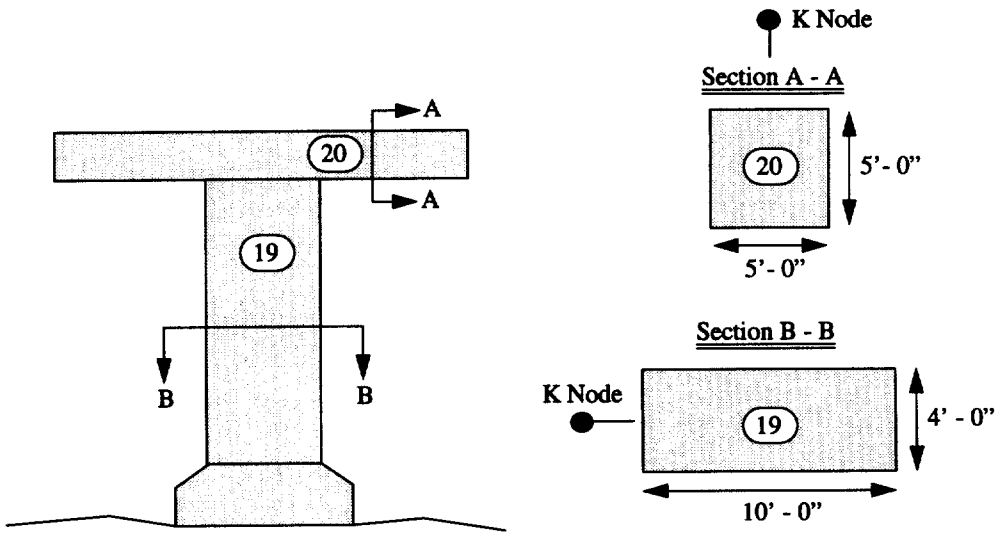

Bent WS 83 (as-built)

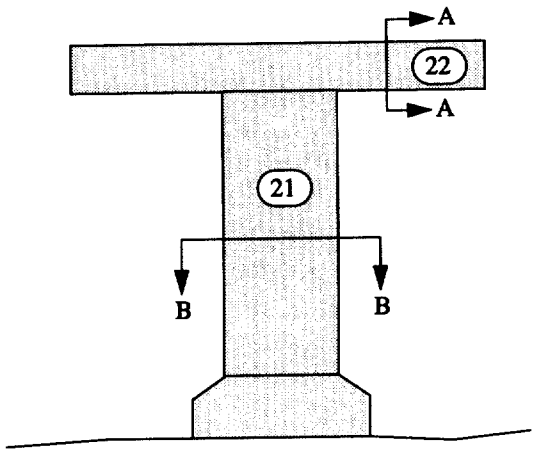

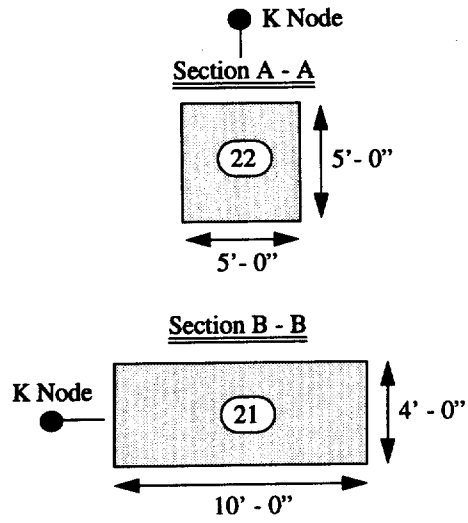

Bent WS 84 (as-built)

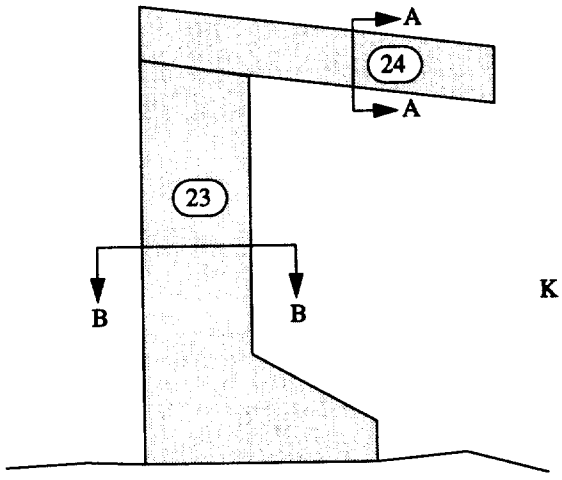

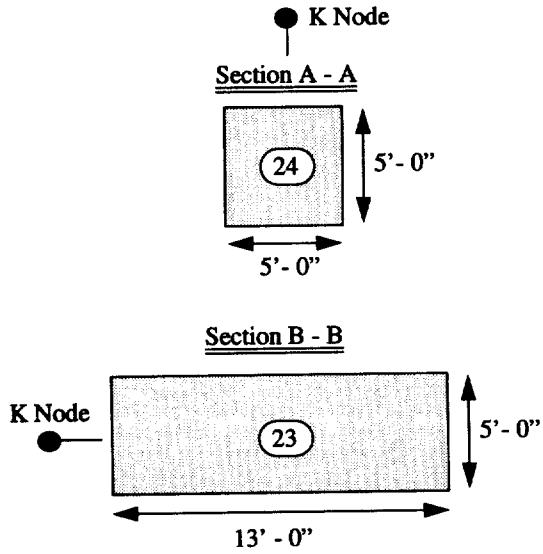

Bent WS 85 (as-built)

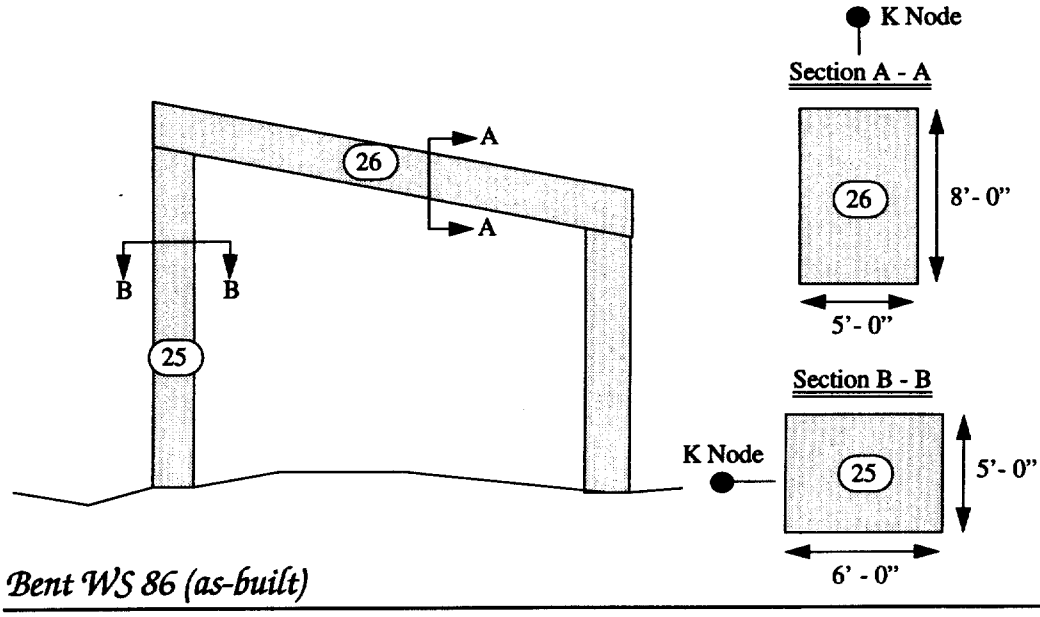

Bent WS 86 (as-built)

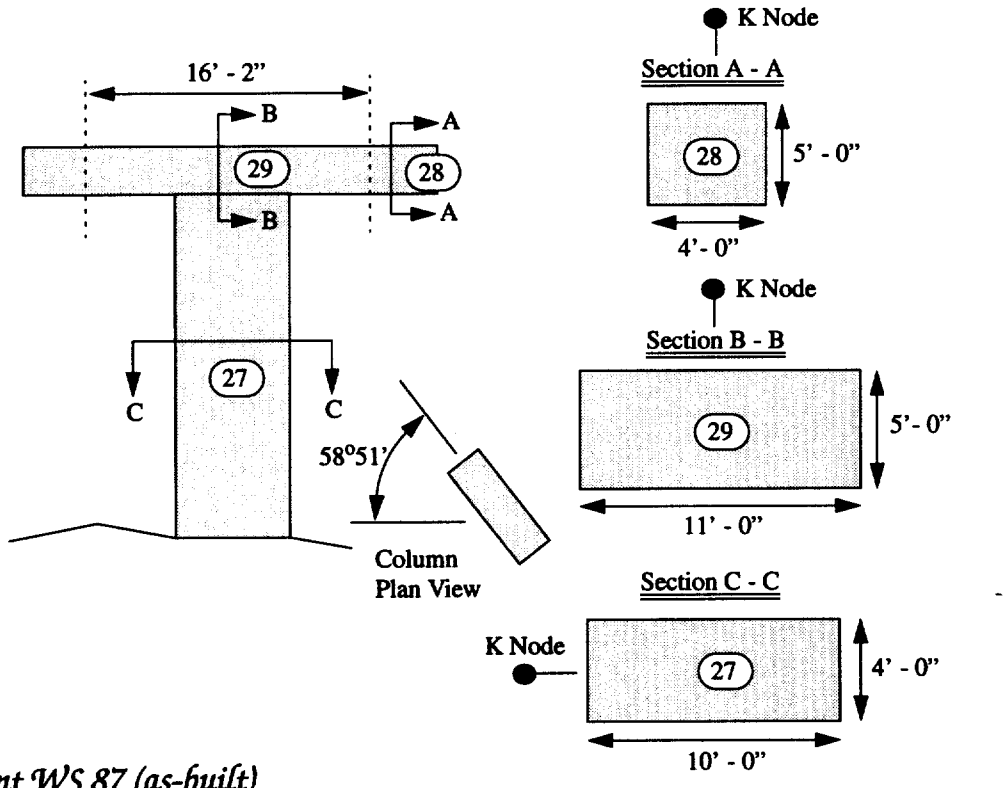

Bent WS 87 (as-built)

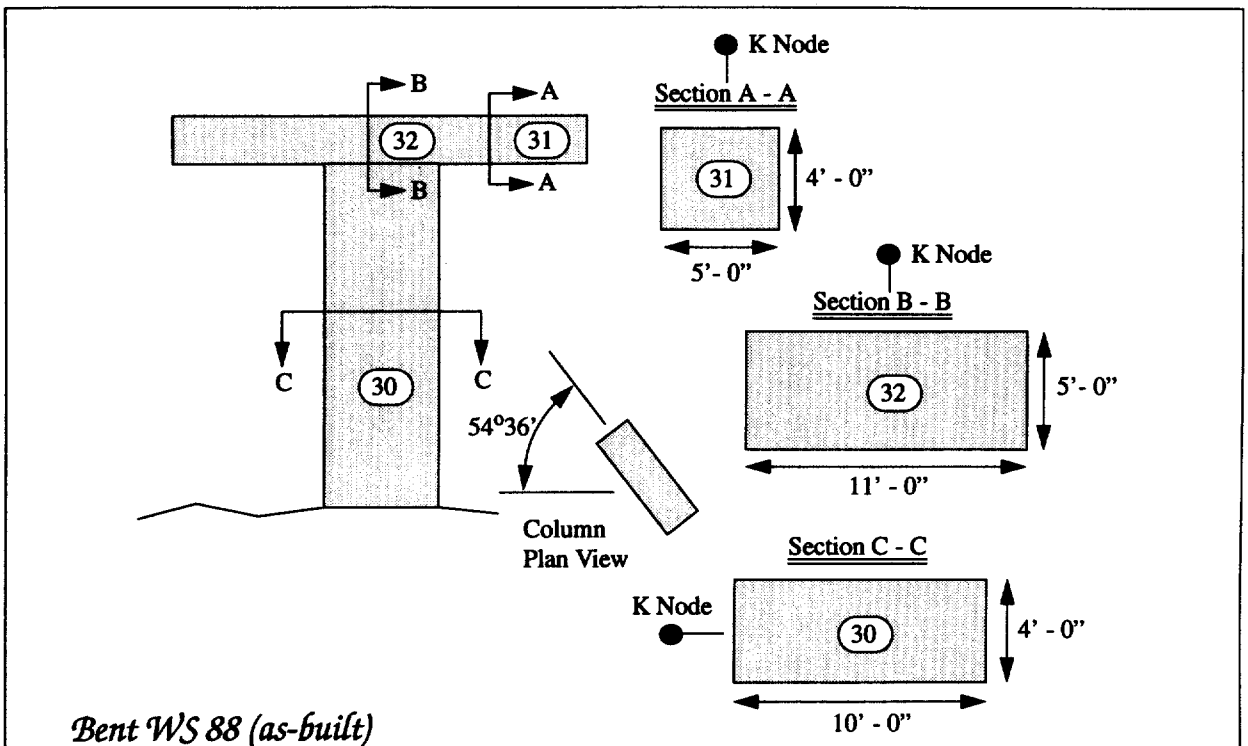

Bent WS 88 (as-built)

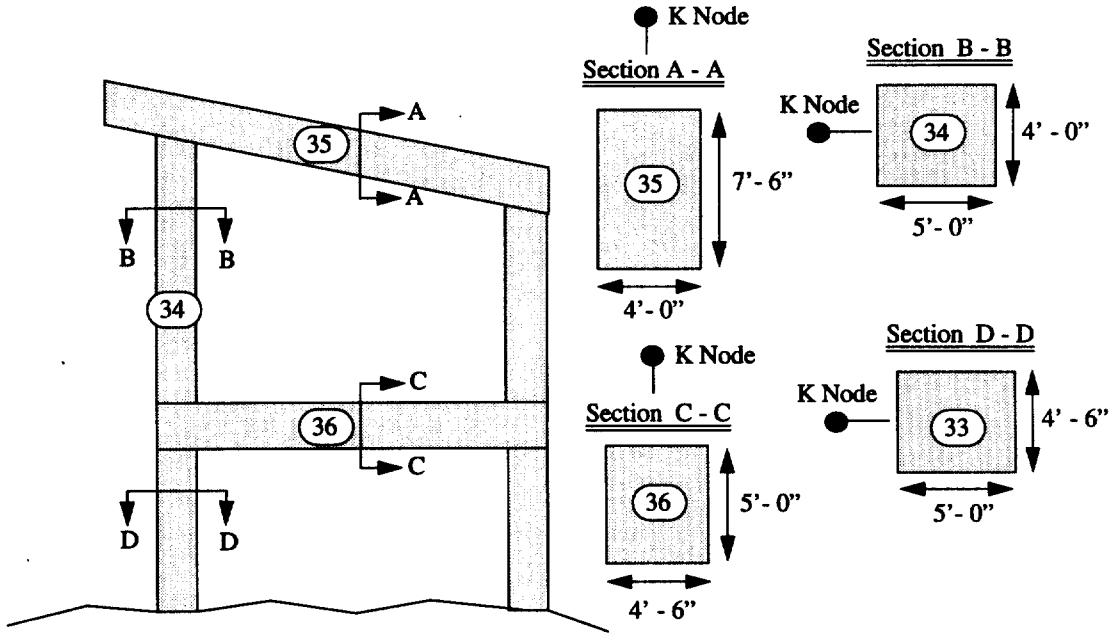

Bent WS 89 (as-built)

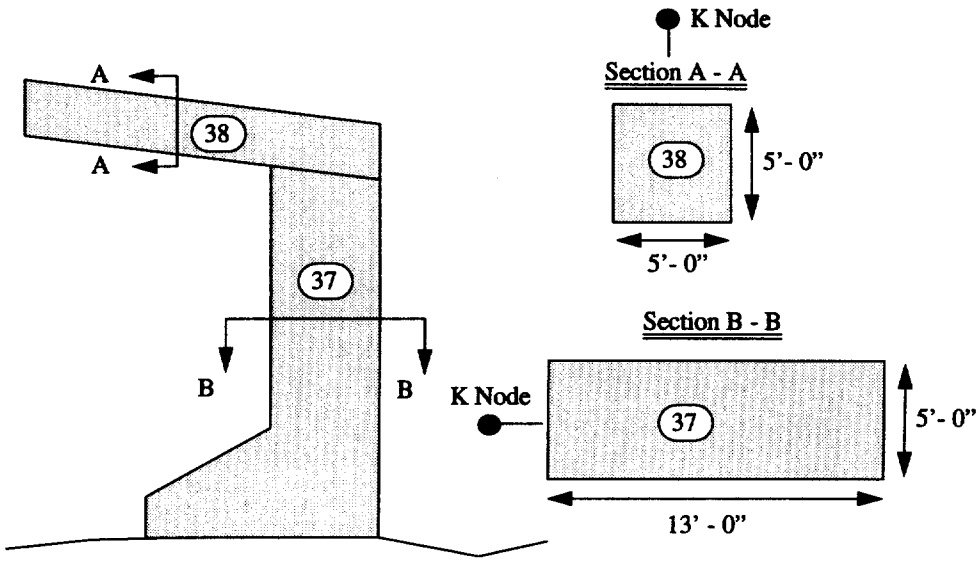

Bent WS 90 (as-built)

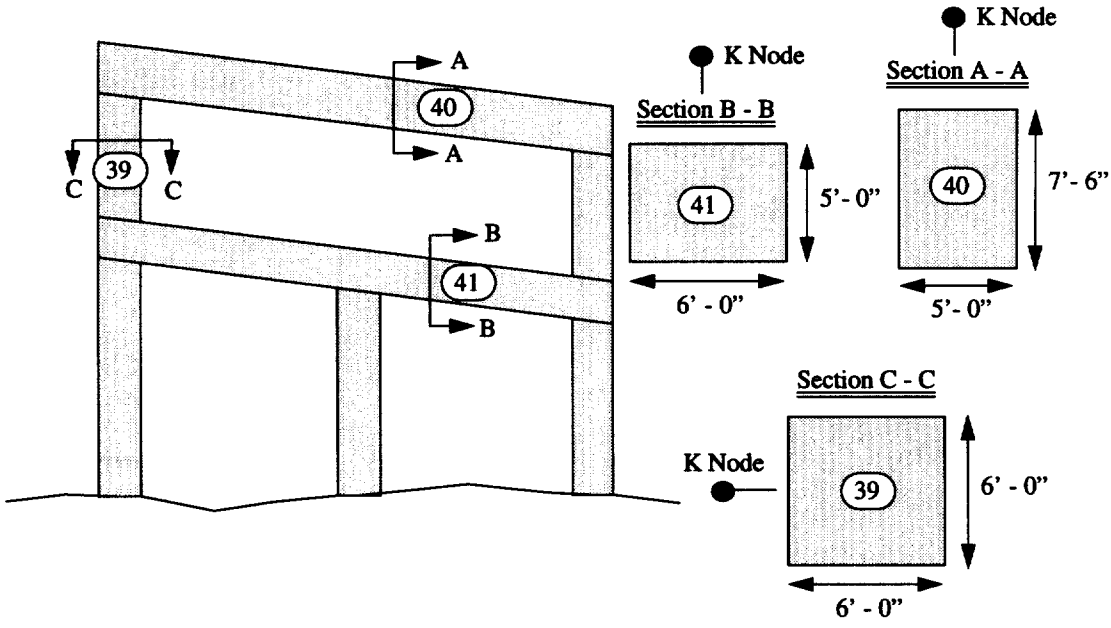

Bent WS 91 (as-built)

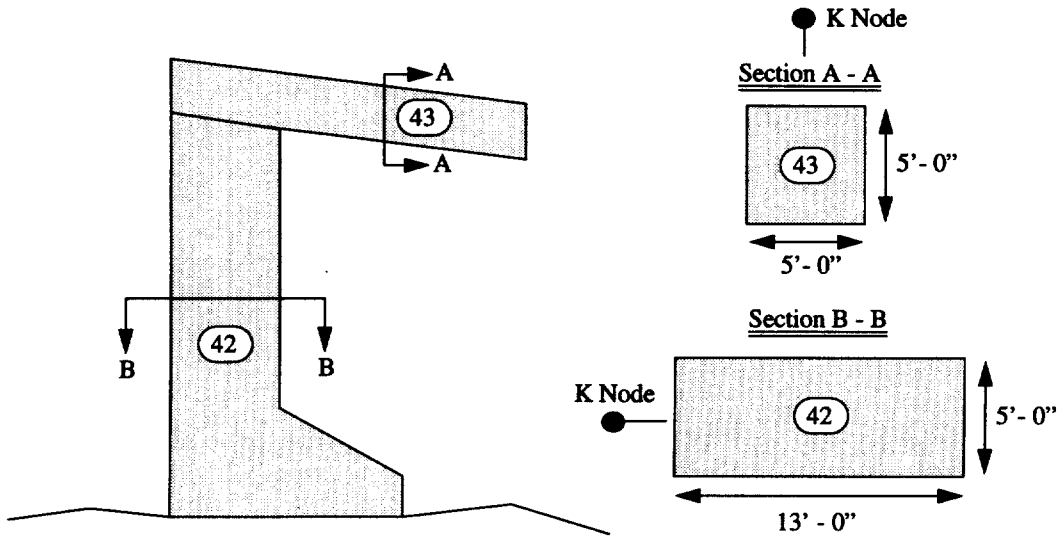

Bent WS 92 (as-built)

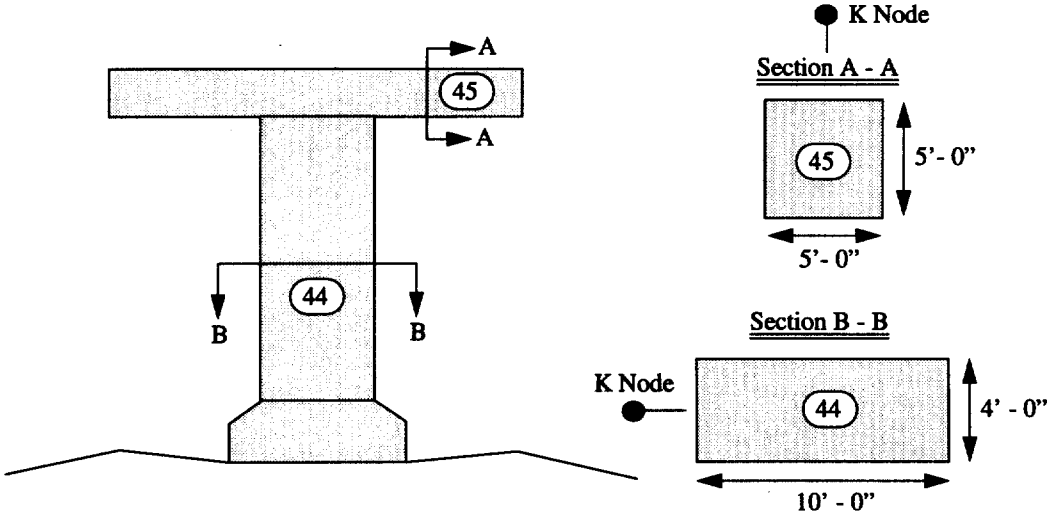

Bent WS 93 (as-built)

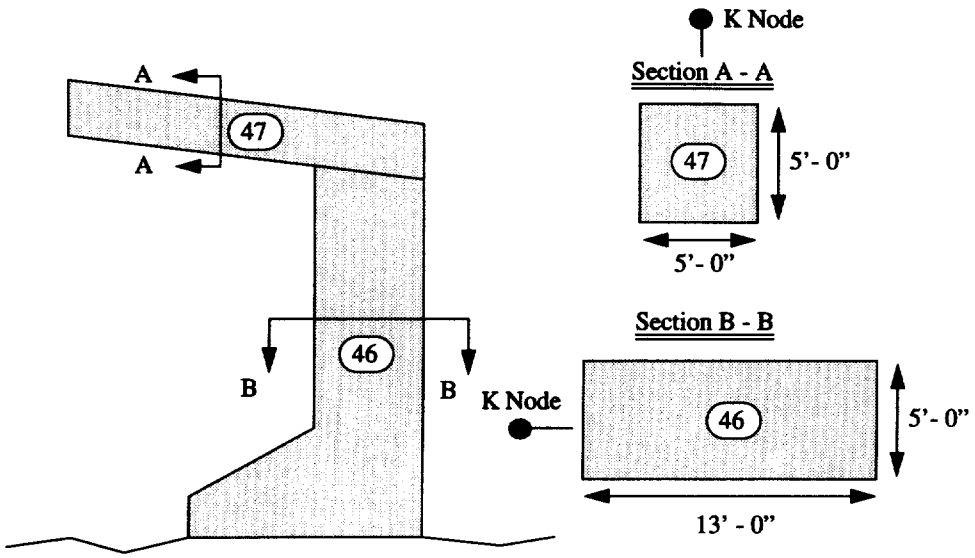

Bent WS 94 (as-built)

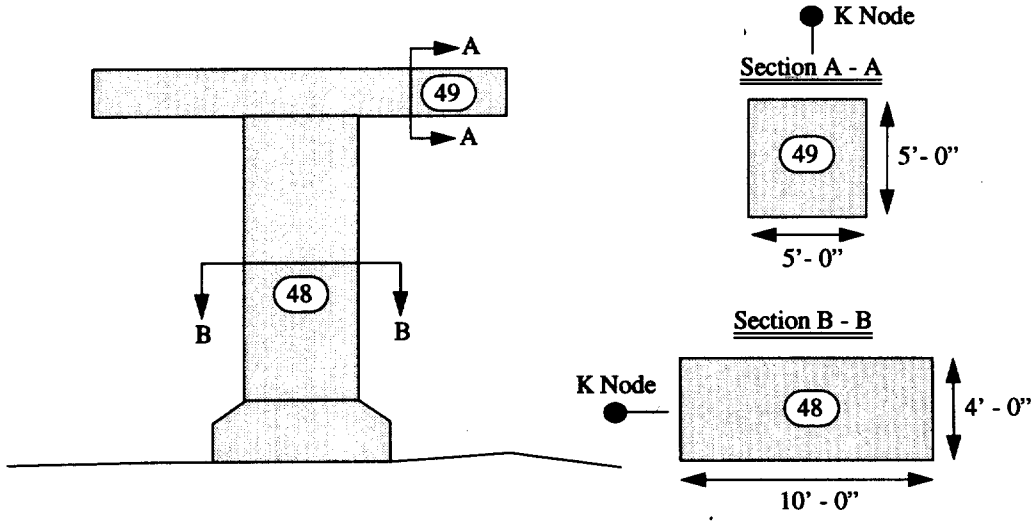

Bent WS 95 (as-built)

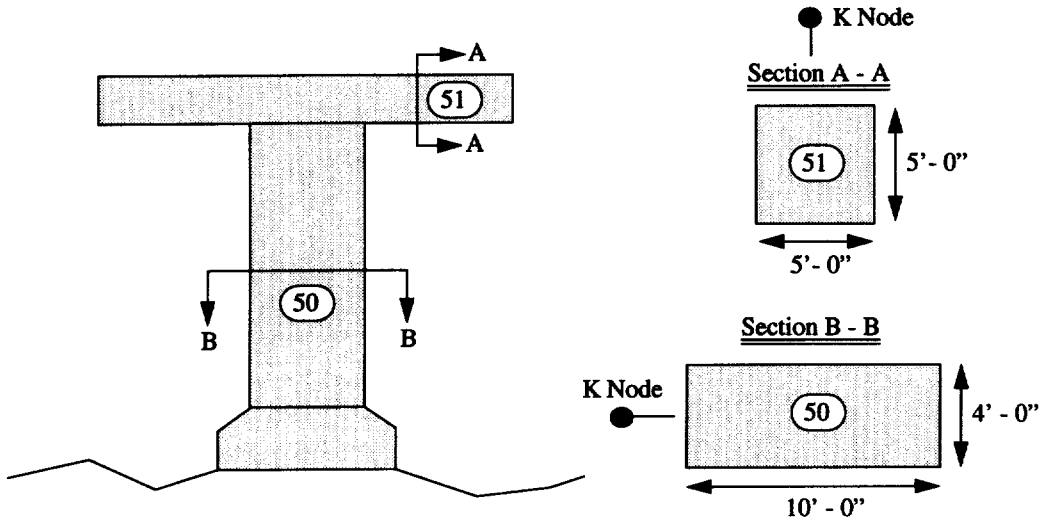

Bent WS 96 (as-built)

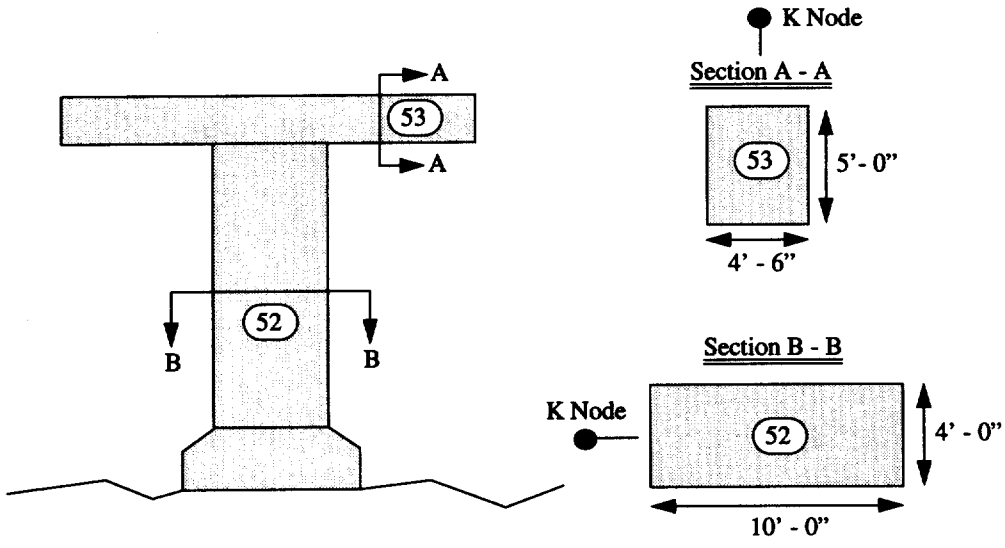

Bent WS 97 (as-built)

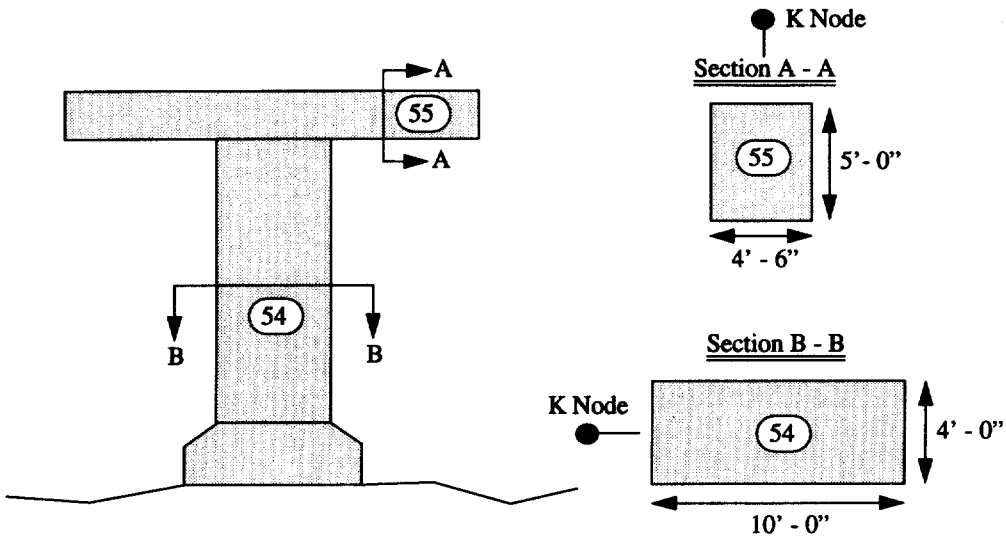

Bent WS 98 (as-built)

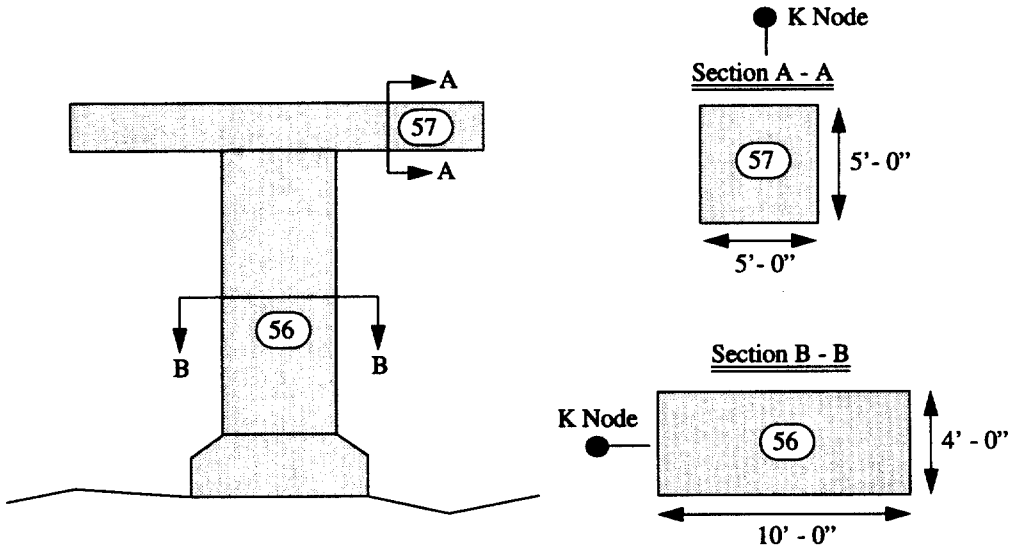

Bent ES 12 (as-built)

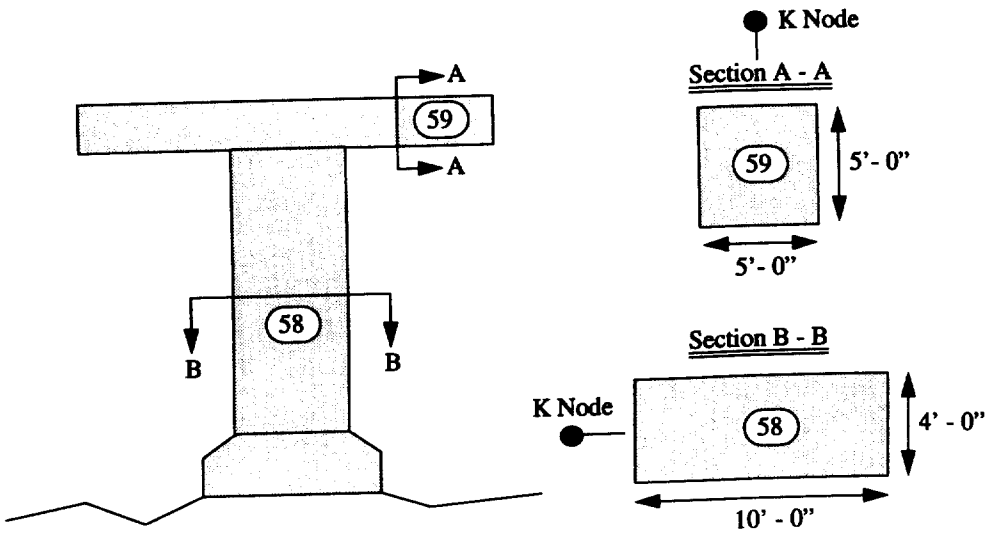

Bent ES 11 (as-built)

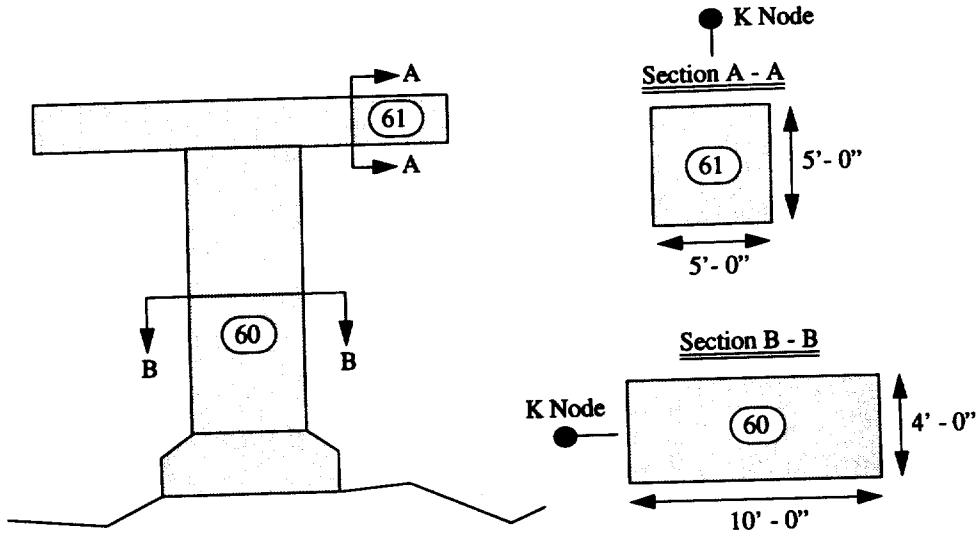

Bent ES 10 (as-built)

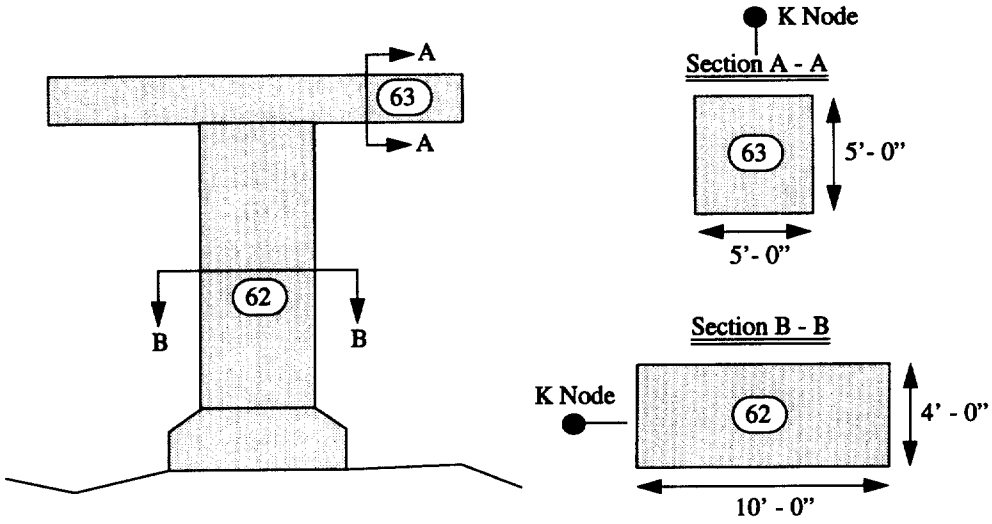

Bent ES 9 (as-built)

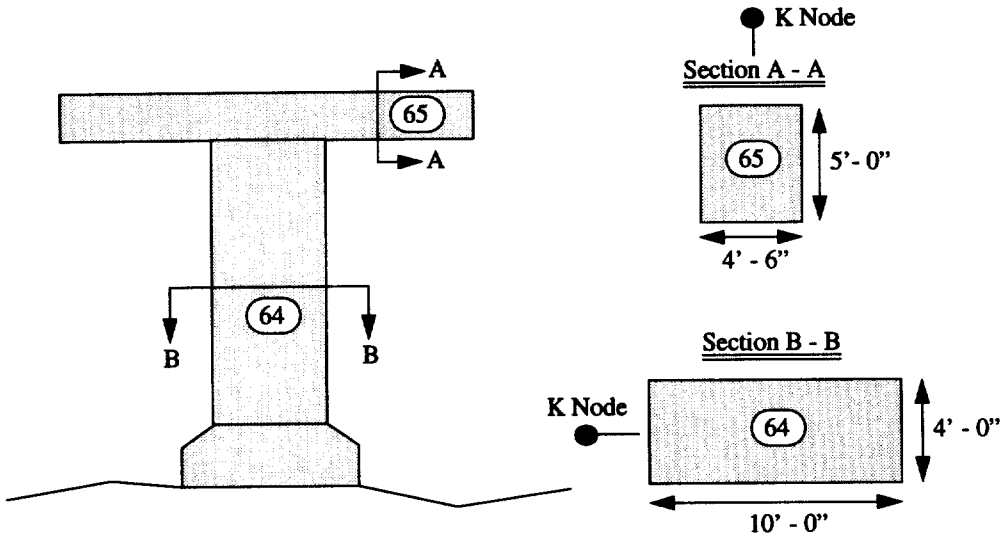

Bent ES 8 (as-built)

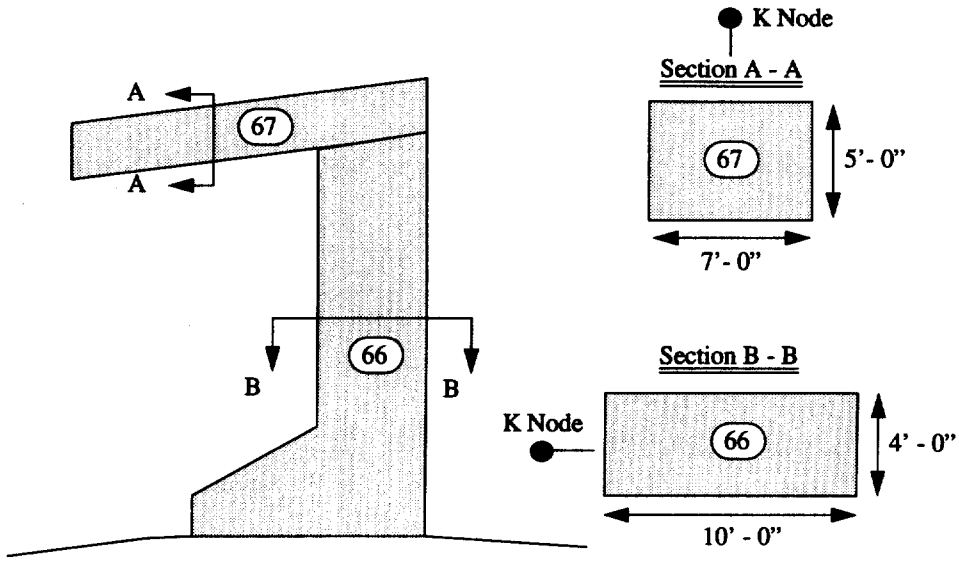

Bent ES 7 (as-built)

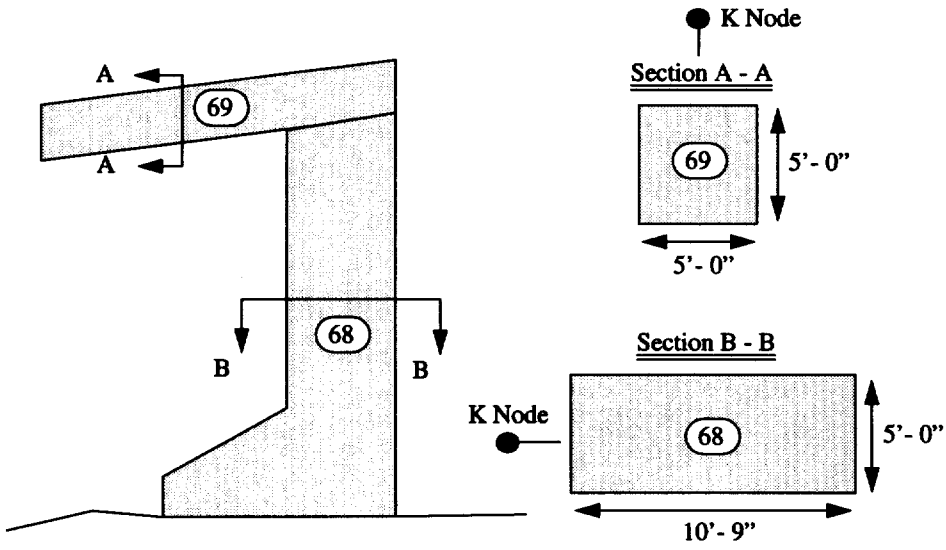

Bent ES 6 (as-built)

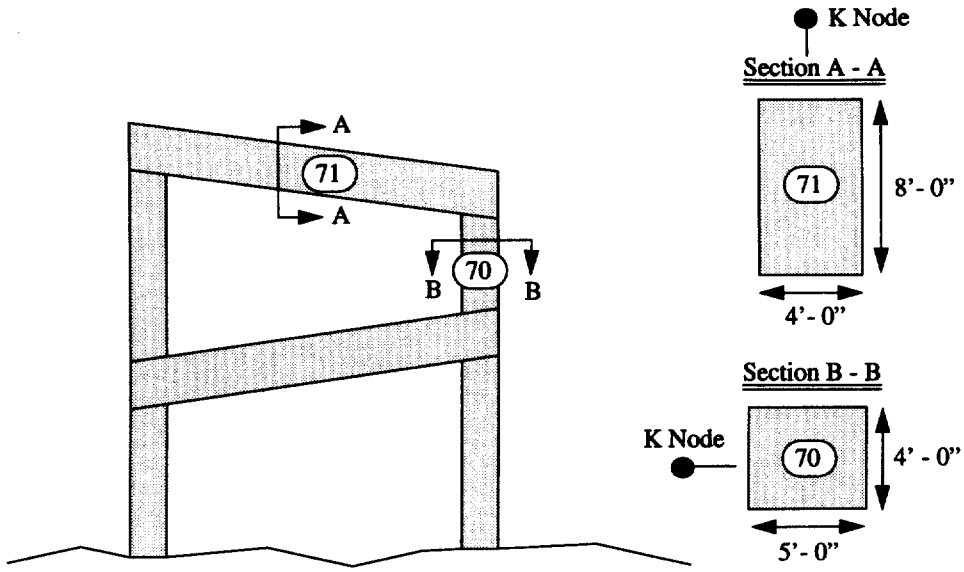

Bent ES 5 (as-built)

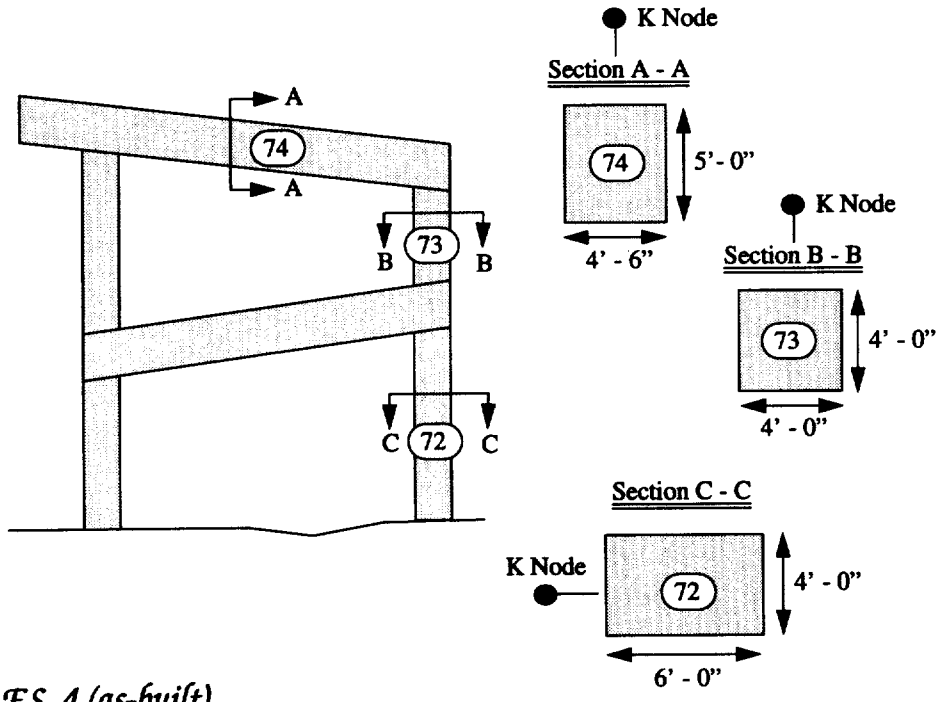

Bent ES 4 (as-built)

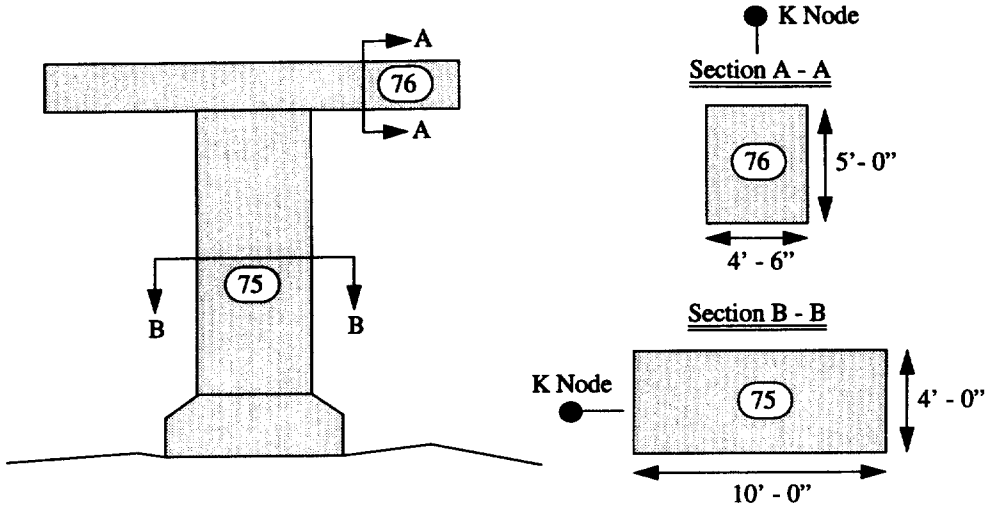

Bent ES 3 (as-built)

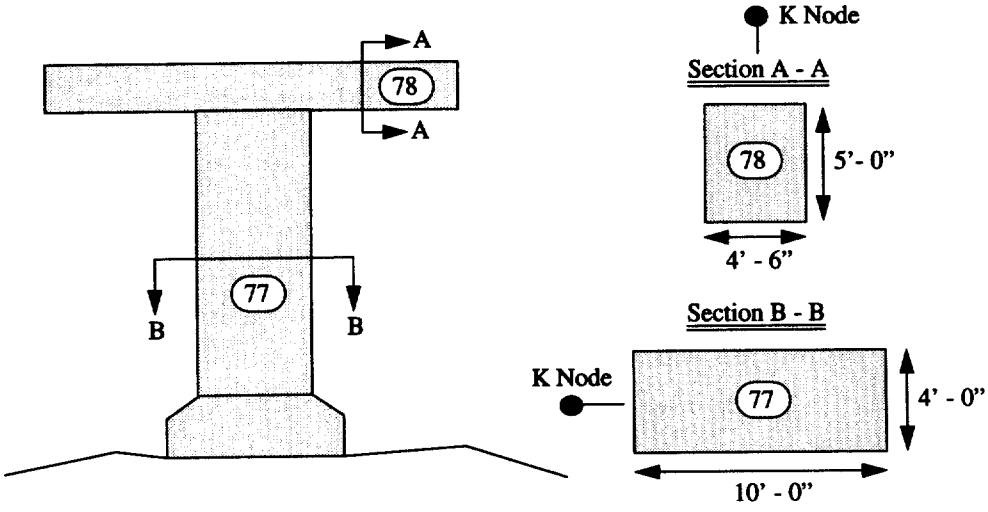

Bent ES 2 (as-built)

Appendix B - Deck Section Properties

24-580-980 Interchange - Deck Properties

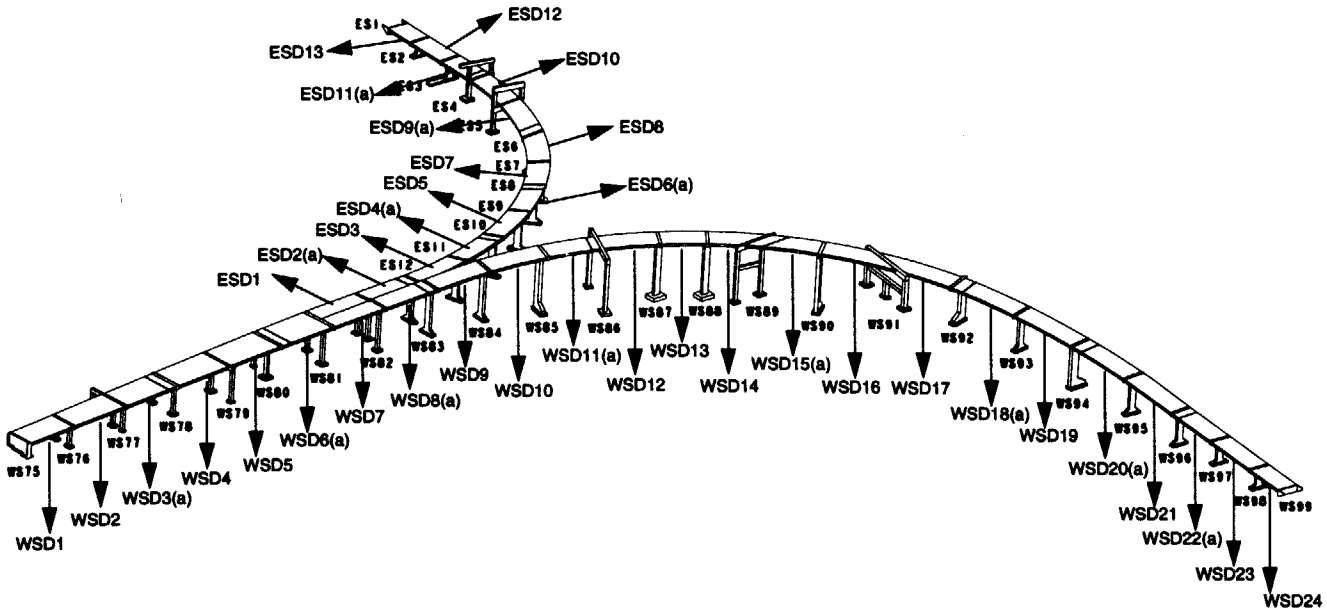

(a) refers to stiffened segment on short span side of expansion joint

Deck Section	Deck cross-section number	Nike material number	Nike user defined integration number
WSD1	7	105	1
WSD2	6	106	2
WSD3(a)	5 (8)	107 (108)	3 (4)
WSD4	4	109	5
WSD5	3	110	6
WSD6(a)	2 (9)	112 (111)	8 (7)
WSD7	1	113	9
WSD8(a)	1 (10)	114 (115)	10 (11)
WSD9	1	116	12
WSD10	1	117	13
WSD11(a)	1 (1)	118 (119)	14 (15)
WSD12	1	120	16
WSD13	1	121	17
WSD14	1	122	18
WSD15(a)	1 (10)	124 (123)	20 (19)
WSD16	1	125	21
WSD17	1	126	22
WSD18(a)	1 (11)	128 (127)	24 (23)
WSD19	1	129	25
WSD20(a)	1 (11)	131 (130)	27 (26)
WSD21	1	132	28
WSD22(a)	1 (10)	134 (133)	30 (29)
WSD23	1	135	31
WSD24	1	136	32
ESD1	1	137	33
ESD2(a)	1 (10)	138 (139)	34 (35)
ESD3	1	140	36
ESD4(a)	1 (10)	141 (142)	37 (38)
ESD5	1	143	39
ESD6(a)	1 (10)	144 (145)	40 (41)
ESD7	1	146	42
ESD8	1	147	43
ESD9(a)	1 (13)	149 (148)	45 (44)
ESD10	1	150	46
ESD11(a)	1 (12)	152 (151)	48 (47)
ESD12	1	153	49
ESD13	1	154	50

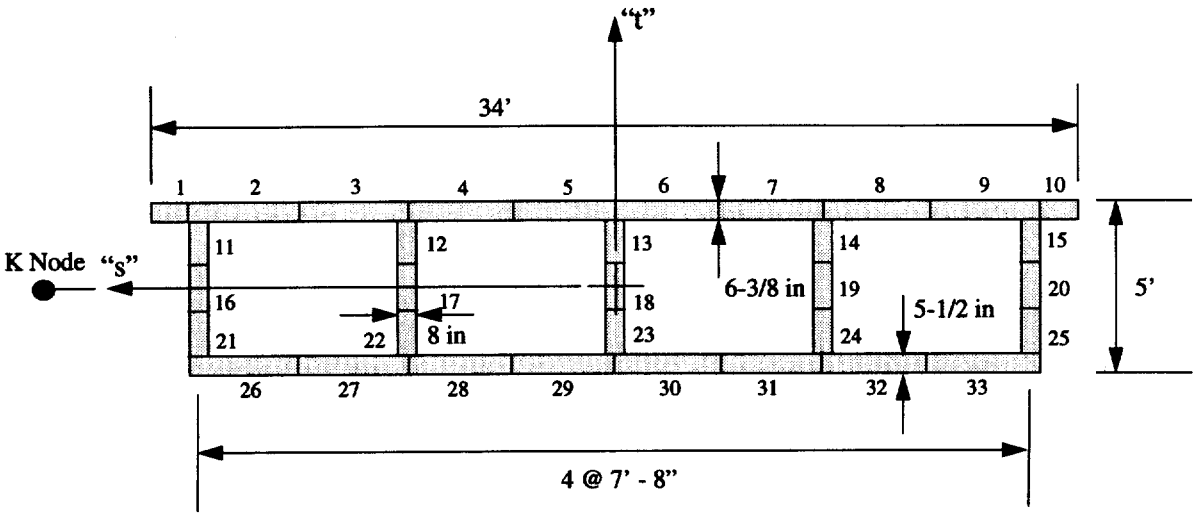

Sections: ESD1, ESD2, ESD3, ESD4, ESD5, ESD6, ESD7, ESD8, ESD9, ESD10, ESD11, ESD12, ESD13

Sections: WSD7, WSD8, WSD9, WSD10, WSD11, WSD12, WSD13, WSD14, WSD15, WSD16, WSD17, WSD18, WSD19, WSD20, WSD21, WSD22, WSD23, WSD24

Four Cell Box Girder Deck Segments **Section 1**

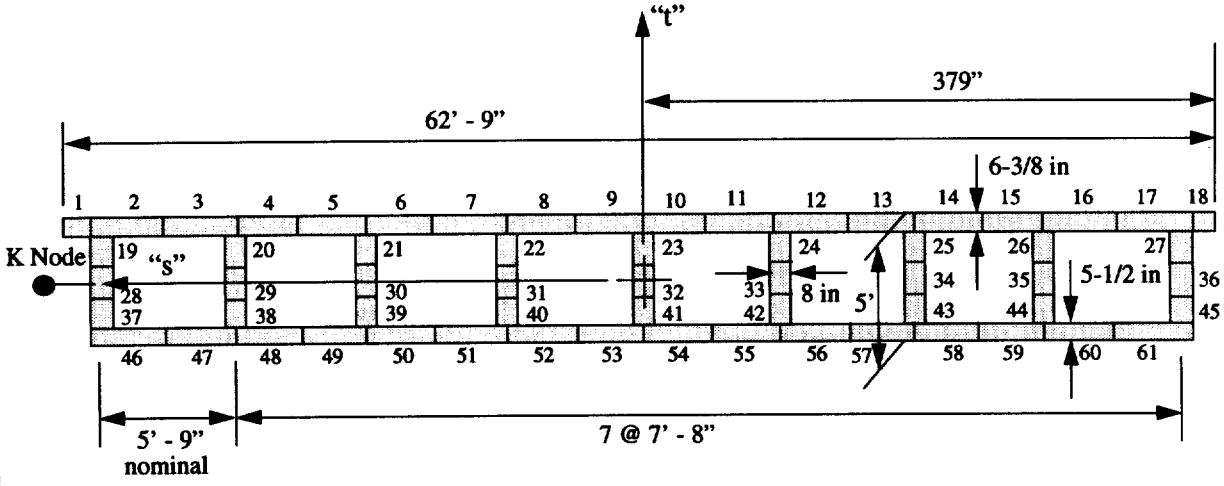

Sections: WSD6

Eight Cell Box Girder Deck Segments **Section 2**

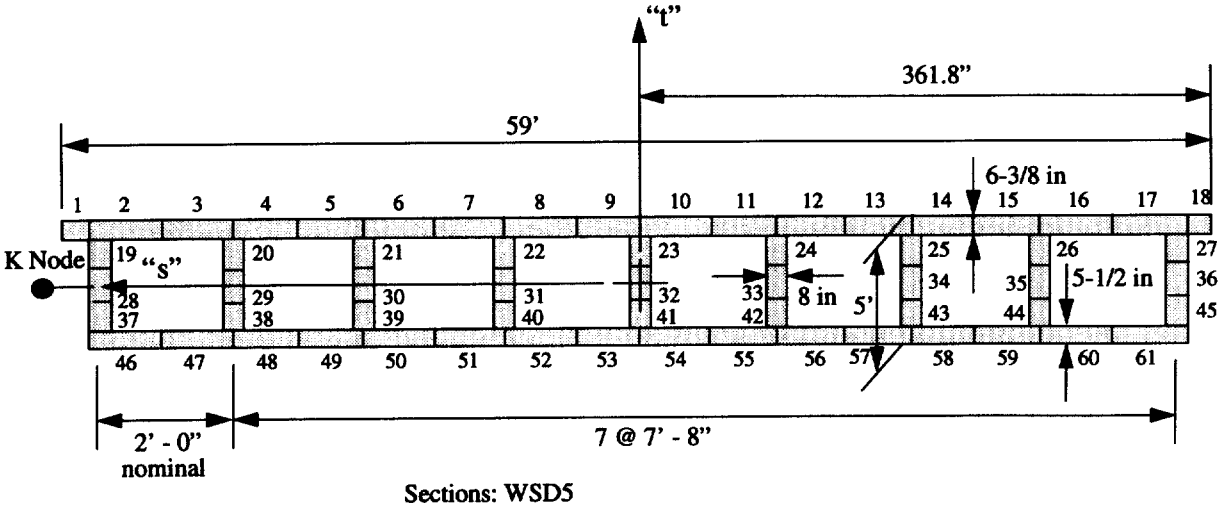

Sections: WSD5

Eight Cell Box Girder Deck Segments — *Section 3*

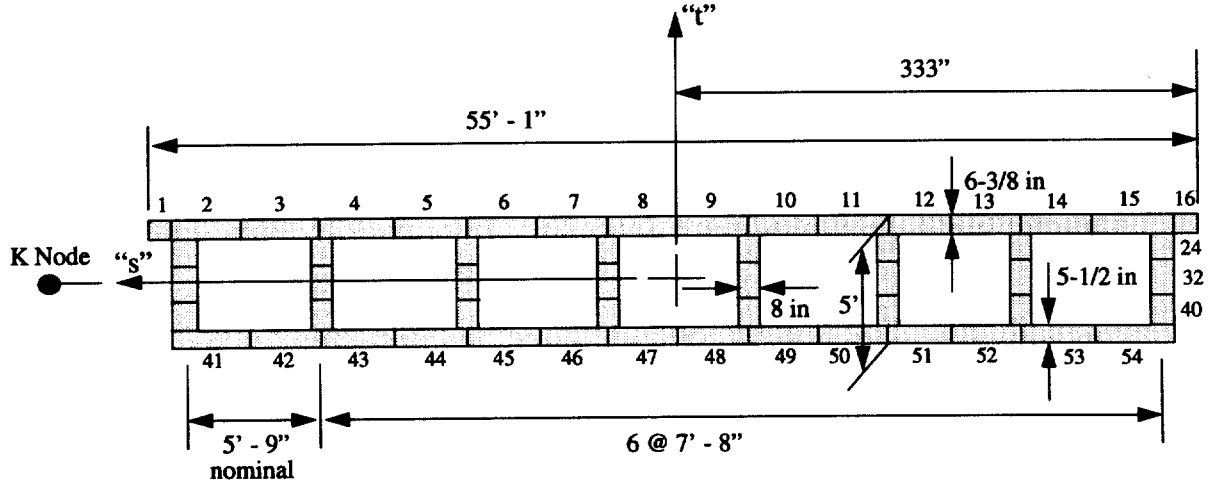

Sections: WSD4

Seven Cell Box Girder Deck Segments — *Section 4*

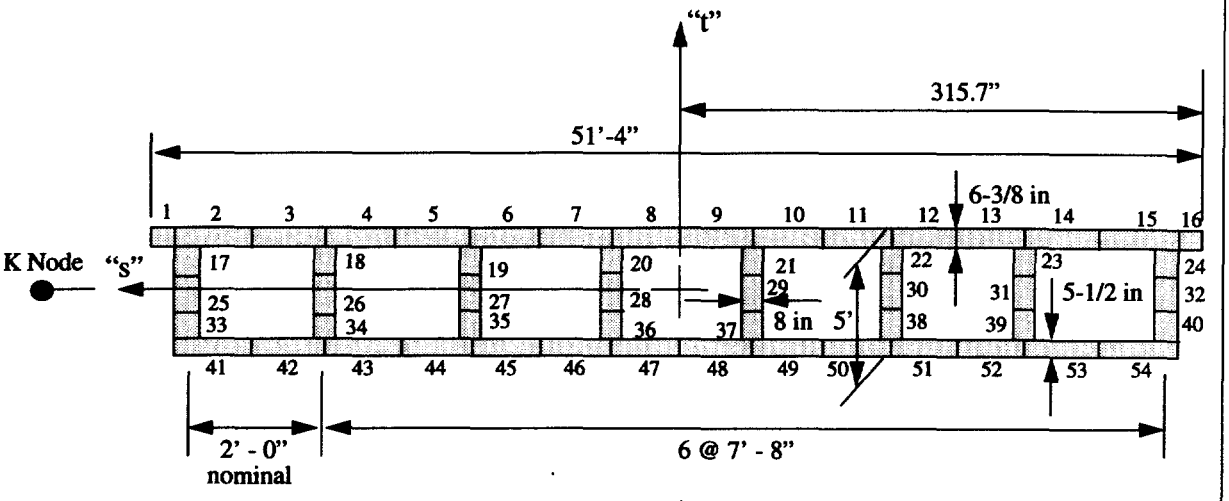

Sections: WSD3

Seven Cell Box Girder Deck Segments — *Section 5*

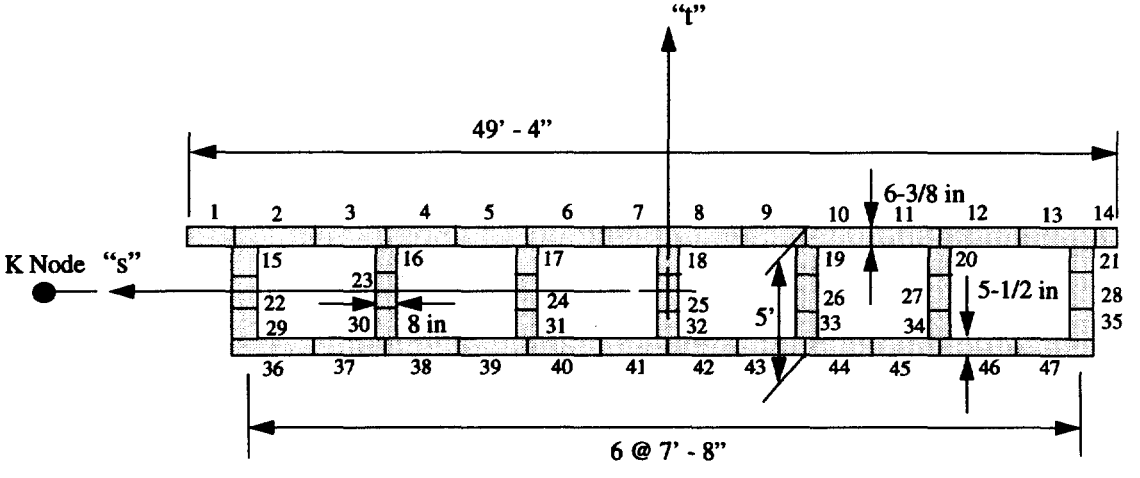

Sections: WSD2

Six Cell Box Girder Deck Segments — *Section 6*

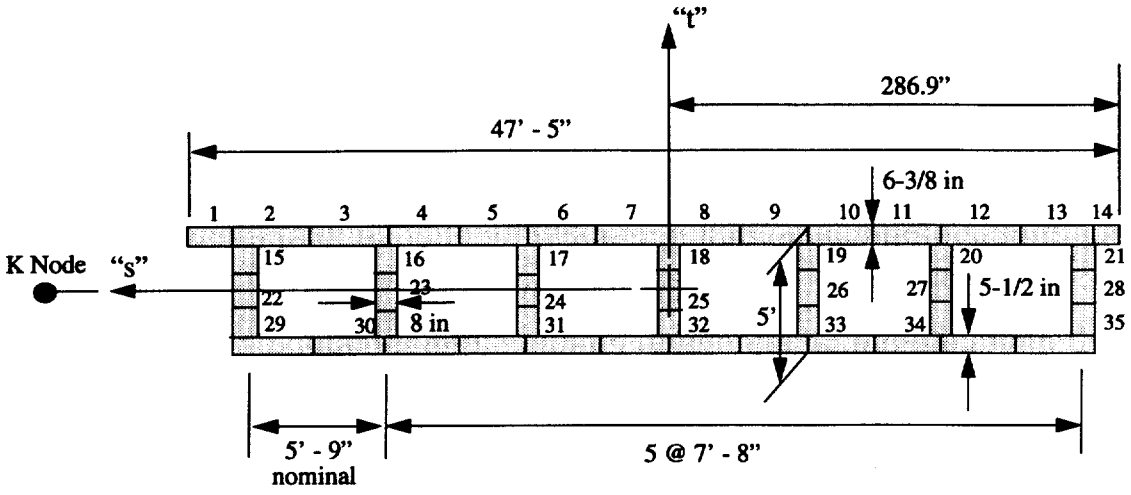

Sections: WSD1

Six Cell Box Girder Deck Segments — *Section 7*

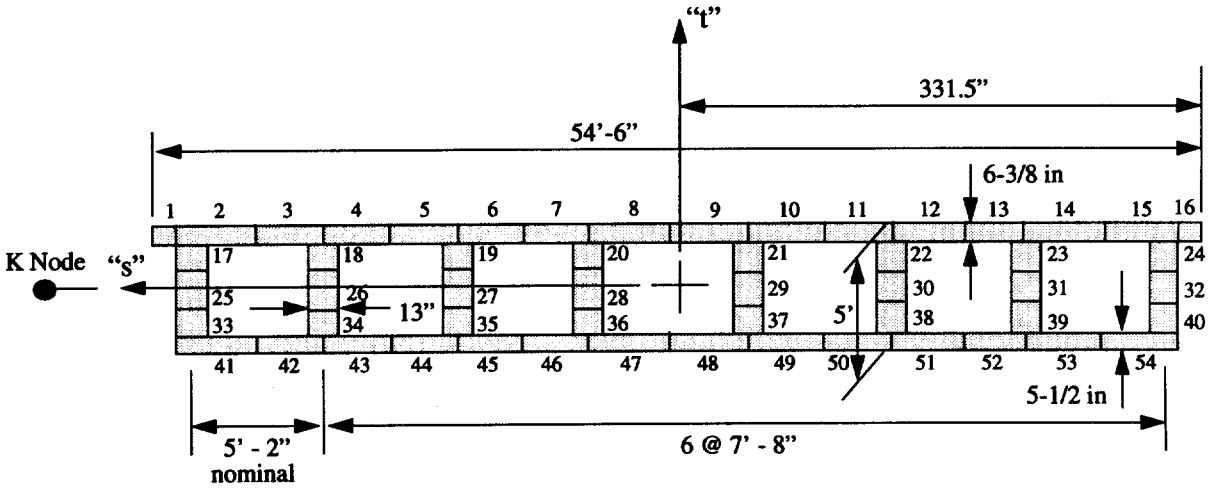

Sections: WSD3A

Expansion Joint Segment - Seven Cell Box Girder Deck Segments — *Section 8*

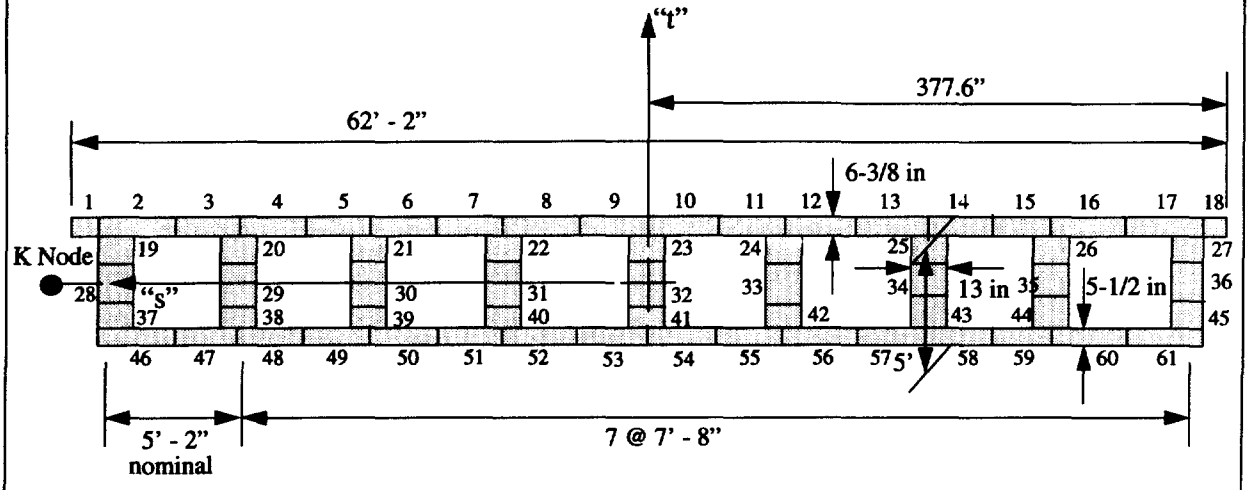

Sections: WSD6A

Expansion Joint Segment - Eight Cell Box Girder Deck Segments — *Section 9*

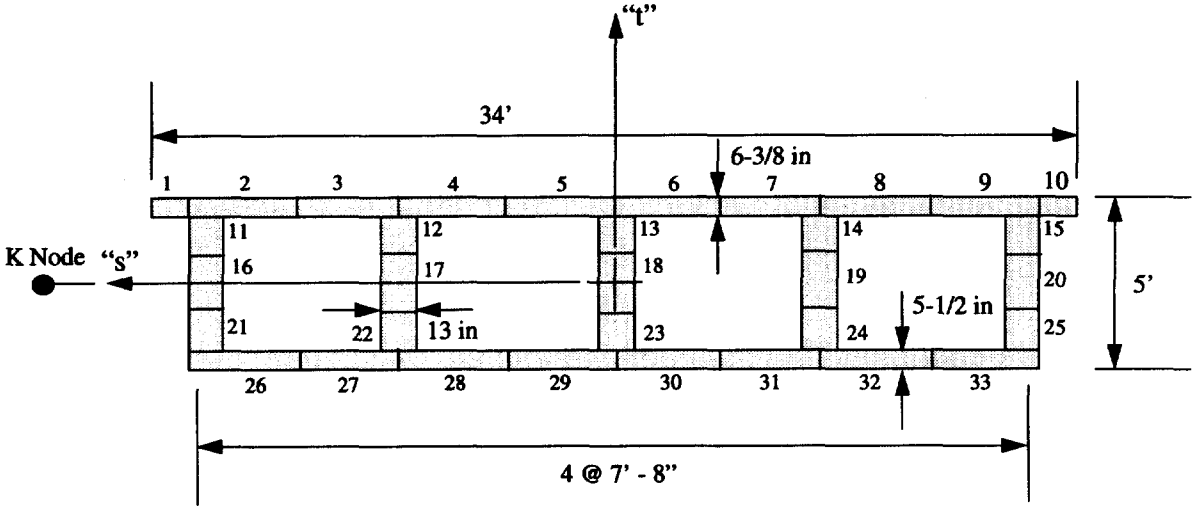

Sections: ESD2A, ESD4A, ESD6A

Sections: WSD8A, WSD11A, WSD15A, WSD22A

Expansion Joint Segment - Four Cell Box Girder Deck Segments — *Section 10*

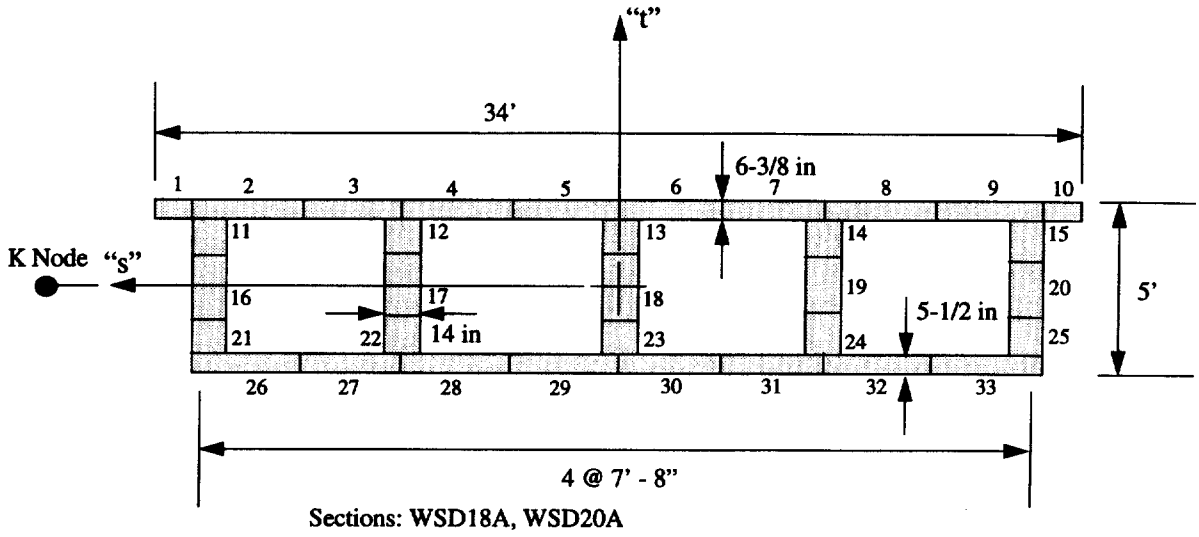

Sections: WSD18A, WSD20A

Expansion Joint Segment - Four Cell Box Girder Deck Segments — *Section 11*

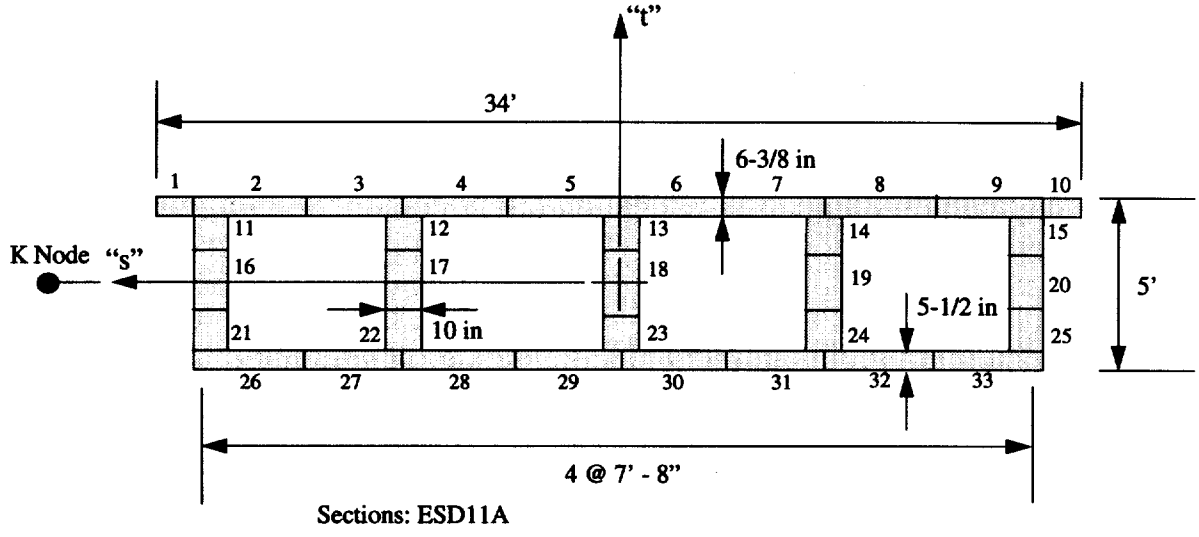

Sections: ESD11A

Expansion Joint Segment - Four Cell Box Girder Deck Segments — *Section 12*

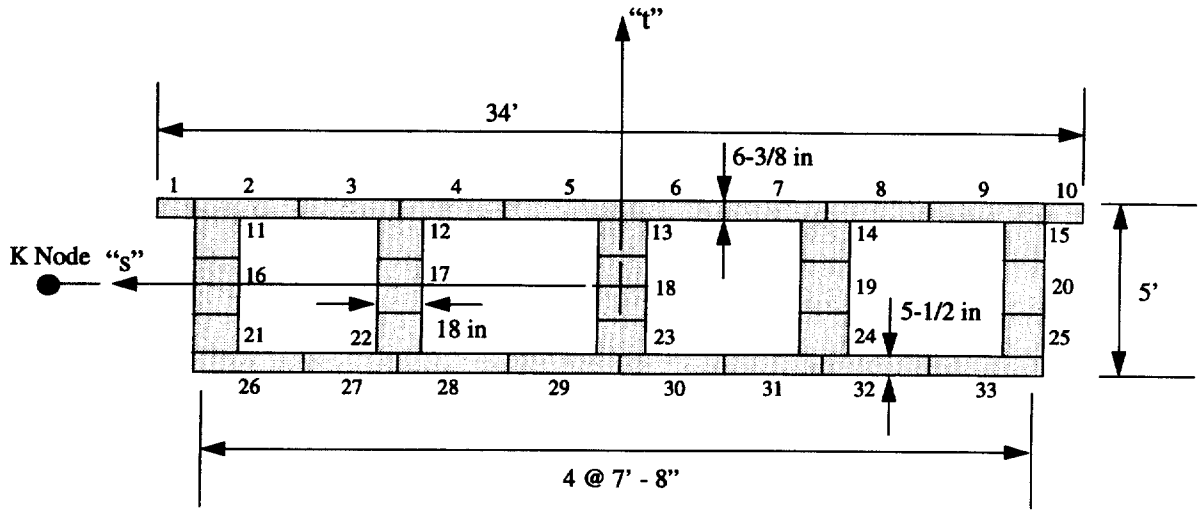

Sections: ESD9A

Expansion Joint Segment - Four Cell Box Girder Deck Segments *Section 13*

Deck Section	Cross-Sectional Area (in2)	Length (ft)
WSD1	9275	80.8
WSD2	9549	97.2
WSD3	10220	97.1
WSD4	10750	97.2
WSD5	11700	97.2
WSD6	12230	97.1
WSD7	6593	97.1
WSD8	6593	97.1
WSD9	6593	98.3
WSD10	6593	99.1
WSD11	6593	85.7
WSD12	6593	88.6
WSD13	6593	69.5
WSD14	6593	69.9
WSD15	6593	96.3
WSD16	6593	99.4
WSD17	6593	112.0
WSD18	6593	118.5
WSD19	6593	117.3
WSD20	6593	117.3
WSD21	6593	115.6
WSD22	6593	96.1
WSD23	6593	96.1
WSD24	6593	69.6
ESD1	6593	97.1
ESD2	6593	95.1
ESD3	6593	100.1
ESD4	6593	98.9
ESD5	6593	99.0
ESD6	6593	98.9
ESD7	6593	85.8
ESD8	6593	104.7
ESD9	6593	124.0
ESD10	6593	99.6
ESD11	6593	78.5
ESD12	6593	78.6
ESD13	6593	56.4

Area	η	ξ	Weight
1	-.960784	.780824	102.000
2	-.806373	.780824	299.6250
3	-.575980	.780824	299.6250
4	-.345588	.780824	299.6250
5	-.115196	.780824	299.6250
6	.115196	.780824	299.6250
7	.345588	.780824	299.6250
8	.575980	.780824	299.6250
9	.806373	.780824	299.6250
10	.960784	.780824	102.0000
11	-.901961	.429491	128.3336
12	-.450980	.429491	128.3336
13	.000000	.429491	128.3336
14	.450980	.429491	128.3336
15	.901961	.429491	128.3336
16	-.901961	-.073344	128.3329
17	-.450980	-.073344	128.3328
18	.000000	-.073344	128.3328
19	.450980	-.073344	128.3328
20	.901961	-.073344	128.3328
21	-.901961	-.576180	128.3335
22	-.450980	-.576180	128.3336
23	.000000	-.576180	128.3336
24	.450980	-.576180	128.3336
25	.901961	-.576180	128.3335
26	-.806373	-.913799	258.5000
27	-.575980	-.913799	258.5000
28	-.345588	-.913799	258.5000
29	-.115196	-.913799	258.5000
30	.115196	-.913799	258.5000
31	.345588	-.913799	258.5000
32	.575980	-.913799	258.5000
33	.806373	-.913799	258.5000

Section #1
Arel=.2533
B=408.0000
H=63.8047

Area	η	ξ	Weight
1	-.965523	.799891	102.0000
2	-.884973	.799891	287.2734
3	-.766085	.799891	287.2734
4	-.647197	.799891	287.2734
5	-.528310	.799891	287.2734
6	-.409422	.799891	287.2734
7	-.290534	.799891	287.2734
8	-.171646	.799891	287.2734
9	-.052759	.799891	287.2734
10	.066129	.799891	287.2734
11	.185017	.799891	287.2734
12	.303905	.799891	287.2734
13	.422792	.799891	287.2734
14	.541680	.799891	287.2734
15	.660568	.799891	287.2734
16	.779456	.799891	287.2734
17	.898344	.799891	287.2734
18	.978894	.799891	102.0000
19	-.933864	.444797	128.3335
20	-.751822	.444797	128.3336
21	-.509100	.444797	128.3336
22	-.266377	.444797	128.3336
23	-.023655	.444797	128.3336
24	.219067	.444797	128.3336
25	.461790	.444797	128.3336
26	.704512	.444797	128.3334
27	.947234	.444797	128.3335
28	-.933864	-.063423	128.3328
29	-.751822	-.063423	128.3329
30	-.509100	-.063423	128.3328
31	-.266377	-.063423	128.3328
32	-.023655	-.063423	128.3328
33	.219067	-.063423	128.3328
34	.461790	-.063423	128.3329
35	.704512	-.063423	128.3329
36	.947234	-.063423	128.3328
37	-.933864	-.571643	128.3336
38	-.751822	-.571643	128.3335
39	-.509100	-.571643	128.3336
40	-.266377	-.571643	128.3336
41	-.023655	-.571643	128.3336
42	.219067	-.571643	128.3336
43	.461790	-.571643	128.3335
44	.704512	-.571643	128.3337
45	.947234	-.571643	128.3337
46	-.884973	-.912877	247.8438
47	-.766085	-.912877	247.8438

Area	η	ξ	Weight
48	-.647197	-.912877	247.8438
49	-.528310	-.912877	247.8438
50	-.409422	-.912877	247.8438
51	-.290534	-.912877	247.8438
52	-.171646	-.912877	247.8438
53	-.052759	-.912877	247.8438
54	.066129	-.912877	247.8438
55	.185017	-.912877	247.8438
56	.303905	-.912877	247.8438
57	.422792	-.912877	247.8438
58	.541680	-.912877	247.8438
59	.660568	-.912877	247.8438
60	.779456	-.912877	247.8438
61	.898344	-.912877	247.8438

Section #2
Arel=.255577
B=758.0679
H=63.1288

Area	η	ξ	Weight
1	-.934589	.800434	102.000
2	-.854096	.800434	269.3438
3	-.737330	.800434	269.3438
4	-.620564	.800434	269.3438
5	-.503797	.800434	269.3438
6	-.387031	.800434	269.3438
7	-.270265	.800434	269.3438
8	-.153499	.800434	269.3438
9	-.036732	.800434	269.3438
10	.080034	.800434	269.3438
11	.196800	.800434	269.3438
12	.313566	.800434	269.3438
13	.430333	.800434	269.3438
14	.547099	.800434	269.3438
15	.663865	.800434	269.3438
16	.780631	.800434	269.3438
17	.897398	.800434	269.3438
18	.977890	.800434	102.0000
19	-.901425	.445232	128.3337
20	-.835096	.445232	128.3335
21	-.580836	.445232	128.3336
22	-.326575	.445232	128.3336
23	-.072315	.445232	128.3336
24	.181945	.445232	128.3336
25	.436206	.445232	128.3336
26	.690466	.445232	128.3335
27	.944726	.445232	128.3336
28	-.901425	-.063141	128.3328
29	-.835096	-.063141	128.3329
30	-.580836	-.063141	128.3328
31	-.326575	-.063141	128.3328
32	-.072315	-.063141	128.3328
33	.181945	-.063141	128.3328
34	.436206	-.063141	128.3329
35	.690466	-.063141	128.3329
36	.944726	-.063141	128.3328
37	-.901425	-.571513	128.3335
38	-.835096	-.571513	128.3336
39	-.580836	-.571513	128.3336
40	-.326575	-.571513	128.3336
41	-.072315	-.571513	128.3336
42	.181945	-.571513	128.3336
43	.436206	-.571513	128.3336
44	.690466	-.571513	128.3336
45	.944726	-.571513	128.3336
46	-.854096	-.912850	232.3750
47	-.737330	-.912850	232.3750

Area	η	ξ	Weight
48	-.620564	-.912850	232.3750
49	-.503797	-.912850	232.3750
50	-.387031	-.912850	232.3750
51	-.270265	-.912850	232.3750
52	-.153499	-.912850	232.3750
53	-.036732	-.912850	232.3750
54	.080034	-.912850	232.3750
55	.196800	-.912850	232.3750
56	.313566	-.912850	232.3750
57	.430333	-.912850	232.3750
58	.547099	-.912850	232.3750
59	.663865	-.912850	232.3750
60	.780631	-.912850	232.3750
61	.897398	-.912850	232.3750

Section #3
Arel=.256106
B=723.6679
H=63.1098

Area	η	ξ	Weight
1	-.961135	.797017	102.000
2	-.869643	.797017	286.4197
3	-.734710	.797017	286.4199
4	-.599778	.797017	286.4192
5	-.464845	.797017	286.4198
6	-.329912	.797017	286.4198
7	-.194980	.797017	286.4192
8	-.060047	.797017	286.4198
9	.074886	.797017	286.4199
10	.209818	.797017	286.4193
11	.344751	.797017	286.4198
12	.479683	.797017	286.4197
13	.614616	.797017	286.4192
14	.749549	.797017	286.4199
15	.884481	.797017	286.4197
16	.975974	.797017	102.0000
17	-.925096	.442490	128.3337
18	-.717871	.442490	128.3336
19	-.441570	.442490	128.3335
20	-.165269	.442490	128.3336
21	.111032	.442490	128.3336
22	.387333	.442490	128.3337
23	.663634	.442490	128.3336
24	.939935	.442490	128.3336
25	-.925096	-.064918	128.3328
26	-.717871	-.064918	128.3329
27	-.441570	-.064918	128.3329
28	-.165269	-.064918	128.3328
29	.111032	-.064918	128.3328
30	.387333	-.064918	128.3328
31	.663634	-.064918	128.3328
32	.939935	-.064918	128.3329
33	-.925096	-.572326	128.3335
34	-.717871	-.572326	128.3336
35	-.441570	-.572326	128.3336
36	-.165269	-.572326	128.3336
37	.111032	-.572326	128.3336
38	.387333	-.572326	128.3335
39	.663634	-.572326	128.3335
40	.939935	-.572326	128.3335
41	-.869643	-.913016	247.1072
42	-.734710	-.913016	247.1073
43	-.599778	-.913016	247.1068
44	-.464845	-.913016	247.1072
45	-.329912	-.913016	247.1073
46	-.194980	-.913016	247.1068
47	-.060047	-.913016	247.1073

Area	η	ξ	Weight
48	.074886	-.913016	247.1073
49	.209818	-.913016	247.1068
50	.344751	-.913016	247.1073
51	.479683	-.913016	247.1073
52	.614616	-.913016	247.1068
53	.749549	-.913016	247.1073
54	.884481	-.913016	247.1072

Section #4
Arel=.255380
B=655.9407
H=63.2298

Area	η	ξ	Weight
1	-.925966	.797485	102.000
2	-.834555	.797485	265.9287
3	-.702417	.797485	265.9287
4	-.570278	.797485	265.9286
5	-.438139	.797485	265.9287
6	-.306001	.797485	265.9280
7	-.173862	.797485	265.9286
8	-.041723	.797485	265.9287
9	.090415	.797485	265.9287
10	.222554	.797485	265.9287
11	.354693	.797485	265.9287
12	.486831	.797485	265.9281
13	.618970	.797485	265.9286
14	.751109	.797485	265.9287
15	.883247	.797485	265.9287
16	.974658	.797485	102.0000
17	-.887954	.442865	128.3336
18	-.811929	.442865	128.3337
19	-.520500	.442865	128.3335
20	-.229071	.442865	128.3336
21	.062358	.442865	128.3336
22	.353788	.442865	128.3336
23	.645217	.442865	128.3336
24	.936646	.442865	128.3337
25	-.887954	-.064675	128.3328
26	-.811929	-.064675	128.3329
27	-.520500	-.064675	128.3329
28	-.229071	-.064675	128.3328
29	.062358	-.064675	128.3328
30	.353788	-.064675	128.3328
31	.645217	-.064675	128.3328
32	.936646	-.064675	128.3329
33	-.887954	-.572215	128.3336
34	-.811929	-.572215	128.3335
35	-.520500	-.572215	128.3336
36	-.229071	-.572215	128.3336
37	.062358	-.572215	128.3336
38	.353788	-.572215	128.3336
39	.645217	-.572215	128.3336
40	.936646	-.572215	128.3334
41	-.834555	-.912993	229.4286
42	-.702417	-.912993	229.4287
43	-.570278	-.912993	229.4286
44	-.438139	-.912993	229.4286
45	-.306001	-.912993	229.4281
46	-.173862	-.912993	229.4286
47	-.041723	-.912993	229.4286

Area	η	ξ	Weight
48	.090415	-.912993	229.4286
49	.222554	-.912993	229.4286
50	.354693	-.912993	229.4287
51	.486831	-.912993	229.4281
52	.618970	-.912993	229.4286
53	.751109	-.912993	229.4287
54	.883247	-.912993	229.4286

Section #5
Arel=.256044
B=631.3713
H=63.2133

Area	η	ξ	Weight
1	-.972973	.793091	102.0000
2	-.867117	.793091	297.5002
3	-.709459	.793091	297.5002
4	-.551802	.793091	297.4996
5	-.394144	.793091	297.5002
6	-.236486	.793091	297.4996
7	-.078829	.793091	297.5002
8	.078829	.793091	297.5002
9	.236486	.793091	297.4996
10	.394144	.793091	297.5002
11	.551802	.793091	297.5002
12	.709459	.793091	297.4996
13	.867117	.793091	297.5002
14	.972973	.793091	102.0000
15	-.932432	.439338	128.3336
16	-.621622	.439338	128.3336
17	-.310811	.439338	128.3336
18	.000000	.439338	128.3336
19	.310811	.439338	128.3336
20	.621622	.439338	128.3336
21	.932432	.439338	128.3336
22	-.932432	-.066961	128.3329
23	-.621622	-.066961	128.3329
24	-.310811	-.066961	128.3328
25	.000000	-.066961	128.3328
26	.310811	-.066961	128.3328
27	.621622	-.066961	128.3328
28	.932432	-.066961	128.3330
29	-.932432	-.573261	128.3336
30	-.621622	-.573261	128.3335
31	-.310811	-.573261	128.3336
32	.000000	-.573261	128.3336
33	.310811	-.573261	128.3336
34	.621622	-.573261	128.3335
35	.932432	-.573261	128.3336
36	-.867117	-.913206	256.6669
37	-.709459	-.913206	256.6669
38	-.551802	-.913206	256.6663
39	-.394144	-.913206	256.6669
40	-.236486	-.913206	256.6663
41	-.078829	-.913206	256.6668
42	.078829	-.913206	256.6668
43	.236486	-.913206	256.6663
44	.394144	-.913206	256.6669
45	.551802	-.913206	256.6669
46	.709459	-.913206	256.6663
47	.867117	-.913206	256.6669

Section #6
Arel=.254545
B=592.0000
H=63.3682

Area	η	ξ	Weight
1	-.955477	.793240	102.0000
2	-.849599	.793240	285.2813
3	-.693614	.793240	285.2813
4	-.537629	.793240	285.2813
5	-.381644	.793240	285.2813
6	-.225659	.793240	285.2813
7	-.069674	.793240	285.2813
8	.086311	.793240	285.2813
9	.242296	.793240	285.2813
10	.398281	.793240	285.2813
11	.554266	.793240	285.2813
12	.710251	.793240	285.2813
13	.866236	.793240	285.2813
14	.972114	.793240	102.0000
15	-.913648	.439458	128.3336
16	-.673135	.439458	128.3336
17	-.352451	.439458	128.3336
18	-.031767	.439458	128.3336
19	.288918	.439458	128.3336
20	.609602	.439458	128.3336
21	.930286	.439458	128.3334
22	-.913648	-.066884	128.3328
23	-.673135	-.066884	128.3328
24	-.352451	-.066884	128.3328
25	-.031767	-.066884	128.3328
26	.288918	-.066884	128.3328
27	.609602	-.066884	128.3329
28	.930286	-.066884	128.3329
29	-.913648	-.573225	128.3336
30	-.673135	-.573225	128.3336
31	-.352451	-.573225	128.3336
32	-.031767	-.573225	128.3336
33	.288918	-.573225	128.3336
34	.609602	-.573225	128.3335
35	.930286	-.573225	128.3337
36	-.849599	-.913198	246.1250
37	-.693614	-.913198	246.1250
38	-.537629	-.913198	246.1250
39	-.381644	-.913198	246.1250
40	-.225659	-.913198	246.1250
41	-.069674	-.913198	246.1250
42	.086311	-.913198	246.1250
43	.242296	-.913198	246.1250
44	.398281	-.913198	246.1250
45	.554266	-.913198	246.1250
46	.710251	-.913198	246.1250
47	.866236	-.913198	246.1250

Section #7
Arel=.255140
B=573.7731
H=63.3629

Area	η	ξ	Weight
1	-.952720	.818700	86.0625
2	-.864798	.818700	285.5089
3	-.729682	.818700	285.5088
4	-.594565	.818700	285.5089
5	-.459449	.818700	285.5094
6	-.324333	.818700	285.5089
7	-.189217	.818700	285.5089
8	-.054100	.818700	285.5088
9	.081016	.818700	285.5088
10	.216132	.818700	285.5088
11	.351248	.818700	285.5088
12	.486364	.818700	285.5094
13	.621481	.818700	285.5083
14	.756597	.818700	285.5094
15	.891713	.818700	285.5088
16	.979636	.818700	86.0625
17	-.912746	.459895	208.5421
18	-.725695	.459895	208.5422
19	-.448135	.459895	208.5421
20	-.170576	.459895	208.5421
21	.106983	.459895	208.5421
22	.384542	.459895	208.5420
23	.662102	.459895	208.5421
24	.939661	.459895	208.5422
25	-.912746	-.053636	208.5408
26	-.725695	-.053636	208.5409
27	-.448135	-.053636	208.5408
28	-.170576	-.053636	208.5408
29	.106983	-.053636	208.5408
30	.384542	-.053636	208.5408
31	.662102	-.053636	208.5409
32	.939661	-.053636	208.5409
33	-.912746	-.567166	208.5421
34	-.725695	-.567166	208.5420
35	-.448135	-.567166	208.5420
36	-.170576	-.567166	208.5421
37	.106983	-.567166	208.5421
38	.384542	-.567166	208.5420
39	.662102	-.567166	208.5420
40	.939661	-.567166	208.5421
41	-.864798	-.911966	246.3214
42	-.729682	-.911966	246.3213
43	-.594565	-.911966	246.3214
44	-.459449	-.911966	246.3219
45	-.324333	-.911966	246.3213
46	-.189217	-.911966	246.3214
47	-.054100	-.911966	246.3214

Area	η	ξ	Weight
48	.081016	-.911966	246.3214
49	.216132	-.911966	246.3214
50	.351248	-.911966	246.3213
51	.486364	-.911966	246.3219
52	.621481	-.911966	246.3208
53	.756597	-.911966	246.3219
54	.891713	-.911966	246.3214

Section #8
Arel=.304775
B=662.9214
H=62.4759

Area	η	ξ	Weight
1	-.957860	.820584	86.0625
2	-.880476	.820584	286.4766
3	-.761461	.820584	286.4766
4	-.642447	.820584	286.4766
5	-.523433	.820584	286.4766
6	-.404418	.820584	286.4766
7	-.285404	.820584	286.4766
8	-.166390	.820584	286.4766
9	-.047376	.820584	286.4766
10	.071639	.820584	286.4766
11	.190653	.820584	286.4766
12	.309667	.820584	286.4766
13	.428682	.820584	286.4766
14	.547696	.820584	286.4766
15	.666710	.820584	286.4766
16	.785725	.820584	286.4766
17	.904739	.820584	286.4766
18	.982123	.820584	86.0625
19	-.922768	.461407	208.5422
20	-.758565	.461407	208.5420
21	-.514908	.461407	208.5421
22	-.271252	.461407	208.5421
23	-.027595	.461407	208.5421
24	.216062	.461407	208.5421
25	.459718	.461407	208.5421
26	.703375	.461407	208.5420
27	.947031	.461407	208.5421
28	-.922768	-.052656	208.5408
29	-.758565	-.052656	208.5410
30	-.514908	-.052656	208.5409
31	-.271252	-.052656	208.5408
32	-.027595	-.052656	208.5408
33	.216062	-.052656	208.5408
34	.459718	-.052656	208.5408
35	.703375	-.052656	208.5407
36	.947031	-.052656	208.5409
37	-.922768	-.566718	208.5420
38	-.758565	-.566718	208.5420
39	-.514908	-.566718	208.5420
40	-.271252	-.566718	208.5421
41	-.027595	-.566718	208.5421
42	.216062	-.566718	208.5421
43	.459718	-.566718	208.5420
44	.703375	-.566718	208.5420
45	.947031	-.566718	208.5420
46	-.880476	-.911875	247.1563
47	-.761461	-.911875	247.1563

Area	η	ξ	Weight
48	-.642447	-.911875	247.1563
49	-.523433	-.911875	247.1563
50	-.404418	-.911875	247.1563
51	-.285404	-.911875	247.1563
52	-.166390	-.911875	247.1563
53	-.047376	-.911875	247.1563
54	.071639	-.911875	247.1563
55	.190653	-.911875	247.1563
56	.309667	-.911875	247.1563
57	.428682	-.911875	247.1563
58	.547696	-.911875	247.1563
59	.666710	-.911875	247.1563
60	.785725	-.911875	247.1563
61	.904739	-.911875	247.1563

Section #9
Arel=.304279
B=755.1613
H=62.4113

Area	η	ξ	Weight
1	-.966912	.807006	86.0625
2	-.817096	.807006	303.6094
3	-.583640	.807006	303.6094
4	-.350184	.807006	303.6094
5	-.116728	.807006	303.6094
6	.116728	.807006	303.6094
7	.350184	.807006	303.6094
8	.583640	.807006	303.6094
9	.817096	.807006	303.6094
10	.966912	.807006	86.0625
11	-.901961	.450508	208.5421
12	-.450980	.450508	208.5421
13	.000000	.450508	208.5421
14	.450980	.450508	208.5421
15	.901961	.450508	208.5421
16	-.901961	-.059721	208.5409
17	-.450980	-.059721	208.5408
18	.000000	-.059721	208.5408
19	.450980	-.059721	208.5408
20	.901961	-.059721	208.5408
21	-.901961	-.569949	208.5420
22	-.450980	-.569949	208.5421
23	.000000	-.569949	208.5421
24	.450980	-.569949	208.5421
25	.901961	-.569949	208.5420
26	-.817096	-.912532	261.9375
27	-.583640	-.912532	261.9375
28	-.350184	-.912532	261.9375
29	-.116728	-.912532	261.9375
30	.116728	-.912532	261.9375
31	.350184	-.912532	261.9375
32	.583640	-.912532	261.9375
33	.817096	-.912532	261.9375

Section #10
Arel=.304992
B=408.0000
H=62.8802

Area	η	ξ	Weight
1	-.968137	.811358	82.8750
2	-.819240	.811358	304.4063
3	-.585172	.811358	304.4063
4	-.351103	.811358	304.4063
5	-.117034	.811358	304.4063
6	.117034	.811358	304.4063
7	.351103	.811358	304.4063
8	.585172	.811358	304.4063
9	.819240	.811358	304.4063
10	.968137	.811358	82.8750
11	-.901961	.454001	224.5838
12	-.450980	.454001	224.5838
13	.000000	.454001	224.5838
14	.450980	.454001	224.5838
15	.901961	.454001	224.5837
16	-.901961	-.057456	224.5824
17	-.450980	-.057456	224.5825
18	.000000	-.057456	224.5824
19	.450980	-.057456	224.5824
20	.901961	-.057456	224.5825
21	-.901961	-.568913	224.5838
22	-.450980	-.568913	224.5838
23	.000000	-.568913	224.5838
24	.450980	-.568913	224.5838
25	.901961	-.568913	224.5838
26	-.819240	-.912322	262.6250
27	-.585172	-.912322	262.6250
28	-.351103	-.912322	262.6250
29	-.117034	-.912322	262.6250
30	.117034	-.912322	262.6250
31	.351103	-.912322	262.6250
32	.585172	-.912322	262.6250
33	.819240	-.912322	262.6250

Section #11
Arel=.315344
B=408.0000
H=62.7292

Area	η	ξ	Weight
1	-.963235	.792295	95.6250
2	-.810662	.792295	301.2188
3	-.579044	.792295	301.2188
4	-.347426	.792295	301.2188
5	-.115809	.792295	301.2188
6	.115809	.792295	301.2188
7	.347426	.792295	301.2188
8	.579044	.792295	301.2188
9	.810662	.792295	301.2188
10	.963235	.792295	95.6250
11	-.901961	.438699	160.4169
12	-.450980	.438699	160.4170
13	.000000	.438699	160.4170
14	.450980	.438699	160.4170
15	.901961	.438699	160.4170
16	-.901961	-.067376	160.4160
17	-.450980	-.067376	160.4160
18	.000000	-.067376	160.4160
19	.450980	-.067376	160.4160
20	.901961	-.067376	160.4160
21	-.901961	-.573450	160.4170
22	-.450980	-.573450	160.4170
23	.000000	-.573450	160.4170
24	.450980	-.573450	160.4170
25	.901961	-.573450	160.4170
26	-.810662	-.913244	259.8750
27	-.579044	-.913244	259.8750
28	-.347426	-.913244	259.8750
29	-.115809	-.913244	259.8750
30	.115809	-.913244	259.8750
31	.347426	-.913244	259.8750
32	.579044	-.913244	259.8750
33	.810662	-.913244	259.8750

Section #12
Arel=.273963
B=408.0000
H=62.3964

Area	η	ξ	Weight
1	-.973039	.826562	70.125
2	-.827819	.826562	307.5938
3	-.591299	.826562	307.5938
4	-.354779	.826562	307.5938
5	-.118260	.826562	307.5938
6	.118260	.826562	307.5938
7	.354779	.826562	307.5938
8	.591299	.826562	307.5938
9	.827819	.826562	307.5938
10	.973039	.826562	70.1250
11	-.901961	.466206	288.7506
12	-.450980	.466206	288.7505
13	.000000	.466206	288.7506
14	.450980	.466206	288.7506
15	.901961	.466206	288.7505
16	-.901961	-.049545	288.7489
17	-.450980	-.049545	288.7488
18	.000000	-.049545	288.7488
19	.450980	-.049545	288.7488
20	.901961	-.049545	288.7488
21	-.901961	-.565295	288.7505
22	-.450980	-.565295	288.7506
23	.000000	-.565295	288.7506
24	.450980	-.565295	288.7506
25	.901961	-.565295	288.7505
26	-.827819	-.911586	265.3750
27	-.591299	-.911586	265.3750
28	-.354779	-.911586	265.3750
29	-.118260	-.911586	265.3750
30	.118260	-.911586	265.3750
31	.354779	-.911586	265.3750
32	.591299	-.911586	265.3750
33	.827819	-.911586	265.3750

Section #13
Arel=.356780
B=408.0000
H=62.2070

Appendix C - Hinge Details

24-580-980 Interchange - Hinge Restrainers

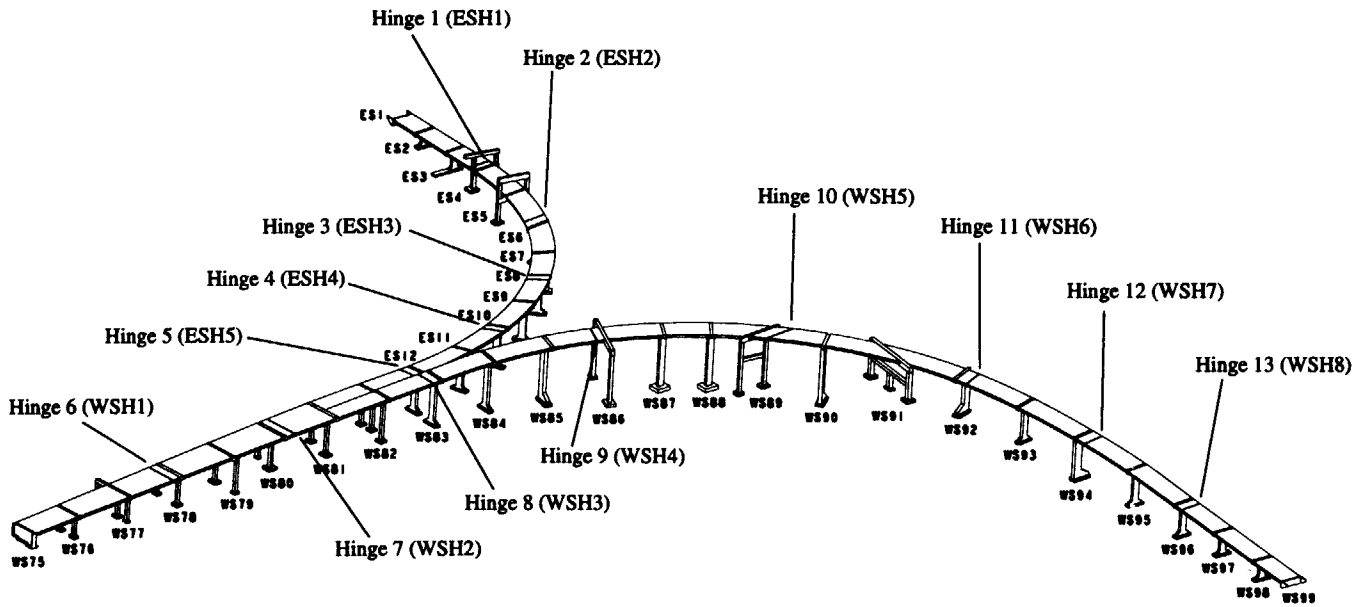

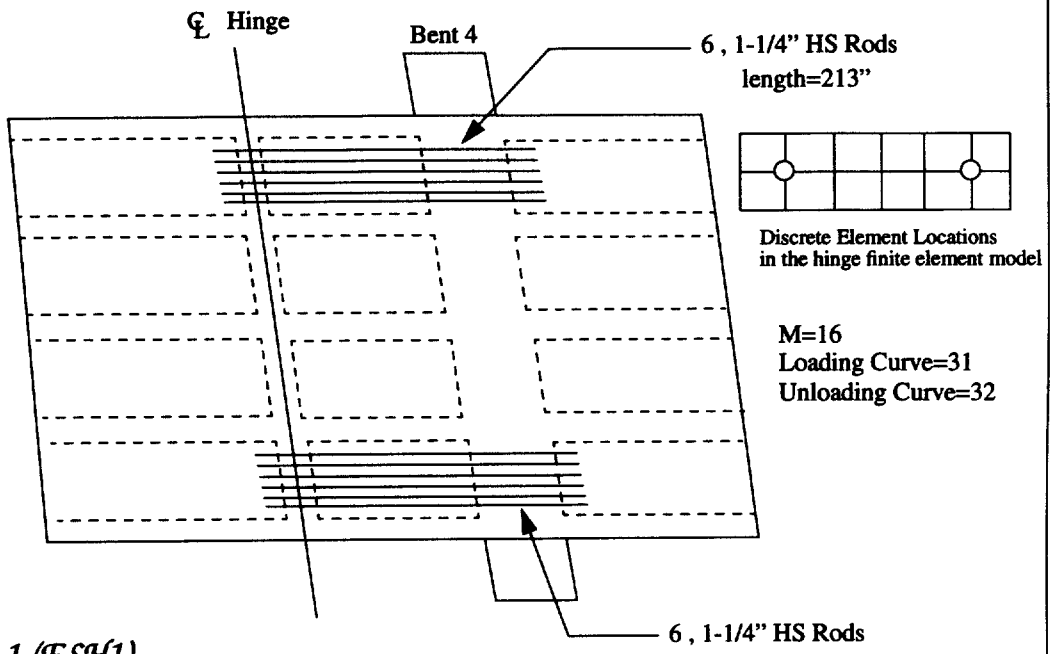

Hinge 1 (ESH1)

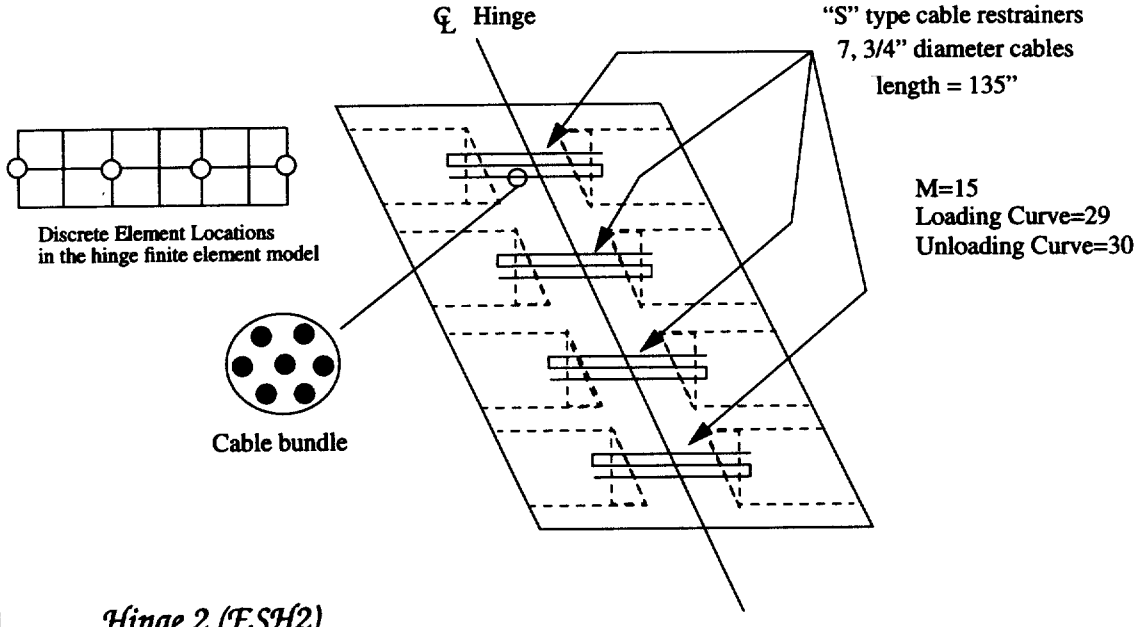

Hinge 2 (ESH2)

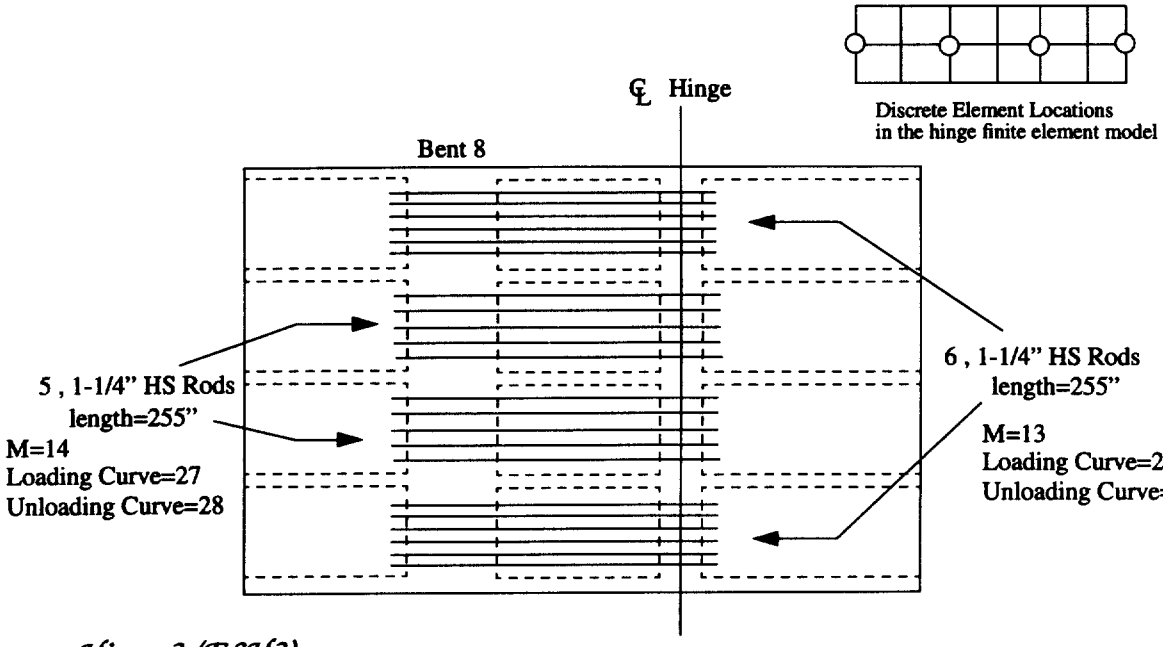

Hinge 3 (ESH3)

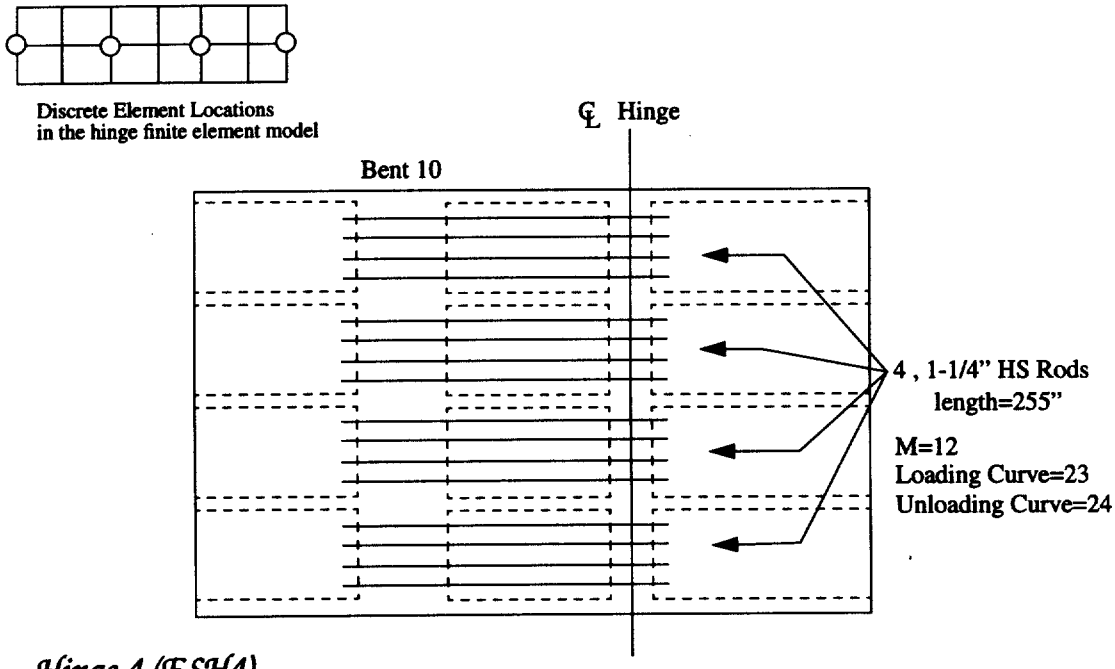

Hinge 4 (ESH4)

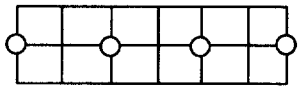

Discrete Element Locations
in the hinge finite element model

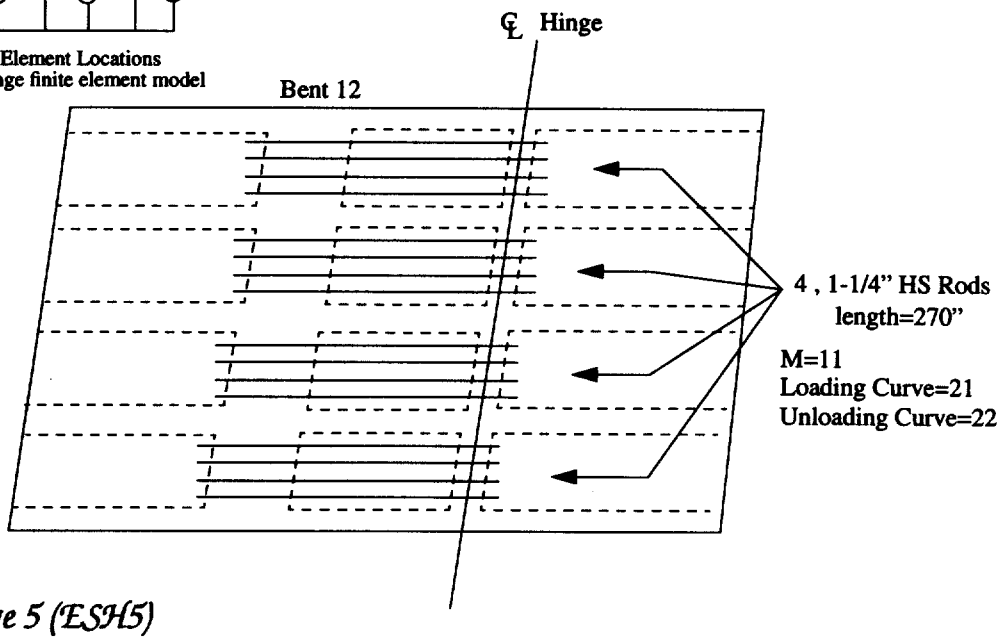

Hinge 5 (ESH5)

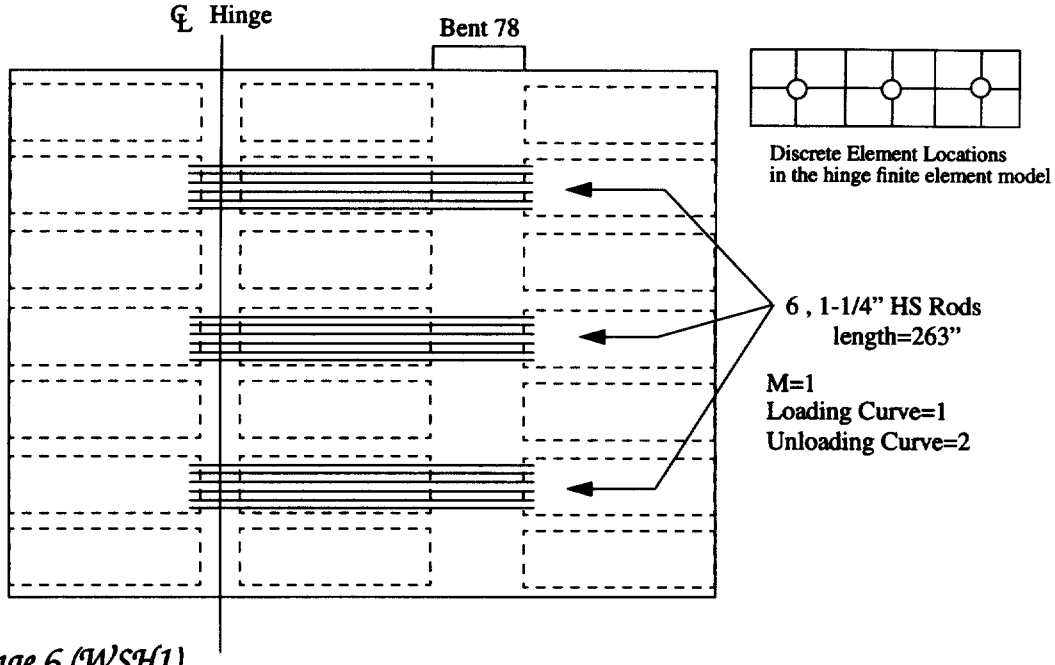

Discrete Element Locations
in the hinge finite element model

Hinge 6 (WSH1)

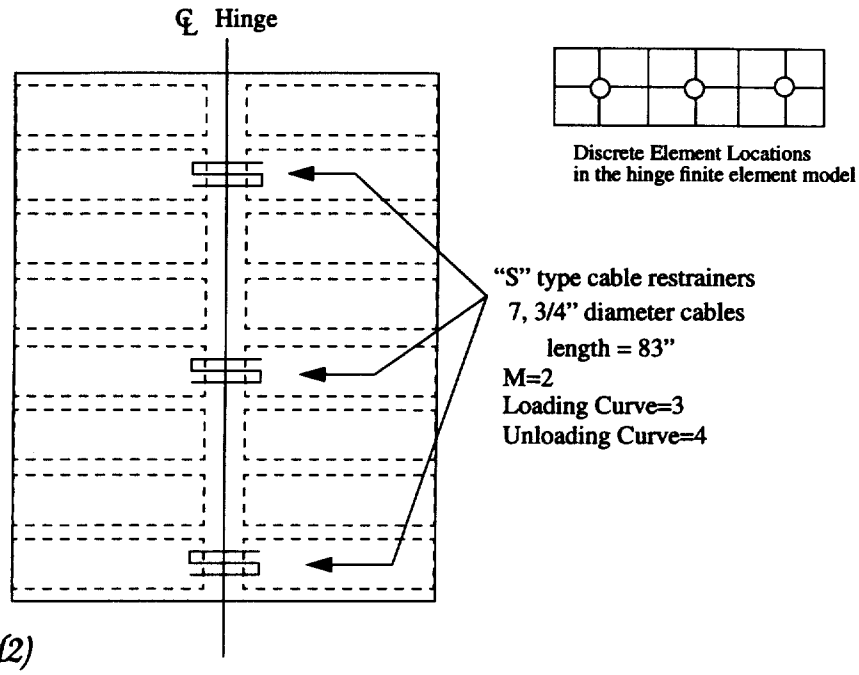

Hinge 7 (WSH2)

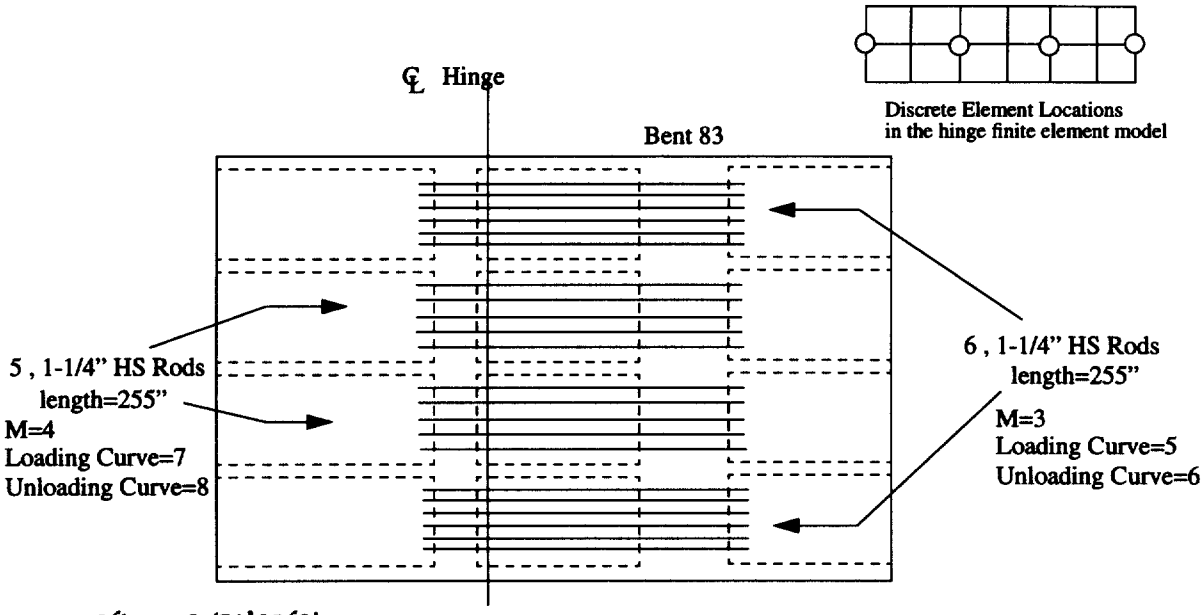

Hinge 8 (WSH3)

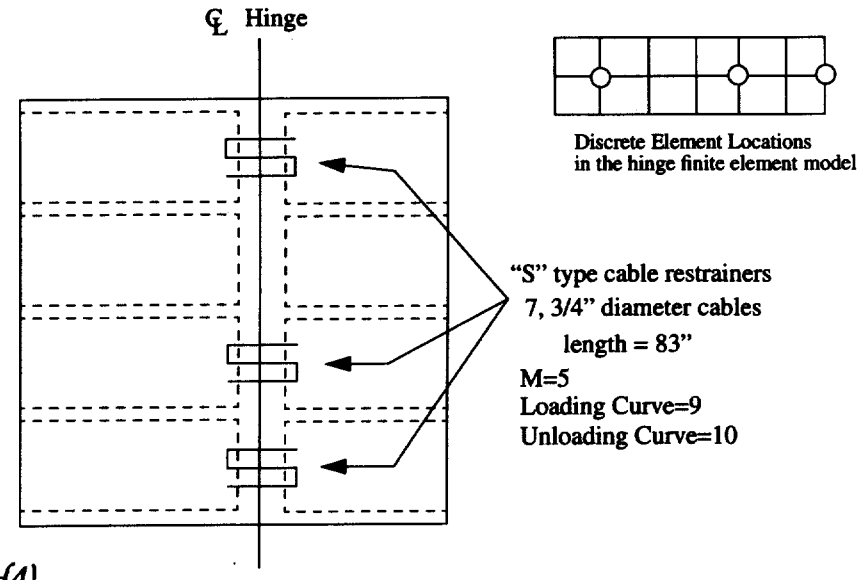

Hinge 9 (WSH4)

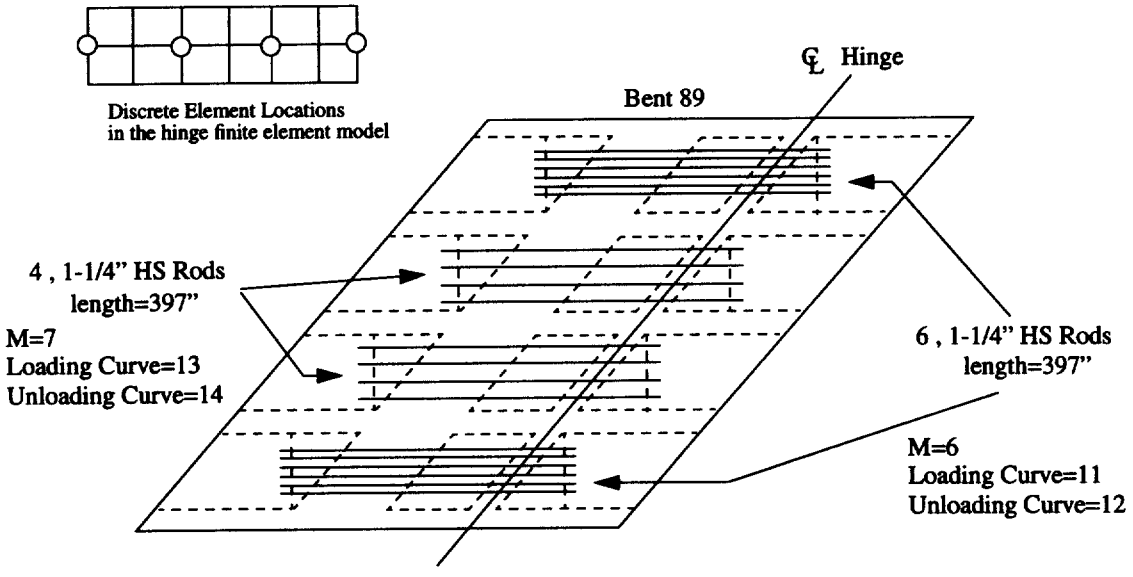

Hinge 10 (WSH5)

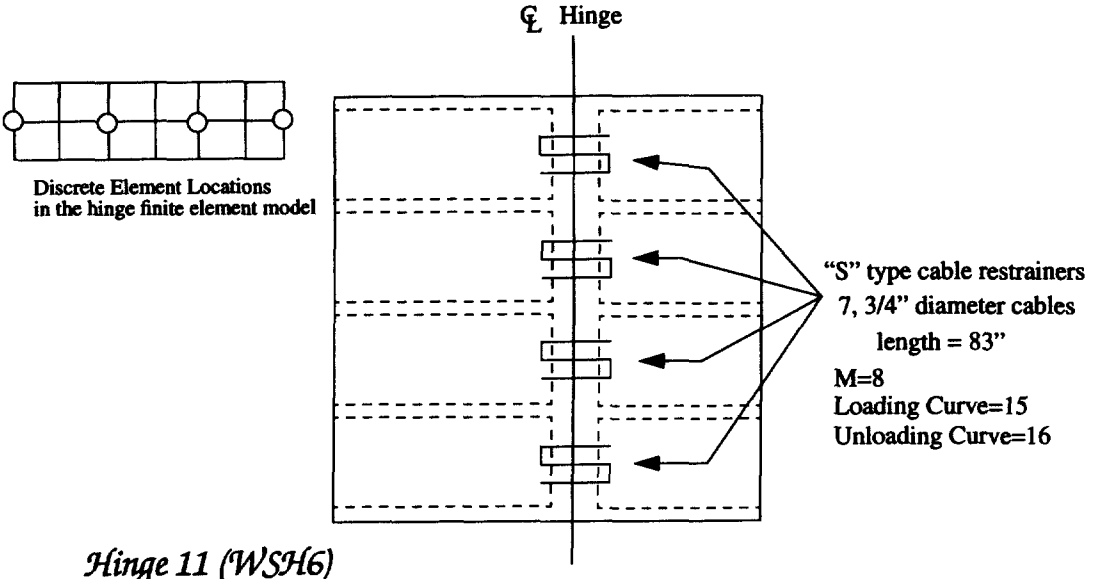

Hinge 11 (WSH6)

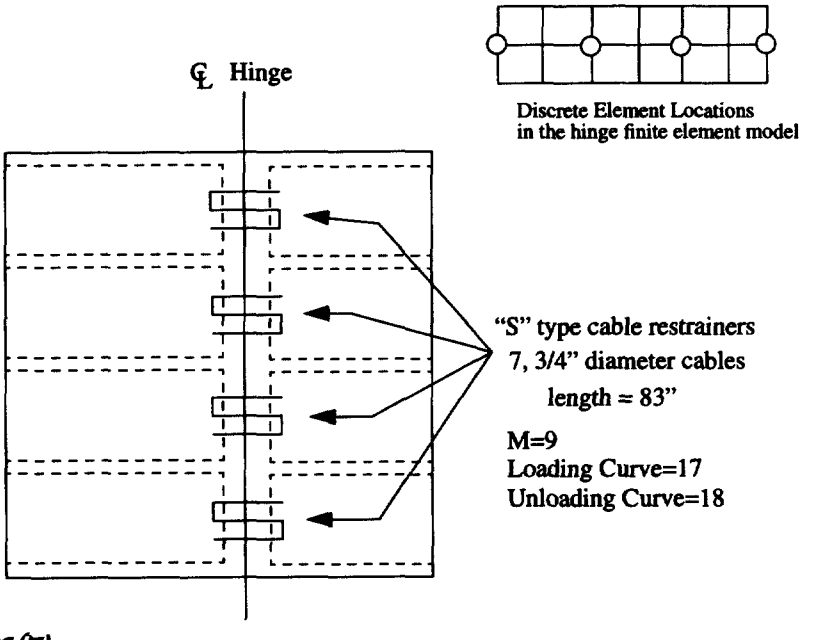

Hinge 12 (WSH7)

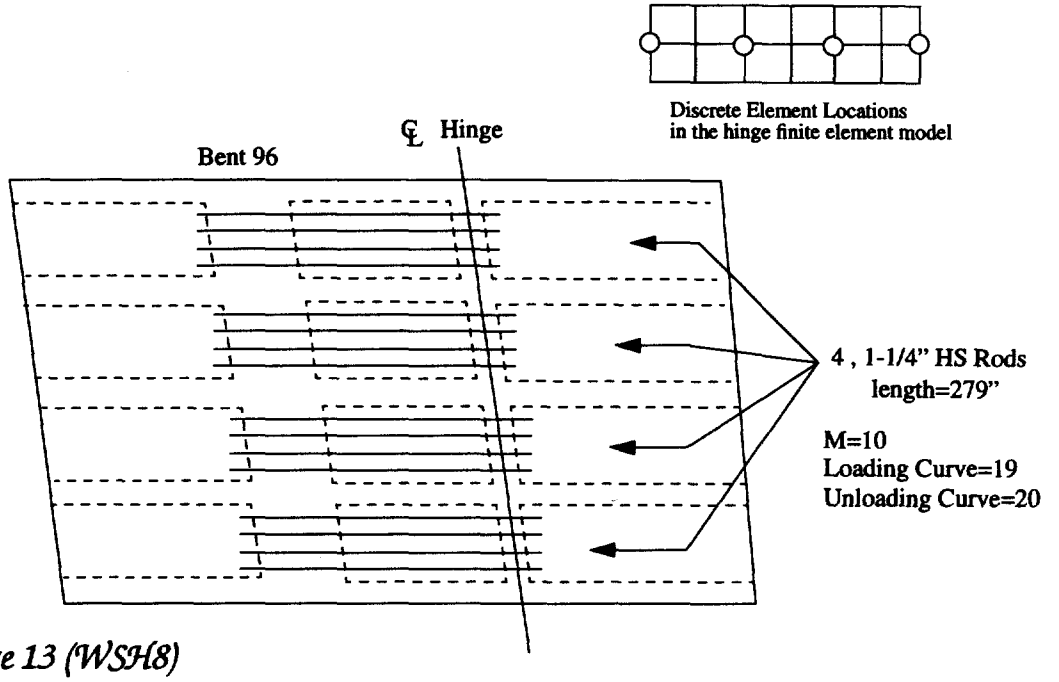

Hinge 13 (WSH8)

Hinge Number and restrainer type	Number of discrete elements	Discrete material number	Parameters for each discrete element			
			Loading direction	Yield force lb	Load curve pairs defining loading lb-in load curve number	Load curve pairs defining unloading lb-in load curve number
1 (ESH1) Steel rods	2	16	Positive	960,000.	(-50.,-2.) (-25.,-1.) (0.,0.) (1.40,960000.) (14.95,1050000.) 31	(-50.,-2.) (0.,0.) (93.,63900000.) 32
			Negative	-1.		
2 (ESH2) Cables	4	15	Positive	907,200.	(-50.,-2.) (-25.,-1.) (0.,0.) (2.37,907200.) (5.92,1145000.) 29	(-50.,-2.) (0.,0.) (59.,22680000.) 30
			Negative	-1.		
3 (ESH3) Steel rods	2	14	Positive	800,000.	(-50.,-2.) (-25.,-1.) (0.,0.) (1.48,800000.) (15.79,875000.) 27	(-50.,-2.) (0.,0.) (99.,53250000.) 28
			Negative	-1.		
	2	13	Positive	960,000.	(-50.,-2.) (-25.,-1.) (0.,0.) (1.67,960000.) (17.89,1050000.) 25	(-50.,-2.) (0.,0.) (112.,63900000.) 26
			Negative	-1.		
4 (ESH4) Steel rods	4	12	Positive	640,000.	(-50.,-2.) (-25.,-1.) (0.,0.) (1.67,640000.) (17.89,700000.) 23	(-50.,-2.) (0.,0.) (112.,42600000.) 24
			Negative	-1.		
5 (ESH5) Steel rods	4	11	Positive	640,000.	(-50.,-2.) (-25.,-1.) (0.,0.) (1.77,640000.) (18.95,700000.) 21	(-50.,-2.) (0.,0.) (118.,42600000.) 22
			Negative	-1.		
6 (WSH1) Steel rods	3	1	Positive	960,000.	(-50.,-2.) (-25.,-1.) (0.,0.) (1.73,960000.) (18.46,1050000.) 1	(-50.,-2.) (0.,0.) (115.,63900000.) 2
			Negative	-1.		
7 (WSH2) Cables	3	2	Positive	907200.	(-50.,-2.) (-25.,-1.) (0.,0.) (1.46,907200.) (3.64,1145000.) 3	(-50.,-2.) (0.,0.) (26.,22680000.) 4
			Negative	-1.		
8 (WSH3) Steel rods	2	3	Positive	960,000.	(-50.,-2.) (-25.,-1.) (0.,0.) (1.68,960000.) (17.89,1050000.) 5	(-50.,-2.) (0.,0.) (112.,63900000.) 6
			Negative	-1.		
	2	4	Positive	800,000.	(-50.,-2.) (-25.,-1.) (0.,0.) (1.68,800000.) (17.89,875000.) 7	(-50.,-2.) (0.,0.) (112.,53250000.) 8
			Negative	-1.		
9 (WSH4) Cables	3	5	Positive	907,200.	(-50.,-2.) (-25.,-1.) (0.,0.) (1.46,907200.) (3.64,1145000.) 9	(-50.,-2.) (0.,0.) (36.,22680000.) 10
			Negative	-1.		
10 (WSH5) Steel rods	2	6	Positive	960,000.	(-50.,-2.) (-25.,-1.) (0.,0.) (2.61,960000.) (27.86,1050000.) 11	(-50.,-2.) (0.,0.) (174.,63900000.) 12
			Negative	-1.		
	2	7	Positive	640,000.	(-50.,-2.) (-25.,-1.) (0.,0.) (2.61.640000.) (27.86,700000.) 13	(-50.,-2.) (0.,0.) (174.,42600000.) 14
			Negative	-1.		
11 (WSH6) Cables	4	8	Positive	907200.	(-50.,-2.) (-25.,-1.) (0.,0.) (1.46,907200.) (3.64,1145000.) 15	(-50.,-2.) (0.,0.) (36.,22680000.) 16
			Negative	-1.		
12 (WSH7) Cables	4	9	Positive	907200.	(-50.,-2.) (-25.,-1.) (0.,0.) (1.46,907200.) (3.64,1145000.) 17	(-50.,-2.) (0.,0.) (36.,22680000.) 18
			Negative	-1.		
13 (WSH8) Steel rods	4	10	Positive	640,000.	(-50.-2.) (-25.,-1.) (0.,0.) (1.84,640000.) (19.58,700000.) 19	(-50.,-2.) (0.,0.) (122.,42600000.) 20
			Negative	-1.		

Appendix D - Retrofit Design for WS and ES Lines

24-580-980 Interchange - Bent Properties (retrofit structure)

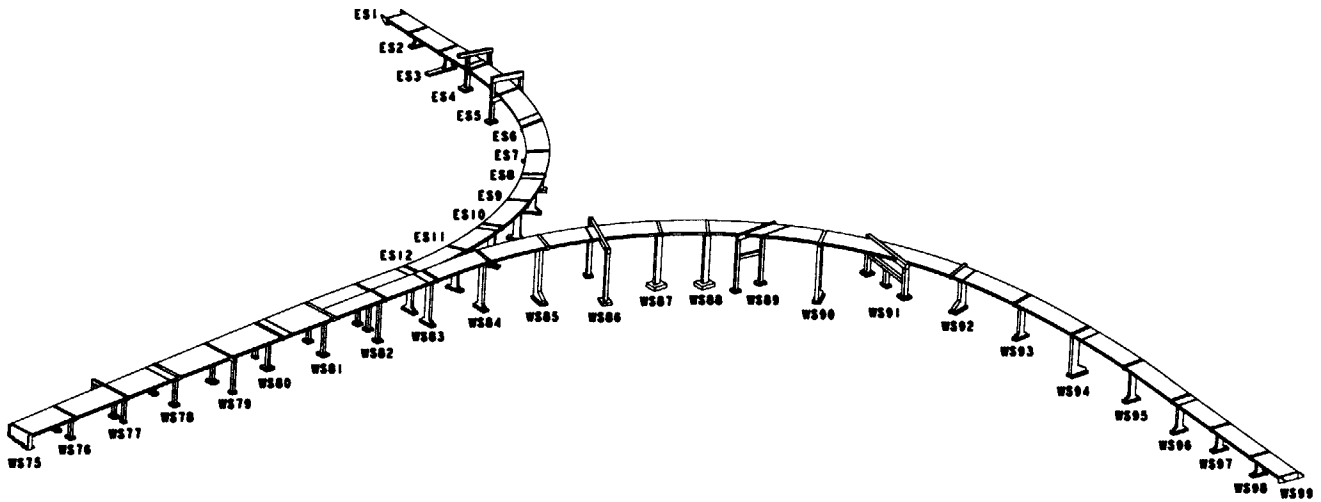

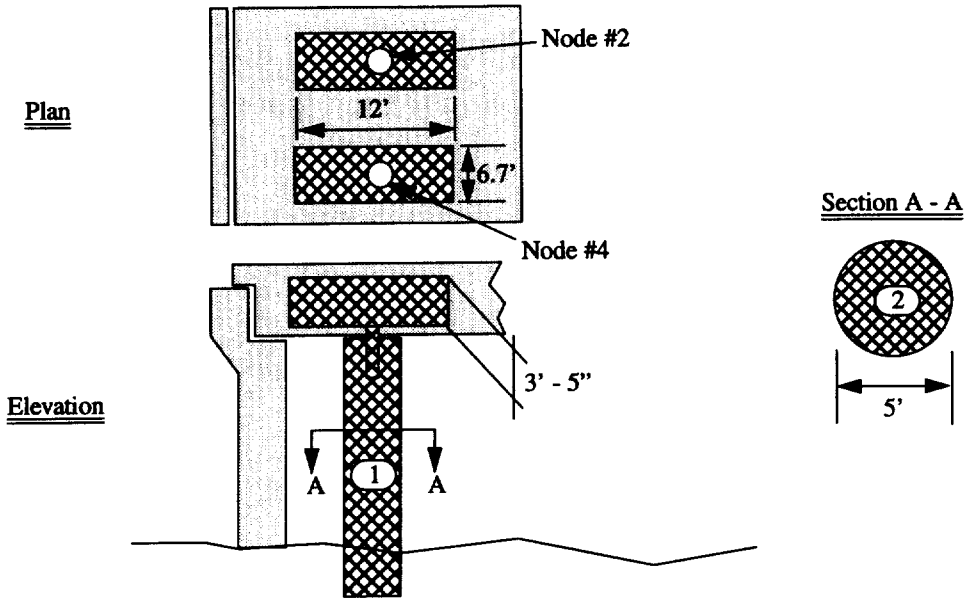

Abutment WS 75 (retrofitted)

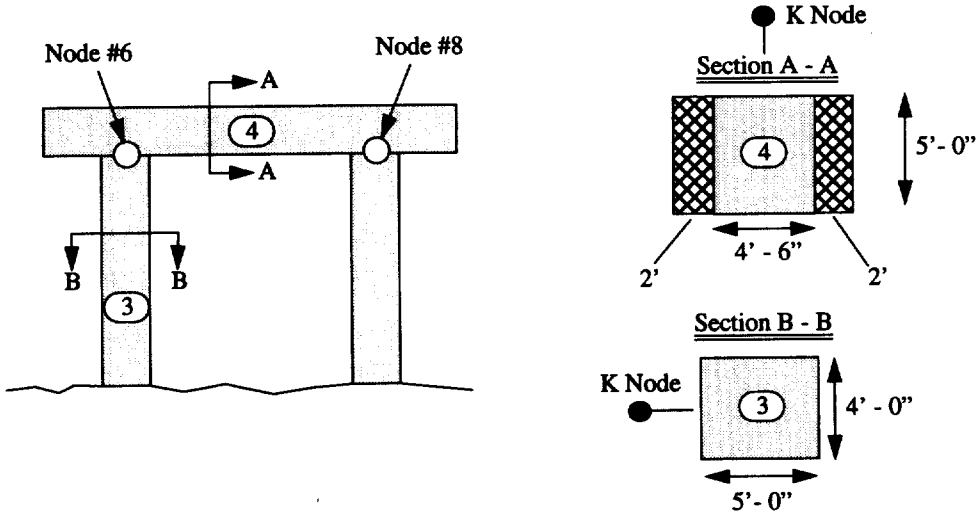

Bent WS 76 (retrofitted)

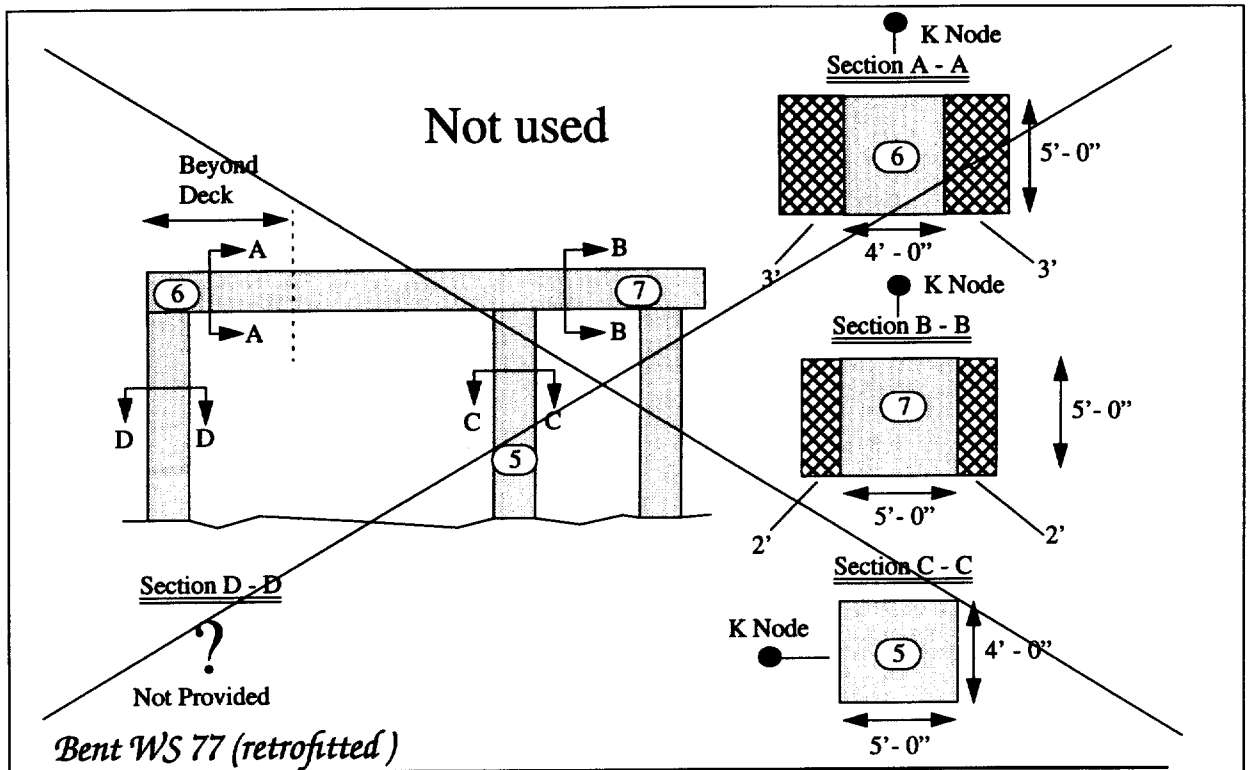

Bent WS 77 (retrofitted)

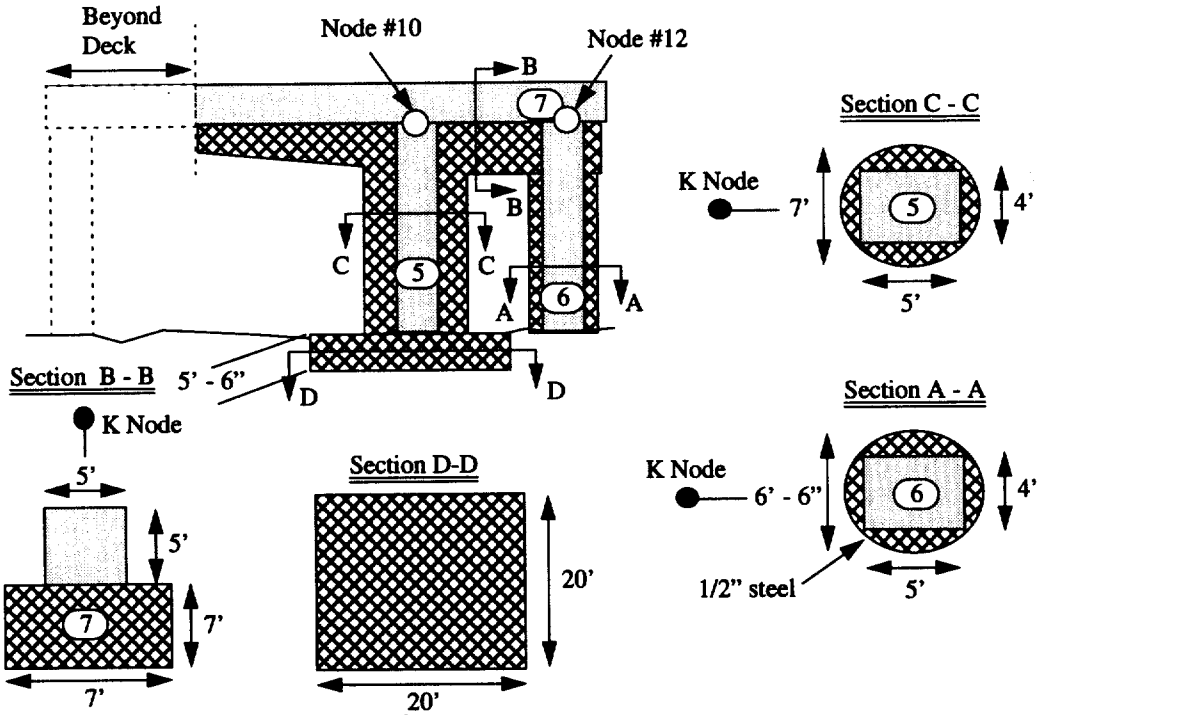

Bent WS 77 (retrofitted - alternate)

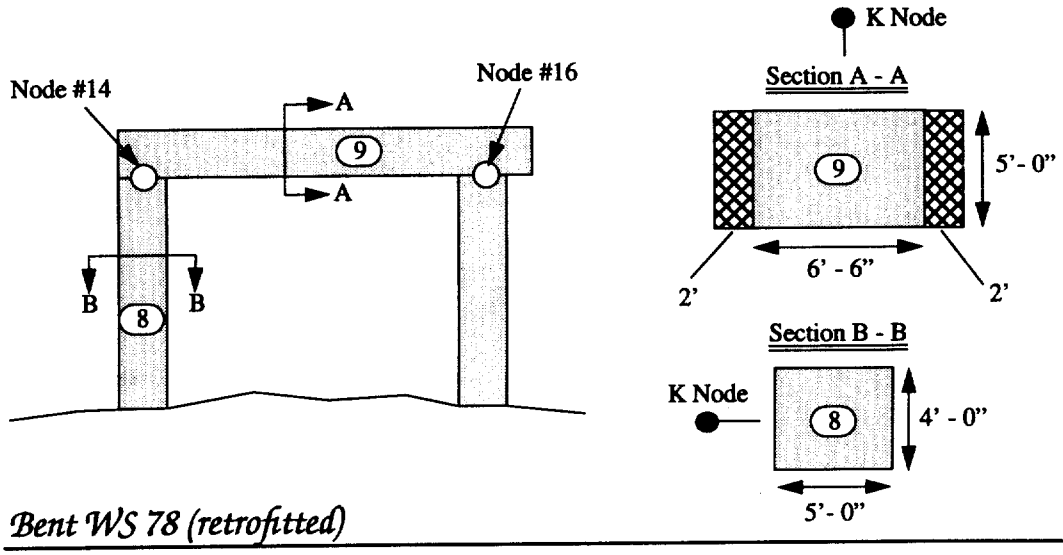

Bent WS 78 (retrofitted)

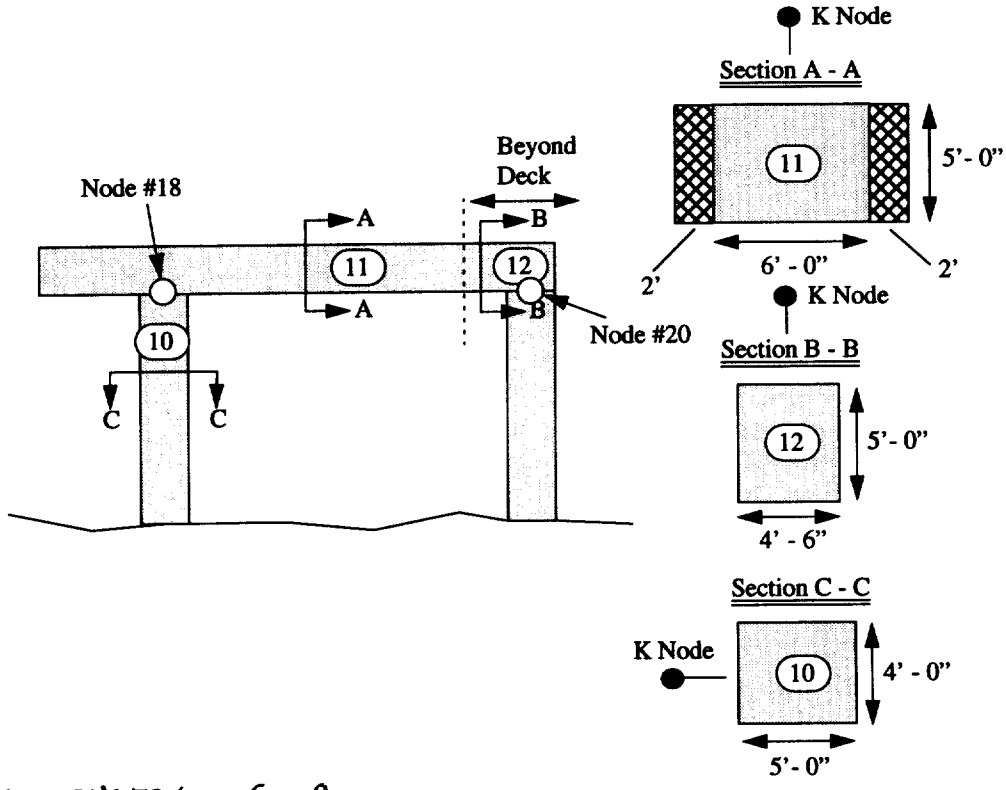

Bent WS 79 (retrofitted)

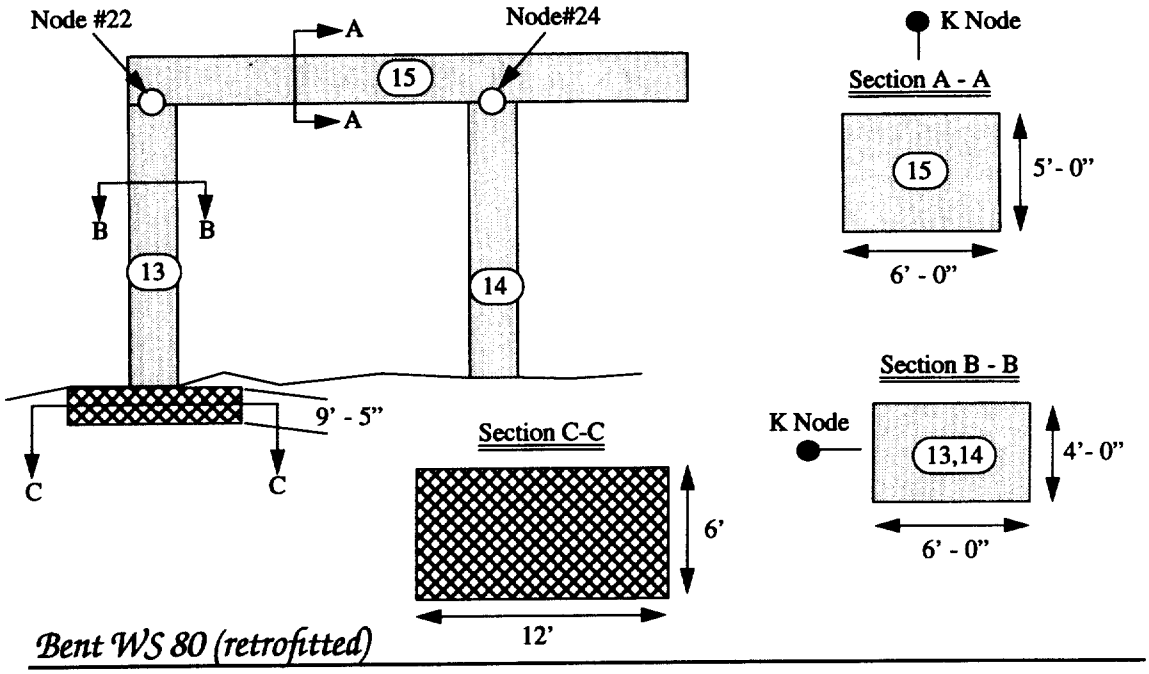

Bent WS 80 (retrofitted)

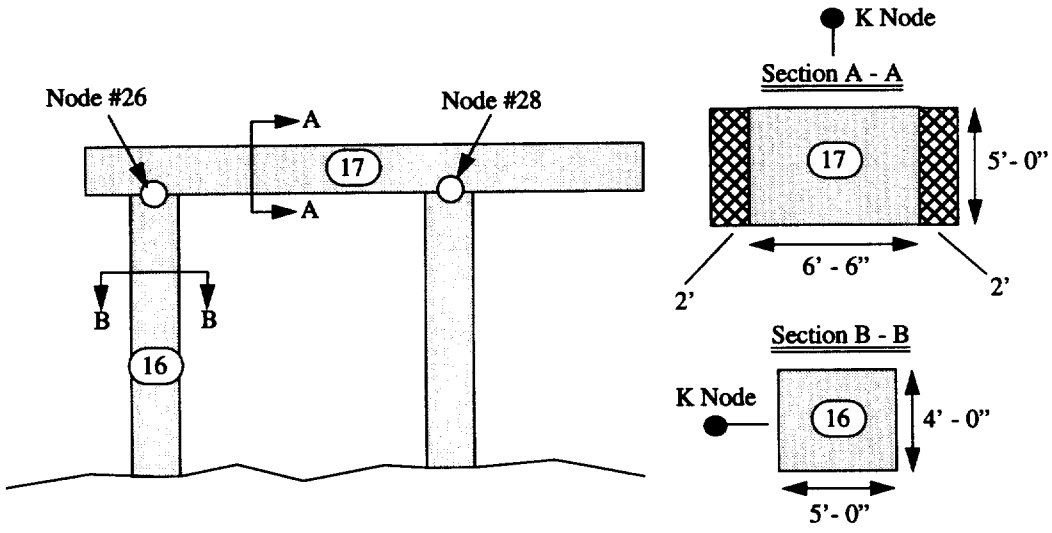

Bent WS 81 (retrofitted)

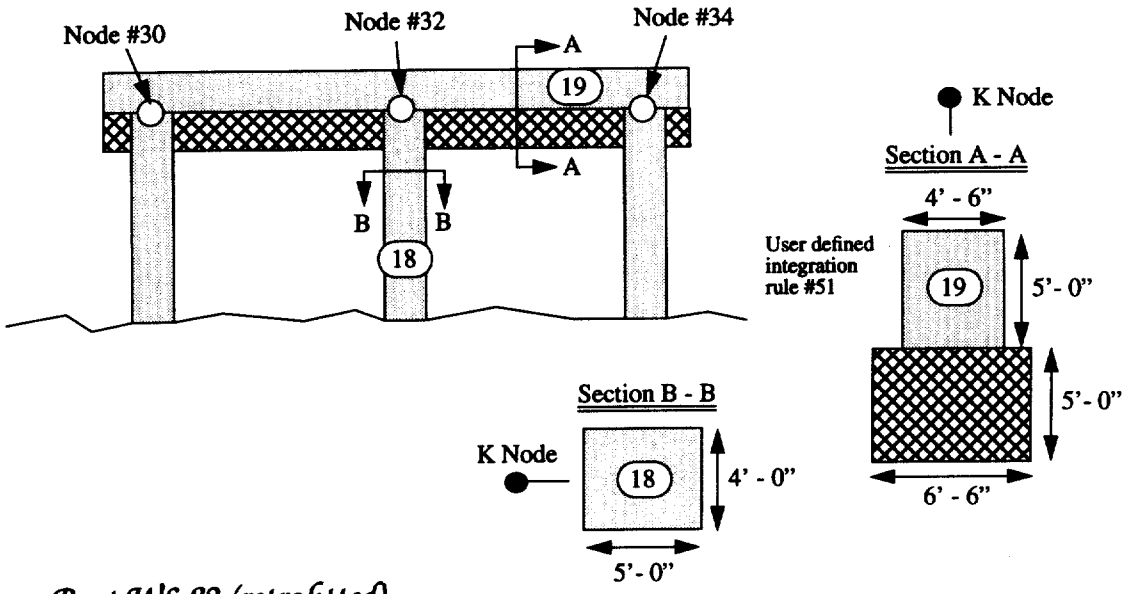

Bent WS 82 (retrofitted)

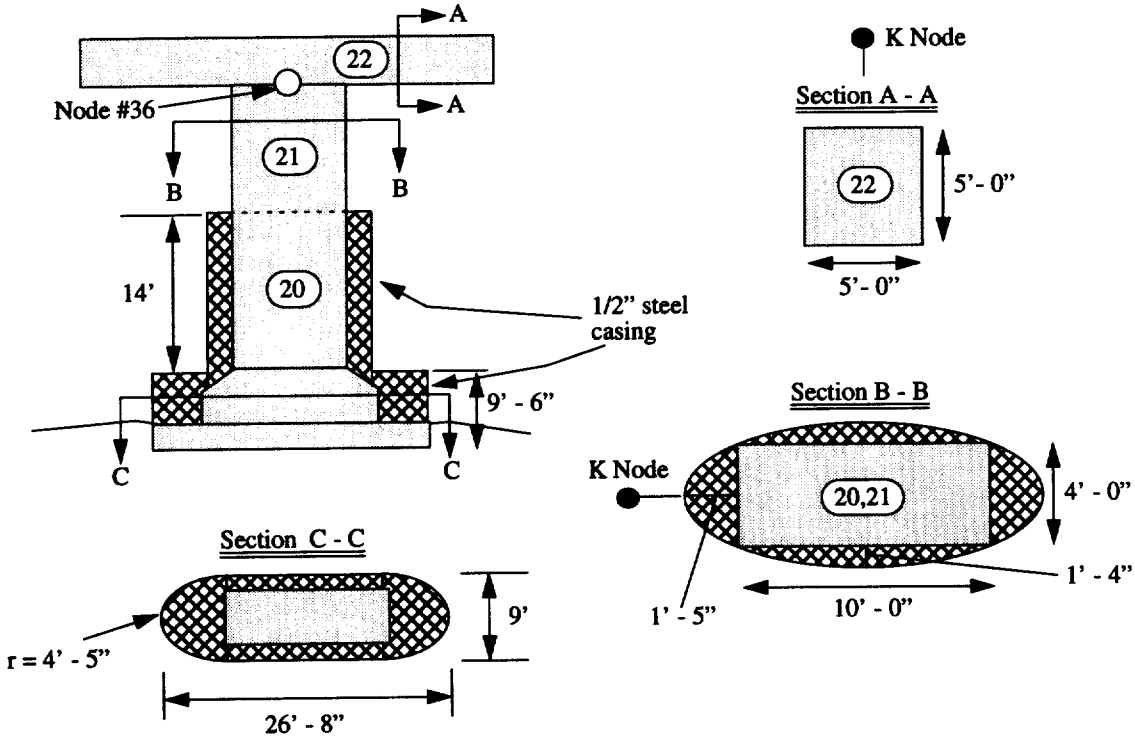

Bent WS 83 (retrofitted)

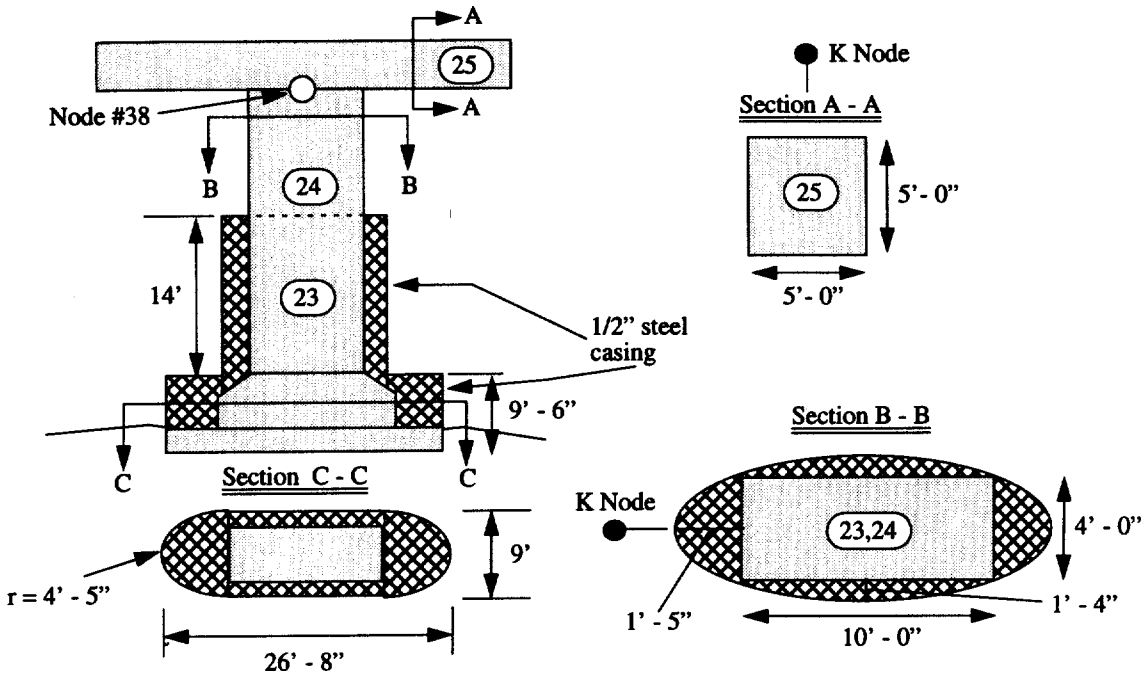

Bent WS 84 (retrofitted)

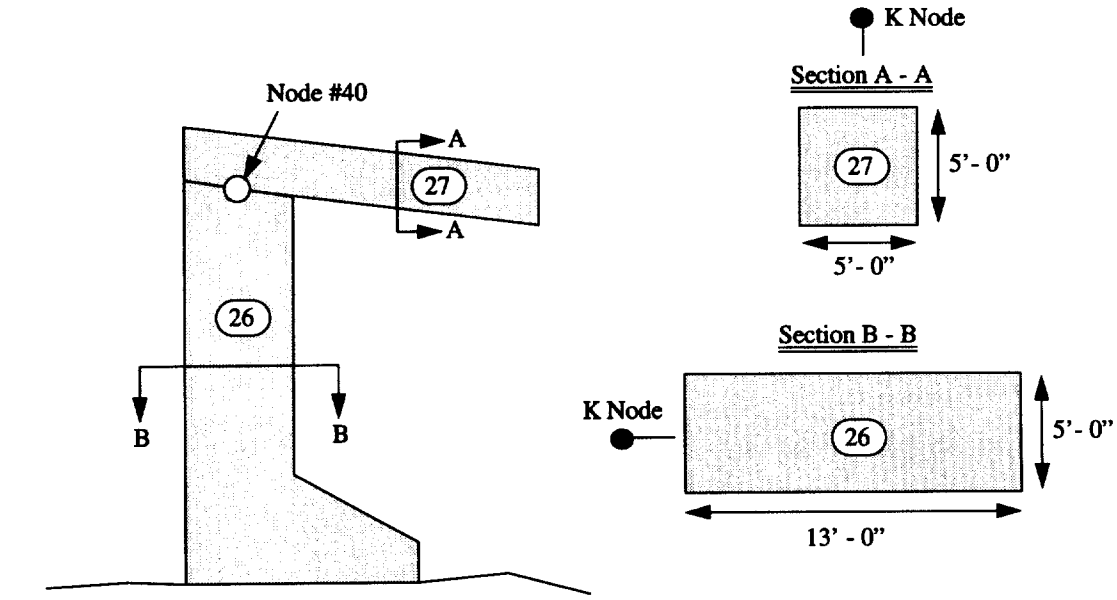

Bent WS 85 (retrofitted)

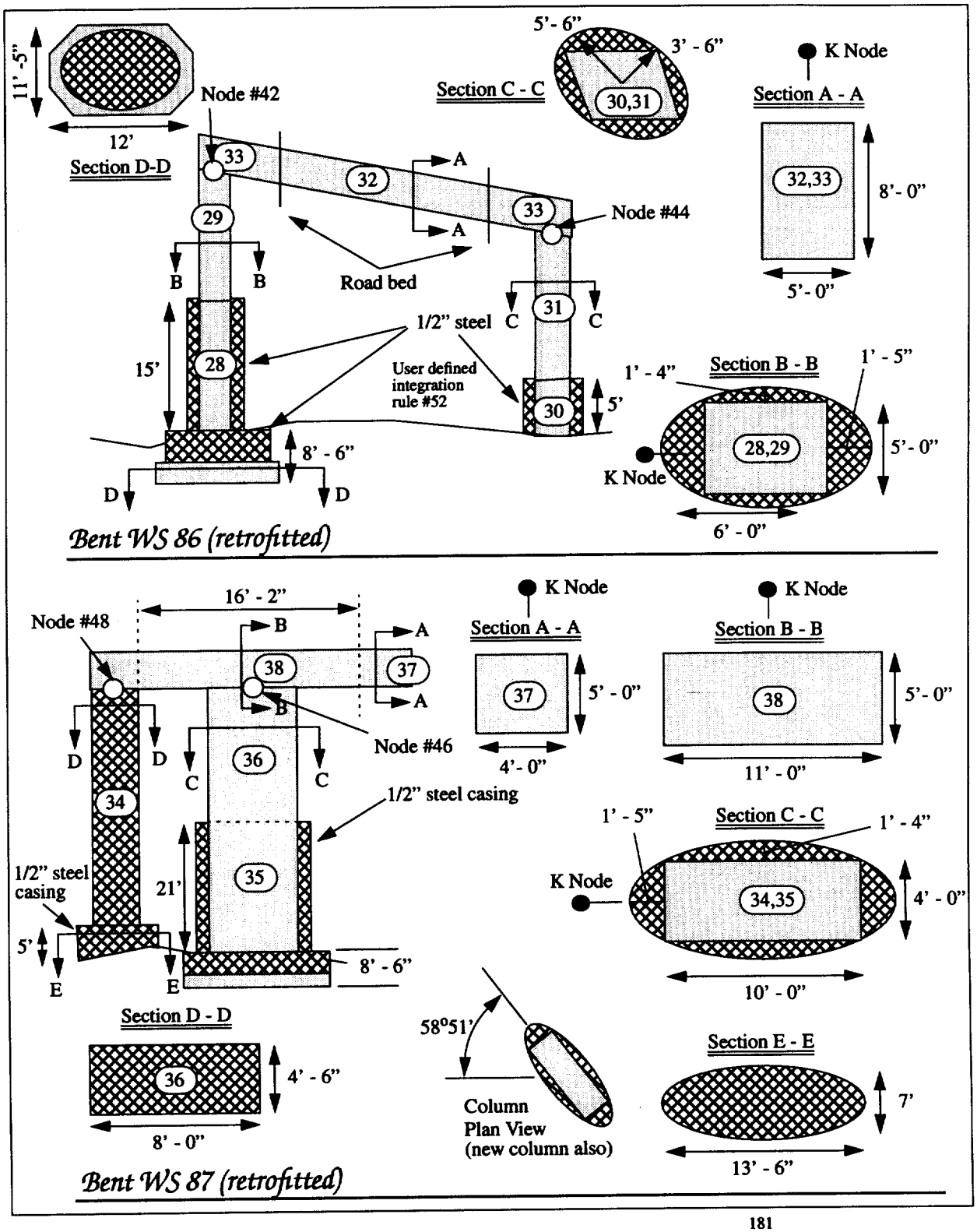
11' -5"
12'
Section D-D
Node #42
33
32
29
A
A
B
B
Road bed
33
Node #44
5'- 6"
3' - 6"
Section C - C
30,31
K Node
Section A - A
32,33
8'- 0"
5'- 0"
31
C
C
1/2" steel
15'
28
User defined
integration
rule #52
30
5'
1' - 4"
Section B - B
1' - 5"
28,29
5'- 0"
K Node
6' - 0"
8' - 6"
D
D
Bent WS 86 (retrofitted)
16' - 2"
Node #48
B
A
38
37
A
B
Node #46
K Node
Section A - A
37
5' - 0"
4'- 0"
K Node
Section B - B
38
5'- 0"
11' - 0"
D
D
C
C
36
34
1/2" steel casing
1/2" steel
casing
21'
35
5'
8' - 6"
E
E
1' - 5"
Section C - C
1' - 4"
K Node
34,35
4' - 0"
10' - 0"
Section D - D
36
4' - 6"
8' - 0"
58°51'
Column
Plan View
(new column also)
Section E - E
7'
13' - 6"
Bent WS 87 (retrofitted)

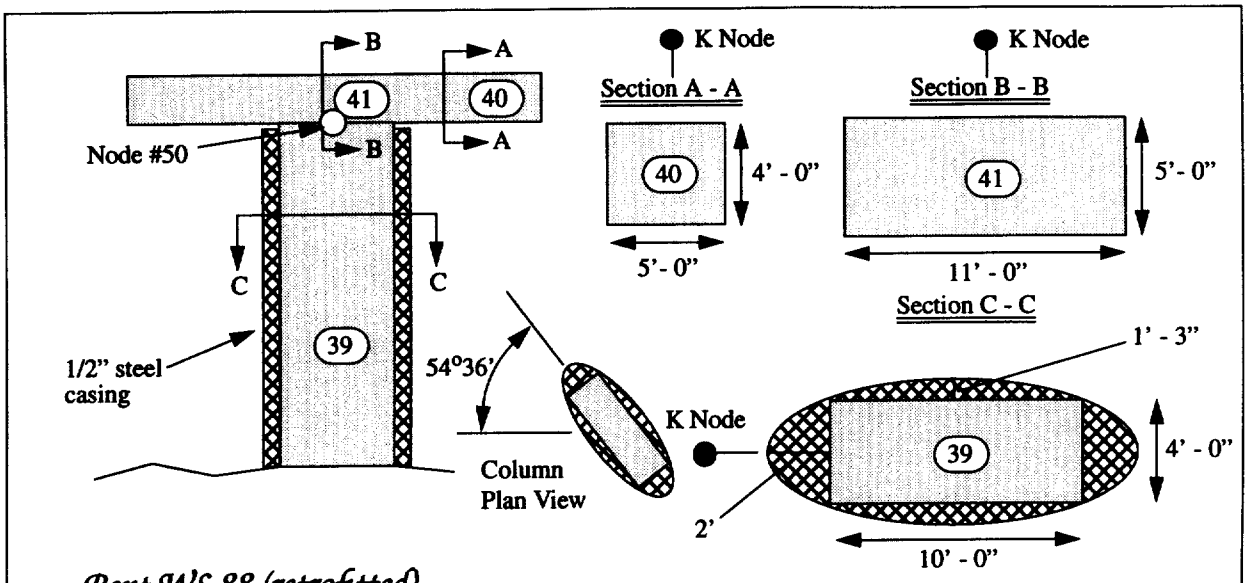

Bent WS 88 (retrofitted)

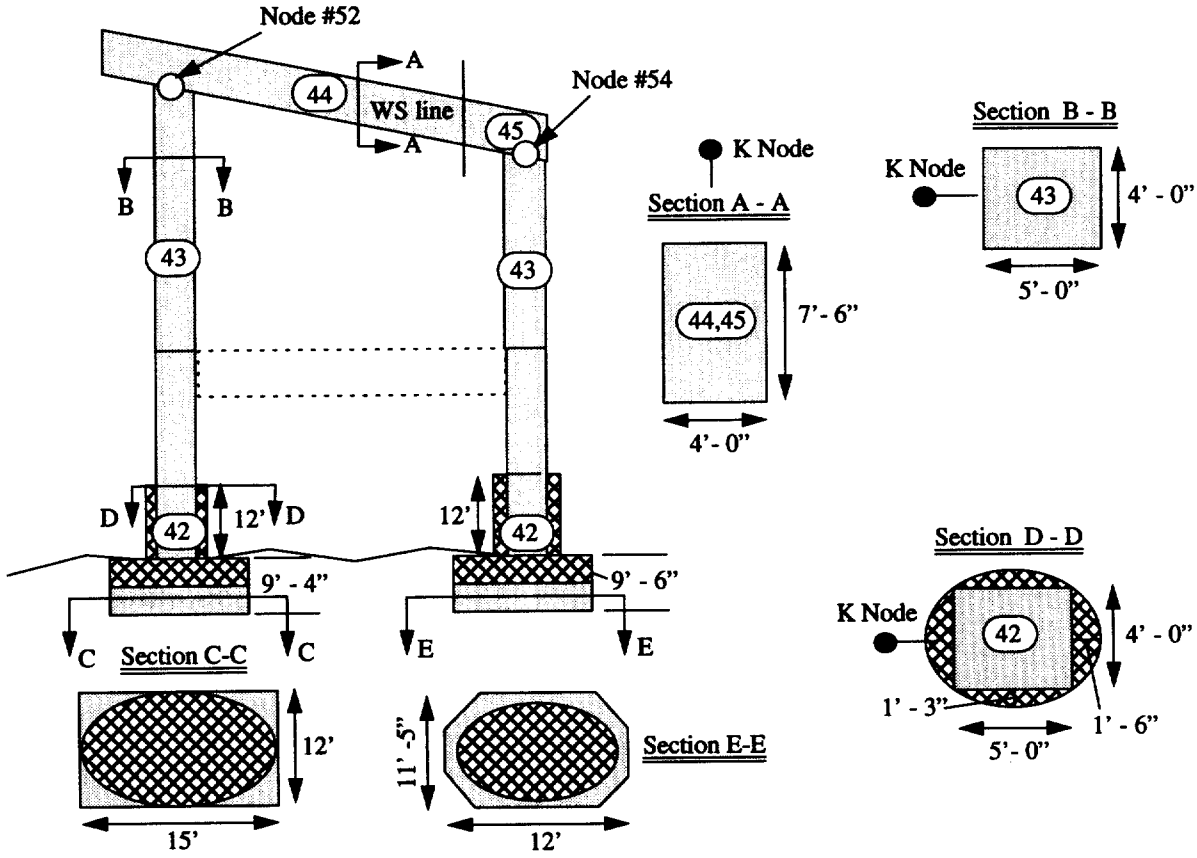

Bent WS 89 (retrofitted)

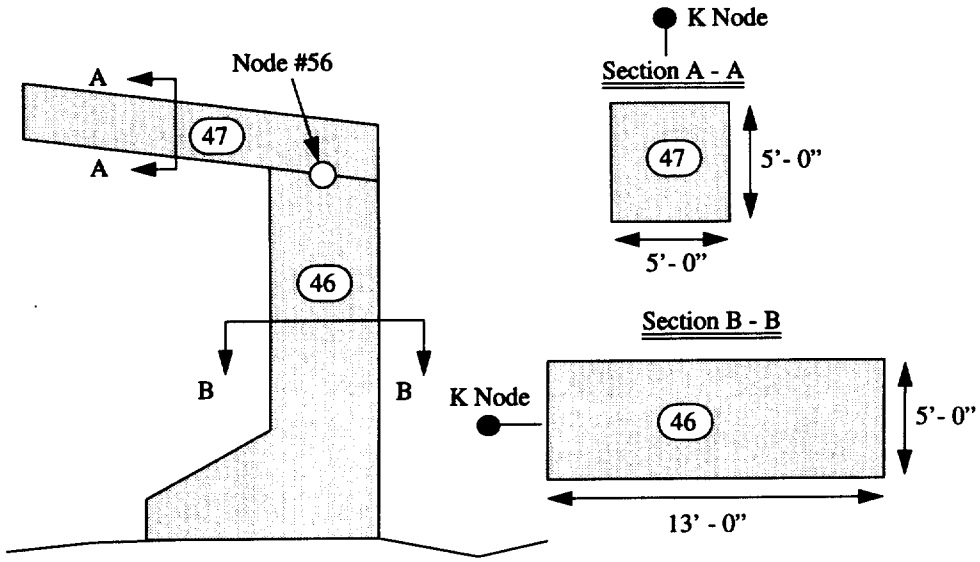

Bent WS 90 (retrofitted)

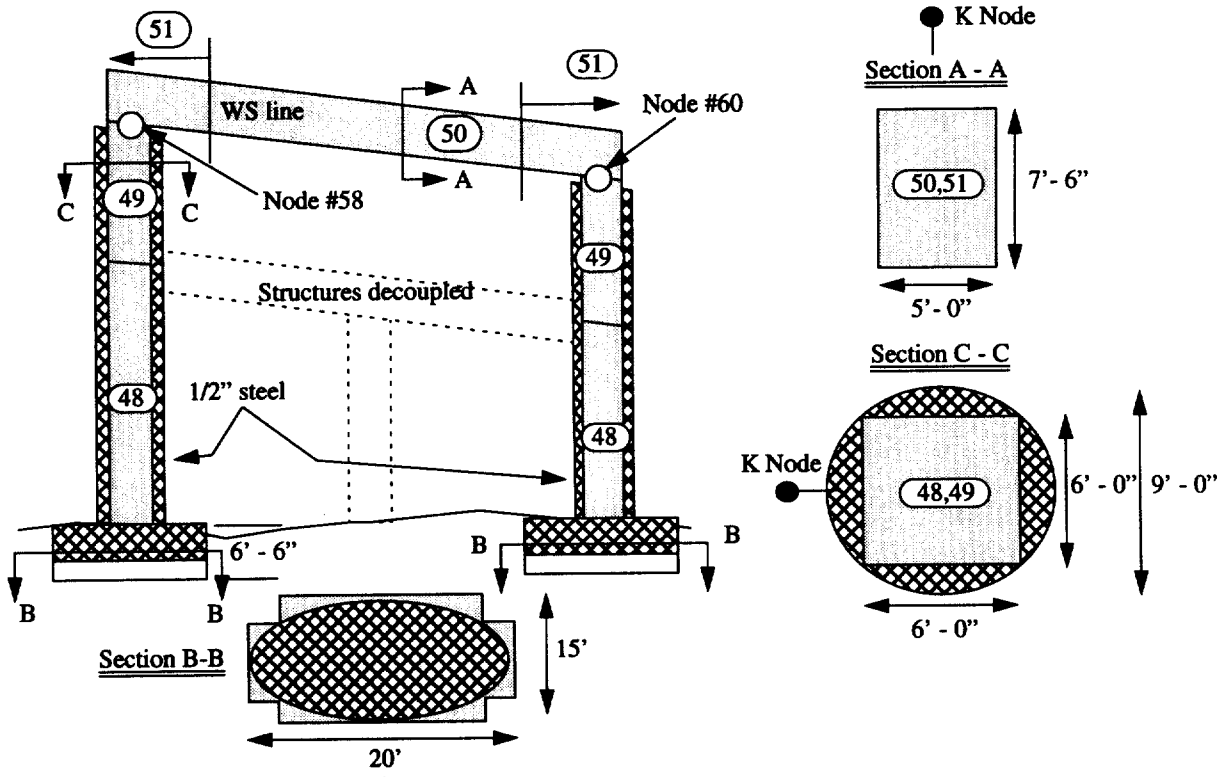

Bent WS 91 (retrofitted)

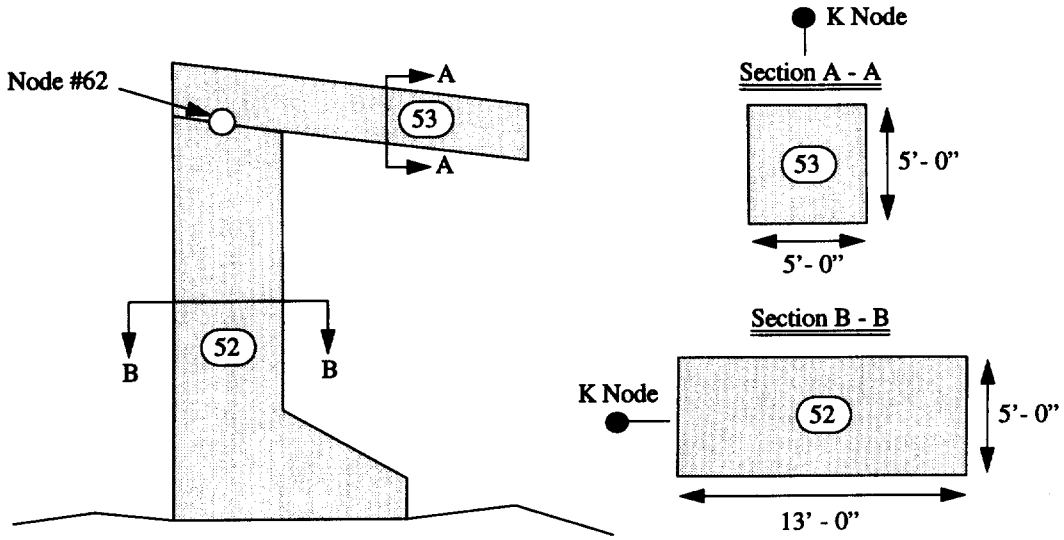

Bent WS 92 (retrofitted)

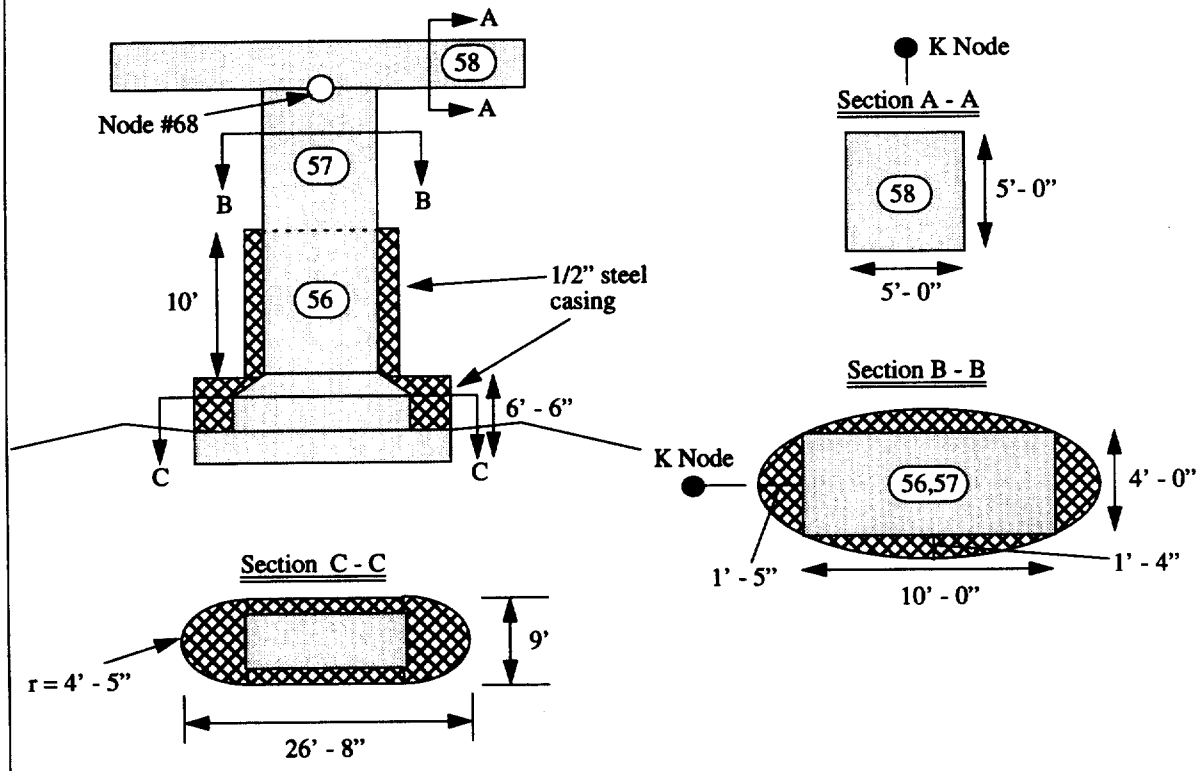

Bent WS 93 (retrofitted)

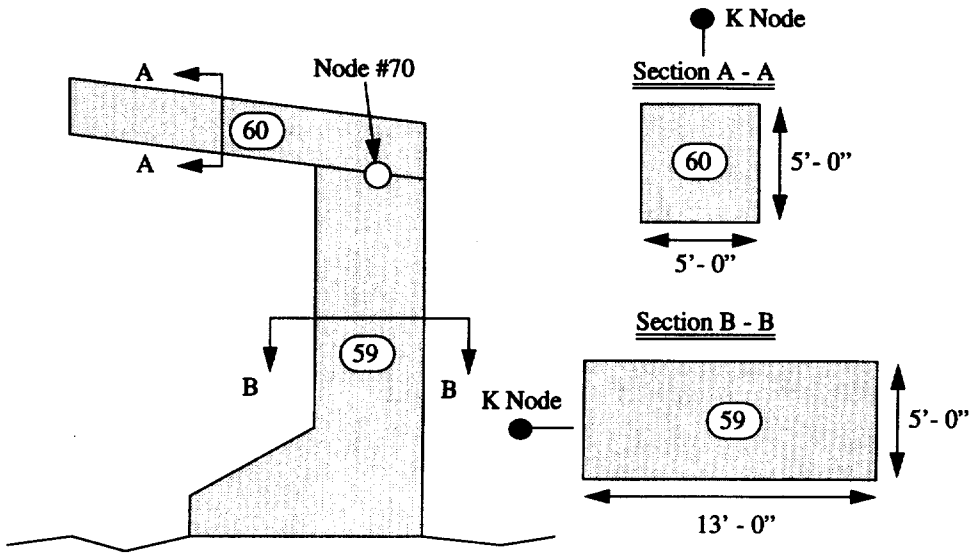

Bent WS 94 (retrofitted)

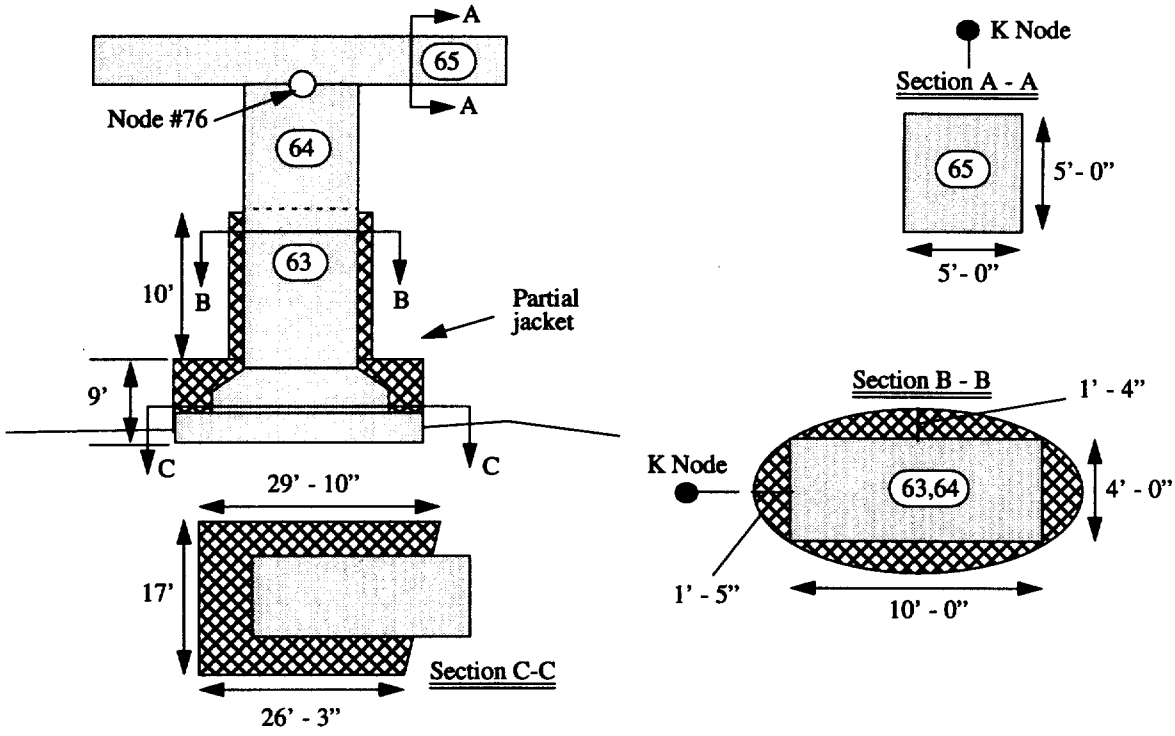

Bent WS 95 (retrofitted)

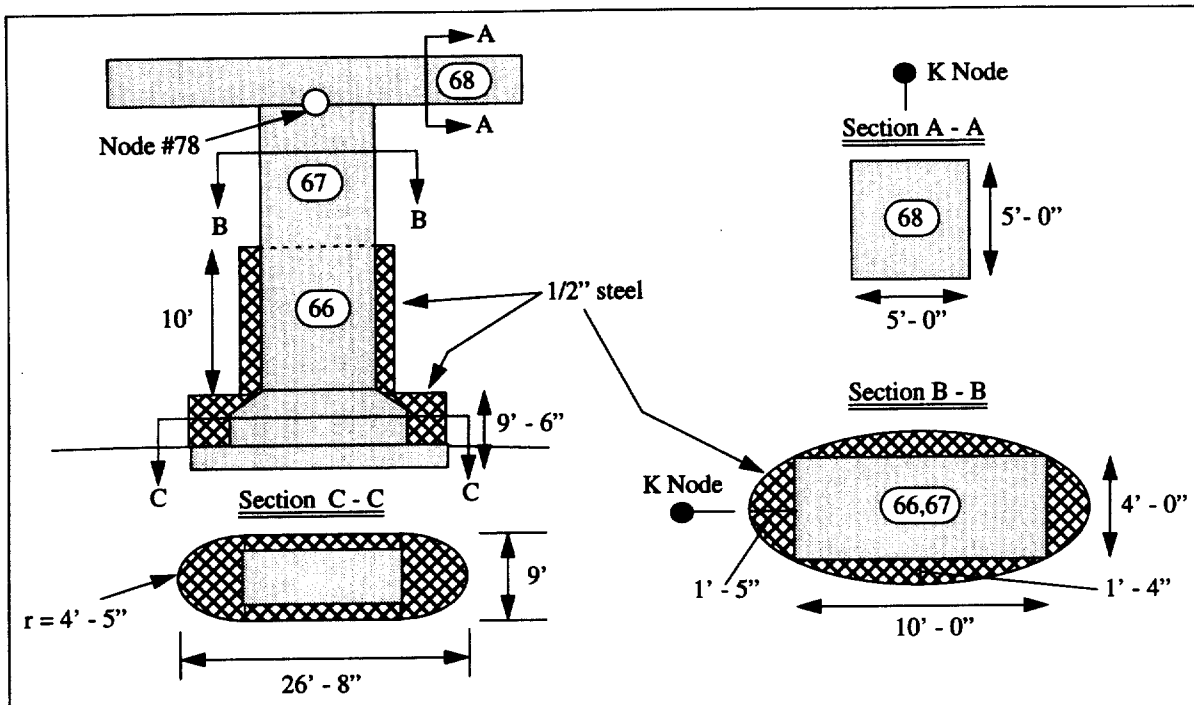

Bent WS 96 (retrofitted)

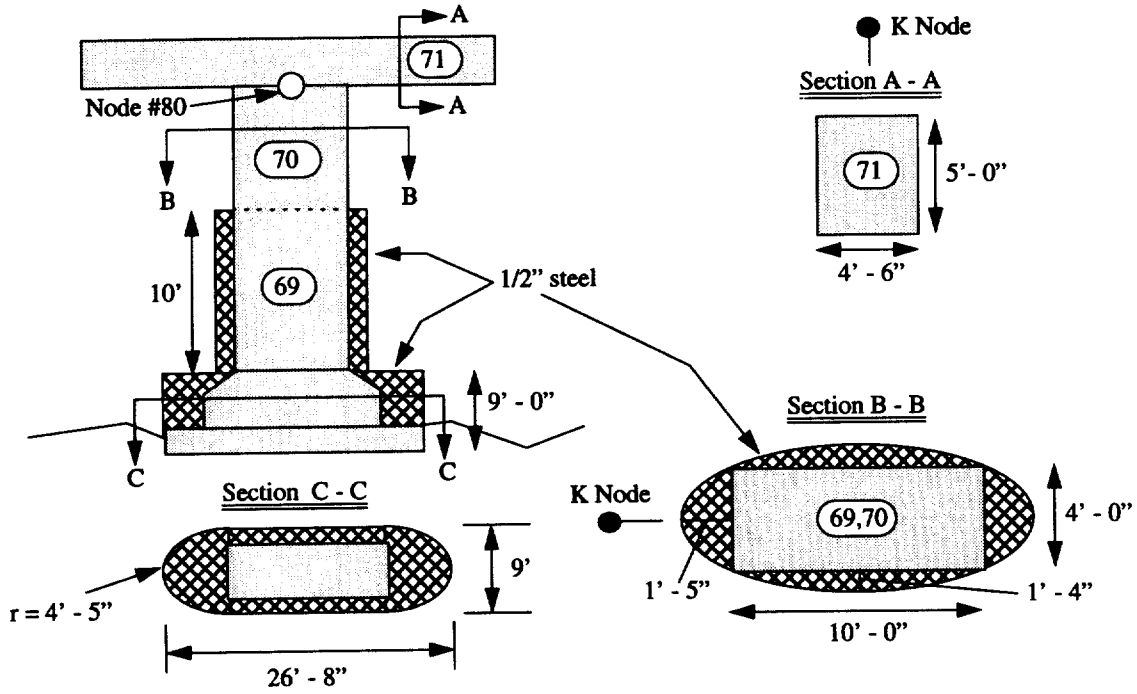

Bent WS 97 (retrofitted)

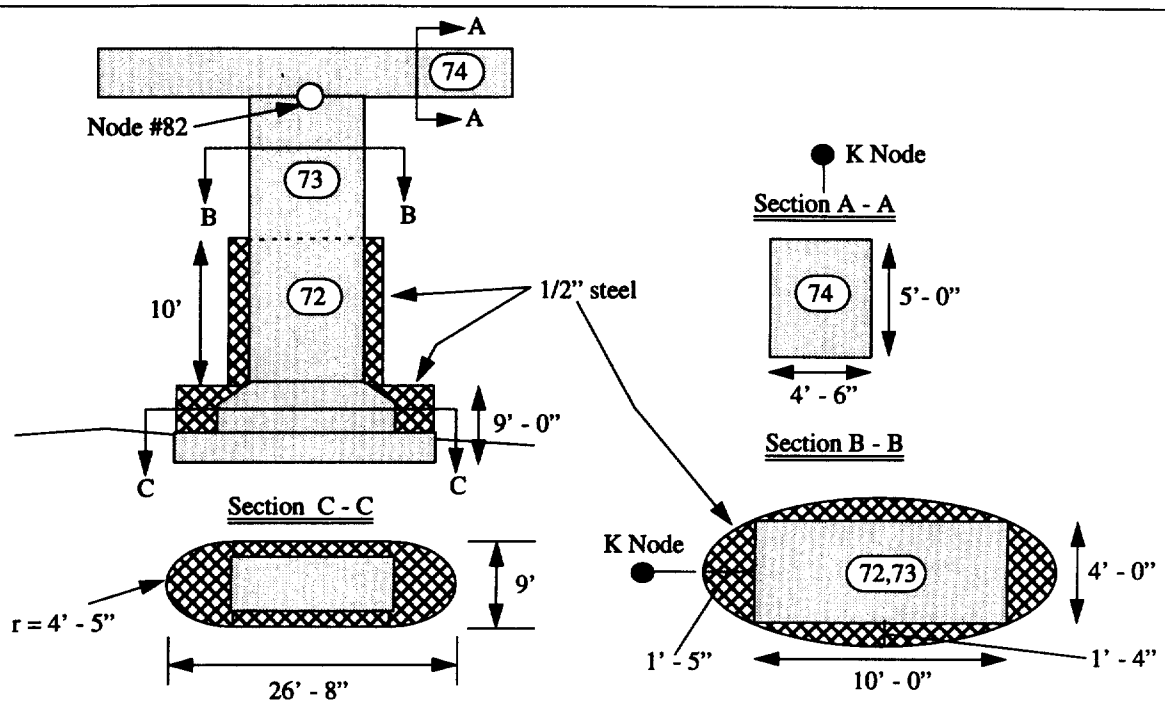

Bent WS 98 (retrofitted)

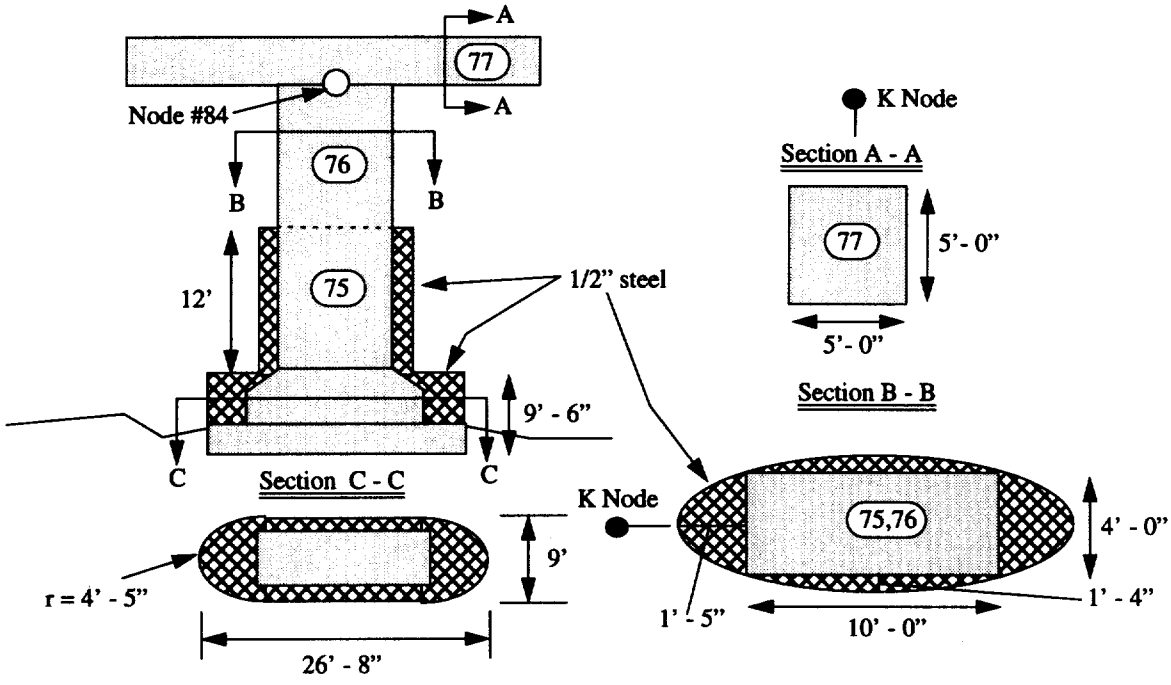

Bent ES 12 (retrofitted)

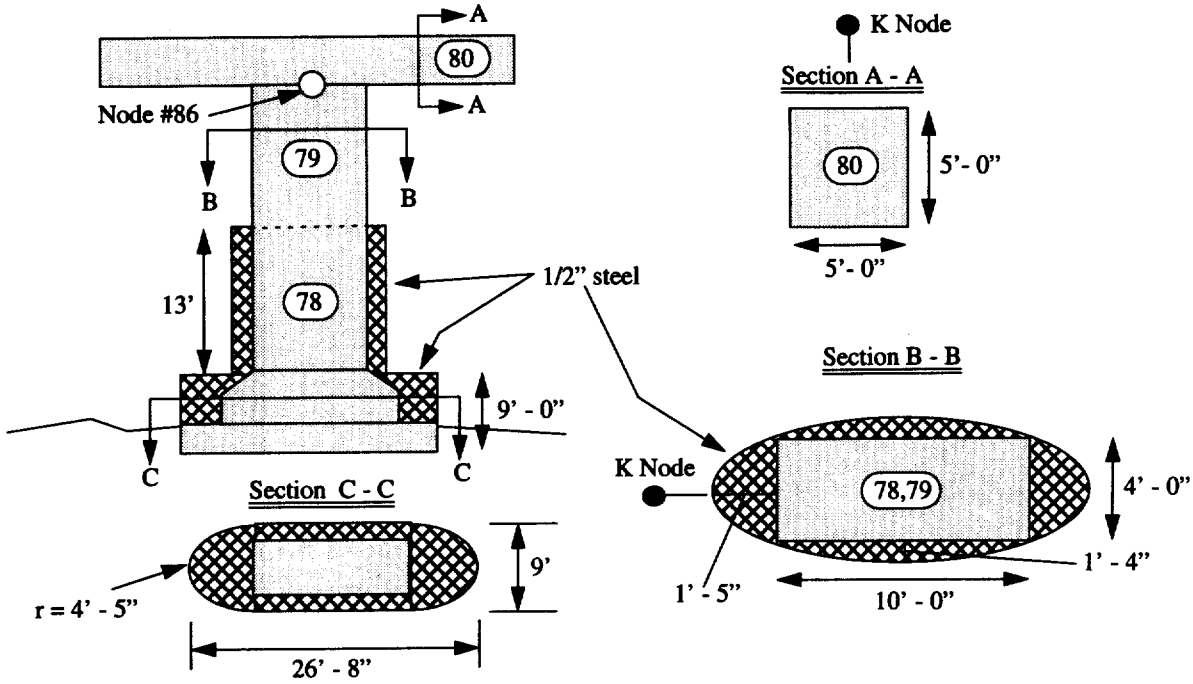

Bent ES 11 (retrofitted)

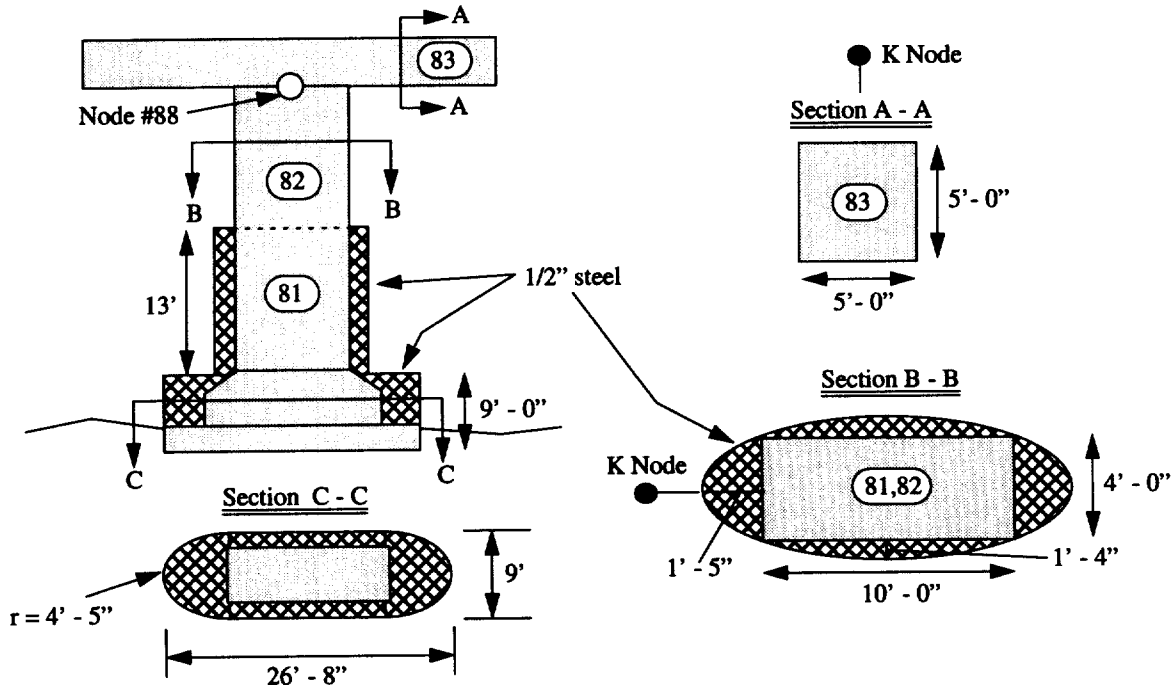

Bent ES 10 (retrofitted)

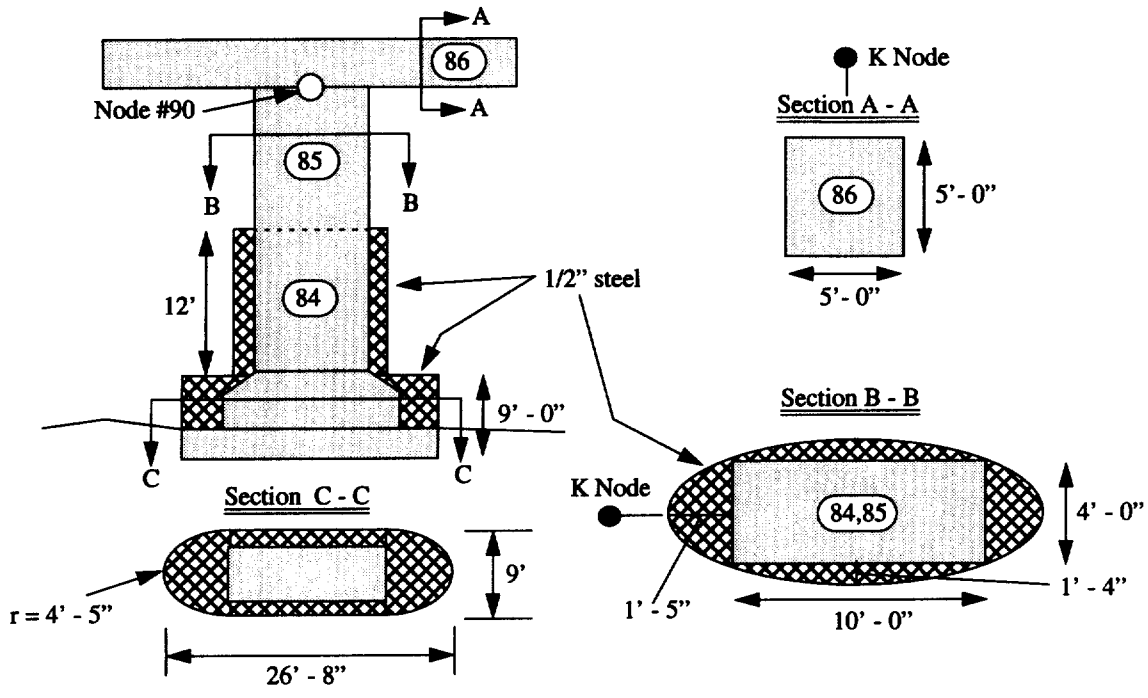

Bent ES 9 (retrofitted)

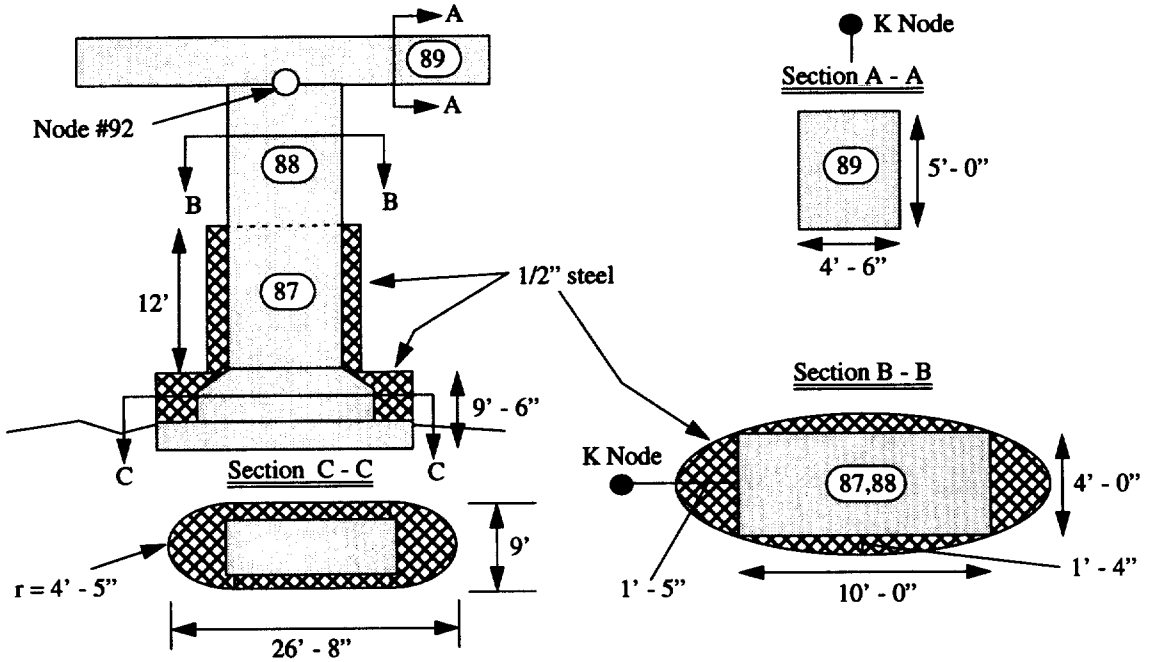

Bent ES 8 (retrofitted)

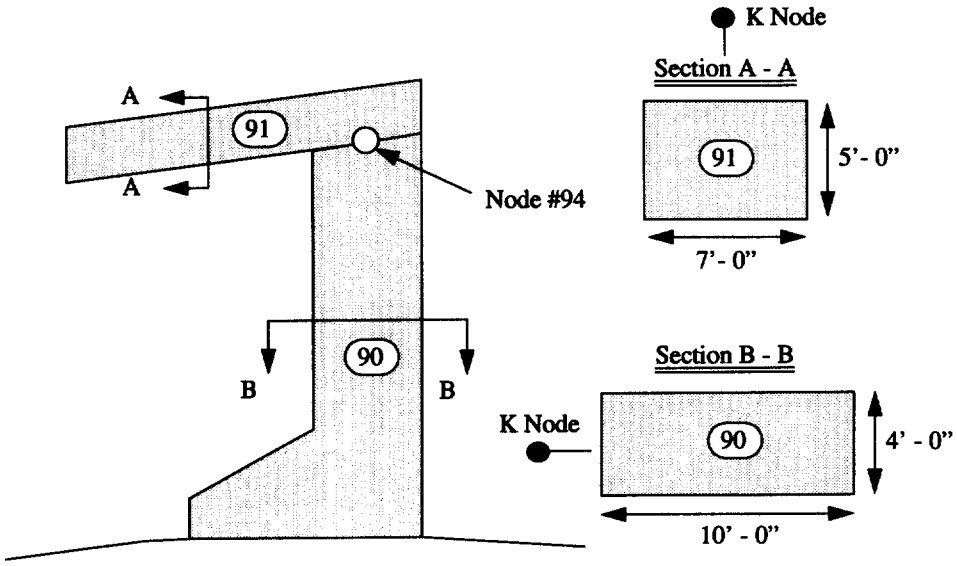

Bent ES 7 (retrofitted)

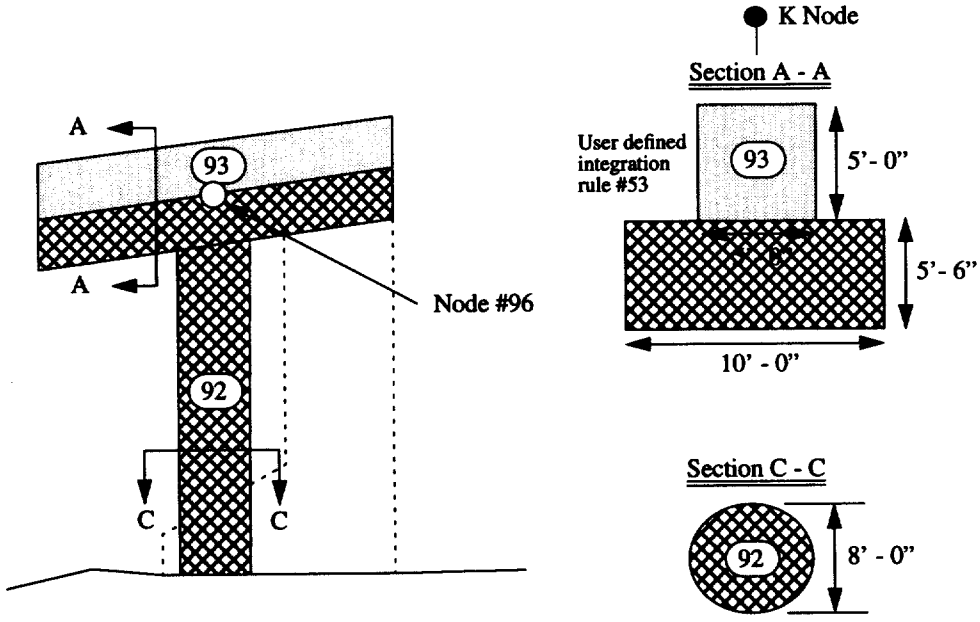

Bent ES 6 (retrofitted)

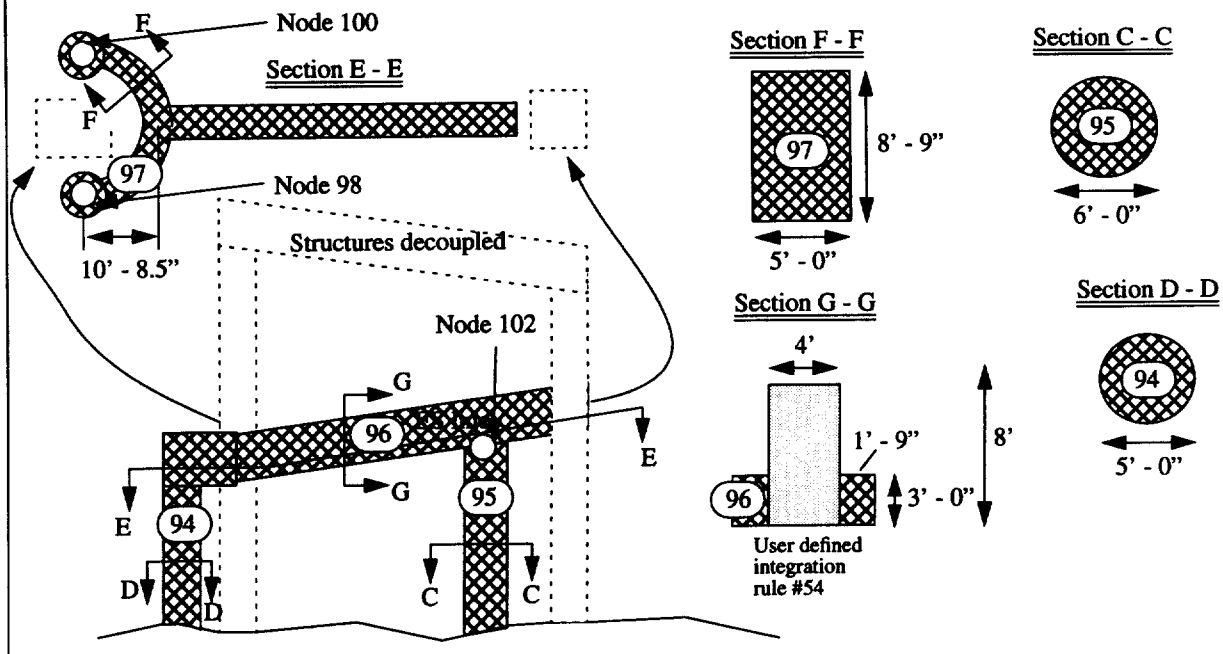

Bent ES 5 (retrofitted)

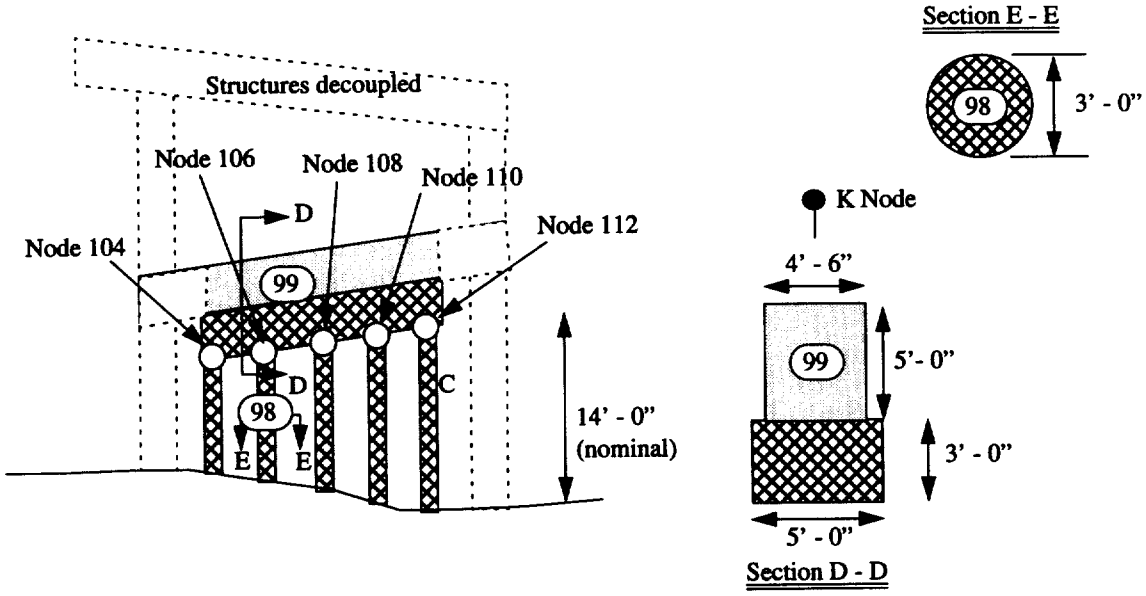

Bent ES 4 (retrofitted)

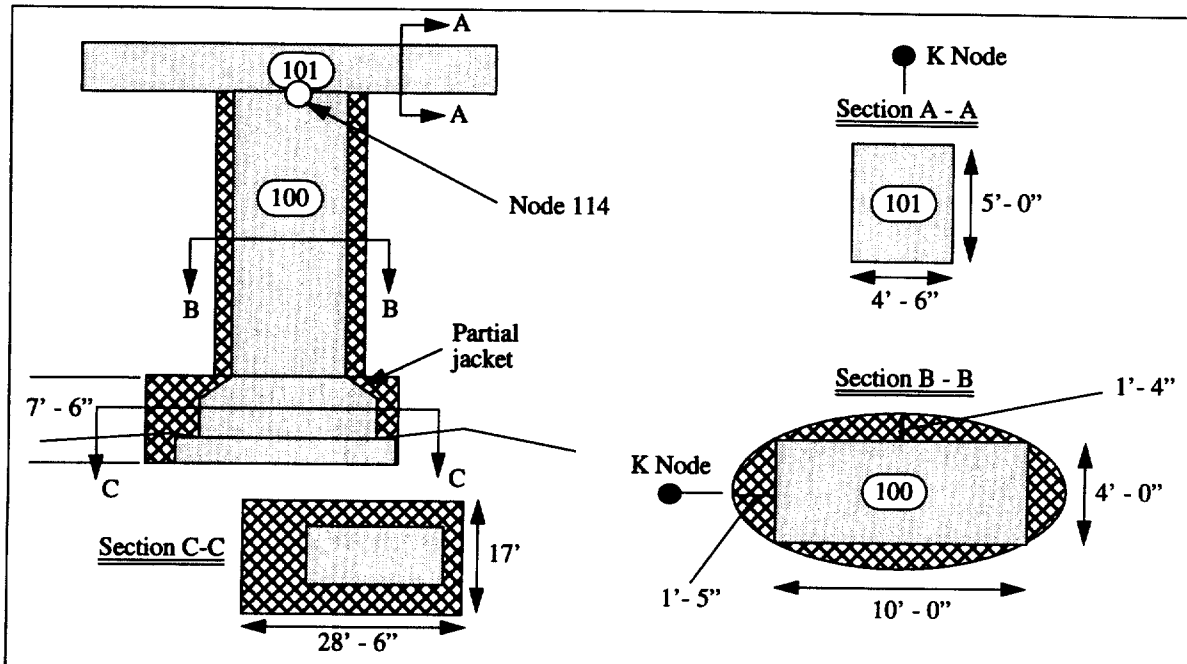

Bent ES 3 (retrofitted)

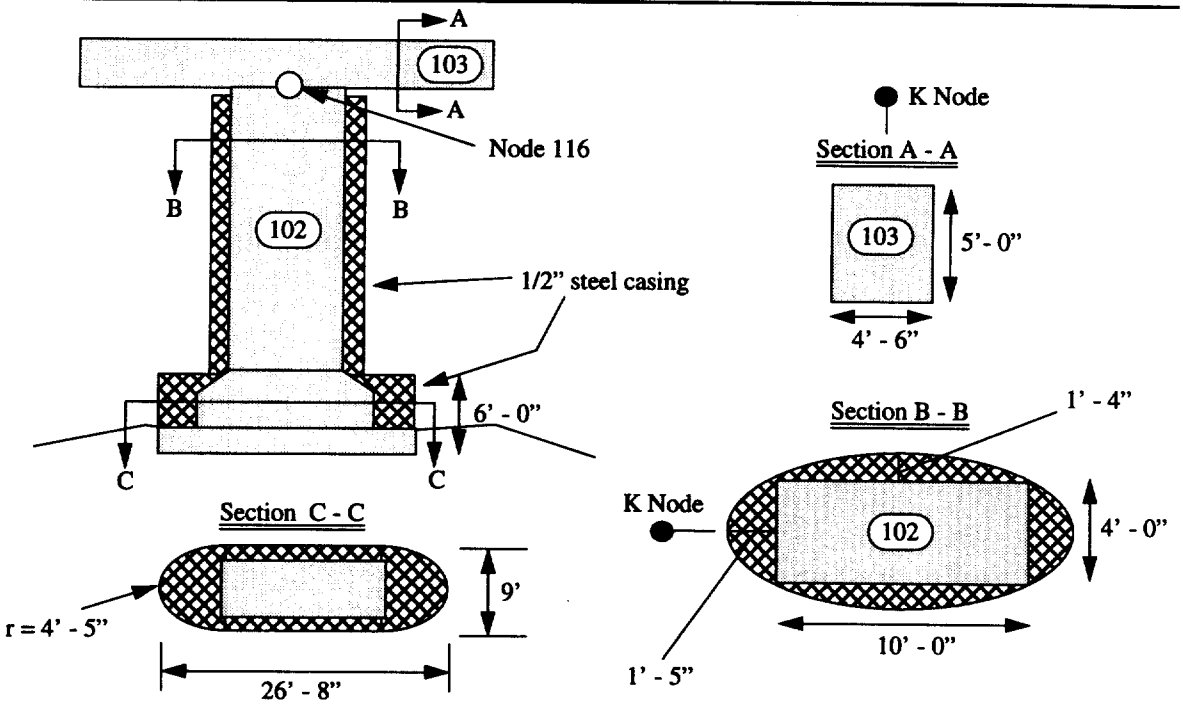

Bent ES 2 (retrofitted)

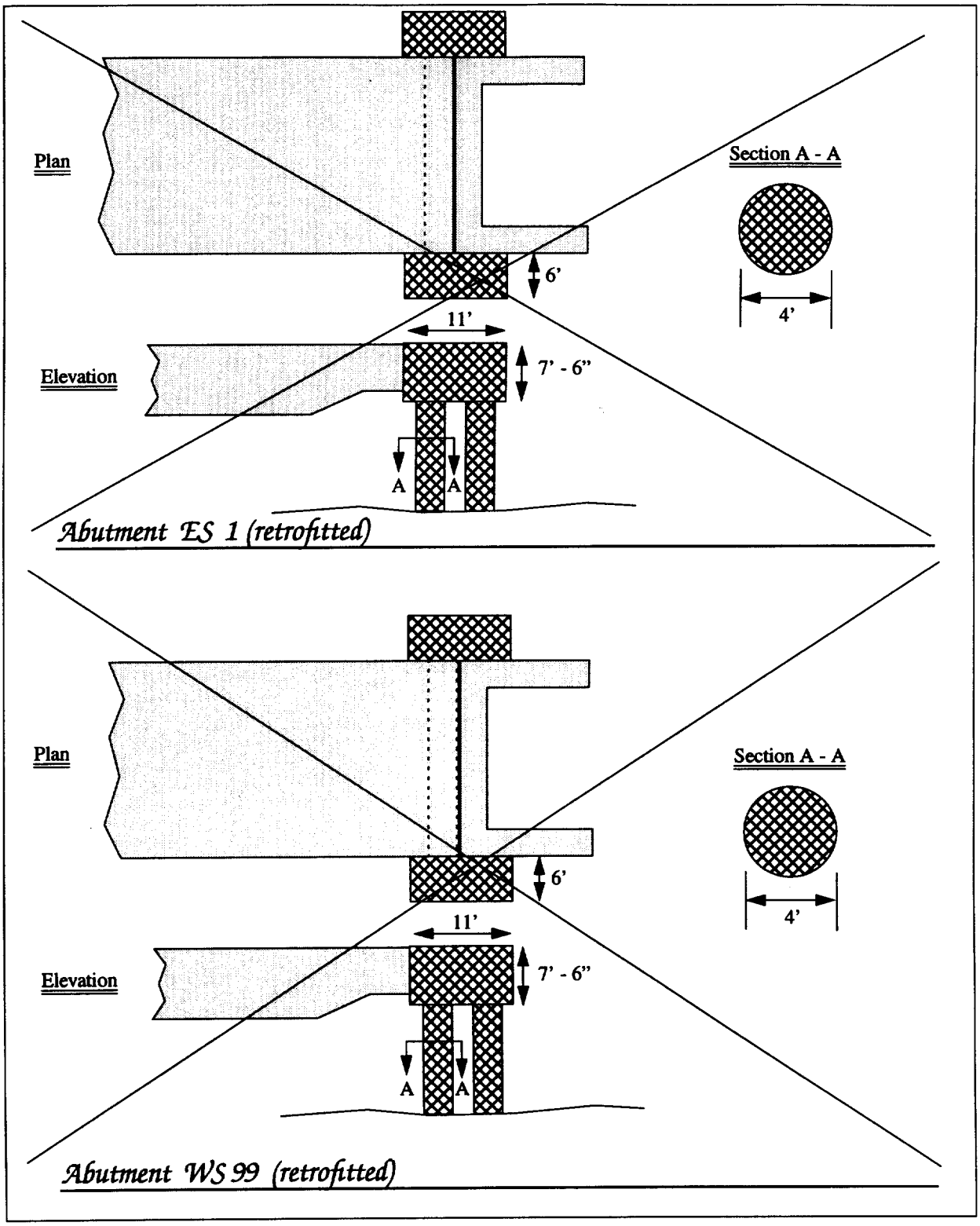
Plan
Section A - A
6'
4'
11'
Elevation
7' - 6"
A
A
Abutment ES 1 (retrofitted)
Plan
Section A - A
6'
4'
11'
Elevation
7' - 6"
A
A
Abutment WS 99 (retrofitted)

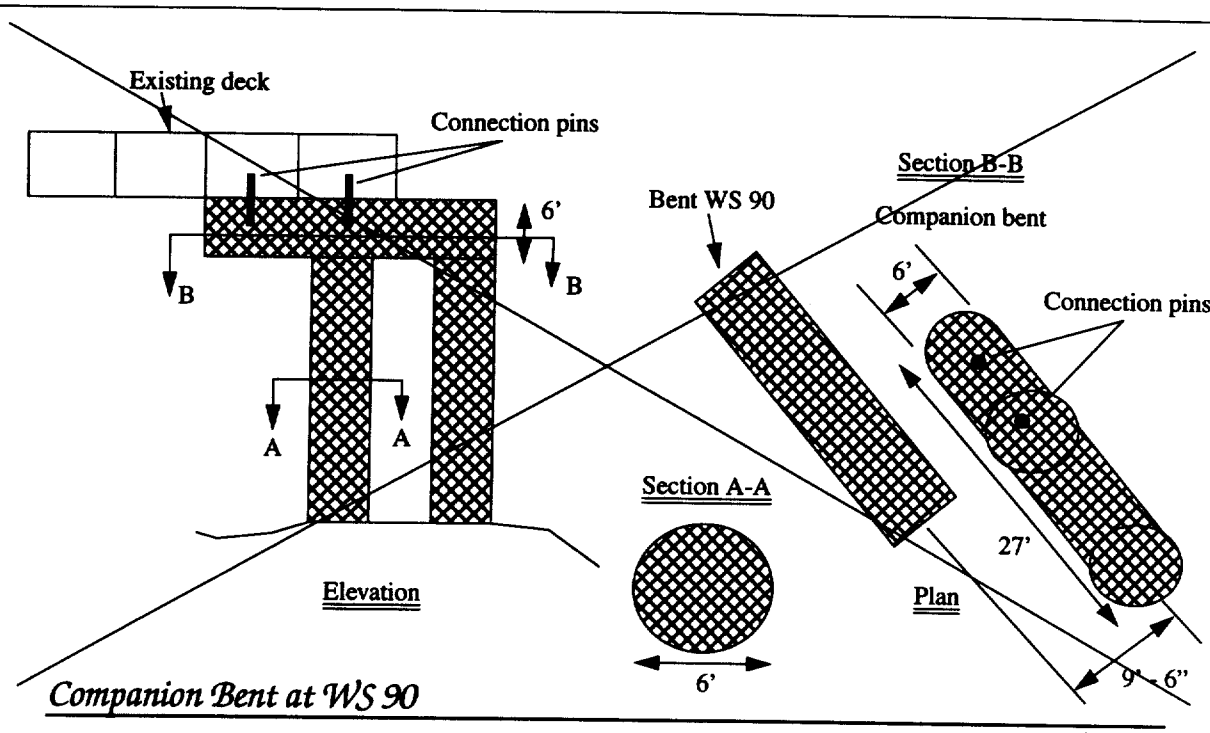

Companion Bent at WS 90

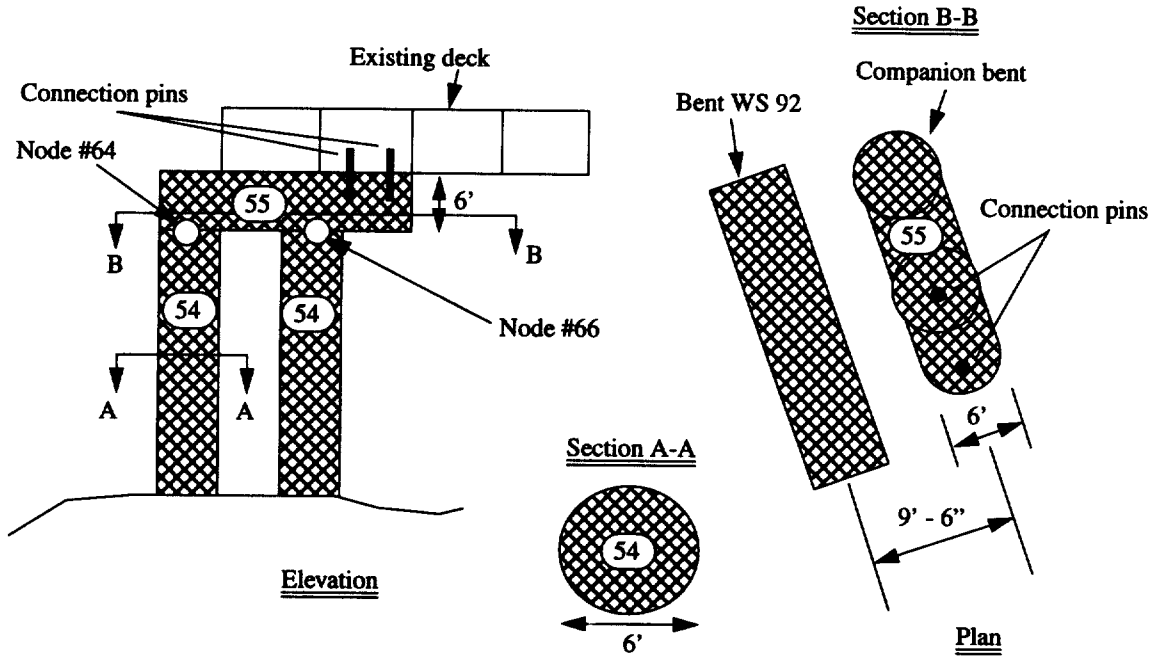

Companion Bent at WS 92

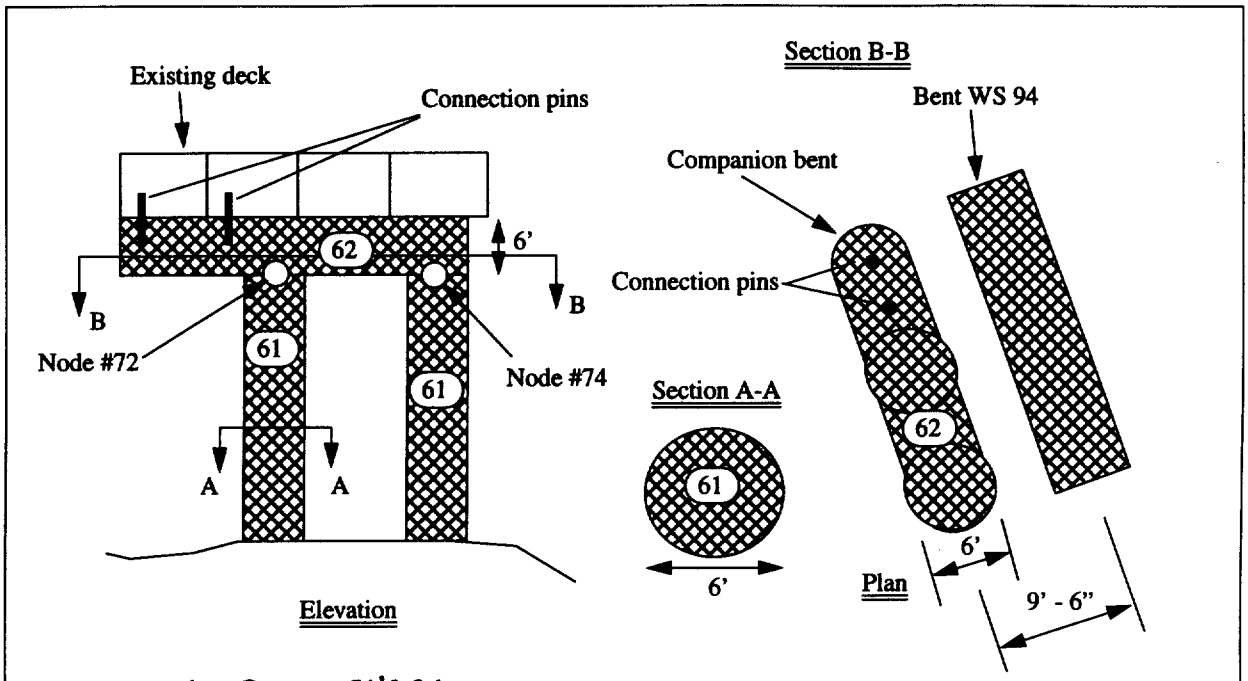

Companion Bent at WS 94

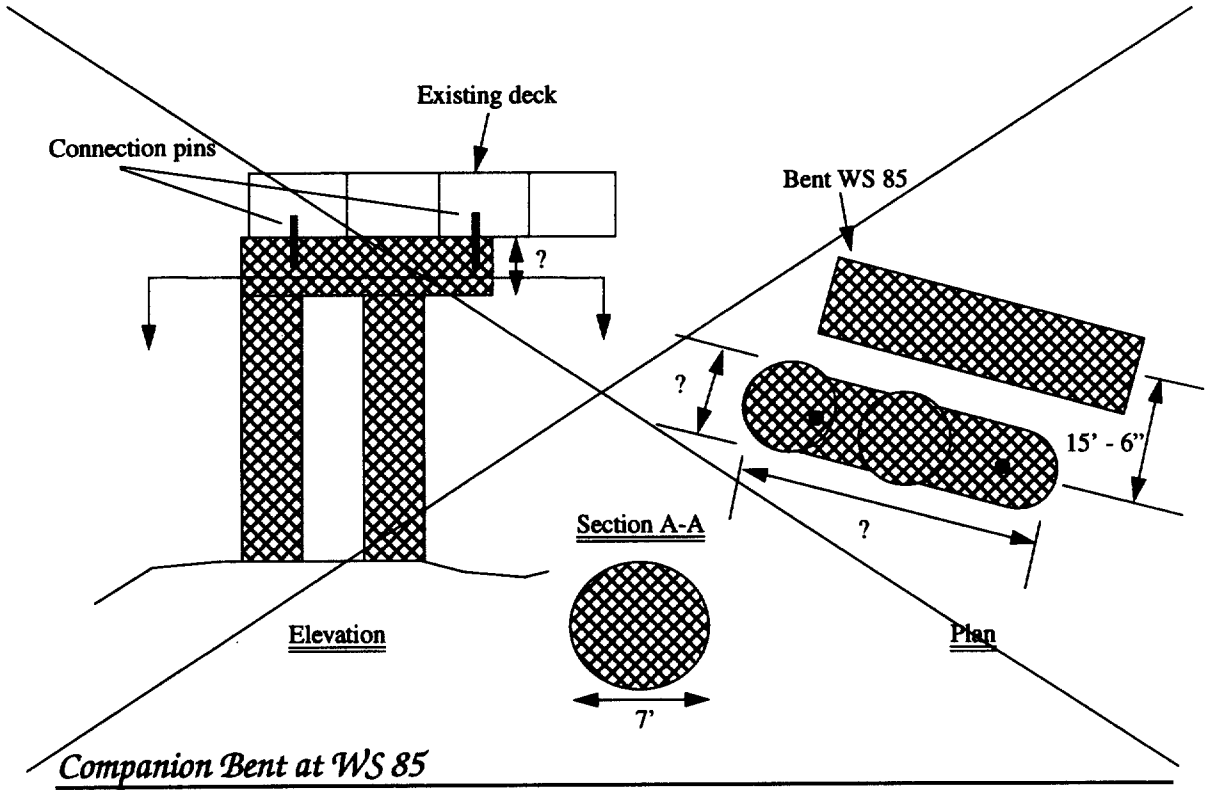

Companion Bent at WS 85

Area	ξ	η	Weight
1	-0.535714	-0.820513	126.2233
2	-0.178571	-0.967949	121.3191
3	0.178571	-0.967949	121.3191
4	0.535714	-0.820513	126.2233
5	0.821429	-0.544872	88.3159
6	0.964286	-0.192308	65.1066
7	0.964286	0.192308	65.1066
8	0.821429	0.544872	88.3159
9	0.535714	0.820513	126.2233
10	0.178571	0.967949	121.3191
11	-0.178571	0.967949	121.3191
12	-0.535714	0.820513	126.2233
13	-0.821429	0.544872	88.3159
14	-0.964286	0.192308	65.1066
15	-0.964286	-0.192308	65.1066
16	-0.821429	-0.544872	88.3159
17	-0.500000	-0.628205	447.0000
18	-0.166667	-0.701923	583.5000
19	0.166667	-0.701923	583.5000
20	0.500000	-0.628205	447.0000
21	-0.500000	0.628205	447.0000
22	-0.166667	0.701923	583.5000
23	0.166667	0.701923	583.5000
24	0.500000	0.628205	447.0000
25	-0.720238	-0.435897	255.0000
26	0.720238	-0.435897	255.0000
27	-0.791667	-0.150641	350.5000
28	0.791667	-0.150641	350.5000
29	-0.791667	0.150641	350.5000
30	0.791667	0.150641	350.5000
31	-0.720238	0.435897	255.0000
32	0.720238	0.435897	255.0000
33	-0.309524	-0.217949	884.0000
34	0.309524	-0.217949	884.0000

Area	ξ	η	Weight
35	-0.309524	0.217949	884.0000
36	0.309524	0.217949	884.0000

Bent WS88

$A_{rel} = 0.891625$

$f_{avg} = 0.9$

b=168

h=78

Area	ξ	η	Weight
1	-0.584416	-0.800000	127.4398
2	-0.194805	-0.962500	121.5030
3	0.194805	-0.962500	121.5030
4	0.584416	-0.800000	127.4398
5	0.863636	-0.512500	74.0907
6	0.974026	-0.175000	58.6777
7	0.974026	0.175000	58.6777
8	0.863636	0.512500	74.0907
9	0.584416	0.800000	127.4398
10	0.194805	0.962500	121.5030
11	-0.194805	0.962500	121.5030
12	-0.584416	0.800000	127.4398
13	-0.863636	0.512500	74.0907
14	-0.974026	0.175000	58.6777
15	-0.974026	-0.175000	58.6777
16	-0.863636	-0.512500	74.0907
17	-0.545455	-0.612500	450.0000
18	-0.181818	-0.693750	605.0000
19	0.181818	-0.693750	605.0000
20	0.545455	-0.612500	450.0000
21	-0.545455	0.612500	450.0000
22	-0.181818	0.693750	605.0000
23	0.181818	0.693750	605.0000
24	0.545455	0.612500	450.0000
25	-0.769481	-0.415625	206.2500
26	0.769481	-0.415625	206.2500
27	-0.824675	-0.140625	264.2500
28	0.824675	-0.140625	264.2500
29	-0.824675	0.140625	264.2500
30	0.824675	0.140625	264.2500
31	-0.769481	0.415625	206.2500
32	0.769481	0.415625	206.2500
33	-0.506494	-0.318750	221.0000
34	-0.168831	-0.318750	221.0000
35	0.168831	-0.318750	221.0000
36	0.506494	-0.318750	221.0000

Area	ξ	η	Weight
37	-0.506494	-0.106250	221.0000
38	-0.168831	-0.106250	221.0000
39	0.168831	-0.106250	221.0000
40	0.506494	-0.106250	221.0000
41	-0.506494	0.106250	221.0000
42	-0.168831	0.106250	221.0000
43	0.168831	0.106250	221.0000
44	0.506494	0.106250	221.0000
45	-0.506494	0.318750	221.0000
46	-0.168831	0.318750	221.0000
47	0.168831	0.318750	221.0000
48	0.506494	0.318750	221.0000

$A_{rel} = 0.906237$
$f_{avg} = 0.9$
b=154
h=80

Bents WS83, WS84, WS87, WS93, WS96, WS97, WS98
ES2, ES8, ES9, ES10, ES11, ES12

Technical Information Department • **Lawrence Livermore National Laboratory**
University of California • Livermore, California 94551